The University Of Sheffield.

Fibre-meshed Textile Electromagnetic Structures

By:

Xiaobin Jia

A thesis submitted in partial fulfilment of the requirements for the degree of Doctor of Philosophy

The University of Sheffield
Faculty of Engineering
Department of Electronic and Electrical Engineering

28/01/2020

Abstract

Over recent decades, electromagnetic components fabricated with commercial textiles have gained significant attention from both industry and academia. They are mainly designed for wearable applications in body-centric communication systems as they can be seamlessly integrated with garments. Compared with traditional electromagnetic components which are normally manufactured from hard materials such as metal, textile-based electronics provide unique advantages such as flexibility, light weight and softness.

This thesis investigated novel textile electromagnetic structures fabricated by a commercial computerized knitting machine. Different electronics such as elliptical waveguides, slotted waveguide antennas (SWA) and frequency selective surfaces (FSS) working at microwave band had been realized with fully textile materials. Knitted polyester was used as a dielectric and silver embedded yarn was knitted to create conducting patterns. Most of the textile electromagnetic structures in this thesis were the first time proposed to the public. Their performances were studied in both simulation and measurement.

Unlike the conventional electromagnetic components, textile structures always experience undesired deformation because they are soft and flexible. In this thesis, a knitted elliptical waveguide was firstly proposed and tested when it was bent to different angles and directions. Results demonstrated that a knitted waveguide bend still provided stable performance. Moreover, textiles are easy to get wet in practice as they normally cannot be well protected within solid enclosures. Moisture effects on textile waveguide performance was also studied. Then, a knitted slotted waveguide antenna was developed from the waveguide and investigated under different conditions. Lastly, two different types of knitted textile FSS were presented and evaluated. One was a cross slot textile FSS which filled the research gap in band-pass textile FSS and other one was ultra-light weight loop FSSs.

Acknowledgement

My story starts from here.

In Sep 2009, I was 19 and it was my first time to go abroad. With a little excitement, curiosity and panic, I started my undergraduate study in EEE department, the University of Sheffield. At that time, I never expect I would stay here for such a long time. I lived here, grew up here, and got all my Bachelor, MSc and PhD degrees here. This year (2019) was the 10th year I have been living here, well, time does really fly! After all these years, Sheffield meant a lot more than just a city or a university to me. Word cannot express my feelings, Thank you, City of Sheffield! Love you, The University of Sheffield!

First of all, I would like to express my sincere thanks to all the staffs in EEE department, not only for your outstanding teaching and lectures, but also the patience and timely help. Special gratitude to my supervisors, Prof Alan Tennant and Prof. Richard J Langley. It is my honor to finish PhD study under their splendid supervision. Their constant encouragement, valuable suggestions make this hard work much easier. Great credit to Dr Simon Bai, he is not only a wise mentor, also a great friend to me. Every time I encounter any problem no matter from work or life, he is always here to help me.

Many thanks to Dr. K. Lee Ford, Dr. Salam Khamas, Dr. Jonathan Rigelsford, Dr. Wei Liu, Mr. Steve Marsden from Communication and Radar Group, Mr Wayne Frankish from EEE workshop and Dr. Paul Webster from Diamond, for their academic help and technical support during all these years. I am also grateful to Prof. Jie Zhang and Dr. Xiaoli Chu, for attending my first-year confirmation review with valuable feedback.

My dear friends Dayle Dai, Wendy Hu, Huayang Xu, Sijin Hu, Wenfei Yin, Fan Wu, I am deeply appreciated our great friendship throughout all these years, you guys are always by my side when I need someone to talk and make me never feel lonely.

Last but not least, particular love to my parents. They are my best support all the time. Without their constant love, it is impossible to finish my oversea study.

Thanks, and love you all.

Publications

1. X. Jia, A. Tennant, “A Knitted Textile Waveguide”, *Antennas and Propagation Conference (LAPC)*, Loughborough, IEEE, P: 679-682, Nov 2014.

2. X. Jia, A. Tennant, “Knitted Textile Waveguide Bending”, *Antennas and Propagation (EUCAP)*, Portugal, 9th European Conference, IEEE, P:1-4, April 2015.

3. X. Jia, A. Tennant, R. Langley “A Knitted Slotted Waveguide Antenna”, *Antennas and Propagation Conference (LAPC)*, Loughborough, IEEE, Nov 2015. (Did not choose to publish)

4. X. Jia, A. Tennant, R. Langley, “A Knitted Waveguide Antenna”, *Antennas and Propagation (EUCAP)*, Switzerland, 10th European Conference, IEEE, April 2016. (Did not choose to publish)

5. X. Jia, A. Tennant, “Moisture Effects on a Knitted Waveguide”, *Antennas and Propagation Conference* (LAPC), Loughborough, IEEE, P: 1-3, Nov 2016.

6. X. Jia and A. Tennant, “A Knitted Slotted Waveguide Antenna and Bending”. (Finished, prepare for Journal)

7. X. Jia and A. Tennant, “Knitted Textile Slotted Frequency Selective Surfaces”. (Finished, prepare for Journal)

8. X. Jia and A. Tennant, “Experimental Ultra-Light-Weight, Knitted Textile Frequency Selective Surface”. (Finished, prepare for Letters)

Contents

Chapter 1. Introduction

1.1 History of Smart Clothing

Almost everyone wears clothing. It keeps us warm, as well as provides the basic protection from the environment. Most of modern garments are fabricated with textiles, which make them comfortable for daily wearing. Benefitting from the rapid development of technology in the last decades, nowadays, more people use smart devices like laptop or smart phone for work and leisure. By integrating traditional clothing and smart devices, smart clothing has become a new trend. It is widely believed that there are three markable steps in the development of smart clothing.

- "Electronics are attached to a garment"

The history of smart clothing might be traced back to 1985, when Harry Wainwright invented a sweatshirt with numbers of electronic components on it. This shirt was able to display a vivid cartoon charter on its surface and was a very early successful approach to attach electronics to a daily clothing [1]. Later in the early 1990s, Steve Mann who was known as "the father of the wearable computer", built the first prototype of a programmable wearable computer [2]. This sophisticated device as shown in Fig.1.14 opened a new path for smart clothing, as it permitted feasibility to attach electronics to daily clothing and perform multiple complex tasks. Benefiting from the rapid development of microchip and circuit integration technology in the last few decades, electronics had made significant achievements in size miniaturization. As the results of the evolution of wireless communications technology, the demand for "Wireless Body Area Networks (WBANs)" increased rapidly. In 1993, the first example of personal communications system named "Body Net" was proposed by Olin Shivers [3]. As a pioneer, he listed the essential components of a personal network architecture including: a computer, communicator, visual display, audio I/O, gestural input, exotic devices, GPS sensor, medical monitor, eye and head sensor. Later, in 1996, T. Zimmerman detailed the infrastructure of "Personal Area Network (PAN)" and developed a PAN prototype in which coupled devices used human body as a channel to exchange information [4]. At this early stage, researches mainly

focused on assembling existing electronics like watches, cellular phones and computers to get rid of the redundant components such as battery, display and control interface. In this way, the compact integrated system might be placed into a small bag to carry for a long time. However, most devices at the time were fabricated by the traditional materials and manufacturing techniques, users suffered uncomfortable wearing due to their weight and rigidity.

Fig.1.11 Steve Mann with his prototype of wearable computer in the early 1990s [2]

- "Electronics are embedded in a garment"

In 2000, Levi's and Philips launched an ICD+ (Industrial Clothing Division) jacket which was believed to be the first garment-like smart cloth in the market as shown in Fig.1.12 [5]. Portable devices such as a control module, a MP3 player, a mobile phone, a pair of earphones and a microphone were embedded in the jacket and interconnected through a wired harness network. This jacket demonstrated a significant progress in the process of integrating electronics with daily clothing as it could support multiple functions and had a nice and tidy appearance compared with the bulk wearable system in Fig.1.11. However, it was still not as wearer-friendly as we expected. Embedded devices added extra weight to the jacket, and usually we were reluctant to wear solid wires and rigid cases against our body. Therefore, what was really needed was a garment which was comfortable to wear and could support desire functions.

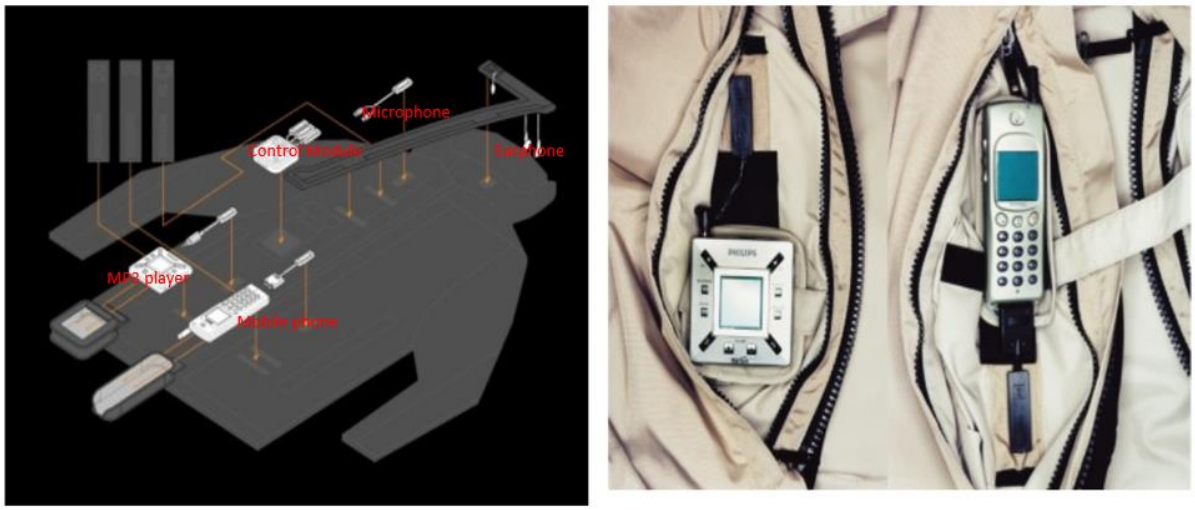

Fig.1.12 Levi's ICD+ jacket in 2000 [5]

- "Electronics are parts of a garment"

Benefiting from the computerized textile manufacturing techniques, textile-based electronics fabricated with conducting yarns successfully attracted the mainstream attention from both academia and industry in the early 2000s. A computerized textile manufacturing machine which permits a fast production were applied to create electromagnetic structures on a cloth. These functional devices were seamlessly integrated with textiles and became parts of garments. Wide range of textile devices have been realized with this technology. In 2000, A. Schmidt and his colleagues successfully demonstrated an on-body wearable identification system [6]. Several RFID tags were built by sewing textile conducting coils into a work glove and a tag reader was integrated with belt clip. In 2001, P.J. Massey from Philips research lab reported A GSM fabric antenna located on the user's back [7]. It was an early attempt to integrate a fully textile antenna with a garment and placed it on user's back to provide a wireless connection between user equipment and a base station. In 2004, a fashion design company named Cute Circuit published a commercial smart cloth "The Hug Shirt" as shown in Fig.1.15 [8]. Awarded as one of the Best Inventions of Year 2006 by The Times, "The Hug Shirt" just looked like any normal shirt you could buy from high street and it was fully washable. Amazingly, it could also send a hug to your loved ones over distance in real time. Embedded with sensors and Bluetooth transceivers, this shirt could capture your body information and send it to the one you want to hug through mobile phone. After receiving the information, "The Hug Shirt" worn on your loved one was able to recreate the hug immediately. "The Hug Shirt" was widely considered as an early success to realize a wearer-friendly smart garment commercially.

Fig.1.15 The “Hug Shirt” in 2004 [9]

After decades’ development, smart clothing demonstrated a promising future as it has already guaranteed a global market value of 1.6 billion USD in 2019 and it is expected to be 5.3 billion USD in 2025 [9]. Textile electronics as key functional components of smart clothing, consequently attracted my research interests.

1.2 Objective of this Project

In this thesis, I reviewed commonly used manufacturing techniques such as printing, weaving, embroidering and knitting which can be used to create textile electromagnetic structures. Among all these techniques, knitting as an old traditional manufacturing process, can create complex textile structures. In this contribution, I investigated a computerized knitting technique. Employing a computerized flat-bed knitting machine, this manufacturing technique can permit a fast and efficient production of large area textile structures with complex patterns or 3-D textile structures.

As the textile wearables have distinct advantages of flexibility, light weight and high-strength-to-weight ratio, I expanded my research interests from textile antennas to other textile electromagnetic structures such as waveguide and frequency selective surface. In this contribution, I evaluated several novel textile waveguides, antennas and frequency selective surfaces created by the computerized knitting technique.

Textile wearables always face a common challenge in practice, they always experience unexpected shape distortions. As the electromagnetic structures are constructed with textile materials, they are usually soft and flexible. Thus, it is difficult to keep them rigid. In this thesis, as the knitted textile waveguide and knitted textile slotted waveguide antenna both had a long linear flexible structure, bending would be shape distortion which most likely to occur. Therefore, it is necessary to investigate the performance of these knitted samples under different bending conditions.

The initiatives of this thesis can be briefly summarized as the following:

- Propose a computerized knitting manufacturing technique that permits the creation of large area functional textiles or 3-D textile structures at a high production rate.
- Present several novel electromagnetic textile structures to the public, including the first 3D textile waveguide, a textile slotted waveguide antenna, the first band-pass textile frequency selective surface and four ultra-light weight FSSs.
- Study these knitted textile electromagnetic structures and investigate their performance under different conditions.

1.3 Thesis Outline

In this project, I mainly focused on the design and evaluation of functional textile structures manufactured by a computerized knitting technique. This new technique employed a computerized flat-bed knitting machine which can permit a mass creation of large area textile structures with complex surface patterns at a high production rate (1.5m/sec at a width of 90cm). Various types of textile electromagnetic structure including waveguides, antennas and frequency selective surfaces were knitted by a commercial computerised knitting machine at Nottingham Trent University (NTU) and tested at the University of Sheffield (UoS).

Chapter 2 listed several existing techniques used to manufacture textile electromagnetic structures. The commonly used manufacturing techniques reported in the open literature included printing, weaving, embroidering and knitting. The advantages and disadvantages of these techniques were detailed and compared. I choose computerized knitting as the manufacturing technique to produce all the samples in this work as it was fast and able to create complex textile structures with high conductivity.

Chapter 3 was the literature review. I reviewed and summarised the previous approaches to the study on textile electromagnetic structures including waveguide, antenna and frequency selective surface from pioneering researches.

Chapter 4 began with the introduction of the theoretical basics of all the electromagnetic structures involved in this project. A few simple examples with numerical analyses were provided as well. This chapter aim to give readers a clear concept of all the principles and theories discussed in the subsequent chapters.

In chapter 5, I presented the study on a knitted textile elliptical waveguide. This knitted X band waveguide was the first prototype reported in the open literature. The properties of the textile materials were also determined by matching the simulated and measured results. Moreover, the performance of a knitted waveguide under different conditions including bending along both E-plane and H-plane, and wetting the sample were investigated. This chapter was my first approach to the study of knitted textile structures and built the fundamental of the thesis.

In chapter 6, a prototype of a knitted slotted waveguide antenna (SWA) working at X band was proposed for the first time. This antenna was developed from the knitted waveguide I demonstrated in chapter 5. After investigating its performance, stitched slots were employed to improve the SWA's performance and extra slots on the waveguide were proved to increase SWA's gain. Four different bending conditions were set up, and their effects on the knitted SWA's reflection coefficient and radiation pattern were studied in both simulation and measurement.

In chapter 7, I extended my research interests to knitted frequency selective surfaces (FSS). Several novel textile FSSs including a cross slot FSS and ultra-light weight hexagonal loop FSSs working at microwave band were manufactured. I managed to build simple equivalent models for these knitted FSSs in simulation. The normal incident, free space reflectivity of all the knitted FSSs were measured and compared with the simulated results.

Chapter 8 drew a conclusion of the whole thesis and discussed the challenges I might face for the further research in this area.

Chapter 2. Manufacturing Techniques

2.1 Introduction

Electronic wearables, as essential components in body centric communications systems, have developed swiftly in both academia and industry in the last few decades [10]. With the increasing demand for flexibility, comfort and light weight, textile based electromagnetic devices are potential solutions to meet these requirements. In the last decade, various types of textile antennas working at different frequencies have been proposed, and examples are presented in Table 2.11 [11-16]. They can retain a similar performance to the ones made with traditional hard materials, while being lighter and more flexible. These early textile antennas usually had a simple "sandwich" structure and were hand-made. Conducting textile were cut to the desired shape and then attached to the textile substrate using glue by hand. In the last decade, this approach was the most commonly used method to create textile RF devices. But this process was obviously time-consuming and inefficient as the conducting textile needs to be trimmed manually and the adhesive will affect the devices' performance. Therefore, it was necessary to seek an alternative that can permit fast production of textile electromagnetic structures with complex patterns. As a result, computerized textile manufacturing techniques attracted particular attention.

Table.2.11 Examples of early textile antennas in last decade

Reference	Year	RF Device	Frequency	Textile Materials	Fabrication Technique
[11]	2000	Antenna (Monopole)	880-960MHz	Polyester interwoven with nickel/copper fiber	Hand-made
[12]	2001	Antenna (PIFA)	500-2000MHz	Copper plated woven nylon + Polyester	Hand-made
[13]	2007	Antenna (Patch)	2450+5500MHz	Conducting woven + Felt	Hand-made
[14]	2007	RFID Tag (Meander Dipole)	869MHz	Conducting cloth	Hand-made
[15]	2009	Antenna (8-element Patch Array)	2450GHz	Nora conducting fabric + Felt	Hand-made
[16]	2010	Antenna (Patch)	1570MHz	Copper plated nylon + Fleece	Hand-made

In this chapter, I summarized and compared state of the art manufacturing techniques used to create textile electromagnetic devices including printing, embroidering, weaving and knitting. The advantages and disadvantages of each technique were discussed. Computerized knitting technique was eventually chosen to fabricate all the textile samples in this thesis.

2.2 Printing Technique

In the traditional approach to manufacturing textile electronics, the "cut to shape" conducting textile was adhered to the commercial textile substrates such as felt or fleece. With printing techniques such as screen printing or inkjet printing, the conducting layer was created by high performance conducting ink or conducting paste and printed on the textile substrate.

Various types of textile RF devices manufactured by specialized screen printing have been published [17-19]. Several screen-printed antennas including two WLAN planar antennas on KERMEL fabric and a UHF compact dipole antenna on silk were presented in [17-18]. And a screen-printed loop FSS on polyester was reported in [19]. In screen printing process, the designed patterns were scooped on a screen first, then conducting ink or paste was squeezed onto the surface of textile substrate through the holes in the screen to form RF components as shown in Fig.2.21. Therefore, it was difficult to change a printing pattern during the manufacturing process.

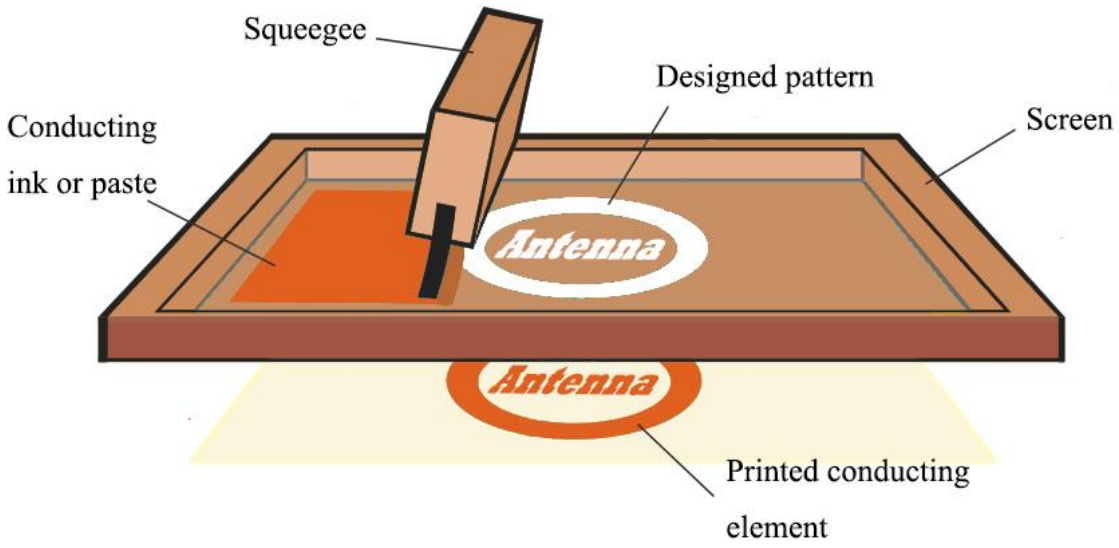

Fig.2.21 Screen printing process

With a digital printer, inkjet printing technique did not require a screen and allowed users to print specific patterns directly from the design with conducting ink. In this way, the printing pattern could be changed flexibly in manufacturing process. An inkjet-printed patch

antenna on felt was presented in [20]. This textile antenna demonstrated a good performance with a total efficiency of 57% and a 10dB bandwidth of 24.5MHz at 2.48GHz.

Generally, printing techniques including screen printing and inkjet printing, can permit a creation of textile electronics with good accuracy and resolution. However, it needed additional time for curing process such as heat to solidify the conducting layer on the textile surface. For example, the sample in [20] required curing for approximately 10 minutes before measurement. Moreover, the conducting layer must be printed thick enough to overcome the roughness of the textile surface and maintain electrically continuity. This resulted in extra thickness to the structure, and the conducting layer was likely to experience unexpected cracks under shape distortion which might stop the textile device from working. Lastly, high performance conducting ink or paste applied in printing process could result in a high cost and cause potential environmental hazards.

The advantages and disadvantages of screen printing and inkjet printing to manufacture textile electronics can be noted as following:

Screen printing:

Advantages:

- It provides a high fabrication accuracy.
- High conductivity of printed conducting pattern.

Disadvantages:

- Extra thickness to the existing textile substrate.
- Designed patterns cannot be changed during manufacturing process.
- Need extra time for curing process.
- Need more preparation time than inkjet printing.
- Conducting patterns are likely to experience cracks or detach from the textile when shape distortion occurs.
- High cost and potential environmental hazards.

Inkjet printing:

Advantages:

- It provides a high fabrication accuracy.
- High conductivity of printed conducting pattern.
- Designed patterns can be changed during manufacturing process.
- Need less preparation than screen printing.

Disadvantages:

- Extra thickness to the existing textile substrate.
- Need extra time for curing process.
- Conducting elements are likely to experience cracks or detach from the textile when shape distortion occurs.
- High cost and potential environmental hazards.

2.3 Embroidery

Instead of being attached to textiles by using adhesive, conducting patterns can be embroidered directly on the textiles by a computerized embroidery machine with conducting threads. RF devices can be seamlessly integrated with daily clothing using commercial conducting threads.

Various types of embroidered textile electronics have been reported [21-26]. Authors in [21-24] presented the designs of different wearable antennas including an UHF RFID tag antenna, a dual-band snail antenna and patch antennas manufactured by a computerized embroidery machine with electro-threads. Authors in [25-26] published details of the manufacture of several embroidered textile FSSs at microwave frequencies. The results in [21-26] indicated that the measured resonant frequencies of the embroidered samples shifted away from the simulated values even the simulated models were constructed with the same exterior size as the embroidered samples. In simulation, the conducting layer such as a patch or a unit cell of an FSS was usually modelled as a continuous conducting surface with a certain conductivity. However, it was found that due to the mechanism of embroidering, air gaps were created between adjacent stitches during manufacturing process. Consequently, these air gaps resulted in a low conductivity of the conducting elements and significantly affected the embroidered textile devices' resonant frequencies. To describe the embroidered RF devices' performance correctly, the conducting elements needed to be modelled as the track of conducting threads formed in a zigzag pattern in simulation [27]. This complex simulated structure resulted in extra meshing cells and a long simulation time. Moreover, it was important to understand the surface current distribution of an embroidered textile electronic before manufacturing. Fig.2.31 presents an embroidered rectangular patch antenna working at 2.47GHz [19]. In Fig.2.31, it can be seen clearly there were air gaps between adjacent conducting stitches on the embroidered patch. These air gaps caused the discontinuity of current flowing horizontally and the current only travelled continuously along the vertical conducting stitches. For the rectangular patch antenna shown in Fig.2.31, its major current direction was vertical. Therefore, the embroidering stitching direction was set to be parallel to the major current direction (vertical) and the embroidered antenna was measured to have a total efficiency of 53%. For an embroidered textile electronic device, the stitching direction must be parallel to its major current direction, otherwise, it would affect the device's performance significantly. Lastly, embroidering was a relatively slow

manufacturing process to create textile electronics. For example, in [25] it took approximately 40 mins to complete a 24-element square textile FSS (42.1mm by 42.1mm by 24), the production rate was about 1060 mm^2/min, which was less than half of the production rate of the knitting technique described later.

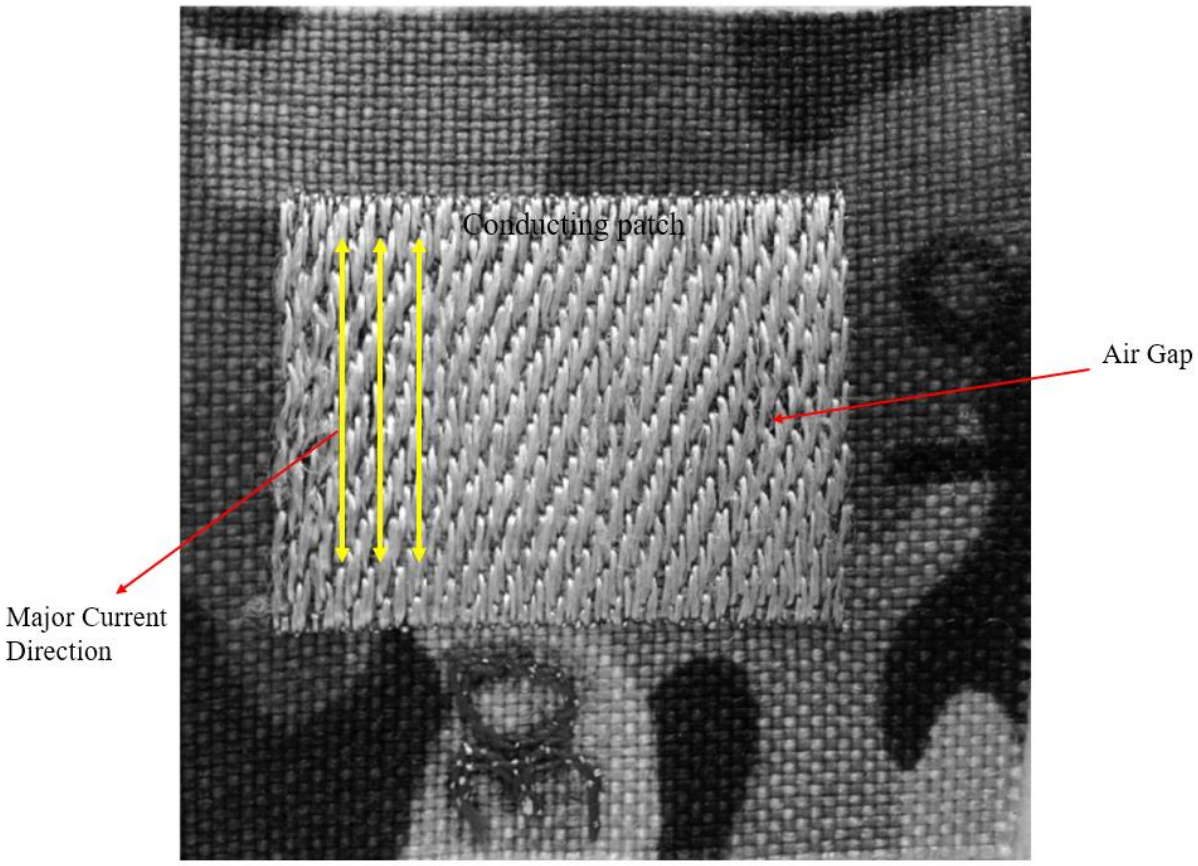

Fig.2.31 An embroidered rectangular patch antenna [19]

The advantages and disadvantages of a computerized embroidering technique to manufacture textile electronics can be summarized as following.

Advantages:

- The conducting patterns can be accurately shaped and seamlessly integrated with garments.
- It is easy to change embroidering design and threads during manufacturing process.
- It creates a firm structure which is robust to the textile shape distortions.
- It makes garment aesthetically pleasing.

Disadvantages:

- Stitching direction must be parallel to the major current direction during embroidering process.
- Low conductivity of embroidered conducting patterns & relatively slow production rate
- Need to build a complex model in simulation to describe an embroidered RF device's performance correctly.
- Adding extra thickness to the existing textile substrate.

2.4 Weaving

With printing or embroidering techniques, conducting elements were formed on the surface of an existing substrate textile, which consequently added an extra thickness to the structure. With a weaving technique, conducting patterns and the substrate textile were both woven in the fabric manufacturing process, which resulted in no additional thickness to structure.

Details of woven textile electronic devices can be found in [28-30]. Authors in [28-29] presented several woven patch antennas working at different frequencies and a woven loop FSS was reported in [30]. A woven patch antenna constructed with conducting Satin fabric and a polyester substrate was tested in [29]. Good agreement was achieved between the measured and simulated results. The fully fabric antenna was able to deliver a maximum measured gain of 6.6 dB at 2.44 GHz with a bandwidth around 6%. Authors in [28] stated that the radiation efficiency of a woven antenna can be improved by using less but thicker conducting threads. A woven loop FSS was also studied in [30]. Good transmission performance with a distinct rejection band was observed from the measurement. When this woven FSS was excited by a normal incident wave, it demonstrated a resonance at 2.5GHz with a bandwidth of 238MHz in the H-plane and a resonance at 2.8GHz with a bandwidth of 854MHZ in the E-plane. Results in [30] showed that a woven FSS exhibited different performances when it was illuminated horizontally and vertically, which means weaving process resulted in different stitch structures in the horizontal and vertical directions.

Compared to embroidering, weaving can permit a production of large area conducting textiles without additional thickness to the structure. Moreover, woven RF components were more “invisible” when they were incorporated with garments. Fig.2.41 shows the weave pattern of a fabric patch antenna [29]. In Fig.2.41, the vertical black rods were conducting yarns and the horizontal white rods were non-conducting yarns. In the weaving process, conducting yarns were arranged in warps (vertical) and interlaced with the non-conducting yarns in wefts (horizontal) to form a conducting rectangular patch. Meanwhile, textile was also fabricated by the interlacements of warp yarns and weft yarns. Therefore, the designed conducting pattern was realized during textile weaving process without additional thickness to structure. However, weaving faced a similar issue as embroidering: conducting paths only existed in one direction. From the weave pattern shown in Fig.2.41, it can also be seen that there were air gaps and non-conducting yarns between adjacent conducting yarns in Weft

which caused the discontinuity of horizontal current flow. The continuous conducting paths only existed along the conducting yarns direction. Therefore, the conducting yarns must be aligned with the major current direction of textile devices, otherwise, it would result in a poor conductivity of the conducting element and affect the textile electronic device's performance significantly.

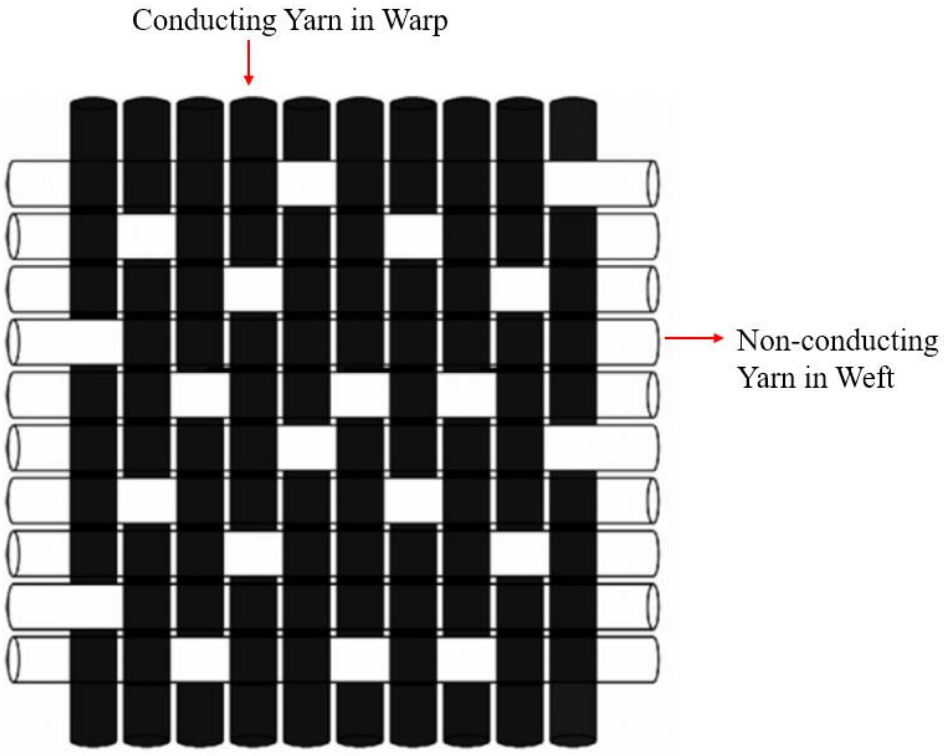

Fig.2.41 Example of a weave pattern [29]

The advantages and disadvantages of a weaving technique to manufacture textile electronics are listed:

Advantages:

- It permits a fast production of large area textile electronics with designed conducting patterns
- The conducting patterns can be integrated with garments seamlessly without additional thickness, which makes the RF devices more “invisible”.
- Woven textile electronics are robust to the textile shape distortion.

Disadvantages:

- Conducting yarns must be aligned with the major current direction of the textile electronics.
- Fabrication accuracy is less than printing and embroidering.
- Yarns and designed conducting patterns cannot be changed easily in manufacturing process.
- Woven fabrics are not naturally stretchable and tend to crease.
- Need practice to use a custom-designed loom [28].

2.5 Knitting

Knitting, as another traditional technique to manufacture textiles, has been developed over the last few decades. Textile RF devices can be fabricated at a high production rate by a computerized, flat-bed knitting machine with commercial conducting yarns. However, only a few publications on knitted textile electronic devices can be found in the open literature.

Authors in [31] proposed a knitted folded dipole antenna mounted on human body. The textile antenna provided a resonance at 870MHz with a bandwidth of 100MHz. Authors in [32] presented four textile patch antennas which were completely fabricated using industrial knitting machinery. Each sample was knitted by different fabric density and the results indicated that all knitted patch antenna resonated at the desired frequency and the textile antenna's efficiency improved as the knitted patches became denser. Beside knitted antennas, authors in [33-34] also presented planar and 2.5-D knitted textile FSSs. The previous study showed that a fully knitted antenna was able to provide a good wearable performance on human body and the knitted textile FSSs demonstrated the desired frequency-filtering properties with a stable response for different polarizations and incident angles.

Knitting and weaving were the most popular methods used to create textiles, but they had completely different manufacturing mechanisms. In the knitting process, yarns were arranged in courses and wales as shown in Fig.2.51 [35]. The intermeshing loops formed by conducting course and wale yarns provided continuous conducting paths in all directions throughout the textile. However, the current had a "better defined" conducting path along a conducting yarn than a joint across two conducting yarns. Consequently, a knitting conducting textile did not have a uniform conductivity in all directions. Like weaving, the designed conducting patterns were also created in manufacturing process, which resulted in no additional thickness to structure. Moreover, with the intermeshing loops, knitting left a more flexible and elastic textile structure than weaving, and knitted textiles were naturally stretchable and more comfortable to wear. Additionally, in practice, yarns necessarily required extra preparation processes such as sizing (applying various types of size material) [36] to reduce breakage and make them suitable for weaving, they can be used directly for knitting [37].As a result, a computerized knitting machine can provide a higher productivity than weaving. Fig.2.52 shows a computerized flat-bed knitting machine (Shima Seiki

SWG091N) with a maximum speed of 1.5m/sec at a maximum width of 90 cm [38]. It took about 2 mins to knit a 200 mm by 35 mm sample (about 3500 mm^2/min) and textile conductivity could reach up to 10^4 σ/m with a commercial silver loaded conducting yarn. Lastly, with conducting yarns, the knitting technique can realize not only planar textile electronics with complex patterns like textile antennas and frequency selective surfaces, but also 3-D fabric-based structures such as textile waveguides. With the highlighted advantages, knitting was considered to be a more suitable textile manufacturing technique compared with the other techniques described above for this PhD project and a computerized knitting machine shown in Fig.2.53 was employed to create all the samples in the thesis.

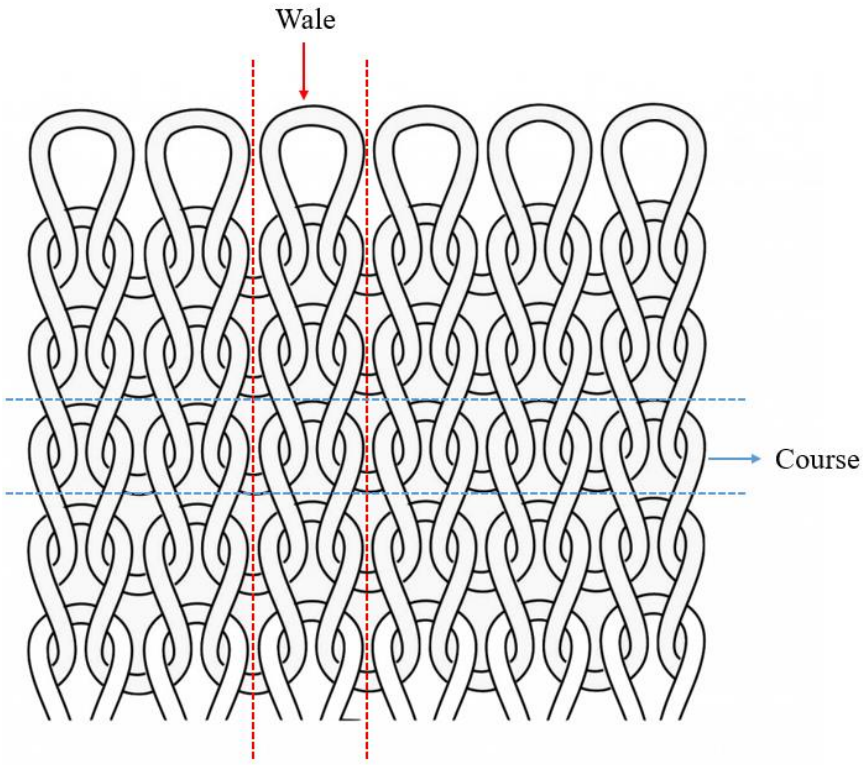

Fig.2.51 Example of a knit pattern [35]

Fig.2.52 A Shima Seiki SWG091N computerized flat-bed knitting

The advantages of knitting technique to manufacture textile electronics are highlighted as following:

Advantages:

- It has the highest production rate among all the textile RF device manufacturing techniques described above.
- It can permit the creation of both planar and 3-D textile structures.
- Continuous conducting paths can exist in all the directions throughout the textile.
- The conducting patterns can be shaped accurately and integrated with garments without additional thickness.
- It is easy to change designed pattern and yarns in knitting process.
- Knitted fabrics are more comfortable to wear and robust to textile shape distortions.

Disadvantages:

- Conductivity of a conducting knitted textile is not uniform in all directions.
- Need particular training to operate a computerized knitting machine

2.5 Conclusion

In this chapter, current manufacturing techniques for textile electromagnetic devices including printing, embroidering, weaving and knitting were introduced and compared. The results showed that with digital manufacturing techniques, conventional RF devices could be made with commercial textiles completely. These techniques were capable for producing a wide variety of textile electronic devices for different applications and their advantages were summarized respectively. Printing technique had the highest fabrication accuracy while it also had the highest cost and potential environmental hazards as conducting ink or paste was involved. Moreover, the printed conducting elements were likely to crack or detach from the textile under shape distortions. Textile RF devices created by the traditional fabric manufacturing techniques such embroidering, weaving and knitting demonstrated a more robust performance under shape distortion and had a better appearance when integrated with garments. With computerised machines, embroidering, weaving and knitting can all permit an efficient, fast and environmental-friendly production of textile RF devices. However, embroidered conducting patterns added extra thickness to textile substrate and usually experienced low continuous conductivity. Weaving had a less fabrication accuracy and woven fabrics tended to crease. Taken all the factors into account, knitting was eventually chosen as the manufacturing technique to fabricate textile RF deceives in this PhD project. It can realize both large area planar textile electronics with complex patterns and 3-D textile electromagnetic structures. Last but not the least, knitted fabrics are very comfortable to wear.

Chapter 3. Literature Review

3.1 Introduction

With the revolution of wireless communications technology, people am now carrying more and more electronic devices to meet increasing personal demands. We use mobile phones to chat with friends, access internet and obtain GPS functionality. Youngsters, the aged and patients may need special sensors to locate positions, detect body motions and monitor health conditions. These “always on” devices need to stay constantly inter-connected and communicating with the outside world. Meanwhile, they also must be low-profile, light weight and not restrict our daily activities. To achieve this goal, wearable devices have developed rapidly in the last decade.

According to [39], depending on the fabrication materials, current wearable devices can mainly be categorized into nontextile devices and fully textile devices as shown in Fig.3.11. Nontextile devices refer to those devices of which are not completely fabricated from textile materials, especially the conducting parts. They can be either customized as ornamental pieces and embedded into wearable accessories such as glasses, rings, bracelet or applied directly on human skin like plasters. Nontextile devices normally allow accurate fabrication as conventional conducting materials such as adhesive copper tape or conducting ink which can be precisely shaped are employed to create the conducting patterns. While they have to compromise flexibility, wearability and user comfort. Fully textile devices refer to devices which are completely fabricated with textile materials. They markedly permit the seamless integration with daily clothing and can provide multi functionalities without sacrifice of wearer comfort. The appearance of “The Hug Shirt” in 2004 altered the concept of traditional clothing and introduced the new generation garments. Benefiting from computerized textile manufacturing techniques, traditional electromagnetic devices such as antennas, sensors, RFID tags can now be made with textile materials. The new generation garments are not only capable of monitoring the wearer’s body information as unobtrusively as possible, also able to provide additional protection to the special class of professionals facing occupational risks and hazards such as military, fire fighter and emergency rescuers. [48] Wearers’ vital signs and surrounding environmental information can be collected and

transmitted to nearby teammates and base stations by the textile devices on the new generation garments.

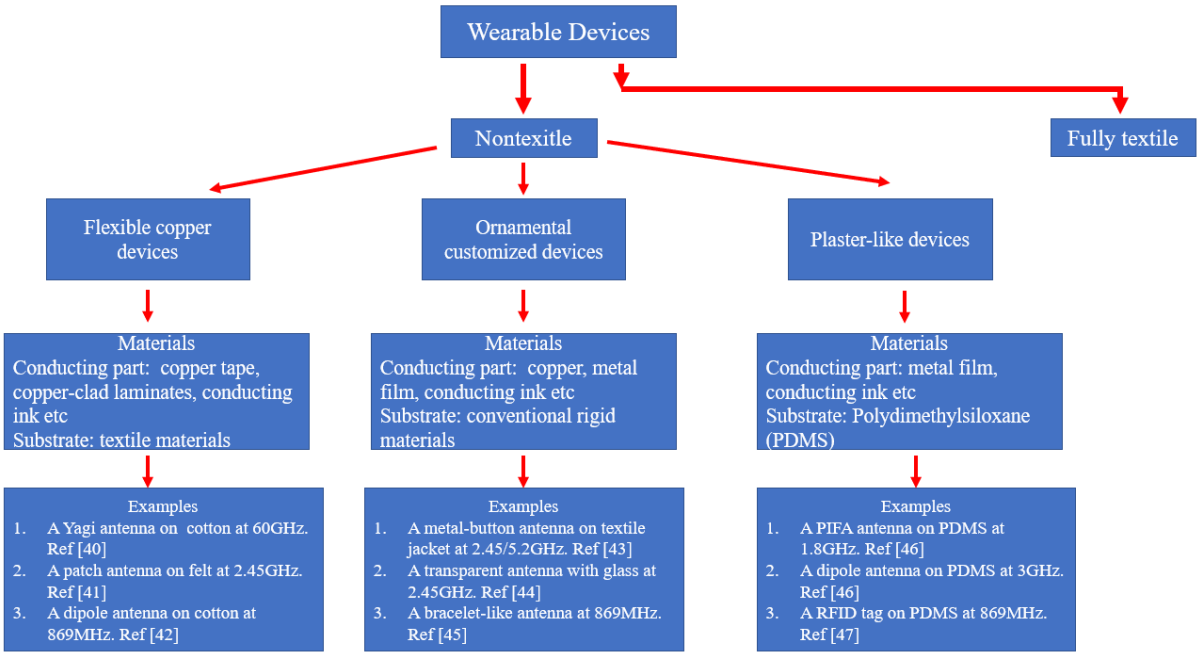

Fig.3.11 Review of existing wearable devices

In this chapter, I am going to review the historical developments of three types of fully textile devices which are studied in this thesis. Previous research on the textile waveguides, textile antennas and textile frequency selective surfaces will be discussed, respectively.

3.2 Textile Waveguide

Waveguide is a basic component used to guide the electromagnetic energy between its endpoints in communications system. It has an attractive feature for body-centric applications as it can provide a good isolation between radiating devices and human body. However, up to date, limited research on textile waveguide can be found in literature. The authors in [49-50] focused on the design of a textile sheet-shaped waveguide in a wireless on-body communications system. In [49], a textile-based sheet-like waveguide was proposed to provide a confined communication channel between wireless sensors at 2.45GHz. It served as a mat and was robust to the presence of human body. In [50], the authors presented a fully textile sheet-like waveguide integrated with AMC structure. It was in the form of jacket and can be worn by a patient for health monitoring. The other existing application of textile waveguide can be found in the wearable substrate integrated waveguide (SIW) antennas. The authors in [51] presented the realization of a compact dual-band textile SIW antennas. The rows of vias minimized the undesired radiation and improved the isolation between antenna and human tissue. The measurement showed that the textile SIW antenna almost had the same gain in free space and on-body deployment, which was 4.2dBi at 2.45 GHz and 5.7dBi at 5.8GHz.

To my best knowledge, the previous research mainly concentrated on the sheet-shape textile waveguide or the wearable antennas in substrate integrated waveguide technology rather than the textile waveguide with a traditional structure. In this thesis, I proposed the first 3D textile waveguide to the public and filled the gap in research

3.3 Textile Antenna

The history of textile antennas can be traced back to 1999, when P. Salonen and his colleagues proposed a small planar inverted-F antenna for wearable applications [55]. This small PIFA exhibited a good dual-band performance at 900MHz and 2.4GHz, which covered GSM and Bluetooth frequency bands, respectively. Authors in [55] also discussed the public concerns on health hazards when antennas were worn on body. It showed that the presence of conducting ground plane on microstrip antenna was able to prevent backward radiation effectively when the antenna was brought closed to human body. Strictly speaking, this PIFA was not a textile antenna, as it was still fabricated with a conventional rigid material (copper), it brought the public an idea of how an antenna could be integrated with garments for wearable applications. In 2001, P.J. Massey from Philips research lab reported A GSM fabric antenna located on the user's back [56]. This was an early prototype of textile antennas reported in the open literature, which had the conducting parts made from copper plated woven nylon and flexible foam. This textile antenna showed an acceptable performance when it was worn on the body, it had a return loss around -6dB at the GSM band with an antenna efficiency of about 50%. Later, numbers of pioneering researchers focused on realizing different antenna structures with commercial textile materials in the last decade. Early approaches to the textile antenna design can be found in Table 3.31[55-60].

Table.3.31 Examples of early textile antennas in the last decade

Reference	Year	Antenna Type	Textile Materials	Frequency/ Rad Eff/ Gain
[55]	1999	Dual band patch	Conducting: copper	0.98+2.36 GHz
		First introduced textile antenna concept	Substrate: air	NA
				NA
[56]	2001	PIFA	Conducting: copper plated nylon	0.9GHz
		First textile antenna	Substrate: flexible foam	70% (free space) 50% (on body)
				NA
[57]	2003	Coaxial-fed patch antenna	Conducting: knitted copper yarn	2.45Ghz
		First compact fully textile antenna	Substrate: fleece	80% (free space)
				6.82dBi (free space)
[58]	2007	Aperture-fed patch antenna	Conducting: copper plated nylon	2.45GHz
			Substrate: fleece	63% (free space)
				5dBi (free space)
[59]	2008	Dual polarized patch antenna	Conducting: copper plated nylon	2.45GHz
		First dual polarized patch antenna	Substrate: flexible foam	65% (free space)
				6.8dBi (free space)
[60]	2010	Circular polarized patch antenna	Conducting: conducting woven yarn	1.65GHz
			Substrate: Cordura fabric(εr=1.88)	70% (free space)
				6dBi (free space)

When textile antennas are integrated with garments, there are always health concerns as the radiating elements are very closed to human body. To minimize the radiation level towards human body, one of the solutions is to select an antenna topology with a rear ground plane such as microstrip antenna. As discussed in [55], the presence of conducting ground plane significantly reduced the microstrip antenna's backward radiation and SAR (Specific Absorption Rate, which is a measure of how much radiating energy is absorbed by human tissue [61]). However, conventional microstrip antennas normally have a three-layer topology and the ground plane is placed at a certain distance from the radiating element. Consequently, this structure increases the thickness of textile antennas and make them less suitable to be worn on body. To overcome this, low profile textile antennas integrated with textile-based matasurfaces such as Electromagnetic Bandgap (EBG) or Artificial Magnetic Conductor (AMC) attracted increasing attentions from last decade. Previous study on textile metasurface-based antenna can be found in Table 3.32 [62-65]. It can be noted that the metasurfaces significantly reduced the antenna's backward radiation and SAR when the

textile antennas were worn on body. However, textile metasurfaces introduced additional complexity to the system and high manufacture costs as metasurfaces normally share a large area periodic structure and need to be properly designed to integrated with textile antennas.

In this thesis, I proposed a textile slotted waveguide antenna (SWA), which is a type of directional antenna as an alternative solution. It had a low backward radiation without a ground plane and was suitable to wear.

Table.3.32 Previous study on textile metasurface-based antenna

Reference	Year	Antenna Type	Metasurface	Textile Materials	Performance Improvement
[62]	2004	2.45GHz Patch Antenna	mushroom-like EBG	Conducting: copper tape	30% size reduction (free space)
		First textile EBG Antenna		Substrate: felt	50% bandwidth increase (free space)
[63]	2009	2.45&5GHz CPW Antenna	Dual-band EBG	Conducting: woven conducting yarn "zelt"	3dB gain enhancement (free space)
		Early EBG-based fully textile antenna		Substrate: felt	12dB back lobe reduction (free space)
					more than 90% SAR reduction (on-body)
[64]	2017	2.45GHz monopole antenna	T-shape EBG	Conducting: ShieldIt conducting textile	70% size reduction to previous design
		Compact EBG-based textile antenna			10% bandwidth increase (free space)
				Substrate: denim material	7.8dB gain enhancement (free space)
					15.5dB back lobe reduction (free space)
					95% SAR reduction (on-body)
[65]	2019	5.8GHz CPW Monopole	Patch type AMC	Conducting: Taffeta copper fabric	2dB gain enhancement (on-body)
		Recent AMC-based textile antenna		Substrate: Pellon fabric	more than 90% SAR reduction (on-body)

Textile antennas are usually inherently flexible and soft. Pioneering researchers found out that when the textile antennas were worn on human body, due to the wearer's daily activities, they experienced inevitable structure deformations. Therefore, it was necessary to evaluate textile antenna's performance under different shape distortions. Bending is one of the common seen shape distortions for a wearable textile antenna. As most part of human body is not flat, a textile antenna needs be bent to mount on a certain area such as head or arm. In 2003, M. Tanaka and J. Jang published the study on a textile microstrip antenna bent around an arm [66]. This wearable antenna was constructed with felt and woven conducting fabric and designed to work at 2.45GHz. Their measurement showed that the antenna's gain

dropped around 2.5dB when the textile antenna was bent around the arm. This was the early approach to evaluate bending effects on a textile antenna with measurement. The study on antenna performance under structure deformations could also be found in [67-68]. In [67, 68], Q. Bai and his colleagues not only evaluated a textile microstrip antenna array's performance under different shape distortions including bending and crumpling, they also managed to build an equivalent model to describe the crumpling, which was another common type of shape distortion might happen to a wearable textile antenna, but more complicated than bending. Their results showed that textile antenna demonstrated a robust matching performance under different bending conditions, while bending affected antenna's radiation pattern significantly.

In this thesis, I evaluated the performance of textile slotted waveguide antenna under different bending conditions to study the its feasibility to be used in practice.

3.4 Textile Frequency Selective Surface

In recent years, benefiting from the computerized manufacturing technique which permitted fast creations of textiles with complex patterns, researches extended their interests from textile antennas to large area textile based electromagnetic structures such as frequency selective surface (FSS). Table 3.41 summarizes key publications about Textile FSS in the recent decade. The earliest approach to manufacturing textile based FSSs in the public literature can be traced back to 2012, when A. Tennant and W. Hurley proposed two textile FSSs knitted by a computerized flat-bed knitting machine [69]. One of the FSSs had a conducting grid structure and the other one had a conducting patch array. Measurement showed that both FSSs demonstrated a desired performance at microwave frequencies. Moreover, it proved that computerized knitting technique with conducting yarns is an efficient and amenable approach to manufacture functional textile structures at a high production rate. In 2013, A. Chauraya and his colleagues from Loughborough University presented another manufacturing technique to produce textile FSSs: computerised embroidering [70]. An array consisting of 24 squares was embroidered on a commercial felt cloth using conducting threads to form a loop FSS structure. This textile FSS exhibited a good band-stop frequency-filtering property at 2GHz. Later in 2014, R.Seager published his study on fabrication of textile FSS. In [71], he compared the normal-incident frequency response of three textile FSSs manufactured with different conducting yarns. The best agreement between measurement and simulation was achieved when the textile FSS was produced using the highest conductivity yarn and highest stitch density. Recently, printing techniques such as screen printing [72] and inkjet printing [73] were also applied to create FSS patterns on the surface of textile materials. In [72, 73], textile FSSs were created by printing techniques with a high fabrication accuracy and good agreement were achieved between the measurement and simulation. [72] presented a band-stop textile FSS in millimetre-wave band and [73] proposed a band-stop textile FSS at 3GHz. However, they also stated that the printing technique suffered a high cost and conducting patterns were difficult to attach to the textiles.

FSS can be mainly categorized into high-pass, low-pass, band-pass and band stop based on its frequency response. From table.3.41, it can be noted that prior work only covers high-pass, low-pass and band-stop textile FSSs and there is no paper on band-pass textile FSSs can be found in the open literature to date. The main reason is because the band-pass

frequency response is usually realized by slot FSSs and it is challenging to cut periodic slots on textile samples. In this thesis, I proposed the first band-pass textile FSS to the public and filled the gap in research.

Table.3.41 Examples of textile FSSs in the recent decade

Reference	Year	Normal Incidence Frequency Response	Textile Materials	Manufacturing Technique	Performance
[23]	2012	High-pass	Conducting: silver nano embedding yarn	Knitting	S11>-6dB (2-8GHz)
		Low-pass	Dielectric: polyester		S11>-6dB (7-11GHz)
[24]	2013	Band-stop	Conducting: silver plated nylon	Embroidering	S21<-10dB (1.9-2.1GHz)
			Dielectric: felt		
[25]	2014	Band-stop	Conducting: conducting Amberstrand yarn	Weaving	S21<-10dB (2.1-2.3GHz)
			Dielectric: cotton		
[26]	2014	Band-stop	Conducting: specialised nano-fabrication conducting ink	Inkjet-printing	S21<-10dB (87-89GHz)
			Dielectric: polyester		
[27]	2017	Band-stop	Conducting: silver Ink	Screen-printing + weaving	S21<-10dB (2.9-3.1GHz)
			Dielectric: nylon fabric		
[28]	2018	Band-stop	Conducting: shieldex conducting yarn	Weaving	S21<-10dB (3.7-5.5GHz)
			Dielectric: polyester		

3.5 Conclusion

In this chapter, I reviewed the previous research on three textile based electromagnetic structures: textile waveguide, textile antenna and textile frequency selective surface. Plenty of work have been done by pioneers on textile antennas, including design and evaluation on various types of antenna fabricated with commercial textile materials, investigation of textile antenna's performance under shape distortions etc. While the study on textile waveguide and textile frequency selective surface was still in infancy. In this thesis, our contribution was to fill the gap in the study on textile waveguide and textile FSS, and proposed several novel textile antennas and textile frequency selective surfaces manufactured by computerized knitting technique.

Chapter 4. Theoretical Background

4.1 Introduction

Chapter 4 reviewed the fundamental background of all the electromagnetic structures involved in this thesis. The theoretical basics about waveguide, slotted waveguide antenna and frequency selective surfaces were detailed, respectively.

4.2 Waveguide

After the publication of Maxwell's equations in early 1860s, electromagnetic waves have been studied for over a century and many engineering applications have been developed. Waveguide, which is a device used to guide waves between its endpoints, can easily find its application in various areas. In telecommunications system, optical waveguides are used for long distance signal transmission [75]. In wireless communications system, waveguides play indispensable roles that provide confined channels between components.

4.21 Propagation Mode

As stated early, waveguide was usually used for the transmission of electromagnetic wave. To describe exactly how the EM waves travel within a waveguide, the concept of the propagation mode of a waveguide was introduced to present E field and H field patterns [76]. Generally, waveguides were analysed by solving the electromagnetic wave equation, which was the reduced form of Maxwell's equations [77]. In the following sections, I took a rectangular waveguide which was the most common type as an example to solve electromagnetic wave equation. With the constraint of boundary conditions determined by the waveguide's material, there were only limited solutions to EM wave equation. Each solution indicated a propagation mode inside the waveguide and was characterized by the cut-off frequency. No propagation mode could exist if the wave frequency is below the cut-off frequency in the waveguide. Usually, a waveguide can support several propagation

modes, and the mode with the lowest cut-off frequency was referred to as the dominant mode of a waveguide. Normally, the waveguides were manufactured based on their dominant modes to guarantee that there was a single mode propagating regardless of how the waveguide was excited. The propagation modes inside a uniform waveguide can be classified into different types:

TE (Transverse Electric) mode: The electric field only exists in the transverse plane of the waveguide. Therefore, it is also called the H mode as it only has magnetic field along the direction of wave propagation.

TM (Transverse Magnetic) modes: The magnetic field only exists in the transverse plane of the waveguide. Therefore, it is also called the E mode as it only has electric field along the direction of wave propagation.

TEM (Transverse Electromagnetic) modes: Both electric and magnetic fields exist only in the transverse plane of the waveguide.

Hybrid modes: Both electric and magnetic field exist along the direction of wave propagation.

TE modes or TM modes can be found in any shaped hollow metallic waveguide such as rectangular, circular or elliptical waveguide with homogenous filling. While this kind of waveguide cannot support TEM mode as the EM wave equation did not have a physical solution under this condition (it was discussed later with the example of rectangular waveguide). There are certain types of transmission lines which can support TEM mode, for example: coaxial cable, parallel plate waveguide and microstrip line [78]. However, these structures were not involved in this thesis. In the following, I introduced two basic types of waveguide: rectangular and elliptical waveguides.

4.22 Rectangular Waveguide

Fig 4.221 shows a typical metallic rectangular waveguide with dielectric filling. It has a rectangular cross section with width a and height b. Moreover, c is the thickness of conducting wall and the waveguide is usually filled with dielectric material which has permittivity ε and permeability μ. The cross-sectional dimensions (a, b) and dielectric property of filling (ε, μ) are the basic parameters of a rectangular waveguide. To analyse it, an equivalent mode is built on Cartesian coordinate system shown in Fig 4.222.

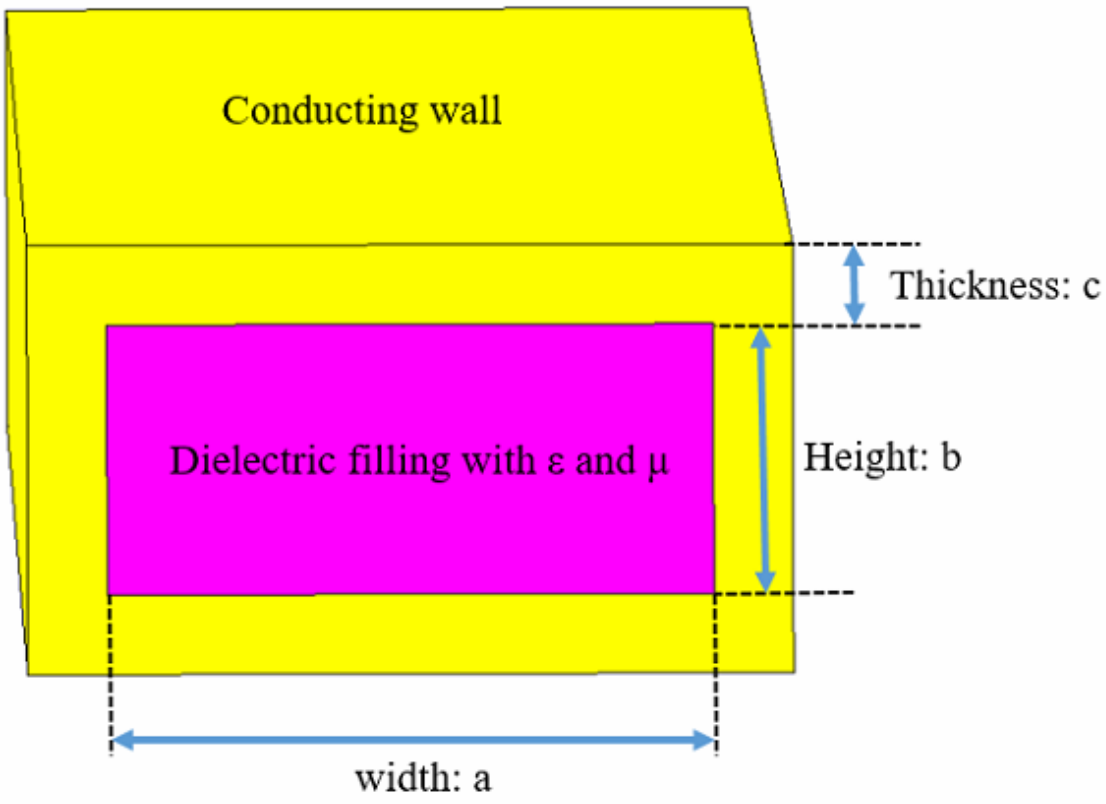

Fig.4.221 A rectangular waveguide with dielectric filling

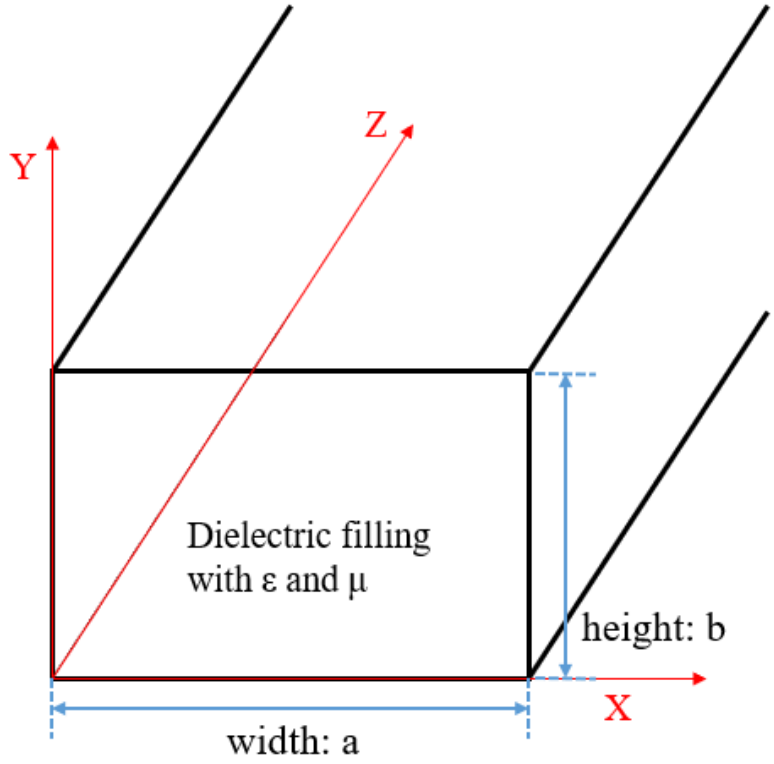

Fig.4.222 An equivalent model for a rectangular waveguide in Cartesian coordinate system

Assume that the waveguide is made of perfect electric conductor (PEC) and filled with lossless homogenous dielectric material (which means the attenuation constant α is 0). Also, the wave is travelling in Z direction as $e^{-j\beta z}$ (β is the phase constant) and its time variant as $e^{j\omega t}$ (ω is the angular frequency). Furthermore, the waveguide is invariant along the Z direction. Therefore, the magnetic field H at time t is $H = H_o \times e^{j\omega t}$ and electric field E at time t is $E = E_o \times e^{j\omega t}$.

$$H = H_o \times e^{j\omega t} \;;\; \frac{\partial H}{\partial t} = j\omega H_o \quad \ldots\ldots\ldots\ldots\ldots (1)$$

According to Faraday's Law:

$$\nabla \times E = -\frac{\partial B}{\partial t} = -\frac{\partial \mu \times H}{\partial t} = -\frac{\partial H}{\partial t} \times \mu \quad \ldots\ldots\ldots\ldots\ldots (2)$$

Put (1) and (2) together:

$$\nabla \times E = -j\omega\, \mu H_o; \left(\frac{\partial}{\partial x}, \frac{\partial}{\partial y}, \frac{\partial}{\partial z}\right) \times \left(E_x, E_y, E_z,\right) = -j\omega\, \mu H_o;$$

X-direction: $$\frac{\partial E_z}{\partial y} - \frac{\partial E_y}{\partial z} = -j\omega\, \mu H_x \quad \ldots\ldots\ldots\ldots\ldots\ldots\ldots\ldots (3)$$

Y-direction: $\frac{\partial E_x}{\partial \mathrm{z}} - \frac{\partial E_z}{\partial x} = -\mathrm{j}\omega\,\mu H_y$ ..... (4)

Z-direction: $\frac{\partial E_y}{\partial \mathrm{x}} - \frac{\partial E_x}{\partial y} = -\mathrm{j}\omega\,\mu H_z$ ..... (5)

The spatial variation along propagation direction (Z-direction) is:

$$\frac{\partial e^{-j\beta z}}{\partial z} = -j\beta e^{-j\beta z},$$

Therefore, (3)~(5) can be represented as

X-direction: $\frac{\partial E_z}{\partial \mathrm{y}} + j\beta E_y = -\mathrm{j}\omega\,\mu H_x$ ..... (6)

Y-direction: $-\mathrm{j}\beta E_x - \frac{\partial E_z}{\partial x} = -\mathrm{j}\omega\,\mu H_y$ ..... (7)

Z-direction: $\frac{\partial E_y}{\partial \mathrm{x}} - \frac{\partial E_x}{\partial y} = -\mathrm{j}\omega\,\mu H_z$ ..... (8)

From (6)~(8), magnetic field can be found using known electric field components. Similarly, if I know the magnetic field, each component of electric field can be obtained respectively.

$$\mathrm{E} = E_o \times e^{j\omega t} \;;\; \frac{\partial \mathrm{E}}{\partial \mathrm{t}} = j\omega E_o \text{ .....} (9)$$

According to Ampere's Law:

$$\nabla \times \mathrm{H} = \frac{\partial \mathrm{D}}{\partial \mathrm{t}} = \frac{\partial E \times \varepsilon}{\partial t} = \frac{\partial \mathrm{E}}{\partial \mathrm{t}} \times \varepsilon \text{.....} (10)$$

(9) and (10) together gives:

$$\nabla \times \mathrm{H} = \mathrm{j}\omega\varepsilon E_o; \left(\frac{\partial}{\partial \mathrm{x}}, \frac{\partial}{\partial \mathrm{y}}, \frac{\partial}{\partial z}\right) \times \left(H_x, H_y, H_z,\right) = \mathrm{j}\omega\varepsilon E_o \text{ .....} (11)$$

With the spatial variation in Z direction, I can have:

X-direction: $\frac{\partial H_z}{\partial \mathrm{y}} + j\beta H_y = \mathrm{j}\omega\,\varepsilon E_x$ ..... (12)

Y-direction: $-\mathrm{j}\beta H_x - \frac{\partial H_z}{\partial x} = \mathrm{j}\omega\varepsilon E_y$ ..... (13)

Z-direction: $\frac{\partial H_y}{\partial \mathrm{x}} - \frac{\partial H_x}{\partial y} = \mathrm{j}\omega\varepsilon E_z$ ..... (14)

(6)~(8) and (12)~(14) can be used to deduce the simple algebraic equations for the transverse components of E_o and H_o.

$$H_x = \frac{j}{K_c^2}\left(\omega\varepsilon\frac{\partial E_z}{\partial y} - \beta\frac{\partial H_z}{\partial x}\right) \text{..... (15)}$$

$$H_y = -\frac{j}{K_c^2}\left(\omega\varepsilon\frac{\partial E_z}{\partial x} + \beta\frac{\partial H_z}{\partial y}\right) \text{..... (16)}$$

$$E_x = -\frac{j}{K_c^2}\left(\beta\frac{\partial E_z}{\partial x} + \omega\mu\frac{\partial H_z}{\partial y}\right) \text{..... (17)}$$

$$E_y = \frac{j}{K_c^2}\left(-\beta\frac{\partial E_z}{\partial y} + \omega\mu\frac{\partial H_z}{\partial x}\right) \text{..... (18)}$$

In equations (15)~(18), K_c is the cut-off wavenumber where $K_c^2 = K^2 - \beta^2 = K^2 + \gamma^2$. And K is the magnitude of wavevector where $K^2 = \omega^2\mu\epsilon$. From equations (15)~(18), if I know the axial components E_z and H_z inside a waveguide, all the transverse components of electric and magnetic field can then be deduced from them [78]. To solve equation (15)~(18), according to electromagnetic wave equation [79], the wave inside the waveguide under the above assumption obeys:

$$\nabla^2 E + K^2 E = 0 \text{..... (19)}$$

$$\nabla^2 H + K^2 H = 0 \text{..... (20)}$$

Then, the E and H field in equation (19)~(20), can be divided into axial direction and transverse plane as shown below.

$$\nabla^2 E = \nabla_{xy}^2 E + \frac{\partial^2 E}{\partial z^2} \text{..... (21)}$$

$$\nabla^2 H = \nabla_{xy}^2 H + \frac{\partial^2 H}{\partial z^2} \text{..... (22)}$$

As the EM wave is travelling along Z direction with propagation factor $e^{j\omega t - j\beta z}$, the field variation in Z direction will be:

$$\frac{\partial^2 E}{\partial z^2} = -\beta^2 E \text{..... (23)}$$

$$\frac{\partial^2 H}{\partial z^2} = -\beta^2 H \text{..... (24)}$$

Equation (19)~(24), together will give:

$$\nabla_{xy}^2 E = -(K^2 - \beta^2)E \ldots\ldots\ldots\ldots\ldots\ldots (25)$$

$$\nabla_{xy}^2 H = -(K^2 - \beta^2)H \ldots\ldots\ldots\ldots\ldots\ldots (26)$$

Recall that K_c is the cut-off wavenumber where $K_c^2 = K^2 - \beta^2$, then (25)~(26) can be simplified as

$$\nabla_{xy}^2 E = -K_c^2\, E \ldots\ldots\ldots\ldots\ldots\ldots (27)$$

$$\nabla_{xy}^2 H = -K_c^2\, H \ldots\ldots\ldots\ldots\ldots\ldots (28)$$

As stated in section 4.21, a rectangular waveguide can support either TE mode or TM mode. Therefore, I am going to discuss it with EM wave equation, respectively.

4.22 a. TE Mode in Rectangular Waveguide

A TE mode wave has only magnetic field along the propagation direction, thus, $E_z = 0$ and $H_z \neq 0$. Let's focus on the H field in the Z direction in equation (28).

$$\nabla_{xy}^2 H_z = \frac{\partial^2 H_z}{\partial x^2} + \frac{\partial^2 H_z}{\partial y^2} = -K_c^2\, H_z \ldots\ldots\ldots\ldots\ldots\ldots (29)$$

The solution to equation (29) is:

$$H_z = A\cos(K_{cx}X)\cos\big(K_{cy}Y\big) \ldots\ldots\ldots\ldots\ldots\ldots (30)$$

where A is a constant.

With $E_z = 0$, I now have everything to solve equation (15)~(18).

$$H_x = -\frac{j\beta}{K_c^2}\frac{\partial H_z}{\partial x} = -\frac{j\beta}{K_c^2}\big(-AK_{cx}\sin(K_{cx}X)\cos\big(K_{cy}Y\big)\big) = \frac{j\beta}{K_c^2}AK_{cx}\sin(K_{cx}X)\cos\big(K_{cy}Y\big)$$

$$H_y = -\frac{j\beta}{K_c^2}\frac{\partial H_z}{\partial y} = -\frac{j\beta}{K_c^2}\big(-AK_{cy}\sin(K_{cy}Y)\cos(K_{cx}X)\big) = \frac{j\beta}{K_c^2}AK_{cy}\sin(K_{cy}Y)\cos(K_{cx}X)$$

$$H_z = A\cos(K_{cx}X)\cos\big(K_{cy}Y\big)$$

$$E_x = -\frac{j\omega\mu}{K_c^2}\frac{\partial H_z}{\partial y} = -\frac{j\omega\mu}{K_c^2}\big(-AK_{cy}\sin(K_{cy}Y)\cos(K_{cx}X)\big) = \frac{j\omega\mu}{K_c^2}AK_{cy}\sin(K_{cy}Y)\cos(K_{cx}X)$$

$$E_y = \frac{j\omega\mu}{K_c^2}\frac{\partial H_z}{\partial x} = \frac{j\omega\mu}{K_c^2}\big(-AK_{cx}\sin(K_{cx}X)\cos\big(K_{cy}Y\big)\big) = -\frac{j\omega\mu}{K_c^2}AK_{cx}\sin(K_{cx}X)\cos\big(K_{cy}Y\big)$$

$$E_z = 0 \ldots\ldots\ldots\ldots\ldots\ldots\ldots\ldots\ldots\ldots \quad (31)$$

As stated in assumptions, the waveguide is made with PEC. Therefore, the electric field at the boundary of the transverse plane must be zero.

Namely,

$$E_y = 0 \text{ at X=0, a; } E_x = 0 \text{ at Y=0, b} \ldots\ldots\ldots\ldots\ldots\ldots\ldots\ldots\ldots \quad (32)$$

Therefore, $K_{cx} = \frac{m\pi}{a}$ and $K_{cy} = \frac{n\pi}{b}$, where m and n are integer numbers from 0. m and n also indicate the numbers of half-wave patterns along the width and height of rectangular waveguide, respectively. It can be easily seen from solutions (31) that m and n cannot be both zero, otherwise, there is no electric and magnetic field inside waveguide.

The cut-off wavenumber: $K_c = \sqrt{K_{cx}^2 + K_{cy}^2}$,

$$K_c = \sqrt{\left(\frac{m\pi}{a}\right)^2 + \left(\frac{n\pi}{b}\right)^2} \ldots\ldots\ldots\ldots\ldots\ldots \quad (33)$$

As $K_c^2 = K^2 - \beta^2 = \omega^2\mu\epsilon - \beta^2$, then $\beta = \sqrt{\omega^2\mu\epsilon - K_c^2} = \sqrt{\omega^2\mu\epsilon - ((\frac{m\pi}{a})^2 + \left(\frac{n\pi}{b}\right)^2)}$

For a propagation mode, the phase constant β must be a real number; otherwise, it will lead to pure attenuation. To achieve this, the term $\omega^2\mu\epsilon$ can not be smaller than K_c^2 and the minimum frequency ω is introduced as cut-off frequency f_c shown as below.

$$f_c = \frac{1}{2\pi\sqrt{\mu\varepsilon}}\sqrt{\left(\frac{m\pi}{a}\right)^2 + \left(\frac{n\pi}{b}\right)^2} \quad \text{(m, n =0,1….; m and n cannot be both 0) …… (34)}$$

When the frequency is below the cut-off frequency, the wave cannot propagate inside the waveguide. At the cut-off frequency, the phase constant β=0 and wave starts to propagate when the frequency slightly exceeds f_c.

Using equation (34), if I know the cross-section dimension of a rectangular waveguide, then the cut-off frequencies can be determined for TE mode.

For example, the cut-off frequencies of an X-band rectangular waveguide in TE mode with a = 22.86 mm and b = 10.16 mm used in this thesis are determined as following. Assume that this waveguide is filled with air.

For TE_{10} mode: $f_c = \frac{1}{2\pi\sqrt{4\pi\times10^{-7}}\times8.85\times10^{-12}}\sqrt{\left(\frac{1\pi}{22.86\times10^{-3}}\right)^2+\left(\frac{0\pi}{11.43\times10^{-3}}\right)^2} = 6.562GHz$

For TE_{20} mode: $f_c = \frac{1}{2\pi\sqrt{4\pi\times10^{-7}}\times8.85\times10^{-12}}\sqrt{\left(\frac{2\pi}{22.86\times10^{-3}}\right)^2+\left(\frac{0\pi}{11.43\times10^{-3}}\right)^2} = 13.123GHz$

For TE_{01} mode: $f_c = \frac{1}{2\pi\sqrt{4\pi\times10^{-7}}\times8.85\times10^{-12}}\sqrt{\left(\frac{0\pi}{22.86\times10^{-3}}\right)^2+\left(\frac{1\pi}{11.43\times10^{-3}}\right)^2} = 14.764GHz$

For TE_{11} mode: $f_c = \frac{1}{2\pi\sqrt{4\pi\times10^{-7}}\times8.85\times10^{-12}}\sqrt{\left(\frac{1\pi}{22.86\times10^{-3}}\right)^2+\left(\frac{1\pi}{11.43\times10^{-3}}\right)^2} = 16.156GHz$

From the calculations shown above, it can be seen that TE_{10} mode has the lowest cut-off frequency among all the TE modes.

4.22 b. TM Mode in Rectangular Waveguide

The TM mode in rectangular waveguide can be analysed in the similar way. A TM mode wave only has electric field along the propagation direction, thus, $H_z = 0$ and $E_z \neq 0$. The E field in the Z direction in equation (27) can be expressed as

$$\nabla_{xy}^2 E_z = \frac{\partial^2 E_z}{\partial x^2} + \frac{\partial^2 E_z}{\partial y^2} = -K_c^2\, E_z \quad \text{..... (35)}$$

The solution to equation (35) is

$$E_z = B\sin(K_{cx}X)\sin(K_{cy}Y) \quad \text{..... (36)}$$

Where B is a constant.

With $H_z = 0$, I now have everything to solve equation (15)~(18).

$$E_x = -\frac{j\beta}{K_c^2}\frac{\partial E_z}{\partial x} = -\frac{j\beta}{K_c^2}\left(B\,K_{cx}\cos(K_{cx}\,X)\sin(K_{cy}Y)\right) = -\frac{j\beta}{K_c^2}BK_{cx}\cos(K_{cx}\,X)\sin(K_{cy}Y)$$

$$E_y = -\frac{j\beta}{K_c^2}\frac{\partial E_z}{\partial y} = -\frac{j\beta}{K_c^2}\left(BK_{cy}\cos(K_{cy}\,Y)\sin(K_{cx}X)\right) = -\frac{j\beta}{K_c^2}BK_{cy}\cos(K_{cy}\,Y)\sin(K_{cx}X)$$

$$E_z = \sin(K_{cx}X)\sin(K_{cy}Y)$$

$$H_x = \frac{j\omega\varepsilon}{K_c^2}\frac{\partial E_z}{\partial y} = \frac{j\omega\varepsilon}{K_c^2}\left(BK_{cy}\cos(K_{cy}Y)\sin(K_{cx}X)\right) = \frac{j\omega\varepsilon}{K_c^2}BK_{cy}\cos(K_{cy}Y)\sin(K_{cx}X)$$

$$H_y = -\frac{j\omega\varepsilon}{K_c^2}\frac{\partial E_z}{\partial x} = -\frac{j\omega\varepsilon}{K_c^2}\left(BK_{cx}\cos(K_{cx}X)\sin(K_{cy}Y)\right) = -\frac{j\omega\varepsilon}{K_c^2}BK_{cx}\cos(K_{cx}X)\sin(K_{cy}Y)$$

$$H_z = 0 \text{..... (37)}$$

As stated in assumptions, the waveguide is made of PEC. Thus, the boundary conditions of a TM mode wave will be:

E_z= 0 at X=0, a; $E_z = 0$ at Y=0, b ..... (38)

Therefore, $K_{cx} = \frac{m\pi}{a}$ and $K_{cy} = \frac{n\pi}{b}$, where m and n are integer numbers from 1. It can be easily seen from solution (37) that if m or n is zero, all the sin terms will be zero. Consequently, there will be no wave propagating inside the waveguide. Therefore, both m and n must be greater than 0. The cut-off frequency f_c for a rectangular waveguide in TM mode is shown as

$$f_c = \frac{1}{2\pi\sqrt{\mu\varepsilon}}\sqrt{\left(\frac{m\pi}{a}\right)^2 + \left(\frac{n\pi}{b}\right)^2} \text{ (m, n=1,2....) ..... (39)}$$

The cut-off frequencies of the same X-band rectangular waveguide in TM mode are determined as following.

For TM_{11} mode: $f_c = \frac{1}{2\pi\sqrt{4\pi\times10^{-7}}\times8.85\times10^{-12}}\sqrt{\left(\frac{1\pi}{22.86\times10^{-3}}\right)^2 + \left(\frac{1\pi}{11.43\times10^{-3}}\right)^2} = 16.16GHz$

For TM_{12} mode: $f_c = \frac{1}{2\pi\sqrt{4\pi\times10^{-7}}\times8.85\times10^{-12}}\sqrt{\left(\frac{1\pi}{22.86\times10^{-3}}\right)^2 + \left(\frac{2\pi}{11.43\times10^{-3}}\right)^2} = 30.25GHz$

For TM_{21} mode: $f_c = \frac{1}{2\pi\sqrt{4\pi\times10^{-7}}\times8.85\times10^{-12}}\sqrt{\left(\frac{2\pi}{22.86\times10^{-3}}\right)^2 + \left(\frac{1\pi}{11.43\times10^{-3}}\right)^2} = 19.75GHz$

The calculations above show that TE_{10} mode has the lowest cut-off frequency (6.562GHz) among all TE and TM modes. Therefore, TE_{10} mode is the dominant mode of the X-band rectangular waveguide.

An X-band rectangular waveguide filled with air is simulated and its E-field and H-field are shown in Fig.4.223 and Fig.4.224, respectively. The simulation shows that this X-band rectangular waveguide is in TE mode since the E-field is in transverse plane and it only has H-field along the wave propagation direction. Moreover, the E-filed distribution shows that there is no variation along the Y direction, and it has one half-wave variation along the X direction. Therefore, this X-band rectangular waveguide is in TE_{10} mode. There are standard dimensions for rectangular waveguides at different frequencies as shown in [80]. In this thesis, a WR-90 X band rectangular waveguide will be employed.

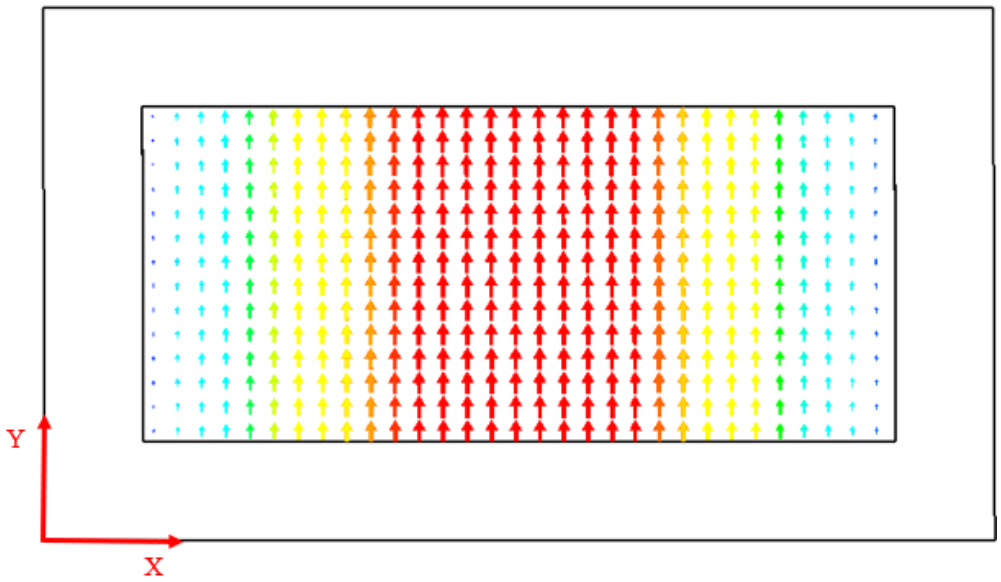

Fig.4.223 TE_{10} mode E-field in transverse plane in a rectangular waveguide

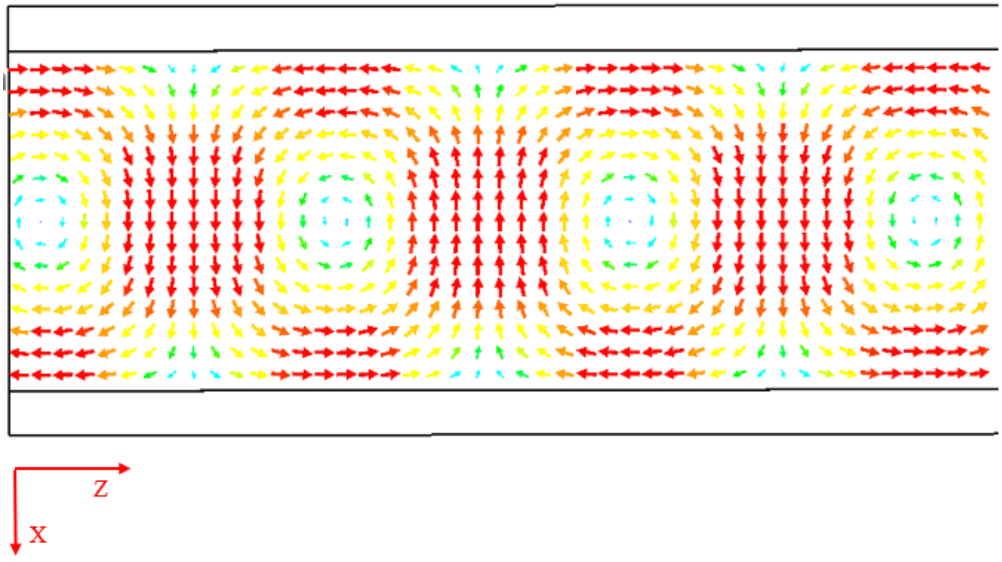

Fig.4.224 TE_{10} mode H-field in propagation direction in a rectangular waveguide

4.23 Elliptical Waveguide

Elliptical waveguide is another type of waveguide I used in this thesis. Fig.4.231 shows a metallic elliptical waveguide with dielectric filling. Its equivalent model in Cartesian coordinate system is show in Fig.4.231. Like the rectangular waveguide, the elliptical waveguide is also filled with dielectric material which has a permittivity ε and permeability μ. The dimensions of the elliptical waveguide are given as Table.4.231.

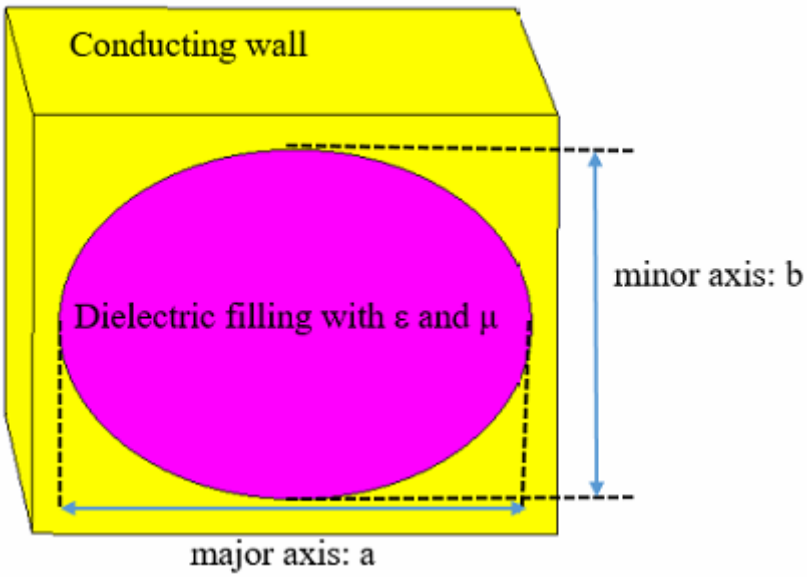

Fig.4.231 An elliptical waveguide with dielectric filling

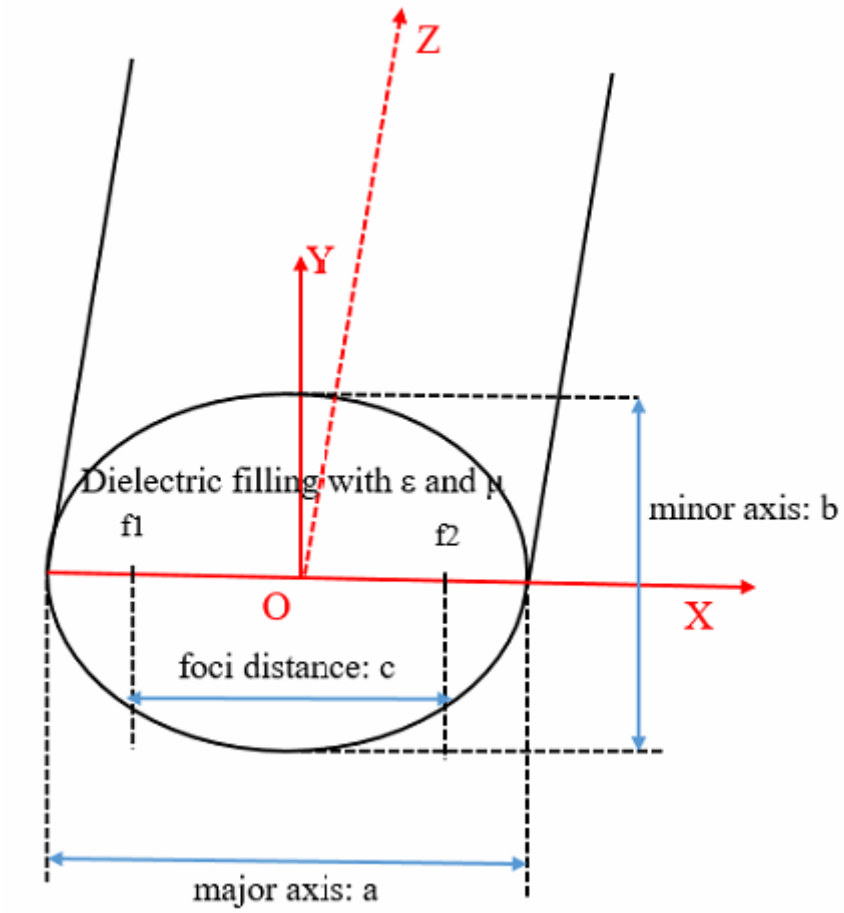

Fig.4.232 An equivalent model for an elliptical waveguide in Cartesian coordinate system

Table.4.231

Major Axis	Minor Axis	Foci Distance	Permittivity	Permeability
a	b	c	ε	μ

The analysis of elliptical waveguide is similar to a rectangular waveguide with the same assumptions, while applies more complicate boundary conditions to solve the EM wave equation. According to [81], the wave travelling inside an elliptical waveguide still obeys electromagnetic wave equation (19)~(20).

$$\nabla^2 E + K^2 E = 0 \ldots\ldots\ldots\ldots\ldots\ldots\ldots\ldots \quad (19)$$

$$\nabla^2 H + K^2 H = 0 \ldots\ldots\ldots\ldots\ldots\ldots\ldots\ldots \quad (20)$$

The cross section of an elliptical waveguide is an ellipse as shown in Fig.3.232 and can be defined mathematically as:

$$D = \left\{(x, y), \frac{x^2}{a^2} + \frac{y^2}{b^2} \leq 1 \;\; (x, y \in R)\right\} \ldots\ldots\ldots\ldots\ldots\ldots\ldots\ldots\ldots\ldots \text{(40)}$$

To solve the EM wave equation for an elliptical waveguide under TE mode and TM mode, different boundary conditions are set up as following, respectively:

In TE mode, there is only E field in transverse plane and H field exist in propagation direction (Z direction). Therefore, EM wave must satisfy:

$$\frac{\partial H_Z}{\partial n}|_{\partial D} = 0 \ldots\ldots\ldots\ldots\ldots\ldots\ldots\ldots\ldots\ldots\text{(41)}$$

In TM mode, there is only H field in transverse plane and E field exist in propagation direction (Z direction). Therefore, EM wave must satisfy:

$$E_Z|_{\partial D} = 0 \ldots\ldots\ldots\ldots\ldots\ldots\ldots\ldots\ldots\ldots\ldots \text{(42)}$$

With equation (41) and (42), EM wave equation could be solved for an elliptical waveguide under TE mode or TM mode. Authors in [81] proposed a polynomial method to find out the complete solutions to EM wave equation and [82] presented mathematical calculations to obtain the normalized cut-off wavelengths of an elliptical waveguide under different propagation modes.

Regarding to propagation mode, the elliptical and rectangular are similar, except one distinct difference. The propagation modes of an elliptical waveguide could be classified as: TE even mode (TE_e), TE odd mode (TE_o), TM even mode (TM_e), TM odd mode (TM_o). This is because when an elliptical waveguide is in TE or TM mode, the even and odd angular Mathieu functions generated from the EM wave equation will have two different solutions, which consequently result in two independent TE or TM modes [83].

4.24 Waveguide bends

Normally, waveguide is a straight long rigid structure, except for flexible waveguide. Electromagnetic waves are confined within the waveguide and travel to a particular destination. If an electromagnetic signal needs to be transmitted in a different direction, waveguide bends are usually applied to arrange the waveguides into the required positions. Fig.4.241l shows a picture of a 90 degree H-plane waveguide bend (WR90).

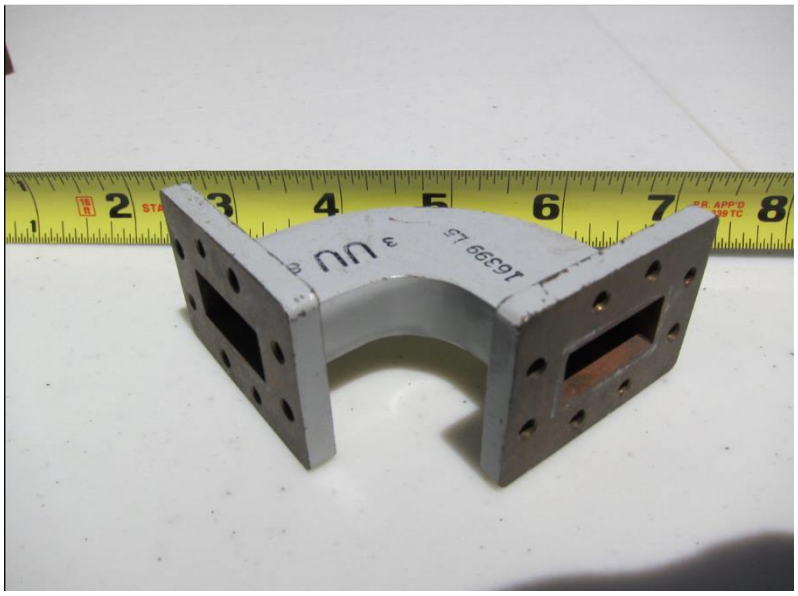

Fig.4.241 Picture of a 90 degree H-plane waveguide bend (WR90) [84]

The investigation of EM wave propagation in a straight metallic waveguide can be traced back to 1897, when Lord Rayleigh initiated an early study on waveguide [85]. In 1939, Buchholz published the detailed analysis of EM wave propagation mode in a gradual-bend waveguide as shown in Fig.4.242 [86]. Since then, numerous researchers have carried out studies on this topic. Different approaches to describe the situation have been proposed, including using exact formulations by Morimoto in 1940 [87], presenting expansion procedures applied to the defining differential equations by in 1946 [88], applying Matrix theoretic techniques by Rice in 1948 [89] and employing approximate formulations of equivalent transmission line theory by Andreasen in 1958 [90]. In 1966, Alan Cochran and Robert Pecina from Bell Telephone Lab published the investigation in EM wave inside waveguide bends of rectangular cross section [91]. With their numerical computations and graphs, fundamental propagation modes of EM wave inside waveguide bends were described precisely. According to their results, the waveguide bend with rectangular cross

section can be presented in cylindrical coordinate system (r, φ, z) as shown in Fig.4.242. The open-end waveguide bend shown in Fig.4.242 has a top at Z = a, bottom at Z = 0, inner wall at r = r_1 and outer wall at r = r_2, respectively.

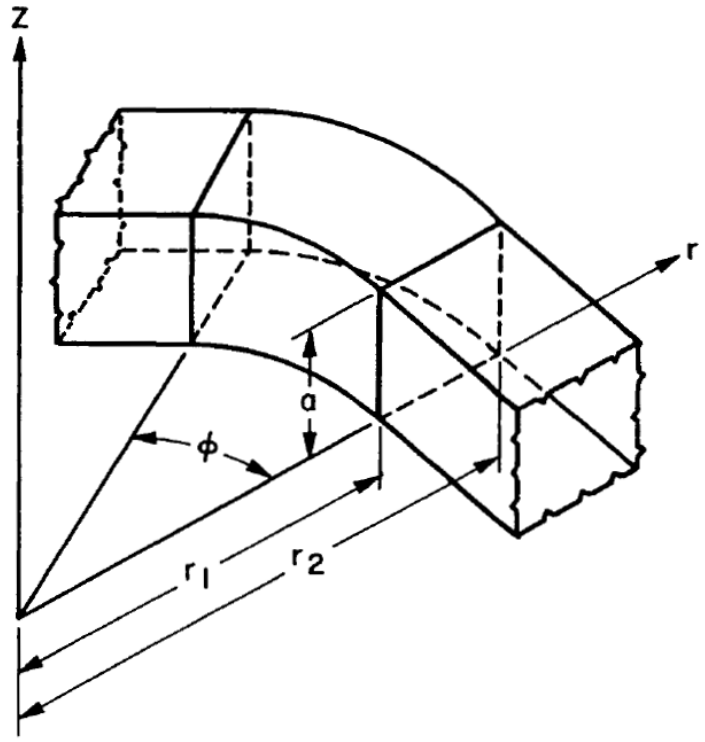

Fig.4.242 Waveguide bend with rectangular cross section [91]

Assume that the waveguide bend in Fig.4.242 is made of perfect electric conductor (PEC), and filled with non-conducting medium with permeability μ and permittivity ε. The EM wave travels along φ direction as $e^{\pm jv\varphi}$ (v is the angular propagation constant) and its time variant as $e^{-j\omega t}$ (ω is the angular frequency). According to vector wave equation [79], EM wave inside the waveguide bend also obeys equation (43):

$$\nabla^2 F + K^2 F = 0 \text{..... (43)}$$

Where $K^2 = \omega^2 \mu\varepsilon$ and F is electric and magnetic fields associated with EM wave.

Two important independent families of vector solutions of (43) are:

$$M = \nabla \times (\text{cu}) \text{..... (44)}$$

$$N = \frac{1}{K} \nabla \times \nabla \times (\text{cu}) \text{..... (45)}$$

Where c is a constant vector which is parallel to z axis in a cylindrical coordinate system and u is the Hertz potentials which satisfies the scalar wave.

Equation (44) and (45) can then be expressed in the general form as:

$$M = \left\{\pm\frac{jv}{r}C_v(hr)e_r - hC_v'(hr)e_\varphi\right\}\binom{sin}{cos}qze^{\pm jv\varphi} \text{..... (46)}$$

$$N = \left\{\frac{q}{k}\left[hC_v'(hr)e_r \pm \frac{jv}{r}C_v(hr)e_\varphi\right]\binom{cos}{-sin}qz + \frac{h^2}{k}C_v(hr)\binom{sin}{cos}qze_z\right\}e^{\pm jv\varphi} \text{..... (47)}$$

Where $C_v$is a general Bessel function of order v and $h = (k^2 - q^2)^{\frac{1}{2}}$.

Under the above assumptions, EM wave inside the waveguide bend shown in Fig. 4.242 can be described by originally selecting either M or N as the electric field.

4.24 a. LE wave (E-plane waveguide bend)

Longitudinal Electric (LE) wave, also known as LE wave, is the field configuration inside the waveguide bend when only M (equation (46)) is selected. When only equation M applies, the electric fields inside the waveguide bend are:

$$E_r = \pm\frac{jv}{r}C_v(hr)\sin\left(\frac{n\pi z}{a}\right)e^{\pm jv\varphi} \text{..... (48)}$$

$$E_\varphi = -hC_v'(hr)\sin\left(\frac{n\pi z}{a}\right)e^{\pm jv\varphi} \text{..... (49)}$$

$$E_z = 0 \text{..... (50)}$$

From equation (48) ~(50), it can be seen that there is no electric field component in z direction and the entire electric field lies in the bending plane. Therefore, a continuously curved waveguide which only supports this propagation mode is referred as E-plane waveguide bend. For an E-plane waveguide bend, only magnetic fields are distorted when the waveguide is bent.

4.24 b. LM wave (H-plane waveguide bend)

Longitudinal Magnetic (LM) wave, also known as LM wave is the field configuration inside the waveguide bend when only N (equation (47)) is selected. When equation N applies, the magnetic fields inside the waveguide bend are:

$$H_r = \pm \frac{k}{\omega\mu}\left(\frac{v}{r}\right) C_v(hr) \cos\left(\frac{n\pi z}{a}\right) e^{\pm jv\varphi} \ldots\ldots\ldots (51)$$

$$H_\varphi = \frac{kh}{\omega\mu} C_v'(hr) \cos\left(\frac{n\pi z}{a}\right) e^{\pm jv\varphi} \ldots\ldots\ldots (52)$$

$$H_z = 0 \ldots\ldots\ldots (53)$$

From equation (51) ~(53), it can be seen that there is no magnetic field component in z direction and the entire magnetic field lies in the bending plane. Therefore, a continuously curved waveguide which only supports this propagation mode is referred as H-plane waveguide bend. For a H-plane waveguide bend, only magnetic fields are distorted when the waveguide is bent.

Generally, in a straight waveguide, the propagating EM wave can be categorized into TE and TM mode as discussed in previous sections. Similarly, the propagating EM wave in a waveguide bend can also be categorized into LE and LM waves. According to results in [91], The LE (0,1) mode in a waveguide bend corresponds to TE (0,1) in a straight waveguide and LM (1,0) mode corresponds to TE (1,0) mode. Moreover, [91] stated that the cut-off frequencies of a waveguide bend with a fixed cross section generally depend on the bending radius r_1 except those for LE (0, n) modes. Fig. 4.243 shows the bending radius dependence of cut-off frequency in different types of waveguide bend.

r_2-r_1 (mm)	a (mm)	r_1 (mm)	Cut-off Frequency (GHz)			
			LM(1,0)	LE(0,1)	LM(2,0)	LE(0,2)
72.14	34.04	38.1	2.05	4.403	4.139	>8.8
		76.2	2.066	4.403	4.149	
		152.4	2.074	4.403	4.153	
		∞	2.077	4.403	4.154	
34.04	72.14	38.1	4.381	2.077	>8.8	4.154
		76.2	4.395	2.077		4.154
		152.4	4.401	2.077		4.154
		∞	4.403	2.077		4.154
22.86	10.16	12.7	6.473	14.75	13.065	>29.4
		25.4	6.522	14.75	13.094	
		50.8	6.544	14.75	13.105	
		∞	6.556	14.75	13.112	
10.16	22.86	12.7	14.687	6.556	>29.4	13.112
		25.4	14.729	6.556		13.112
		50.8	14.744	6.556		13.112
		∞	14.75	6.556		13.112

WR90 H-plane bend →

WR90 E-plane bend →

Fig.4.243 Bending radius dependence of cut-off frequencies in standard waveguide bends [91]

In this thesis, WR90 waveguide was the standard waveguide used in both simulation and measurement. Therefore, the last two rows in Fig.4.243, which are the WR90 H-plane bend and WR90 E-plane bend, are important. For the WR90 H-plane bend, LM (1,0) mode is the dominant mode. Moreover, it can be seen from Fig.4.243 that with bending radius r_1 increasing, cut-off frequencies at LM (1,0) mode increases slightly, then remain the same after bending radius reaches a certain value (one wavelength). For the WR90 E-plane bend, LE (0,1) mode is the dominate mode. From Fig.4.243, it can be seen that with bending radius r_1 increasing, cut-off frequencies at LE (0,1) mode always remain the same.

4.3 Slotted Waveguide Antenna

In this thesis, I also investigated a knitted slotted waveguide antenna. Therefore, it was useful to review basics about a slotted waveguide antenna.

The history of slotted waveguide antenna (SWA) can be traced back to 1943, when John Kemp attempted to detail the propagation modes for different types of waveguide, he also found out that a metallic waveguide can transform to a radiating antenna if there are some slots on the waveguide wall [92]. As this kind of antenna is developed from waveguide, it is named as slotted waveguide antenna (SWA). SWAs are easy to fabricate to conform to the surface on which they are mounted, as only needs to cut slots on the walls. With the advantage of supporting high frequency radiation with a high directivity (For example: 26.3dBi at 94GHz in [93]) SWA finds its popular applications in radar and aircraft navigation systems. Fig.4.321 presents an example of a slotted waveguide antenna. It is a metallic rectangular waveguide with four slots on the top wall, where a is the waveguide width, b is the waveguide height, c is the distance between the last slot and the end, d is the offset that the slots are away from centerline, e is the separation between two adjacent slots, l is the slot length and w is the slot width.

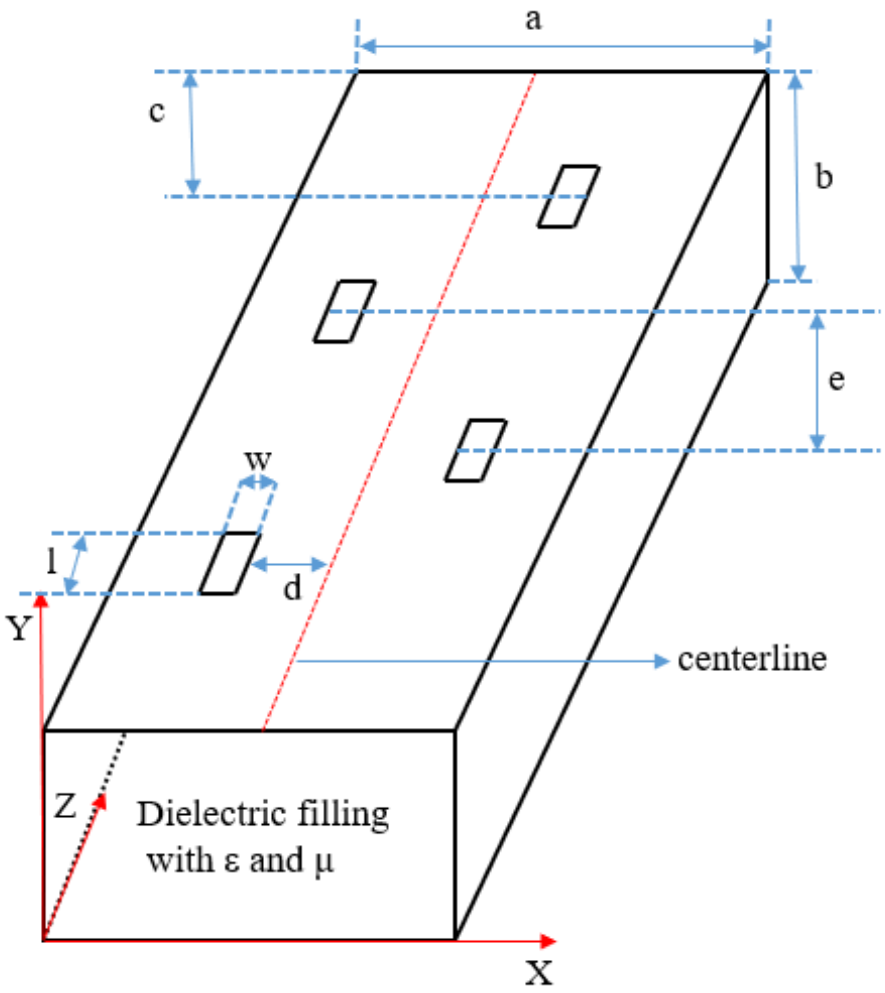

Fig.4.321 Geometry of a slotted waveguide antenna with four slots

Recall the analysis for rectangular waveguide in section 4.22, I can assume this SWA is in dominant TE10 mode. Therefore, the EM wave travelling inside the waveguide can be expressed as:

$$H_x = \frac{j\beta}{K_{cx}} A \sin(K_{cx}X)$$

$$H_y = 0$$

$$H_z = A \cos(K_{cx}X)$$

$$E_x = 0$$

$$E_y = -\frac{j\omega\mu}{K_{cx}} A \sin(K_{cx}X)$$

$$E_z = 0 \text{..... (54)}$$

where $K_{cx} = \frac{\pi}{a}$, and A is a constant determined by the SWA input power.

The H-fields tangent to a conducting surface will induce electric currents on the waveguide's top wall. From equation (54), the current density on the top surface where the slots are mounted can be deduced as:

$$J_x \propto A\cos(K_{cx}X), \text{ determined by } H_z \text{..... (55)}$$

$$J_z \propto \frac{j\beta}{K_{cx}} A\sin(K_{cx}X), \text{ determined by } H_z \text{ ..... (56)}$$

From equation (55)~(56), it can be seen that the surface current on the top wall of the SWA consists of x-component and z-component. Normally, the slots on a SWA are narrow, with a width less than a tenth of wavelength (w $<0.1\lambda$). Therefore, if the slots are mounted in the way as shown in Fig.4.321, they will only cause the discontinuity of x-component surface current flow. Consequently, in this case, the x-component surface current is mainly responsible for the antenna's radiation as it has to travel around the slots. From equation (55)~(56), I can also find out that if the slots sit on the centerline of the waveguide (red dash line in Fig.4.321) where $X = \frac{a}{2}$, the cos term in x-component surface current will be:

$$A\cos(K_{cx}X) = A\cos\left(\frac{\pi}{a}\times\frac{a}{2}\right) = A\cos(\frac{\pi}{2}) = 0 \text{..... (57)}$$

As a result, there will be no radiation for this SWA as the X-component surface current density J_x is zero. Hence, the slots must be offset from the center line of the waveguide and the offset distance d will determine the current density and hence determine how much power a SWA can radiate.

For a SWA as shown in Fig.4.321, the waveguide serves as a transmission line and the slots on the top surface are formed in a 2 by 2 array acting as the radiating element. The length of the slots is associated with antenna's resonant frequency and l is usually be approximately half wavelength in air ($\lambda_0/2$). The separation, e, between two adjacent slots is chosen to be about half of guided wavelength ($\lambda_g/2$), where guided wavelength is the wavelength inside a waveguide. According to [19], at a certain frequency, the input impedance of the slots on the waveguide is the same when they are spaced approximately half guided wavelength from

each other. In this case, all the slots can be viewed as being parallel connected and the equivalent input impedance of a SWA can be simply calculated as: [94]

$$Z_{in} = \frac{1}{NY_s} \quad \text{..... (58)}$$

Where N is the number of slots and Y_s is admittance of a slot.

The distance between the last slot and the end of waveguide, c, is always designed to be a quarter of guided wavelength ($\lambda_g/4$), so that the terminal can be treated as an open circuit according to transmission line theory [94]. The guided wavelength of a SWA can be calculated from equation (59):

$$\Lambda_g = \frac{1}{\sqrt{\left(\frac{1}{\lambda_0}\right)^2 - \left(\frac{1}{\lambda_c}\right)^2}} \quad \text{..... (59)}$$

Where λ_0 is the wavelength in air and λ_c is the cut-off wavelength of waveguide in the SWA.

Typically, the dimensions of a SWA are shown in Table 4.321.

Table 4.321 Dimensions of a SWA

c	d	e	l	w
$\lambda_g/4$	$0 < d < \frac{a}{2}$	$\lambda_g/2$	$\lambda_0/2$	$<0.1\lambda_0$

4.4 Frequency Selective Surface

Periodic structures which consist of repetitive lattices can be widely found in nature. Theoretically, most of objects materials are periodic at the atomic scale. At a larger scale, the commonest example of periodic structures can be seen is the honeycomb. In electromagnetism, according to [95], a frequency selective surface (FSS) is defined as *a* "*two-dimensional periodic surface consisting of infinite conducting patch or aperture elements*". Basically, the name of FSS reflects its function, it can act as a filter in wireless communications system to separate electromagnetic waves of different frequencies. Due to its distinct frequency-filtering property, its applications can be found in various fields such as microwave ovens, antenna radomes, metamaterials, and stealth materials. FSSs has been developed rapidly in the last few decades, from typical narrow band FSS, broadband FSS, multi band FSS, compact FSS to curved FSS [96-100]. The study on frequency selective surface emerged in late 1960s, when R. Ulrich found the close interrelations between a thin metallic inductive grid and its complementary capacitive grid. He also stated that at certain frequency region (wavelength > unit cell size), both metallic grids could be described by simple transmission line equivalent circuits and had frequency-filtering properties [101]. Later, lots of researchers proposed their mathematical and experimental analyses on FSSs and various types of FSS have been demonstrated [102-104]. According to their results, for an FSS, its periodic unit cells mainly determines its frequency-filtering property. With different unit cells, an FSS can be configured as a low-pass filter, high-pass filter, band-pass filter or band-stop filter according to different applications.

According to [95], An FSS is formed by an infinite array consisting of identical elements, and these identical elements are referred as FSS's unit cells. In [105], Munk described the FSS structures operational principle in details. According to his explanation, the incident EM wave reaches the FSS structure and produces the induce currents into the unit cell. The shape and dimension of the unit cell define the currents which then generate new scattered fields on FSS. The resultant EM filed around an FSS is created by the incident fields and produced scattered fields. Therefore, the desired frequency-filtering property of an FSS structure can be determined by its properly designed unit cells.

When an incident plane wave (E_i) hits an FSS, transmission and reflection will both occurs. The transmission coefficient T and reflection coefficient Γ can be defined as:

$$T = E_t/E_i \quad \text{..... (60)}$$

where E_t is the transmitted wave.

$$\Gamma = E_r/E_i \quad \text{..... (61)}$$

where E_r is the reflected wave.

According to [106], under the hypothesis of a perfect conducting single-resonant freestanding FSS and it is designed properly to avoid grating lobe, when the FSS is excited by a normal incident wave it can be analysed as a two-port network as shown in Fig.4.41.

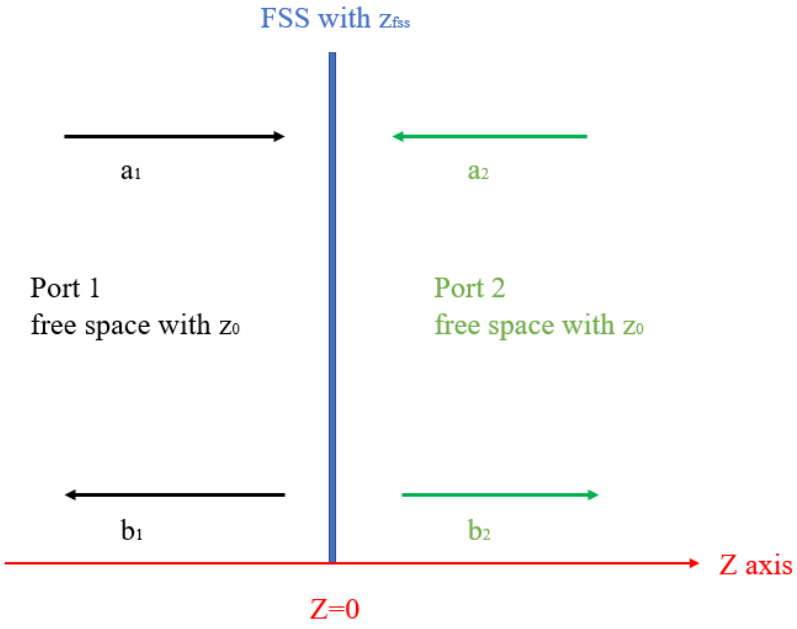

Fig.4.41. Two-port model of a freestanding FSS

FSS plane is assumed to be infinitesimally thin with impedance z_{fss} at the original position in Z axis (Z=0). Area to the left (Z<0) and to the right (Z>0) is free space with impedance z_0 and is defined as port 1 and port 2 in the network, respectively. The incident wave is a and reflected wave is b, their relationship is described by scattering matrix S of FSS as:

$$b = S_{fss}\, a \quad \text{..... (62)}$$

where $a = (a_1, a_2)^T$, $b = (b_1, b_2)^T$ and $S_{fss} = \begin{pmatrix} S_{11} & S_{12} \\ S_{21} & S_{22} \end{pmatrix}$

Here $a_{1,2}$ and $b_{1,2}$ are the amplitude of incident and reflected wave at each port respectively.

$$\begin{pmatrix} b_1 \\ b_2 \end{pmatrix} = \begin{pmatrix} S_{11} & S_{12} \\ S_{21} & S_{22} \end{pmatrix} \begin{pmatrix} a_1 \\ a_2 \end{pmatrix} \ldots\ldots\ldots\ldots\ldots\ldots\ldots\ldots\ldots\ldots \quad (63)$$

At port 1, S_{11} is the same as the FSS's reflection coefficient Γ and S_{21} is the same as the FSS's transmission coefficient T.

According to the statements in [106],

$$b_1 = -\frac{z_0/z_{fss}}{2+z_0/z_{fss}} a_1 + \frac{2}{2+z_0/z_{fss}} a_2 \ldots\ldots\ldots\ldots\ldots\ldots\ldots\ldots\ldots\ldots \quad (64)$$

$$b_2 = \frac{2}{2+z_0/z_{fss}} a_1 - \frac{z_0/z_{fss}}{2+z_0/z_{fss}} a_2 \ldots\ldots\ldots\ldots\ldots\ldots\ldots\ldots\ldots\ldots \quad (65)$$

Therefore, S11 which is also the FSS's reflection coefficient Γ can be expressed as

$$\Gamma = \left| -\frac{z_0/z_{fss}}{2+z_0/z_{fss}} \right| \ldots\ldots\ldots\ldots\ldots\ldots\ldots\ldots\ldots\ldots \quad (66)$$

S21 which is also the FSS's transmission coefficient T can be expressed as

$$T = \left| \frac{2}{2+z_0/z_{fss}} \right| \ldots\ldots\ldots\ldots\ldots\ldots\ldots\ldots\ldots\ldots \quad (67)$$

Equation (66) and (67) has also been derived by a similar analysis in [107]. Since z_0 is a constant (free space impedance), the reflection coefficient of a lossless freestanding FSS is only related to its impedance, z_{fss}.

In [108], the authors derived the impedance of an arbitrarily shaped FSS when it is excited by a normal incident wave as:

$$z_{fss} = -j \frac{\sum_{p=-\infty}^{+\infty} \sum_{q=-\infty}^{+\infty} \tilde{J}^*(p,q) \tilde{\bar{G}}(p,q) \tilde{J}(p,q)}{2\tilde{J}^*(0,0) \tilde{\bar{G}}(0,0) \tilde{J}(0,0)}, \; where\; p \neq 0, q \neq 0 \ldots\ldots\ldots\ldots\ldots \quad (68)$$

According to [108], the expression of FSS reactance has the same pole-zero properties as a passive LC circuit. Therefore, it is possible to approximate an FSS frequency response by an equivalent circuit.

In this thesis, two types of FSS, cross slot FSS and hexagonal loop FSS are involved. I am going to discuss them respectively in the following.

4.41 Cross Slot FSS

Fig.4.411 presents a single layer, thin metallic cross slot FSS oriented in Z direction. This is a freestanding 4 by 4 grid with a thickness less than 0.1λ, where λ is the wavelength at the FSS's resonant frequency.

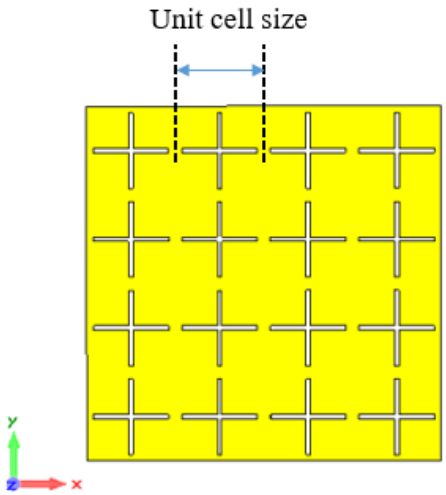

Fig.4.411 A freestanding thin metallic cross slot FSS

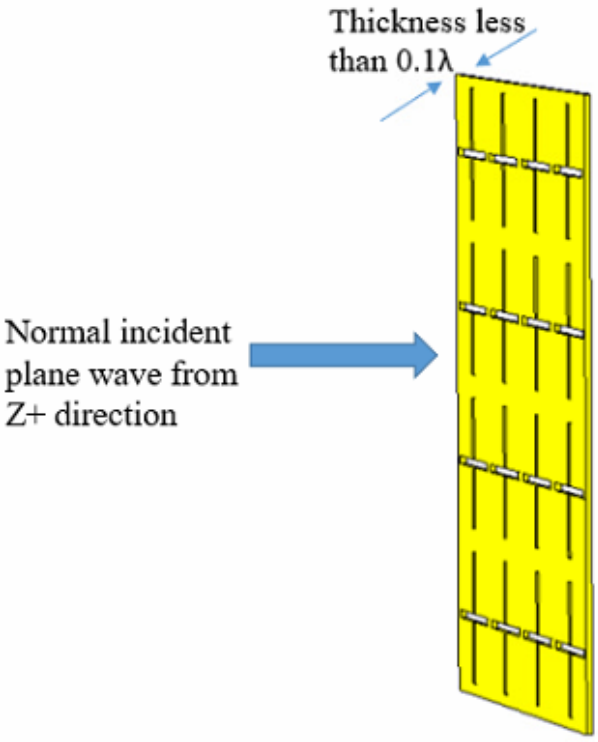

Fig.4.412 A cross slot FSS is excited by a normal incident plane EM wave

According to the statement in [95], if a cross slot FSS is excited by a normal incident plane electromagnetic wave from Z+ direction as shown in Fig.4.412, its performance can be approximately described as a lump parallel LC circuit shown in Fig.4.413 with three idealizations:

1. The cross slot FSS is infinitely thin
2. The metallic cross slot FSS is perfectly conducting without loss.
3. The cross slot FSS works at certain frequency range where wavelength > unit cell size

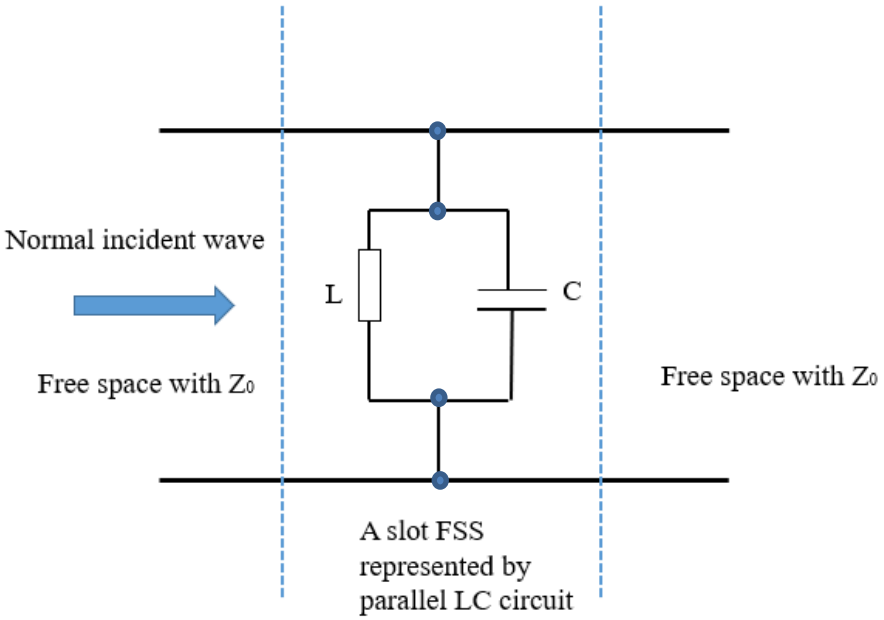

Fig.4.413 Equivalent circuit for a cross slot FSS

The admittance of the circuit shown in Fig.4.413 can be found out as:

$$Z_{fss} = \frac{1}{\frac{1}{j\omega L} + j\omega C} = \frac{j\omega L}{1-\omega^2 LC} \quad \text{..... (69)}$$

Substitute (69) into (66), the reflection coefficient of a cross slot FSS is

$$\Gamma = \left| -\frac{z_0/z_{fss}}{2+z_0/z_{fss}} \right| = \left| -\frac{z_0}{2z_{fss}+z_0} \right| = \left| -\frac{z_0}{2\frac{j\omega L}{1-\omega^2 LC}+z_0} \right| \quad \text{..... (70)}$$

From Equation (69), it can be seen that at the resonant frequency, $\omega_0 = \sqrt{\frac{1}{LC}}$, z_{fss} is infinitesimally large and equation (70) Γ equals 0. It means that the FSS is equivalent to an

open circuit at its resonant frequency and the incident wave is able to pass through the FSS without reflection. Therefore, this cross slot FSS can be classified as a band-pass FSS, where ω_0 is the resonant frequency.

4.42 Hexagonal Loop FSS

Fig.4.421 presents a single layer, thin metallic hexagonal loop FSS. When this structure is excited by a normal incident plane electromagnetic wave from Z+ direction as shown in Fig.4.422, with the same idealizations listed in section 4.41, this loop FSS can be approximately described as a lumped series LC equivalent circuit as shown in Fig.4.423 [95].

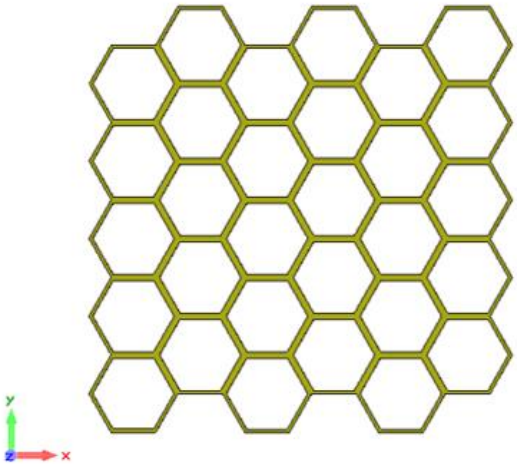

Fig.4.421 A freestanding thin metallic hexagonal loop FSS

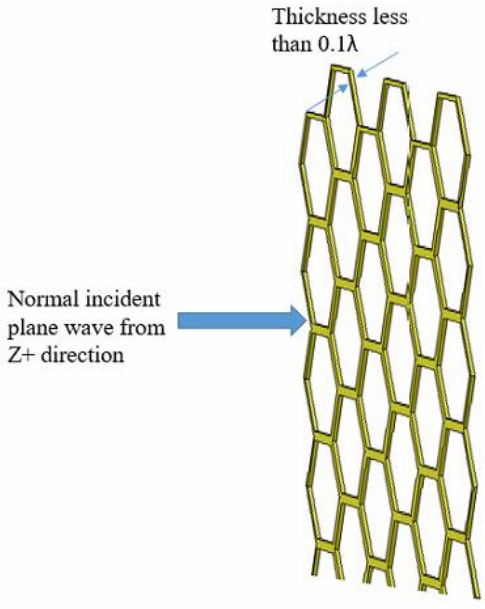

Fig.4.422 A hexagonal loop FSS is excited by a normal incident plane EM wave

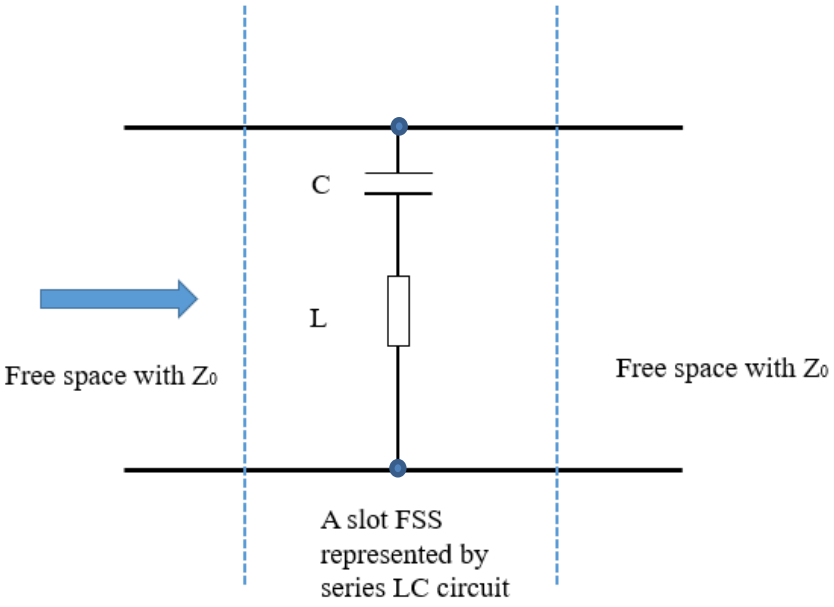

Fig.4.423 Equivalent circuit for the hexagonal loop FSS

The impedance of the circuit shown in Fig.4.423 can be expressed as:

$$Z_{fss} = \frac{1}{j\omega C} + j\omega L = \frac{1-\omega^2 LC}{j\omega C} \quad \text{..... (71)}$$

Subtitute (71) into (66), the reflection coefficient of a hexagonal loop FSS is

$$\Gamma = \left| -\frac{z_0/z_{fss}}{2+z_0/z_{fss}} \right| = \left| -\frac{z_0}{2z_{fss}+z_0} \right| = \left| -\frac{z_0}{2\frac{1-\omega^2 LC}{j\omega C}+z_0} \right| \quad \text{..... (72)}$$

From Equation (71), it can be seen that at resonant frequency $\omega_0 = \sqrt{\frac{1}{LC}}$, z_{fss} is 0 and equation (72) Γ equals 1. It means that the FSS is equivalent to a short circuit at its resonant frequency and the incident wave is totally reflected at this particular frequency. Therefore, this hexagonal loop FSS can be classified as a band-stop FSS and ω_0 is known as its resonant frequency.

4.5 Conclusion

In this chapter, the fundamental basics associated with waveguide, slotted waveguide antenna and frequency selective surface were reviewed. Examples and equations were also given to help readers to obtain a better understanding of all the theories used in this thesis.

Chapter 5. A Knitted Textile Waveguide

5.1 Introduction

In the last decade, with the fast development of new materials and manufacturing techniques, wearable devices for body-centric communications system have attracted significant attention due to certain advantages such as flexibility, light weight and high-strength-to-weight ratio [10]. Moreover, as electromagnetic devices are made with commercial clothing materials, they can be integrated seamlessly with garments to support various functions such as on-body/off-body wireless communications. For example, lots of research has been done on textile antennas [55-60]. The textile antennas gave me the inspiration to make a textile waveguide as waveguide is a basic component used to guide the electromagnetic energy between its endpoints in communications system.

This chapter began with the presentation of a knitted textile waveguide with an elliptical cross-section [109]. Then, based on the waveguide's performance, the dielectric property of the knitted polyester and the conductivity of the textile sleeve were studied. Since the knitted waveguide was flexible and it was difficult to keep the waveguide rigid, its performance under distortion conditions were tested [110]. The impact of moisture on the knitted waveguide's performance was also studied [111]. Finally, conclusions were drawn based on the agreements achieved between simulation and measurement.

5.2 Knitted Waveguide Structure

Fig.5.21 shows a knitted waveguide with an elliptical cross-section designed for X-band. It was fabricated by Shima Seiki SWG091N computerized flat-bed knitting machine at NTU and was basically a conducting textile sleeve filled with knitted polyester inside. The conducting sleeve was knitted with the highest available knitting density (20 stitches/inch and 25 rows/inch) to achieve the best conductivity. The approximated dimensions of the knitted waveguide are given in table.5.21.

(a) (b)

Fig.5.21 A knitted waveguide: (a) Top view; (b) Side view

Table.5.21 Dimensions of the knitted waveguide

Major Axis	Minor Axis	Whole Length	Thickness of Sleeve
27mm	20mm	320mm	1mm

A pair of transitions were designed to feed the knitted waveguide. Fig.5.22 shows the basic structure of a waveguide transition. The transition was a metallic open-ended waveguide with the same cross section as the knitted waveguide. A commercial 50 Ω N-type connector was mounted on the top wall of transition with its Teflon dielectric ending at the inner wall. The probe extended about a quarter wavelength ($\lambda/4$) into the transition to match the input impedance. The distance between the centre of probe and rear inner wall of the transition is referred to as the back short length and should be a quarter guided wavelength ($\lambda_g/4$) to

ensure that the reflected wave is in phase with the incident wave. The dimensions of the transition are given in table.5.22.

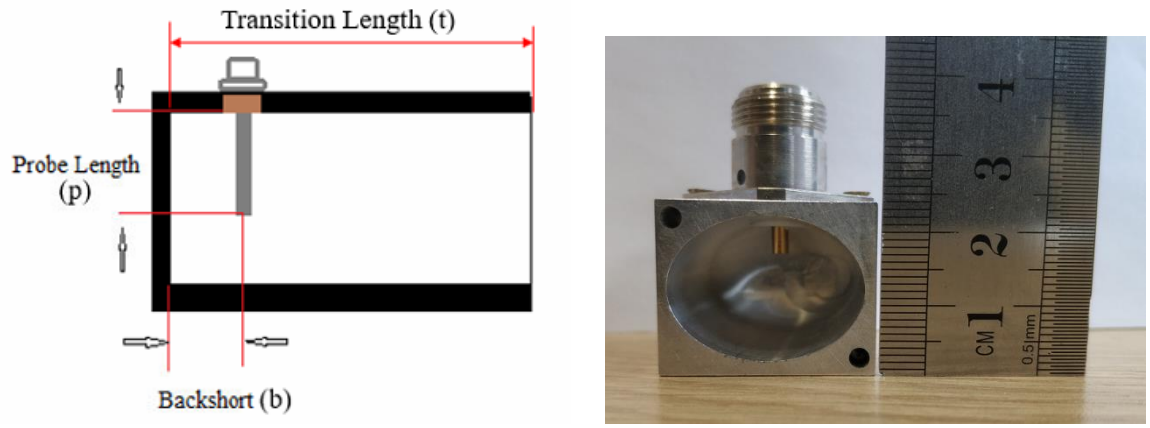

(a) (b)

Fig.5.22 Configuration of a waveguide transition: (a) Side view; (b) Front view

Table.5.22 Dimensions of transition

Transition Length (t)	Black short Length (b)	Probe Length (p)
30mm	7mm	5.6mm

5.3 Knitted Waveguide Performance

The input return loss (S11) and forward transmission (S21) of waveguides were measured using a vector network analyzer (VNA). Before the measurement, a SMA two-port calibration was done. A set of 85052D SMA calibration kits, two SMA cables and two SMA to N adapters were used in the two-port calibration process. The measurement setup is shown in Fig.5.31.

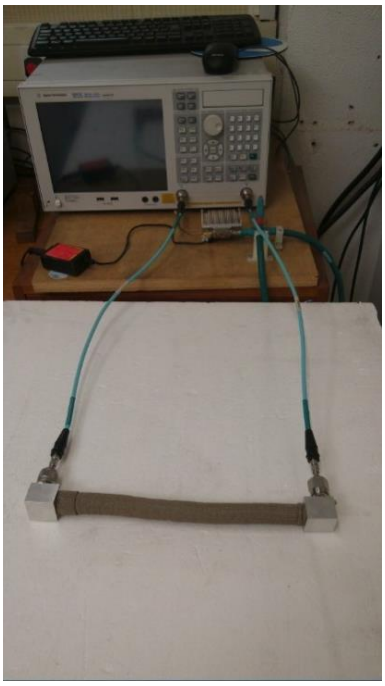

Fig.5.31. S-parameters measurement for knitted waveguide

The measured S-parameters of the knitted waveguide are presented in Fig.5.32. From the results, it can be seen that there was a distinct cut-off frequency at approximately 7.6GHz, where S21reached -10dB. The working frequency of this knitted waveguide was from 7.4GHz to 10.5GHz while the S11 was just below -10 dB and the average of S21 was about -7dB within the working frequency band. It can also be seen that both S11 and S21 showed ripples. The ripples were primarily caused by the impedance mismatch introduced by the transitions. Since there were SMA to N adapters employed in the calibration process, they also introduced the impedance mismatch in measurement. Additionally, the transitions cannot be manufactured precisely to the desired dimensions. Therefore, the multiple reflections caused by the impedance mismatch from the terminations resulted in the ripples in S11 and S21. The cause of ripples in S-parameter plot were studied in the next section.

The relatively high S11 and low S21 might not only be caused by the impedance mismatch at the transitions, but the poor dielectric property of the knitted polyester or the low conductivity of the textile sleeve. Therefore, the dielectric property of the knitted polyester and the conductivity of the textile sleeve were determined separately in the following sections.

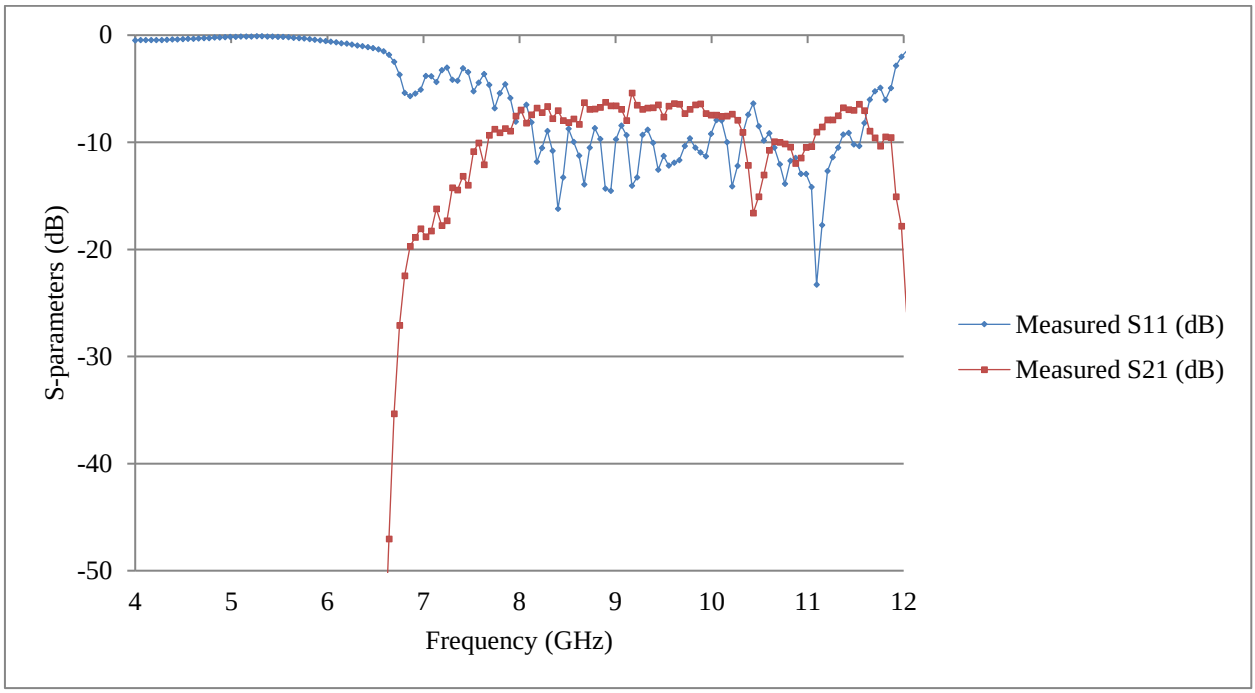

Fig.5.32 Measured S-parameters of the knitted waveguide

5.4 Dielectric Property of Knitted Polyester

The knitted sample was manufactured by Nottingham Trent University, I did not know the specified permittivity or dielectric loss constant of the knitted polyester. To find out the dielectric property of knitted polyester, an aluminium waveguide with a hollow inner which had the same dimensions as the knitted polyester was manufactured as shown in Fig.5.41. It served as a reference waveguide and the dimensions are given in table.5.41.

(a) (b)

Fig.5.41 Configuration of metallic waveguide: (a) Top view; (b) Front view

Table.5.41 Dimensions of hollow metallic waveguide

Width	Height	Major Axis	Minor Axis	Foci Distance	Whole Length
40mm	30mm	27mm	20mm	18mm	320mm

The same measuring methodology used in section 5.3 was applied to the metallic waveguide to determine the relative permittivity ε_r and the dielectric loss tanδ of the knitted polyester. First, the hollow metallic waveguide was simulated and measured, and Fig.5.42 shows the simulated and measured S21 for the hollow metallic waveguide. From Fig.5.42, it can be seen that the hollow metallic waveguide had a same cut off frequency and transmission loss level as expected. In this way, the hollow metallic waveguide was tested and could serve as a reference waveguide.

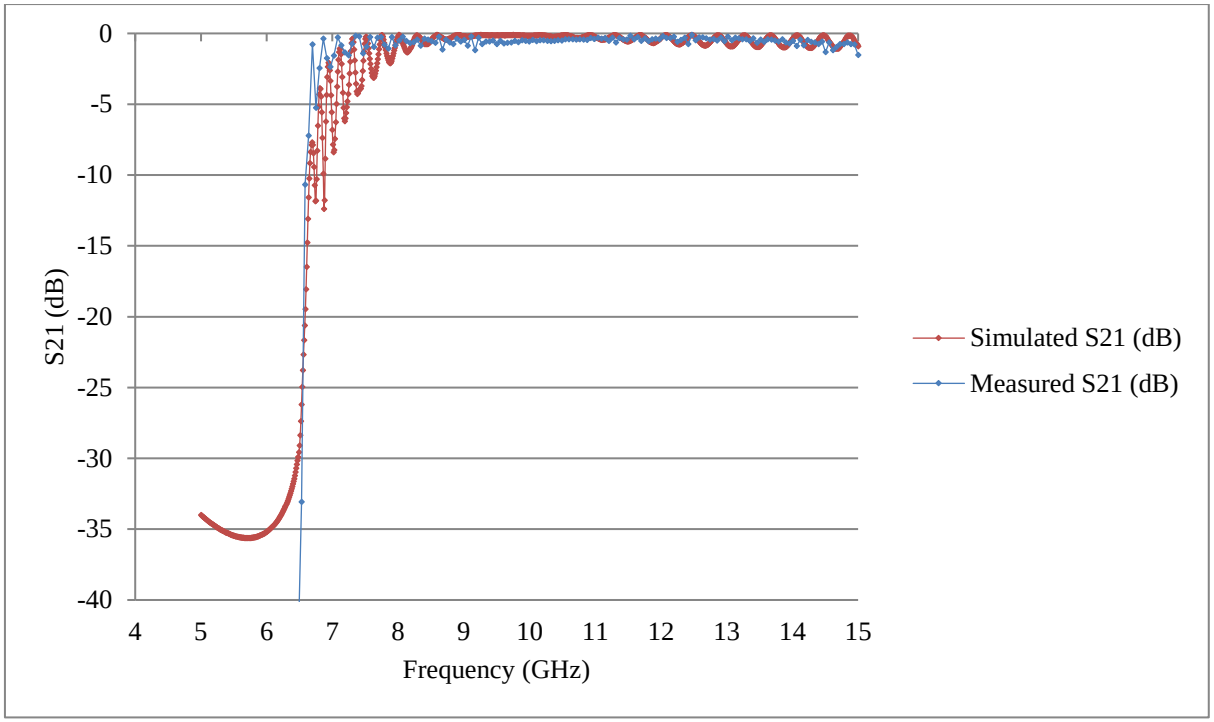

Fig.5.42 Simulated and measured S21 of hollow metallic waveguide

Then, the knitted polyester was inserted into the metallic reference waveguide and the waveguide with the dielectric material was modelled and simulated. For the knitted polyester in the simulation, its relative permittivity ε_r determined the waveguide's cut off frequency and its dielectric loss constant tanδ determined the waveguide's transmission gain level (S21), respectively. Therefore, the simulated S-parameters were optimised to match the measured results by adjusting ε_r and tanδ of the knitted polyester. The measured and simulated S21 of the metallic waveguide filled with knitted polyester are shown in Fig.5.43 respectively.

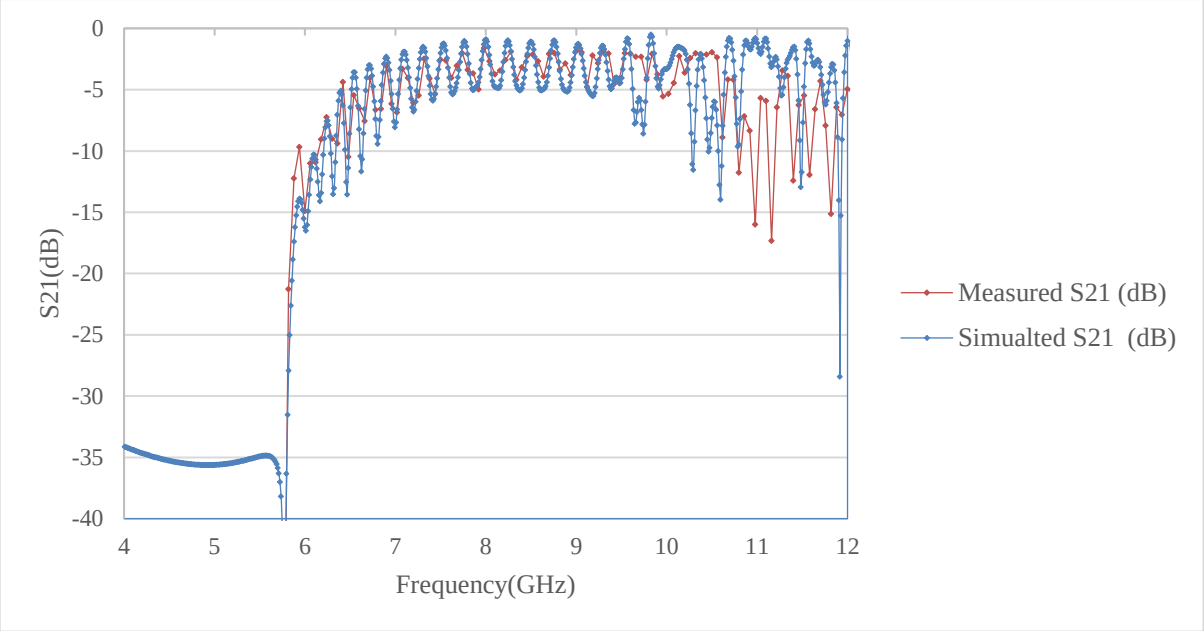

Fig.5.43 Simulated and measured S21 of metallic waveguide filled with knitted polyester

Fig.5.43 shows that the metallic waveguide filled with knitted polyester had the same cut-off frequency f_c in simulation and measurement. The simulated and measured cut-off frequency f_c of this waveguide was about 5.8 GHz. From the two curves, it can also be seen that good agreement was achieved between the measured and simulated S21 within the waveguide's working frequency when ε_r =1.3 and tanδ = 0.001 were set to the knitted polyester in simulation. The simulated and measured S21 both reached -3 dB from 7GHz to 9.5GHz which showed that the knitted polyester had an acceptable dielectric property at relatively high frequency, and it was suitable for knitted waveguide applications. The simulated E-field inside the waveguide is shown in Fig.5.44.

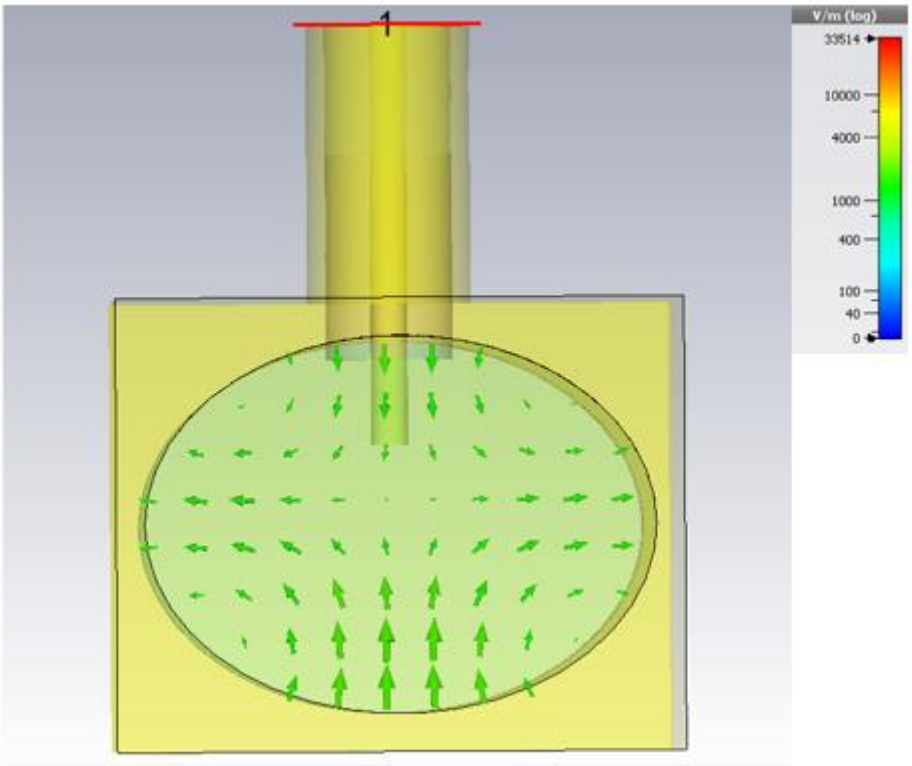

Fig.5.44. Simulated E-field of metallic waveguide filled with knitted polyester

According to [81], Fig.5.44 shows that the metallic waveguide filled with knitted polyester was in TE_{o21} mode. Based on the numerical analysis done in [92], the normalized cut-off wavelength (λ_c/a) for a TE_{o21} elliptical metallic waveguide with an eccentricity of 0.67 was approximately 1.72. The elliptical waveguide had a major axis of 27mm. Therefore, the cut-off wavelength was:

$$\lambda_c = 1.72 \times 27 = 46.44mm$$

The previous results showed that the relative permittivity ε_r of knitted polyester was approximately 1.3, so the theoretical cut-off frequency of the metallic waveguide with knitted polyester was:

$$f_c = \frac{c}{\lambda_c\sqrt{\varepsilon_r}} = \frac{300}{46.44 \times \sqrt{1.3}} \approx 5.67GHz$$

The simulated and measured cut-off frequency of the metallic waveguide with knitted polyester was about 5.8GHz, which generally agreed with the theoretical value. Therefore,

the metallic waveguide was designed and manufactured properly, and the dielectric property of knitted polyester was determined correctly.

Ripple Analysis

In Fig.5.42 and Fig.5.43, both simulated and measured S21 plots showed ripples. To confirm the cause of ripples, following simulations were made.

First, the metallic waveguide filled with knitted polyester was fed directly by two waveguide ports at its ends in simulation as shown in Fig. 5.45. The metallic elliptical waveguide had a length of 320mm, and its dimensions are shown in table 5.41. The simulated S21 of the direct-fed waveguide was shown in Fig. 5.46.

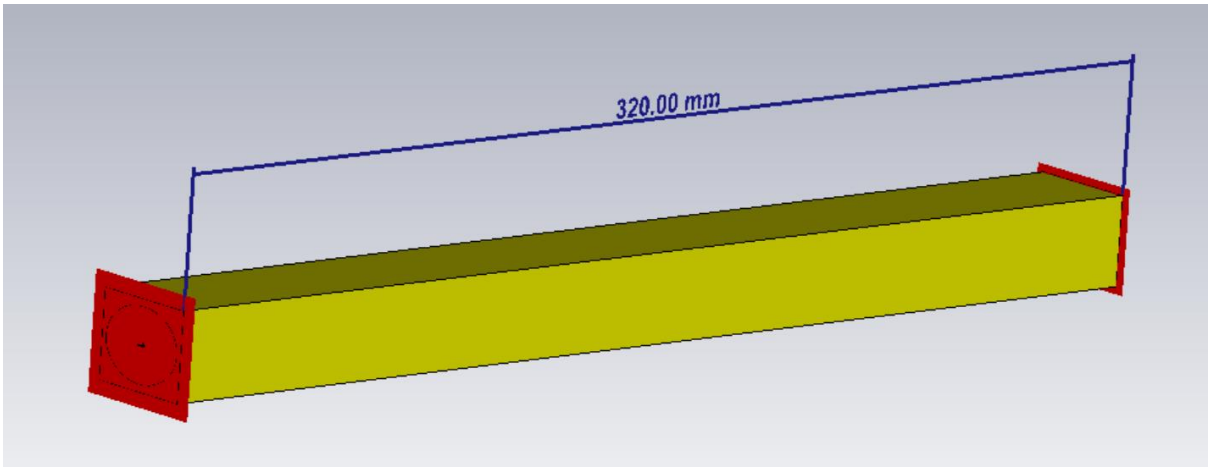

Fig.5.45 Metallic waveguide with knitted polyester direct fed by waveguide ports in CST

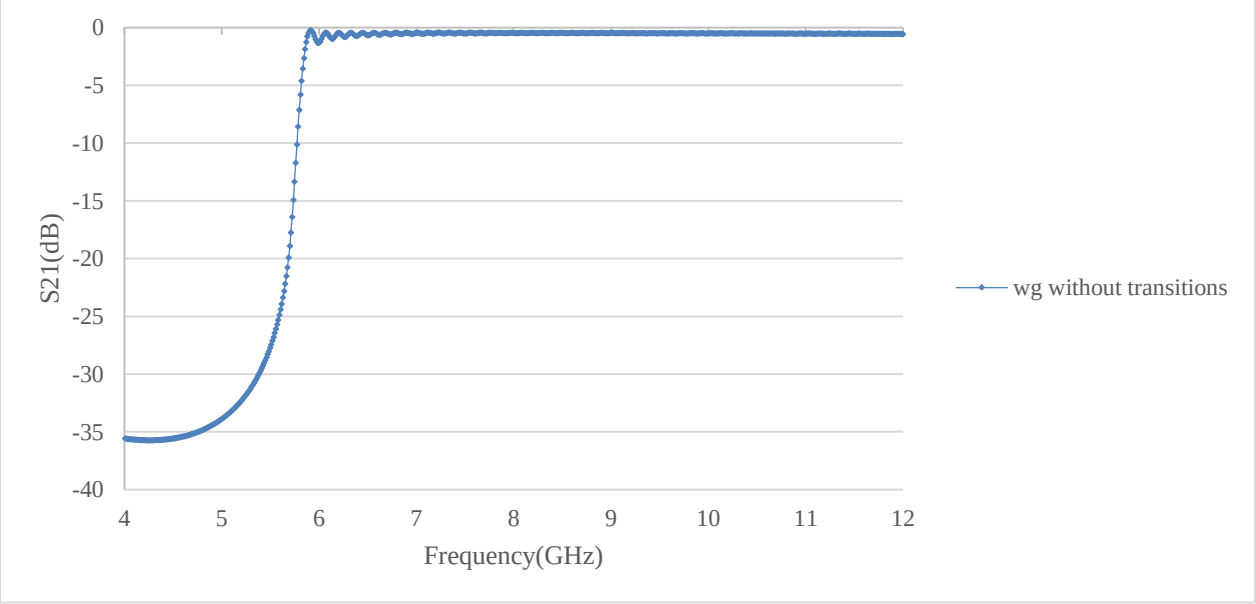

Fig.5.46 Simulated S21 of direct fed waveguide with knitted polyester

In Fig.5.46, simulated S21 shows small ripples when it approached 0 after waveguide's cut-off frequency. In simulation, the impedance of waveguide port was set automatically matched to waveguide's impedance. Therefore, when the waveguide was directly fed by two waveguide ports, there was no impedance mismatch throughout the interconnect. In [112], Sareh. T and Mohammadreza. K proposed a Fabry–Perot interferometric method to describe waveguide transmission and the transmitted power in a FP cavity was expressed as equation (72)

$$\frac{transmitted\ power}{input\ power} = \frac{I_t}{I_i} = \frac{(1-R^2)G}{(1-GR)^2+4GRsin^2\left(\frac{\delta}{2}\right)} \quad \text{..... (72)}$$

Where R is the reflectivity of waveguide's internal facets, $G = e^{-\partial L}$ is the total loss of waveguide of length L, $\delta = \frac{4\pi n_g L}{\lambda}$ is the round-trip phase shift, and $n_g = \frac{C}{V_g}$ is the group index of waveguide. From equation (72), it can be seen that in a waveguide, the transmitted power oscillates with term $4GRsin^2\left(\frac{\delta}{2}\right)$ as the rest terms in numerator and denominator are all constant in this case. Consequently, waveguide's S21 oscillated between its maximum equation (73) and minimum value equation (74) and small ripples were observed in Fig.5.46.

$$\left(\frac{I_t}{I_i}\right)_{max} = \frac{(1-R^2)G}{(1-GR)^2} \quad \text{..... (73)}$$

$$\left(\frac{I_t}{I_i}\right)_{min} = \frac{(1-R^2)G}{(1+GR)^2} \quad \text{..... (74)}$$

Next, the same waveguide was fed by two transitions designed in section 5.2 and simulated as shown in Fig.5.47. The metallic waveguide filled with knitted polyester had the same length of 320mm and its simulated S21 was plotted in Fig.5.48.

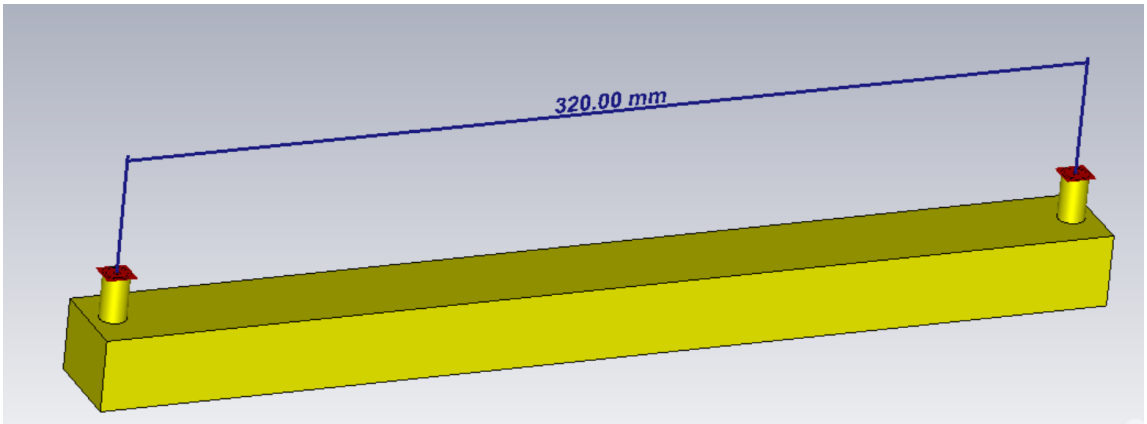

Fig.5.47 Metallic waveguide with knitted polyester fed by transitions in CST

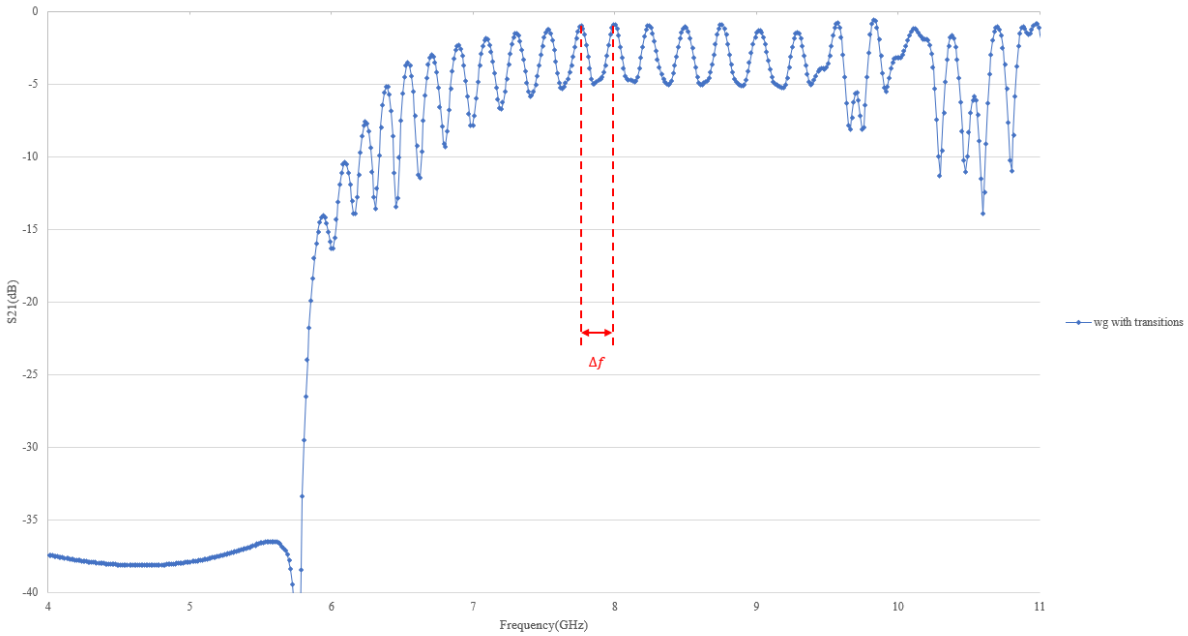

Fig.5.48 Simulated S21 of transition fed waveguide with knitted polyester

Fig.5.48 shows that the waveguide's S21 had larger ripples when it was fed by two transitions in simulation. According to the statement in [113], the larger impedance difference at the interconnect resulted in the larger dips in S-parameter plot. It means that transitions introduced impedance mismatch at the interconnects and caused the large ripples in Fig.5.48. [113] also proposed a method to measure the distance between impedance mismatch from the S-parameter plot which in this case was the waveguide's length.

$$\Delta f = \frac{1}{2T} \quad \text{..... (75)}$$

$$L = \frac{cT}{\sqrt{\varepsilon_r}} \quad \text{..... (76)}$$

Where Δf is the frequency spacing between two dips as shown in Fig.5.48, T is the traveling time between the interconnect, C is the speed of light, ε_r is the relative permittivity of dielectric in the waveguide and L is the length of waveguide.

In Fig.5.48, Δf was about 0.4GHz on average. Substitute equation (75) into equation (76), the waveguide's length can then be calculated as:

$$L = \frac{cT}{\sqrt{\varepsilon_r}} = \frac{c}{2\Delta f\sqrt{\varepsilon_r}} = 328mm \quad \text{..... (77)}$$

Which generally agreed with the simulated waveguide's length 320mm. The error likely came from the average of frequency spacing Δf. From Equation (77), we can also notice that for transition-fed waveguide with different lengths, the frequency spacing between dips Δf in S-parameter plot should become smaller when the waveguide is longer. And it was confirmed by the simulated results of waveguide with different lengths in Fig.5.49. The longest transition-fed waveguide had the smallest Δf.

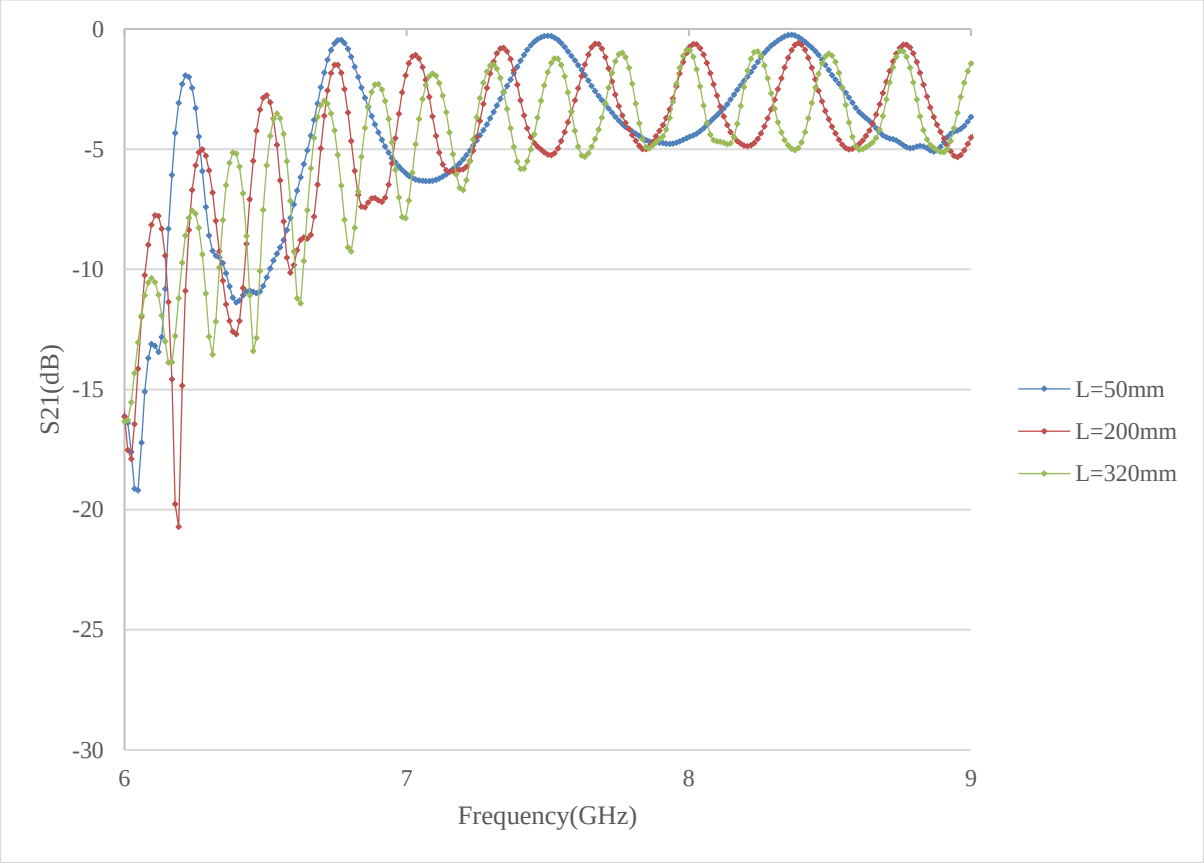

Fig.5.49 Simulated S21s of transition-fed waveguide with different lengths

5.5 Conductivity of Textile Sleeve

The textile sleeve was knitted by a conducting yarn formed by embedding silver nano particles on the surface of a 235 Denier 34 filament Polyamide 6.6 yarn [114]. To determine the conductivity of the textile sleeve, a standard WR-90 waveguide with SMA connectors shown in Fig.5.51 was used as a reference waveguide and a solid PTFE bar shown in Fig.5.51 was chosen as the filling for the rectangular waveguide.

Fig.5.51. WR-90 waveguide with SMA connectors and PTFE bar

The dielectric property of the PTFE was determined by applying the similar method described in section 5.4. The measured and simulated S21 of the WR-90 waveguide filled with PTFE are shown in Fig.5.52.

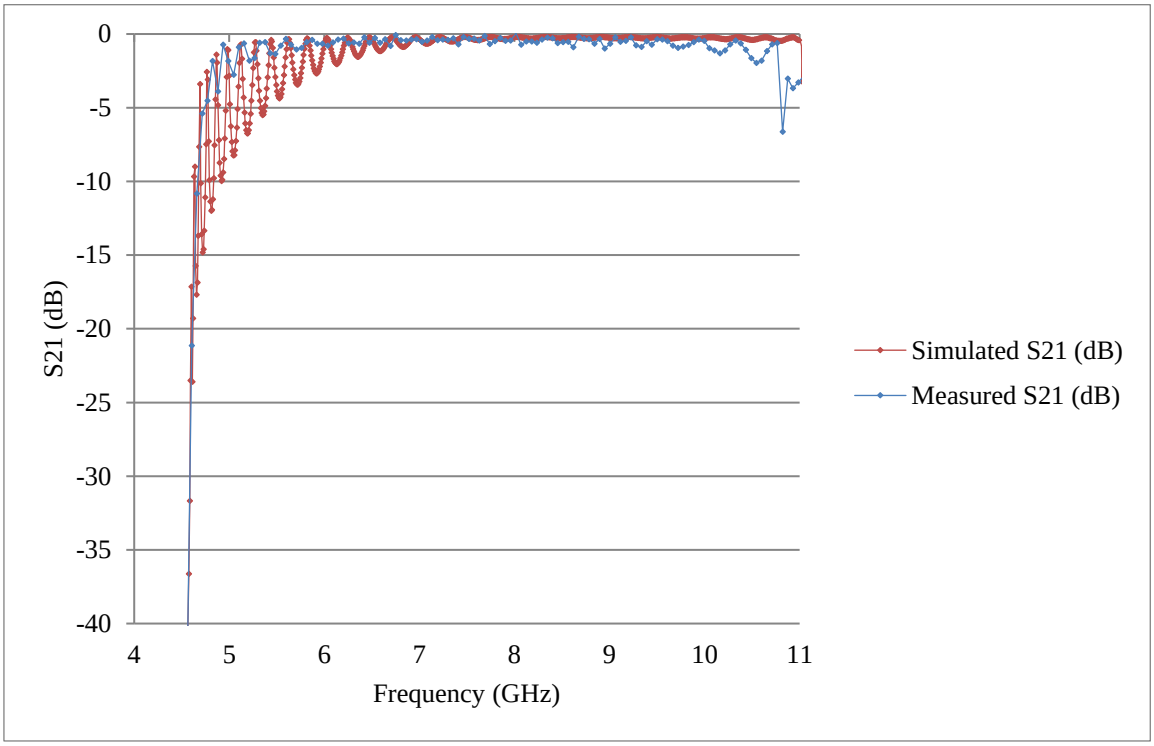

Fig.5.52. Comparison of measured and simulated S21 of WR-90 waveguide filled with PTFE

From Fig.5.52, it can be seen that the simulated S21 agreed the measured result when the PTFE was optimized to have $\varepsilon_r = 2.04$ and $\tan\delta = 0.0003$ in the simulation. In simulation and measurement, the WR-90 waveguide filled with PTFE had a distinct cut-off frequency at 4.75GHz and the S21 approached 0 within the working frequency. Therefore, the dielectric property of PTFE was determined, and PTFE was proved suitable for waveguide applications. Then, the performance of the textile sleeve filled with PTFE shown in Fig.5.53 was measured. The Measured S21 of textile sleeve filled with PTFE is shown in Fig.5.54.

Fig.5.53. Textile sleeve filled with PTFE with WR 90 transitions

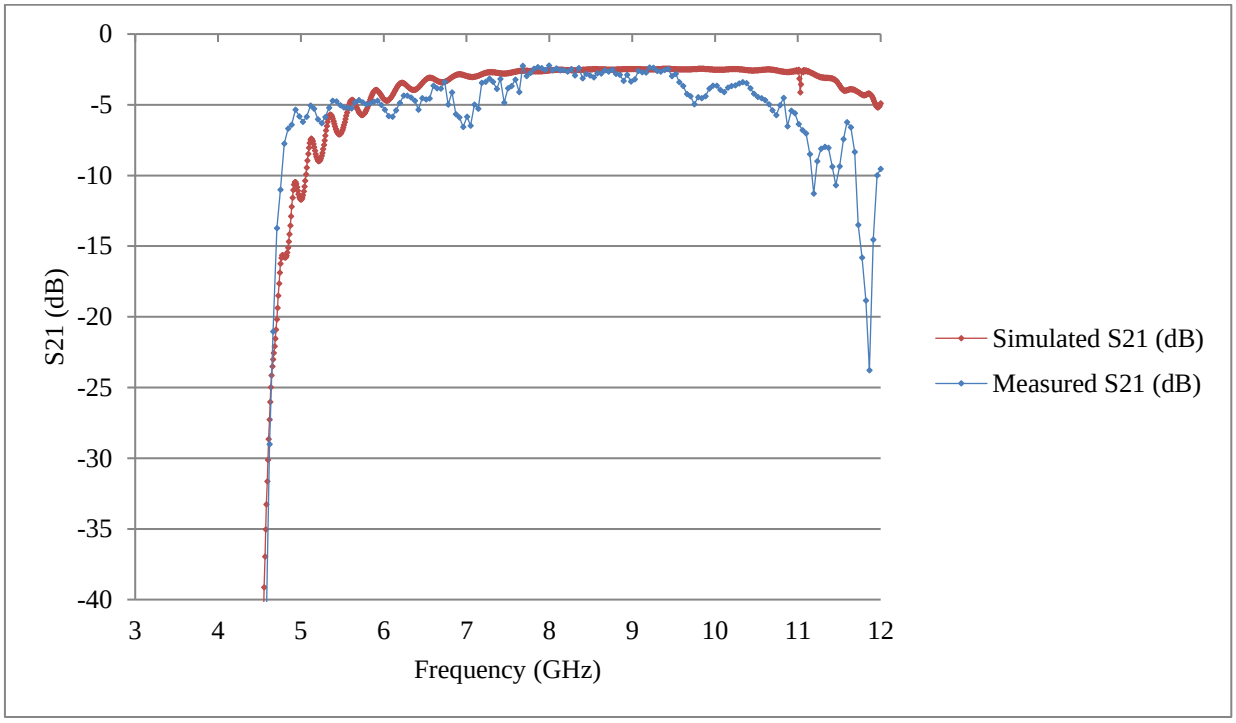

Fig.5.54. Measured and simulated S21 of textile sleeve filled with PTFE///

A parameter sweep was taken for the conductivity of the textile sleeve in simulation and the simulated S21 was optimized to match the measured S21 when the textile sleeve had a conductivity of 4000 S/m as shown in Fig.5.44. Fig.5.54 shows that the textile sleeve with PTFE had a distinct cut-off frequency at 4.75 GHz in both simulation and measurement. Furthermore, both simulated and measured S21 reached -3dB and achieved an acceptable

agreement within the working frequency between 7GHz to 11GHz. Therefore, the conductivity of textile sleeve was determined to be approximately 4000 S/m. To confirm the above result, the experiment in section 4.5 repeated with the textile sleeve filled with ROHACELL 51 foam and the textile sleeve was set to have conductivity of 4000 S/m in the simulation. The comparison of measured and simulated S21 of textile sleeve filled with foam is shown in Fig.5.55.

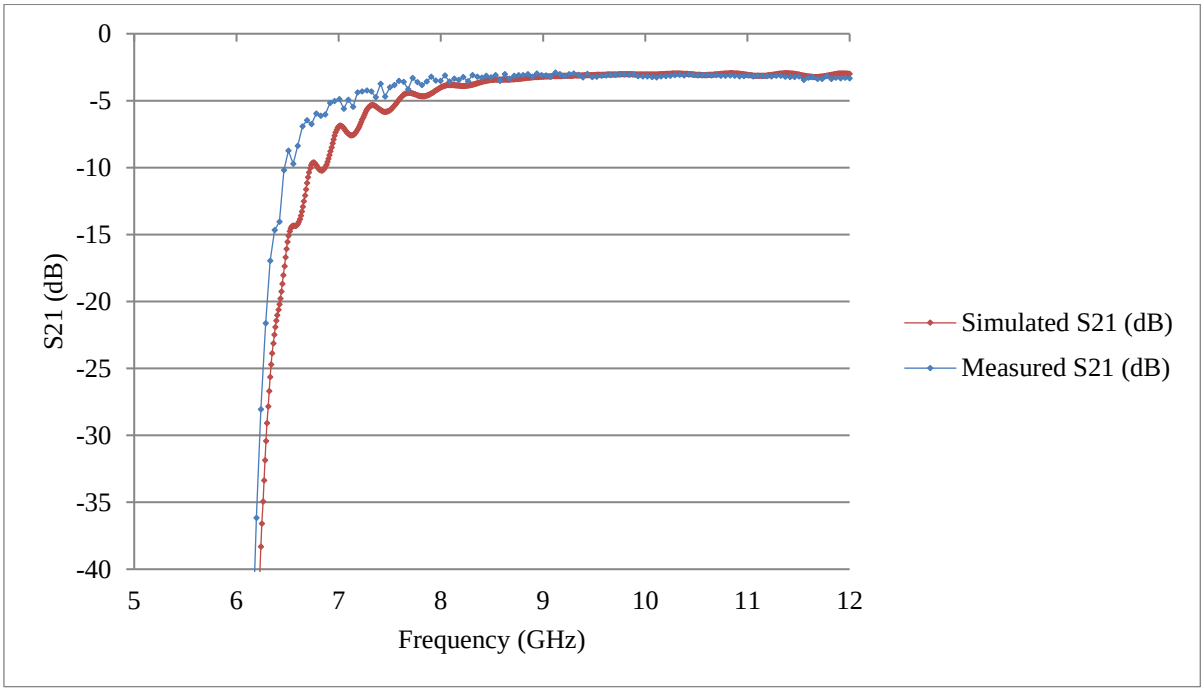

Fig.5.55. Measured and simulated S21 of textile sleeve filled with Rohacell foam

In Fig.5.55, the simulated and measured S21 achieved a good agreement from 9GHz to12GHz. With the above results, the textile sleeve could be concluded to have a conductivity of approximately 4000 S/m, and it was suitable for the knitted applications.

5.6 Kitted Waveguide under Bending

In the previous sections, I investigated a knitted textile waveguide and determined the properties of the textile materials. The results showed that this straight textile waveguide provided a reasonable waveguide performance. Due to its textile nature, the knitted waveguide was flexible and in practice it was difficult to keep the waveguide straight all the time. Thus, it was useful to evaluate the knitted waveguide's performance under shape distortions. The knitted textile waveguide was a long linear soft structure. Therefore, the most likely shape distortion occur to the waveguide in practice was bending. Bending can be in both horizontal and vertical directions. The horizontal and vertical directions corresponded to the waveguide's principle H-plane and E-plane, respectively. To study the knitted waveguide's performance under bending, three different bending conditions were set in both bending directions: 90 degree, 180 degree and 180 degree with a sharp corner in measurement. Fig.5.61 shows two pieces of wooden board. They were slotted according to the different bending conditions and served as the bases. The knitted waveguide was then clamped on the wooden board. For both H-plane and E-plane bending, three different conditions were achieved by keeping one end of the knitted waveguide fixed while moving the other end to the different grooves. The knitted waveguide was fed by two 50 Ω SMA cables and the same measuring methodology used in section 5.3 was applied.

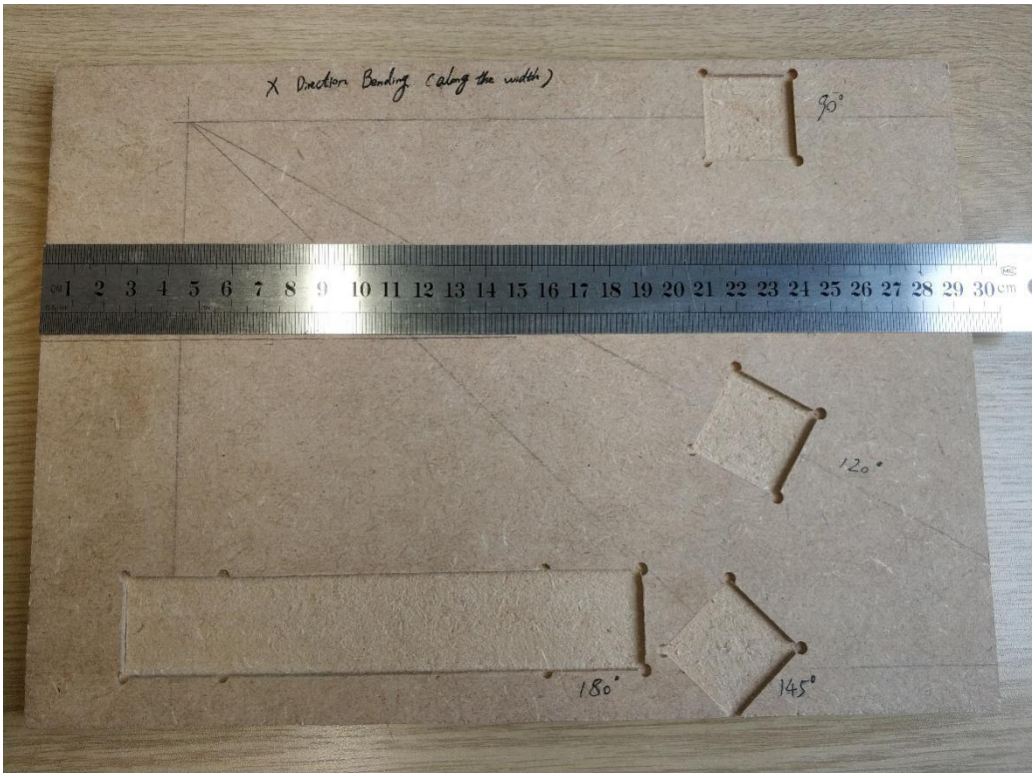

(a)

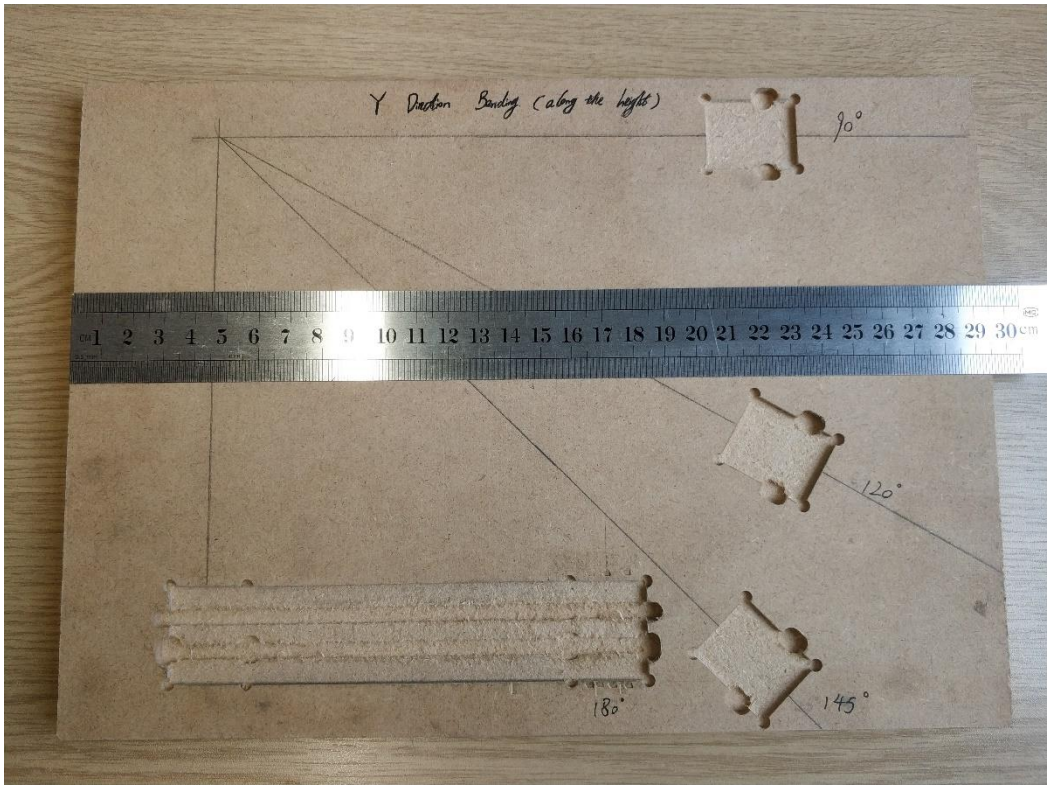

(b)

Fig.5.61 Two pieces of bending boards (a) H-plane bending (b) E-plane bending

5.61 H-plane bending

In this section, the effects that principle H-plane bending had on the knitted waveguide performance were studied based on simulation and measurement. Since CST 2012 cannot support elliptical cylinder bending, a rectangular waveguide (WR-90) constructed with the same materials as the elliptical knitted waveguide was simulated instead.

Simulation (H-plane bending):

The waveguide was simulated when it was straight and when it was bent to 90 degree and 180 degree along H-plane as shown in Fig.5.611 (a,b,c) respectively. The simulated S21 of the waveguide under different conditions are presented in Fig.5.612.

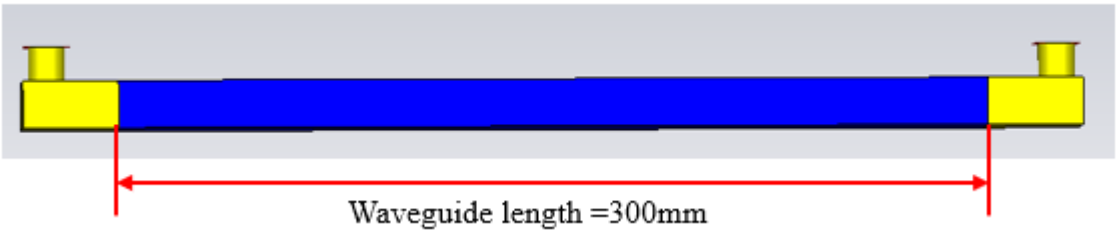

(a)

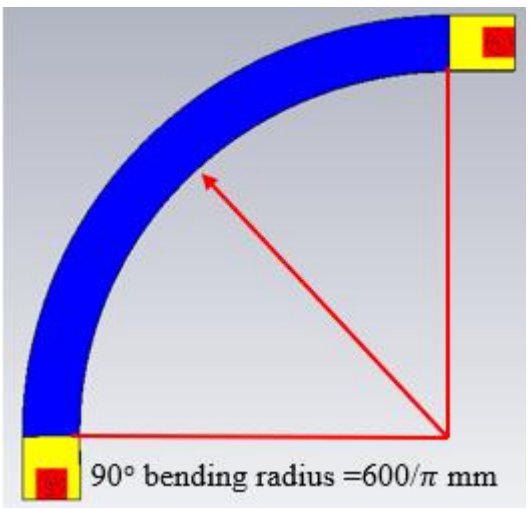

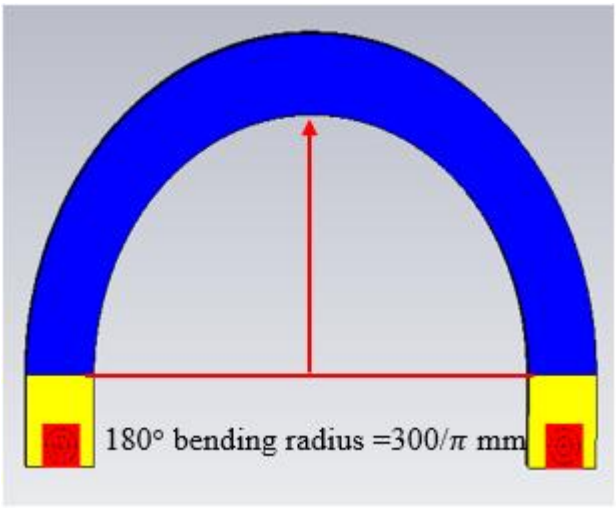

(b) (c)

Fig.5.611. Waveguide under different H-plane bending in simulation

(a): Straight, (b): Bending angle 90 degree, (c): Bending angle 180 degree

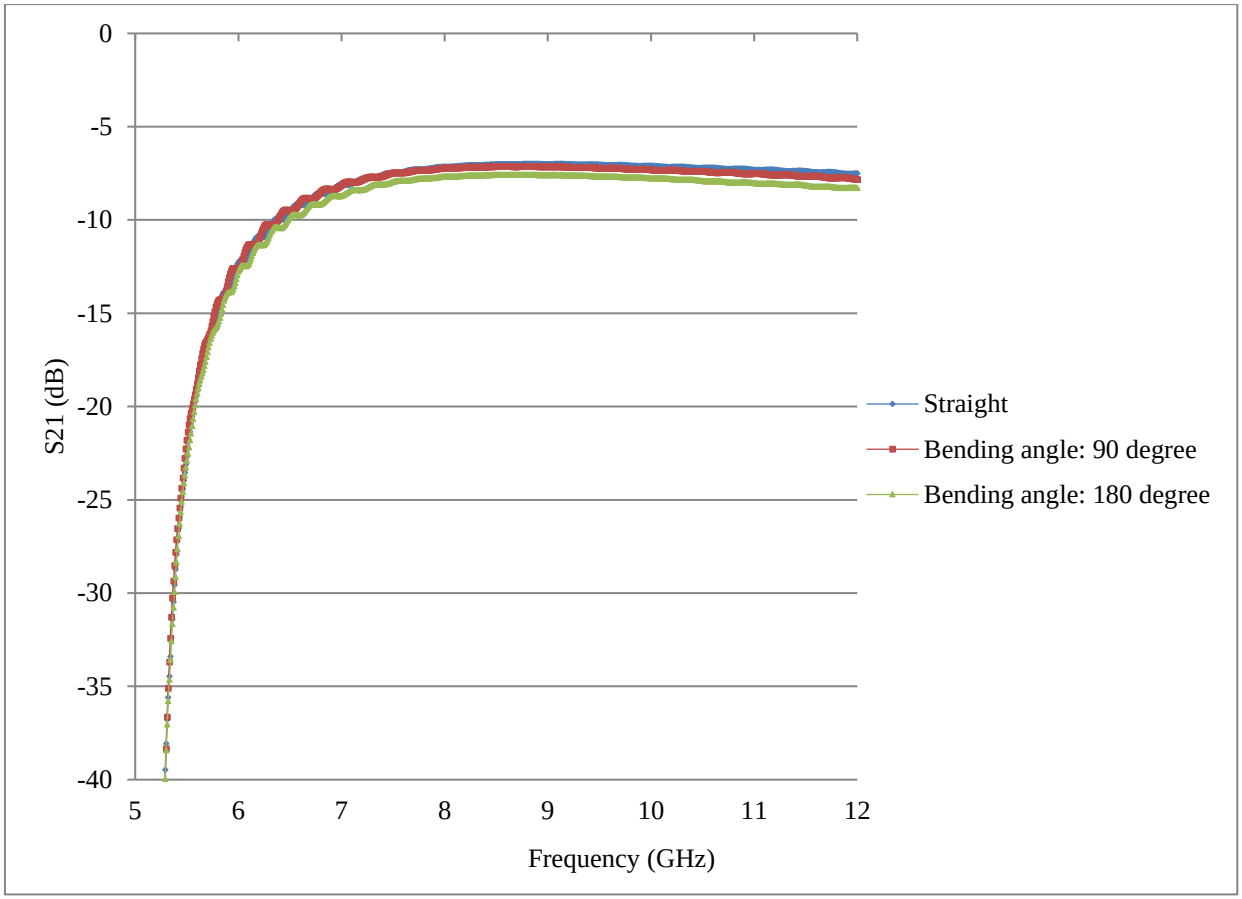

Fig.5.612. Comparison of simulated S21s of waveguide under different H-plane conditions

From the simulated results presented in Fig.5.612, it can be seen that the waveguide had almost the same cut-off frequencies under different H-plane conditions in simulation. Simulation agreed with the conclusion drawn from waveguide bends in section 4.24. In simulation, the waveguide bend was in LM (1,0) dominant mode, and the minimum H-plane bending radius was 300/πmm which was greater than the one wavelength 300/7mm at 7GHz. Therefore, the cut-off frequency was expected to remain the same under 90 and 180 degree H-plane bending in simulation. Moreover, with the bending angle increasing, the average S21 decreased slightly, about 0.4dB drop was noticed from a straight waveguide to a 180 degree H-plane waveguide bend.

Measurement (H-plane bending):

To exam the knitted waveguide's performance under H-plane bending in practice, it was measured by a VNA under different conditions as shown in Fig.5.613. To make the bending

condition more severe, two transitions were placed next to each other and a sharp corner occurred in H-plane as shown in Fig.5.613(c). The measured S21 of the knitted waveguide under different H-plane conditions are presented in Fig.5.614. Fig.5.614 shows that the knitted waveguide worked from 8GHz to 10GHz with a S21 gain around -7dB under different H-plane conditions. According the statements in section 4.24, the cut-off frequency was expected to remain the same when it was straight and under 90 degree or 180 degree H-plane bending as the bending radius was always larger than one wavelength, and become slightly smaller when a sharp corner occurred as the bending radius was less than one wavelength. Measured results showed that the knitted waveguide had almost the same cut-off frequency at 7.4GHz under different H-plane conditions. In measurement, the knitted waveguide's cut-off frequency was not sensitive to the H-plane bending, even the bending radius was smaller than one wavelength as long as the waveguide was in its dominant mode. The reason is because the waveguide was made by textile materials and it was flexible and robust to the H-plane bending. Fig.5.614 also shows that the S21 of the straight knitted waveguide remained almost the same within its working frequency under 90 degree and 180 degree bending. However, the average S21 of the knitted waveguide dropped about 1 dB when the sharp corner occurred. This is due to the fact that internal transmission loss increased when the bending radius became very small in H-plane.

(a)

(b)

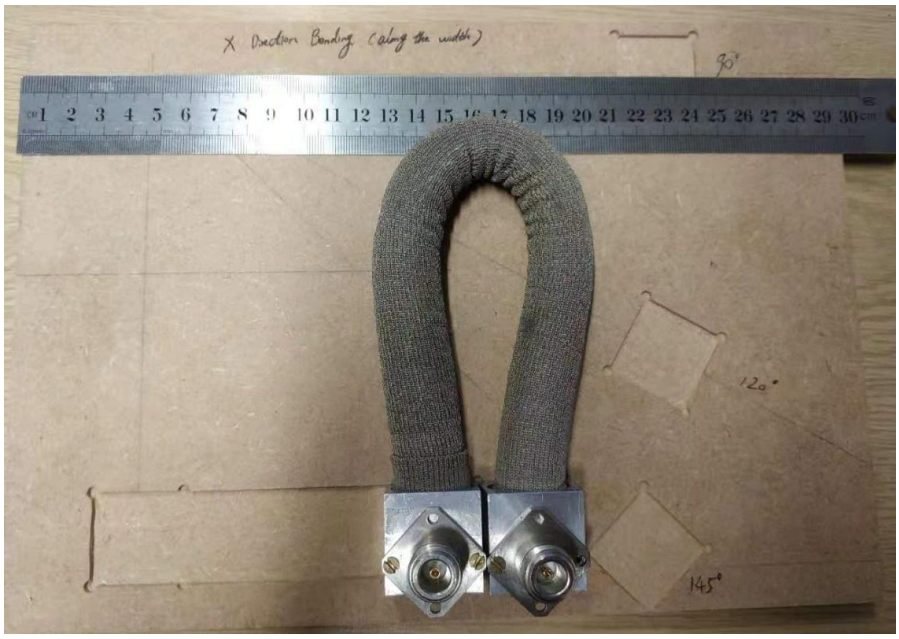

(c)

Fig.5.613 Knitted waveguide under principle H-plane bending.

(a): Bending angle: 90 degree, (b): Bending angle: 180 degree,

(c): Bending angle: 180 degree with a sharp corner

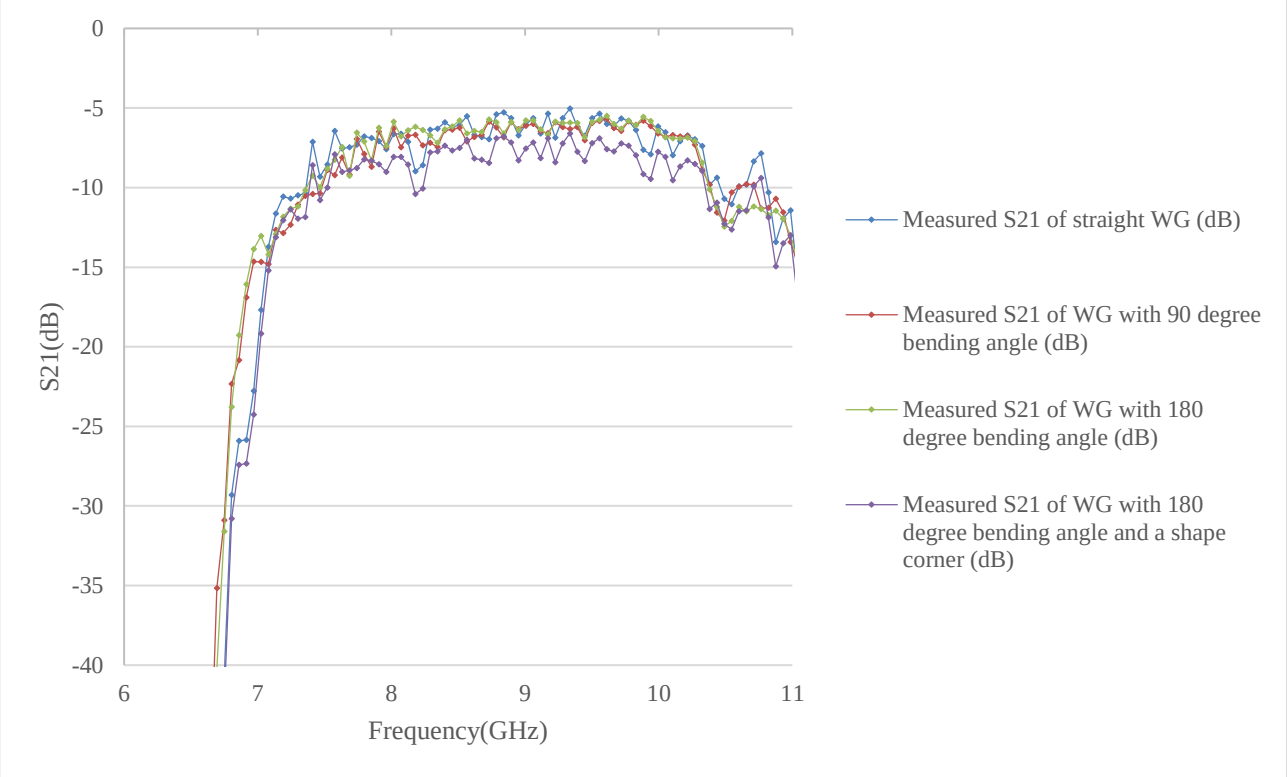

Fig.5.614. Comparison of measured S21 of knitted waveguide under different H-plane conditions

5.62 E-plane Bending

In this section, the effects that principle E-plane bending has on the knitted waveguide performance were studied based on simulation and measurement. The rectangular waveguide in section 5.61 was used again for simulation.

Simulation (E-plane bending):

Similarly, the waveguide was simulated when it was straight and when it was bent to 90 degree and 180 degree along E-plane as shown in Fig.5.621(a,b,c) respectively. The simulated S21 of the waveguide under different conditions are presented in Fig.5.622.

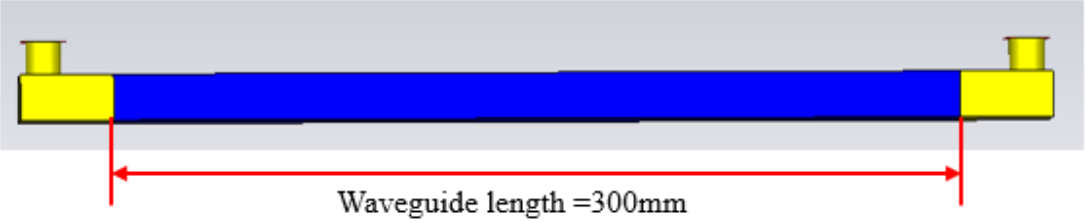

(a)

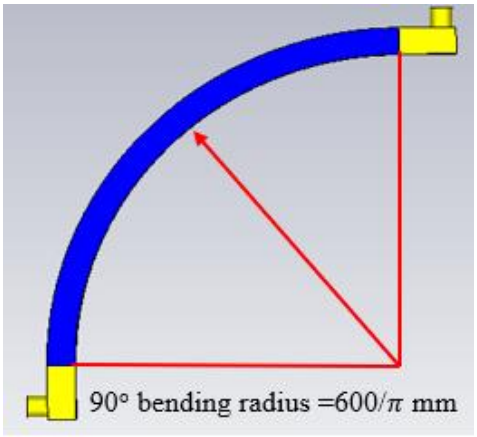

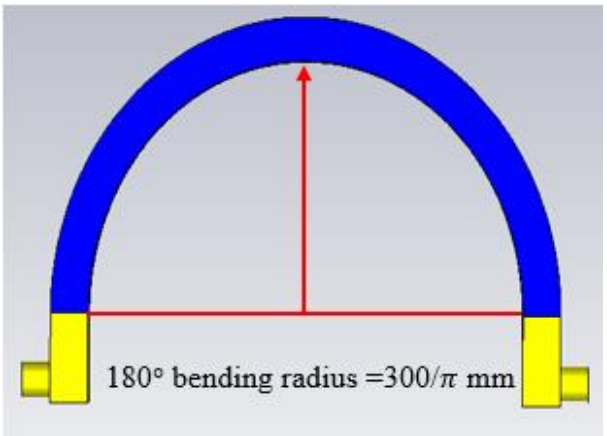

(b) (c)

Fig.5.621. Waveguide under different E-plane conditions in simulation

(a): Straight, (b): Bending angle 90 degree, (c): Bending angle 180 degree

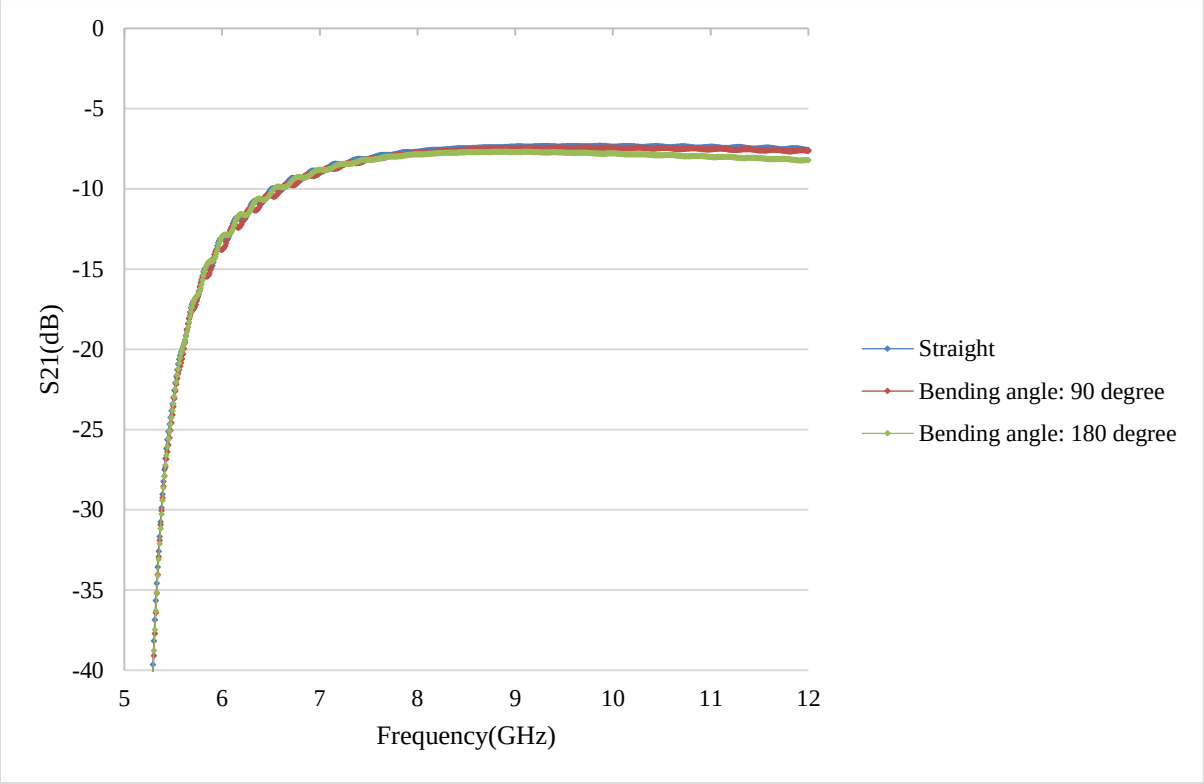

Fig.5.622. Comparison of simulated S21 of waveguide under different E-plane conditions

Fig.5.622 shows that in simulation, the knitted waveguide had a similar cut-off frequency when it was straight and when it was bent to 90 degree and 180 degree along E-plane. Simulation agreed with the conclusion drawn in section 4.24. For E-plane bending, when the waveguide was in LE (0,1) dominant mode, the cut-off frequencies always remained the same when the bending radius changed. Moreover, in simulation, with the bending angle increased, the average S21 decreased slightly, about 0.4 dB drop from a straight waveguide to a 180 degree E-plane waveguide bend.

Measurement (E-plane bending):

To exam the knitted waveguide performance under E-plane bending in practice, it was measured by a VNA under different conditions as shown in Fig.4.623. Similarly, to make the bending condition more severe, two transitions were placed next to each other and a sharp corner occurred in E-plane as shown in Fig.5.623(c). The measured S21 of the knitted waveguide under different E-plane conditions are presented in Fig.5.624. Fig.5.624 shows that the knitted waveguide worked from 8 GHz to 10 GHz with a S21 gain around -7 dB under different E-plane conditions. It also showed that the cut-off frequency of the knitted waveguide almost remained the same at 7.4 GHz when the bending angle increased even a

sharp corner occurred. The measured cut-off frequencies of the knitted waveguide under different E-plane conditions agreed with the simulation and conclusions drawn in section 4.24. Moreover, Fig.5.624 shows that the S21 of a straight knitted waveguide remained almost the same within its working frequency under 90 degree and 180 degree bending conditions. However, the average S21 of the knitted waveguide dropped about 1 dB when the bending condition became severe. This is due to the fact that stretching to the sleeve could result in a lower conductivity and compression to the knitted polyester resulted in a higher internal transmission loss particular when a sharp corner occurred.

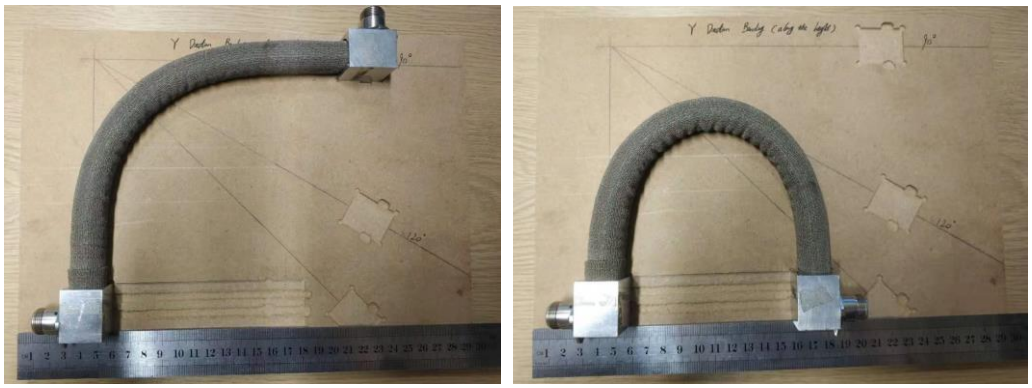

(a) (b)

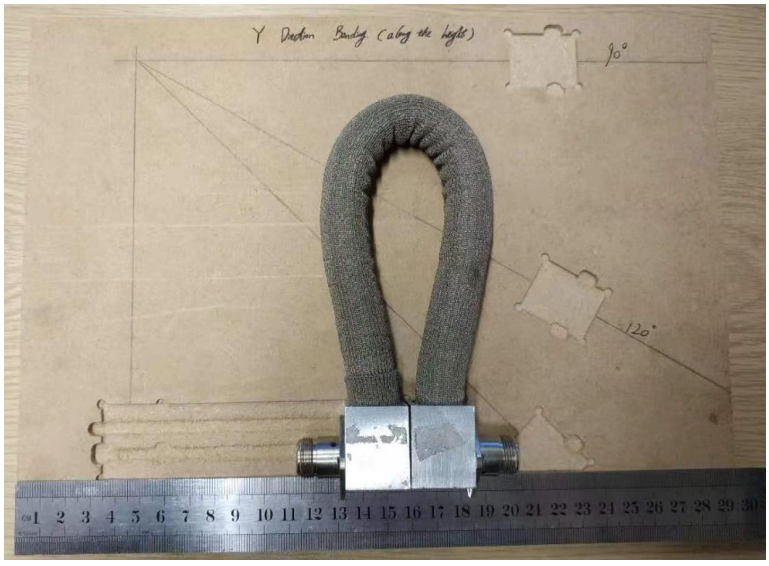

(c)

Fig.5.623. Knitted waveguide under principle E-plane bending.

(a): Bending angle: 90 degree, (b): Bending angle: 180 degree,

(c): Bending angle: 180 degree with a sharp corner

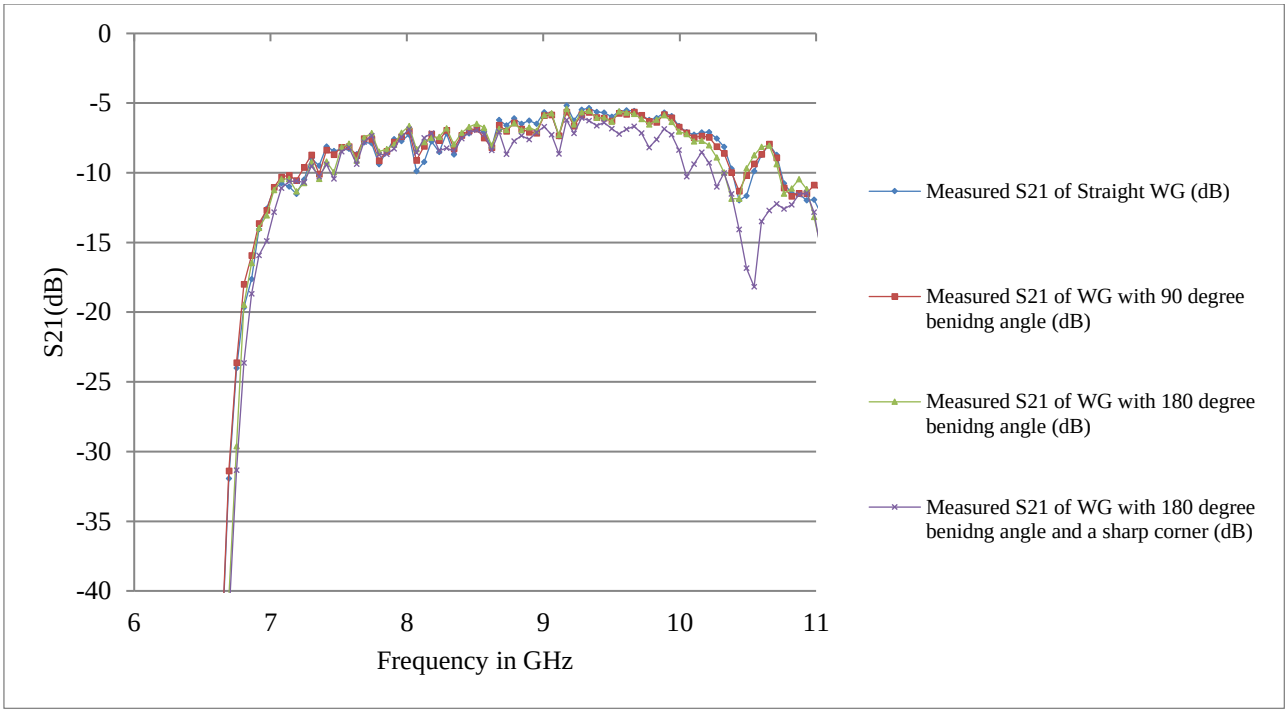

Fig.5.624. Comparison of measured S21 of knitted waveguide under different E-plane conditions

Generally, the knitted waveguide was robust to both H and E plane bending. Its cut-off frequency was not sensitive to bending as long as the waveguide bend was in its dominant mode. However, when the bending condition became severe and a sharp corner occurred in either E-plane or H-plane, it caused approximately 1 dB drop for the average transmission gain (S21) of a knitted waveguide within it working frequency.

5.7 Moisture effects on knitted waveguide's performance

In section 5.6, I demonstrated that a bent knitted waveguide can still provide a reliable transmission. Therefore, it is possible to not only integrate this knitted waveguide with garments, also can be applied to replace conventional solid waveguide bends in communications system. However, rain is an inevitable weather factor when dealing with the construction of the outfield communications system and textile materials are easy to get wet. Thus, it is necessary to study the impact of moisture on the performance of a knitted textile waveguide.

5.71 Measurement setup

The same knitted textile waveguide was employed in this section. Its reflection coefficient (S11) and forward transmission (S21) were measured by a VNA at room temperature (approximately 20℃). To investigate the moisture effects, a dry sample was measured at first as shown in Fig.5.31. Then, 20ml of Evian spring water was poured on the sample as shown in Fig.5.711 and the wet sample was measured hourly until it was completely dry again.

Fig.5.711 Pour 20ml water on the sample then measure

5.72 Results and discussion

The measured S-parameter of a dry knitted textile waveguide is shown in Fig.5.721.

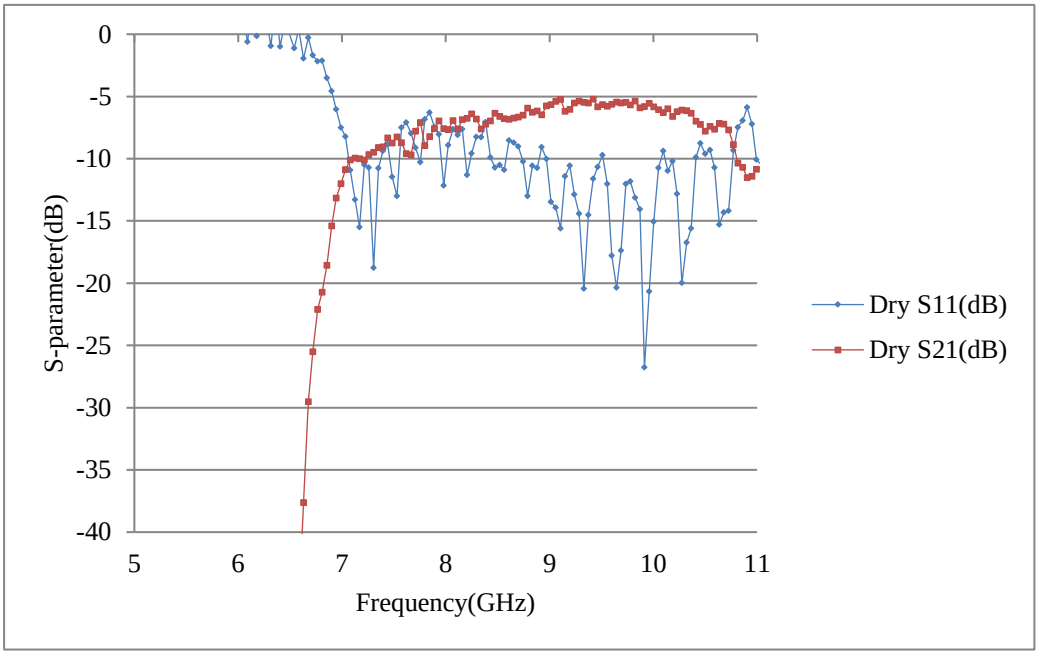

Fig.5.721 Measured S-parameter of a dry sample

Fig.5.721 shows that the knitted waveguide had a distinct cut-off frequency at about 7GHz and approximately -6dB transmission gain within its working frequency band. Then, 20ml water was poured on the knitted waveguide and its S-parameter was measured after the water was totally absorbed by the knitted sample. Fig.5.722 shows the measured S-parameters of the wet sample. From Fig.5.722, it can be seen that there was no significant transmission (S21) and input signal was almost reflected when the sample was completely wet. The knitted waveguide stopped working when it absorbed 20ml of water. It may be due to the fact that water has a high dielectric constant around 73 from 7GHz to 12GHz at 20℃ [115] and it totally reflected the signal when the inner knitted polyester was completely wet. After that, the wet sample was drying at room temperature, and measurement was taken at every hour. It turned out that the knitted waveguide did not have a significant transmission performance until after 24 hours.

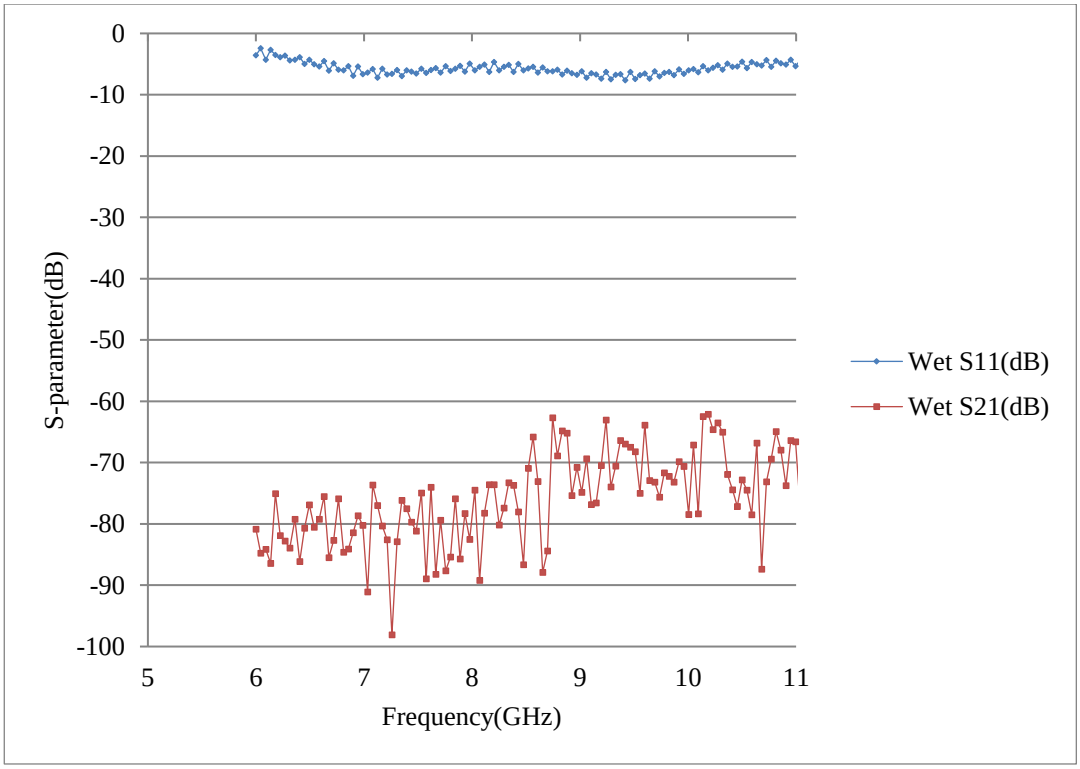

Fig.5.722 Measured S-parameter of a wet sample

Fig.5.723 shows the measured S21 of the wet sample at every time intervals after drying 24 hours. From Fig.5.723, it can be seen that the S21 reached -20 dB and the knitted waveguide started to have reasonable transmission characteristics after 24 hours. Moreover, the half-wet sample had the same cut-off frequency as the dry sample while the average transmission gain was much lower than the dry sample. This is because water in the knitted waveguide was evaporating and after 24 hours, the remained water in the sample was not enough to totally reflect the signal and it only attenuated the transmission. Fig.5.723 also shows that the transmission gain (S21) of the knitted waveguide increased as time passed. This is due to the fact that with less water in the sample, the internal loss of the knitted waveguide was lower, which resulted in a higher S21. Fig.5.723 shows that after 51 hours, the S21 of the knitted waveguide almost returned to its original value. It proved that water did not damage the sample and the knitted waveguide was able to provide almost the same performance after completely drying. The slight difference between the S21 after 51 hours drying and its original value was mainly caused by the measurement variation as the knitted waveguide was disconnected from the VNA for drying after every measurement and the VNA had to be set up every time for a new test. Moreover, dimensional changes to the textile sample during the water evaporating process also contributed errors. For example, knitted textile will have some unexpected crumples on the surface when it gets wet and dries again.

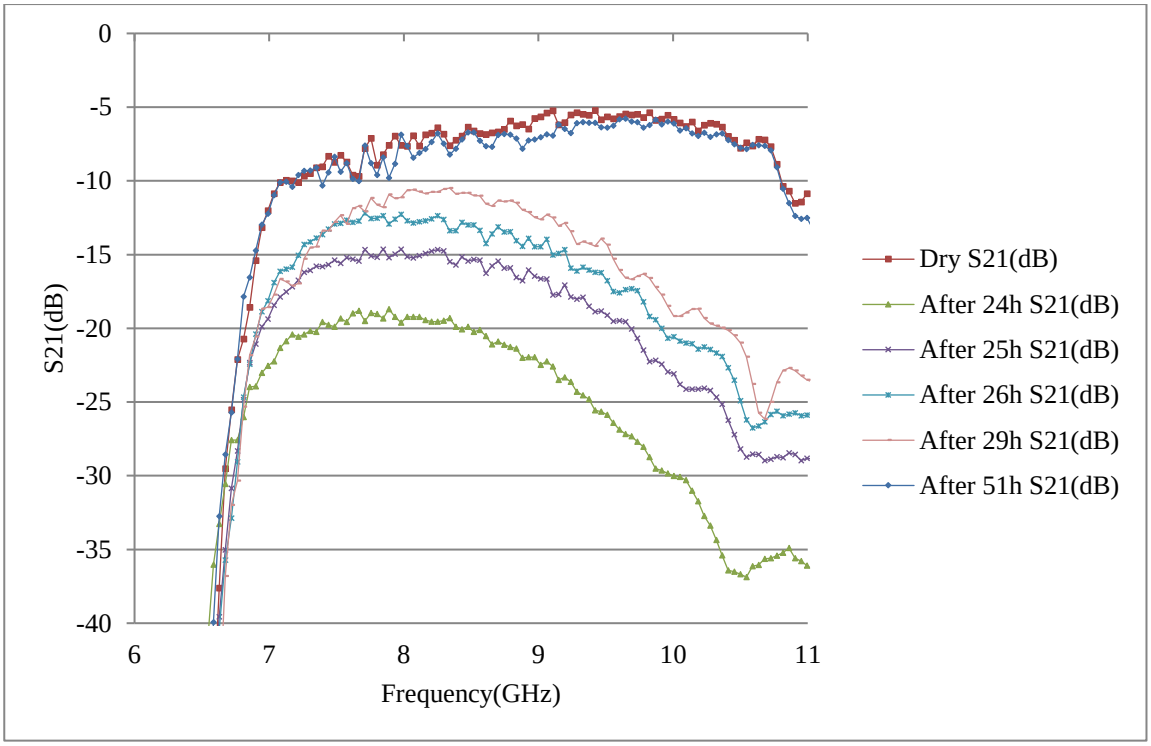

Fig.5.723 Comparison of measured S21 of a dry sample and drying sample at different time

In conclusion, water had significant effects on the performance of the knitted waveguide. The results showed that when the sample was completely wet, the knitted waveguide stopped working. The knitted waveguide started to work with a low transmission gain after drying 24 hours at room temperature and returned to its original performance when it was completely dry. Therefore, the knitted textile waveguide needs to be water-proofed thoroughly in practise.

5.8 Conclusion

In this chapter, a knitted textile waveguide working at X band was presented. To my best knowledge, this is the first 3D textile waveguide proposed to the public. It had a typical waveguide transmission performance within its working frequency. Properties of the textile materials employed in the project were also determined. The knitted polyester was tested to have a relative permittivity (ε_r) around1.3 and a dielectric loss constant ($\tan\delta$) about 0.001. The conductive textile sleeve was verified to have a conductivity of approximately 4000 S/m. Both textile materials provided an alternative to the traditional material in waveguide design and were tested suitable for transmission application.

The performance of a knitted waveguide under bending was demonstrated. During the shape distortion study, both H-plane and E-plane were involved, and measurement generally agreed with simulation. It can be concluded that the knitted waveguide could provide a stable performance under H and E plane bending. The waveguide's cut-off frequency almost remained the same as the bending angle increased. However, when a severe shape distortion happened and a sharp corner occurred in either E-plane or H-plane, the waveguide's transmission gain decreased slightly, about 1dB drop for S21 within working frequency. Therefore, a sharp corner needs to be avoided during the application of knitted waveguide.

The moisture effect on knitted waveguide's performance was also studied as the textile materials are easy to get wet in practice. The results showed that water decreased the waveguide's transmission gain significantly, even stopped the waveguide from working. Thus, the knitted waveguide must be water-proofed completely when it is applied in practice.

The properties of all the textile materials employed in the project were determined. With the above results, the equivalent models of knitted samples manufactured with the same materials can be built directly in CST. It was also an early approach to waveguide transition design, knitted sample fabrication and measurement. Moreover, the study on knitted waveguide's performance under shape distortions showed that the knitted waveguide was able to function well after bending. Therefore, the knitted waveguide not only is an alternative to the conventional bent metallic waveguide but provides the possibility to develop the knitted slotted waveguide array for wearable applications.

Chapter 6. A Knitted Slotted Waveguide Antenna

6.1 Introduction

Waveguide is a structure commonly used to guide signal between its endpoints in a system. With the physical constraint of a waveguide, a signal can travel to a long distance with the minimum loss. In 1893, J. J. Thomson proposed a very early waveguide structure to the public [116]. Due to the rapid development of radar in World War II, waveguide gained special attention in the communications industry due to its high-power rating. Electromagnetic wave propagating in a metallic waveguide was then analyzed mathematically by Lord Rayleigh in 1897 [117]. In 1943, John Kemp detailed the propagation properties of waves within rectangular and circular waveguides [92]. In his publications, he also stated that the metallic waveguide was able to radiate electromagnetic wave into space through slots on the tube wall. According to his statement, it is possible to convert a waveguide from a transmission device into an antenna, and this kind of antenna is known as slotted waveguide antenna (SWA). The first slotted waveguide antenna was introduced by Watson in 1943 [118]. And in 1961, A. Hu presented a slotted rectangular waveguide antenna with four slots on its broadside [119]. Their results indicated that the four-slot linear array on a rectangular waveguide was able to provide a directional radiation characteristic with a directivity of 12dBi. Later in 1963, J. Ramsay published the details of mathematical analyses of different slotted arrays based on rectangular waveguide [120]. After decades of development, a slotted waveguide antenna is now able to provide either a dual polarized radiation characteristic or a dual-band working frequency [121-122].

In chapter 5, I presented a knitted textile waveguide and investigated its performance under shape distortions [109-110]. In [110], the results proved that the knitted textile waveguide still functioned well when it was bent. Therefore, I developed a textile slotted waveguide antenna based on the knitted waveguide in this chapter. Chapter 6 began with the introduction of a knitted textile SWA [123]. Its performance was studied in simulation and

measurement, and the structural improvements were also discussed. Then, the knitted SWA were tested under shape distortions. Four different bending conditions were set up and discussed respectively. Finally, conclusions were drawn according to the comparison of simulated and measured results.

6.2 Antenna Structure and Its Performance

This section detailed the design and evaluation of knitted slotted waveguide antennas (SWA) with four slots. The reflection coefficient (S11) of antenna was measured by an Agilent E5071C network analyzer and the antenna's radiation characteristic was measured in an anechoic chamber in the University of Sheffield.

6.21 A knitted SWA with four slots

Antenna Structure (SWA with four stretched slots):

Fig.6.211 presents the simulated model of a slotted waveguide antenna in CST. The SWA was designed to work at 9.15GHz. It had one end short circuited and four thin rectangular slots were arranged in a 2 by 2 array on it. The simulated SWA in Fig.6.211 was constructed using the same textile materials that I studied in the last chapter, the dark blue part was conducting textile and the light red part was knitted polyester. The properties of the textile materials are shown in Table.6.211. Using the analysis from section 4.3, the SWA was designed to have dimensions as shown in Table.5.212.

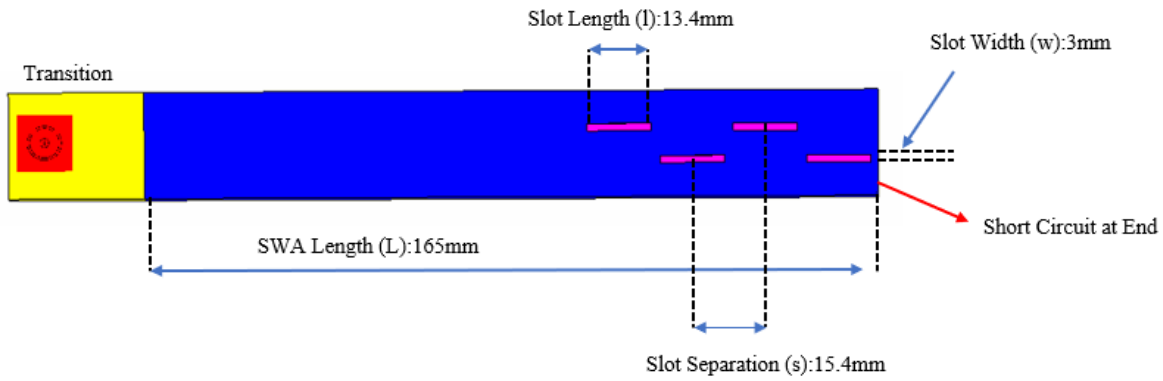

Fig.6.211 Simulated knitted SWA with four slots

Table.6.211 Properties of textile materials

ε_r of knitted polyester	tanδ of knitted polyester	σ of textile sleeve
1.5	0.001 at 10GHz	4000 S/m

Table.6.212 Dimensions of a slotted waveguide antenna

Major Axis	Minor Axis	Slot length (l)	Slot width (w)	Slot Separation (s)	Distance between the last slot and end	Slot offset from SWA centreline
29mm	21mm	13.4mm	3mm	15.4mm	8.7mm	3.6mm

The first prototype of knitted SWA is shown in Fig.6.212. The conducting textile sleeve was manufactured using the same conducting yarn and knitting density (20 stitches/inch and 25 rows/inch) as the textile waveguide in chapter 5. With the method described in chapter 5, the relative permittivity ε_r of the knitted polyester used for knitted SWA was verified to be 1.5 and the conductivity of textile sleeve was assumed to remain 4000 S/m as shown in Table 6.211. The slots were formed during the knitting process and expected to have the same size as the simulated models. However, from Fig.6.212, it can be seen that all the slots were stretched when the knitted polyester was inserted into the sleeve. These stretched slots were referred to as stretched slots and this sample was called stretched sample in the following.

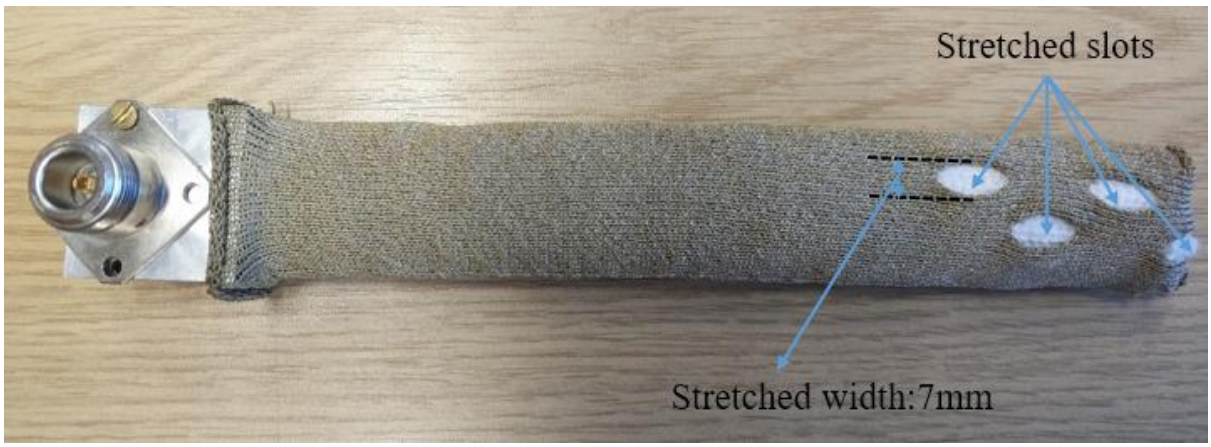

Fig.6.212 Photograph of a knitted SWA with four unstitched slots.

Results and Discussions (SWA with four stretched slots):

The measured reflection coefficient (S11) of the knitted SWA with four stretched slots was compared with the S11 of the simulated model and the result is shown in Fig.6.213. Fig.6.213 shows that the measured S11 of the knitted SWA with four stretched slots generally agreed with the simulated results. The SWA presented a dual band behaviour, with measured resonant frequencies at 8.63GHz and 9.15GHz compared with the simulated ones of 8.61GHz and 9.16GHz. At 9.15 GHz, the antenna had a bandwidth of 80MHz. The slight shift between the measured resonant frequencie and simulated one was due to the flexible nature of textiles materials as the SWA cannot be knitted exactly the same as the simulated model.

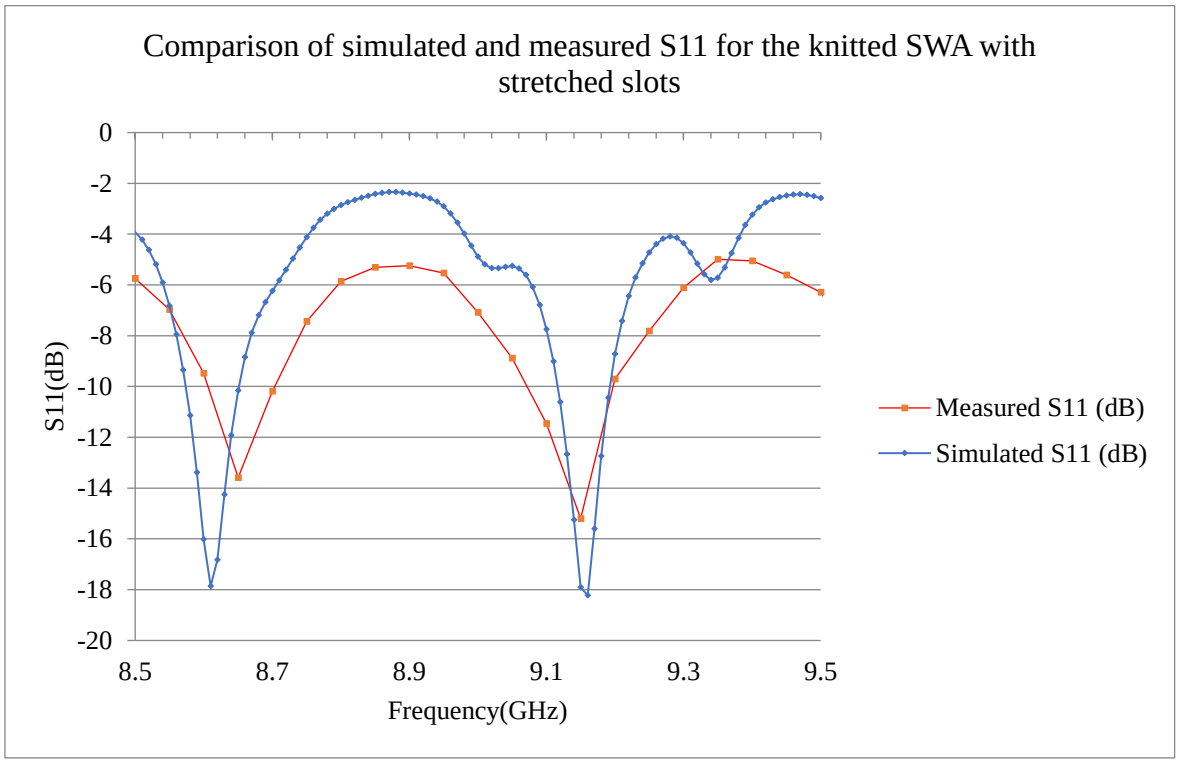

Fig.6.213 Simulated and measured return loss of knitted SWA with four stretched slots

The radiation pattern of the knitted SWA with four stretched slots was measured at 9.15GHz and compared with simulated results. Fig.6.214 presents the comparison of normalized H-plane radiation patterns between the simulation and measurement at same frequency respectively. From Fig.6.214, it can be seen that the SWA had a directional radiation characteristic. The antenna had a 3dB beam width of approximate 34 degree in H-plane compared with its simulated value 27 degree as shown in Fig.6.214. 7 degree difference between the measured and simulated 3dB beam width was mainly caused by the deformation

of the slots on the knitted sample as they were stretched. Fig.6.214 shows that the measured radiation pattern generally matched to the simulated results.

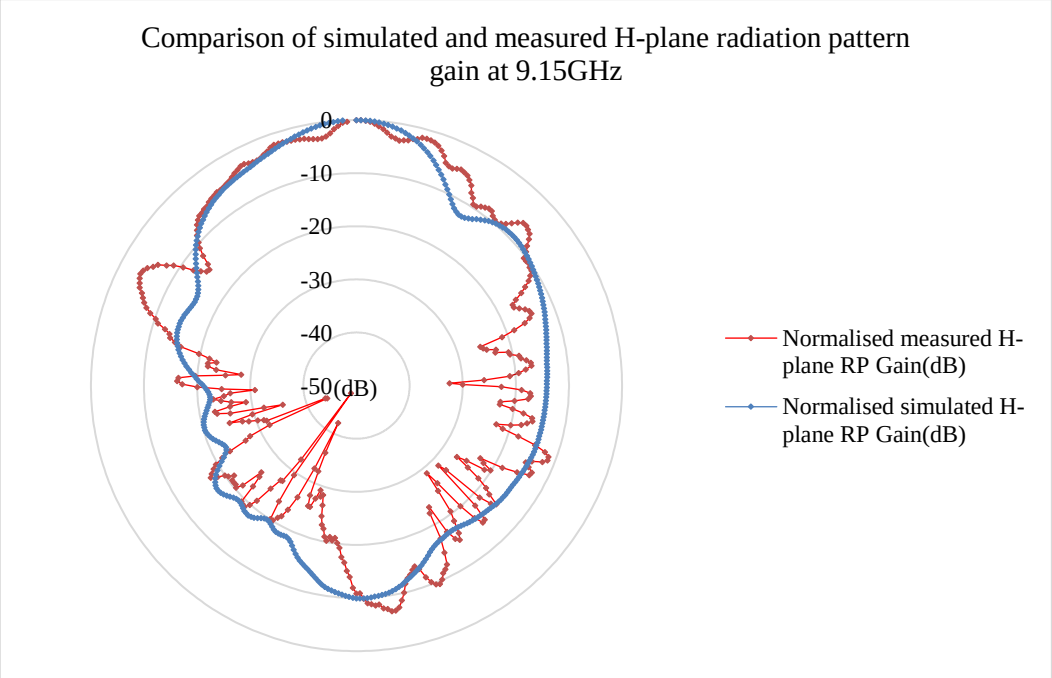

Fig.6.214 Comparison of simulated and measured H-plane radiation pattern (RP) of knitted SWA with four stretched slots

*6.22 A knitted SWA with four stitched slots (2*2 array)*

Antenna Structure (SWA with four stitched slots):

From section 6.21, it can be seen that the slots on the knitted sample were stretched. They became more elliptical rather than rectangular with a maximum slot width of 7mm. In order to keep slots at the desired shape and dimensions, all the slots were stitched by a non-conducting cotton yarn as shown in Fig.6.221. The widths of different slots are compared in Table.6.221. From Fig.6.221 and Table.6.221, it can be seen that the slots were almost at the desired shape and dimensions after stitching. The slotted sample shown in Fig.6.221 had the same geometry with the first prototype shown in Fig.6.212. Tape was used to provide a firm connection between the transition and knitted SWA as shown in Fig.6.212. The slots with stitches were termed as stitched slots and this sample was named as stitched sample in the subsequent discussions.

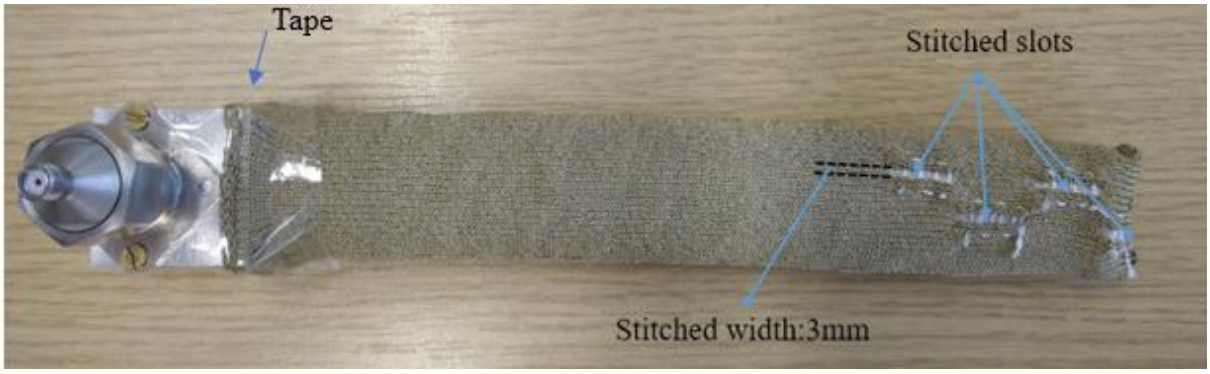

Fig.6.221 Photograph of a knitted SWA with four stitched slots.

Table.6.221 Comparison of different slot widths

Simulated slot width	Stretched slot width	Stitched slot width
3mm	7mm	Approximate 3mm

Results and Discussions (SWA with four stitched slots):

The measured reflection coefficient (S11) of the knitted SWA with four stitched slots was compared with the S11s of the simulated model and the stretched sample in Fig.6.222. Fig.6.222 shows that after stitching, the SWA still retained a dual band behaviour with the

measured resonant frequencies at 8.69GHz and 9.185GHz. Compared with the simulated model and the stretch sample, the resonant frequencies of the stitched sample shifted upwards slightly, around 30MHz. At 9.185GHz, the SWA with stitches achieved a better impedance matching condition (S11 below -30dB) with a bandwidth of 170MHz. Although the stitched slots resulted in slightly higher resonant frequencies, the SWA's bandwidth was doubled and input impedance matched better than the sample without stitches. For the knitted SWA with four stitched slots, the shift between the measured and simulated resonant frequencies was mainly caused by the fact that previously the slots were stretched, and the length of slots became shorter after being stitched.

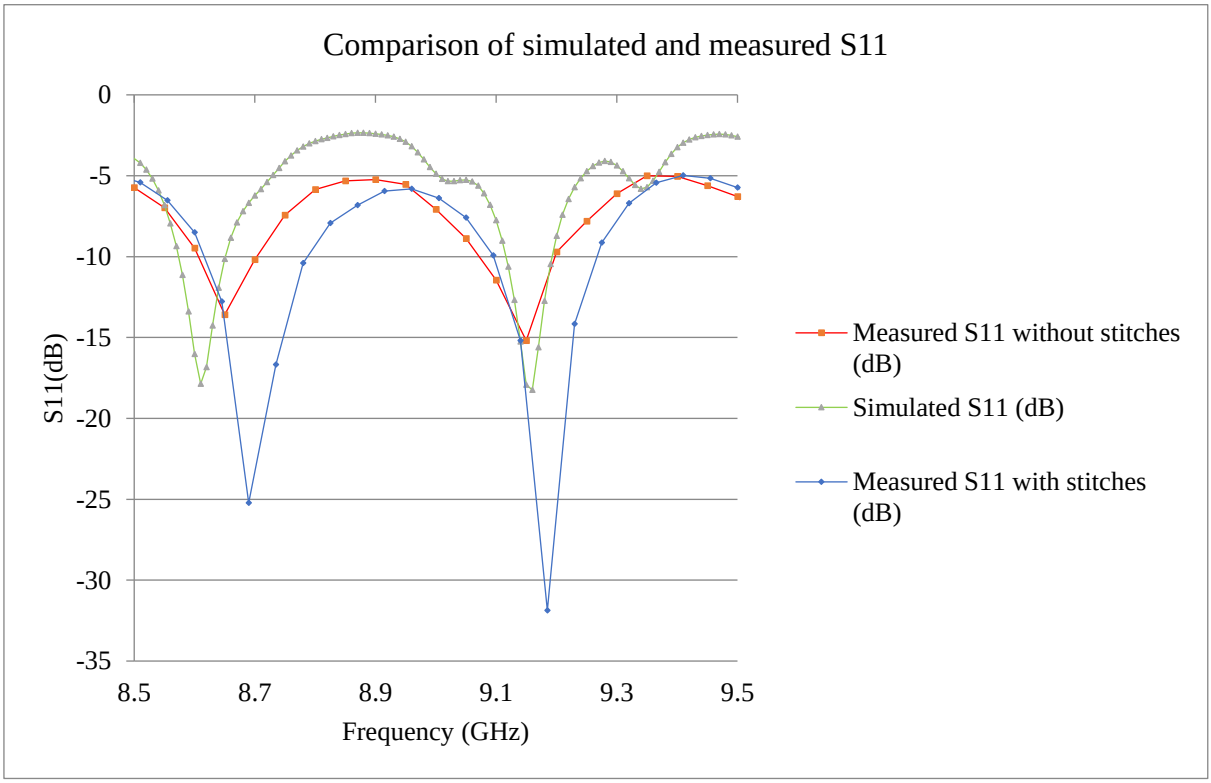

Fig.6.222 Simulated and measured S11of knitted SWA with four stitched slots

The radiation pattern of the knitted SWA with four stitched slots was measured at 9.18GHz. Fig.6.223 presents the comparison of the H-plane measured radiation patterns between the samples with four stretched and stitched slots at 9.18GHz. From Fig.6.223, it can be seen that the stitched sample had a similar measured radiation pattern to the stretched sample, but more directional. Fig.6.223 shows that for the measured H-plane radiation pattern, the stitched SWA had a 3dB beam width of about 26 degree compared with 34 degree beam width of the stretched SWA, which was closer to the simulated value 27 degree. According to the measurement, the stitched sample had a maximum gain of 2.33dB at 9.18GHz with a

front to back ratio more than 10 dB. To conclude, the stitched slots only increased the antenna's bandwidth and improved the input impedance matching condition, also made the antenna more directional.

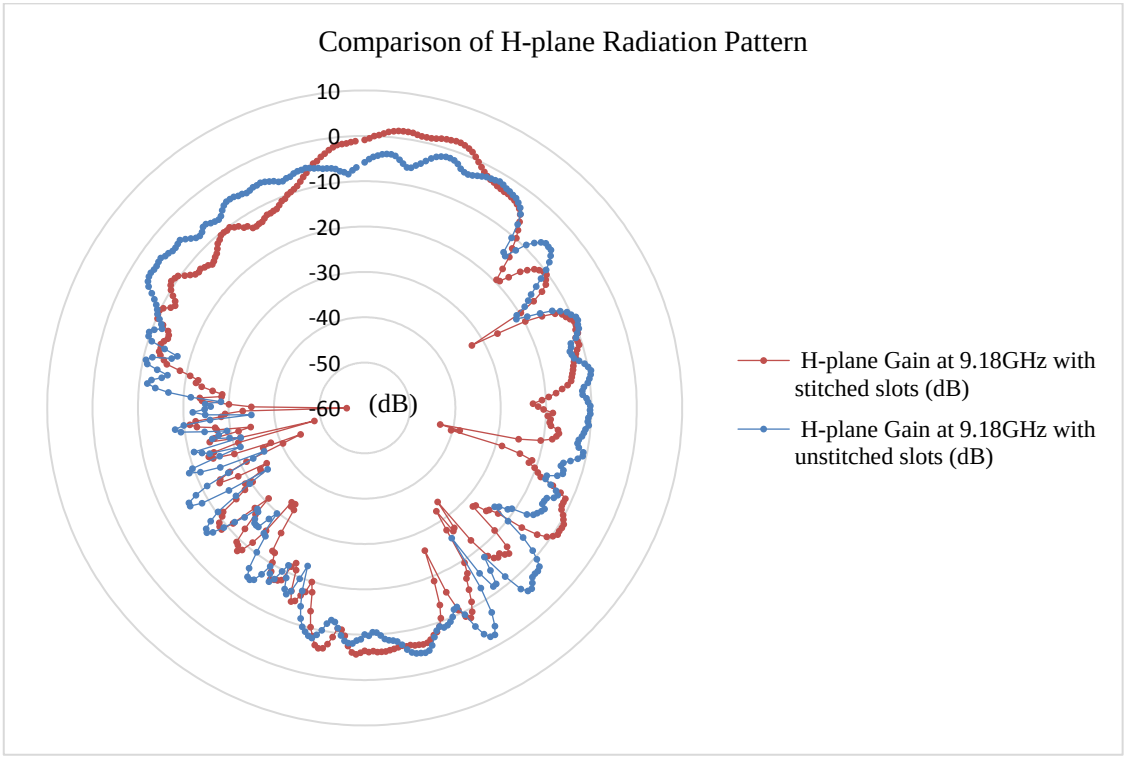

Fig.6.223 Comparison of measured H-plane radiation pattern (RP) between knitted SWA with four stitched and stretched slots

*6.23 A knitted SWA with six slots (2*3 array)*

In section 6.22, it was established that stitching the slot can improve the knitted SWA's performance. However, the maximum measured gain of the stitched sample with four slots only reached 2.33dB, which was still relatively low. According to basic array factor theory [124], the gain of a slotted waveguide antenna can be increased further by adding more slots on the SWA. In this section, a SWA with 6 slots was simulated to exam its radiation performance against a SWA with 4 slots.

Antenna Structure in Simulation (SWA with six stitched slots):

Fig.6.231 presents a simulated model of a knitted SWA with six slots arranged in a 2 by 3 array. It was constructed with the same textile materials and geometry as the four-slot SWA shown in Fig.6.211.

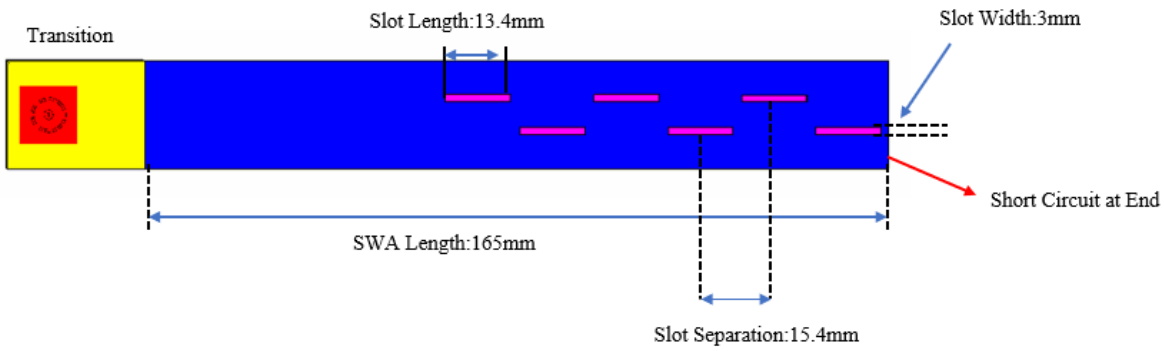

Fig.6.231 Diagram of the simulated knitted SWA with six slots

Results and Discussions of simulation (SWA with six stitched slots):

The comparison of the simulated reflection coefficient (S11) between the knitted SWA with 4 slots and 6 slots is shown in Fig.6.232. From Fig.6.232, it can be seen that in simulation, with two more slots, the knitted SWA still presented a dual band behaviour. However, its resonant frequencies shifted downwards compared with the knitted SWA with four stitched slots, from 8.61GHz to 8.58GHz and from 9.16GHz to 9.08GHz. For the SWA, two additional slots resulted in a longer effective electrical length of the slots. Consequently, the SWA's resonant frequency shifted 80MHz downwards from its previous value (9.16GHz).

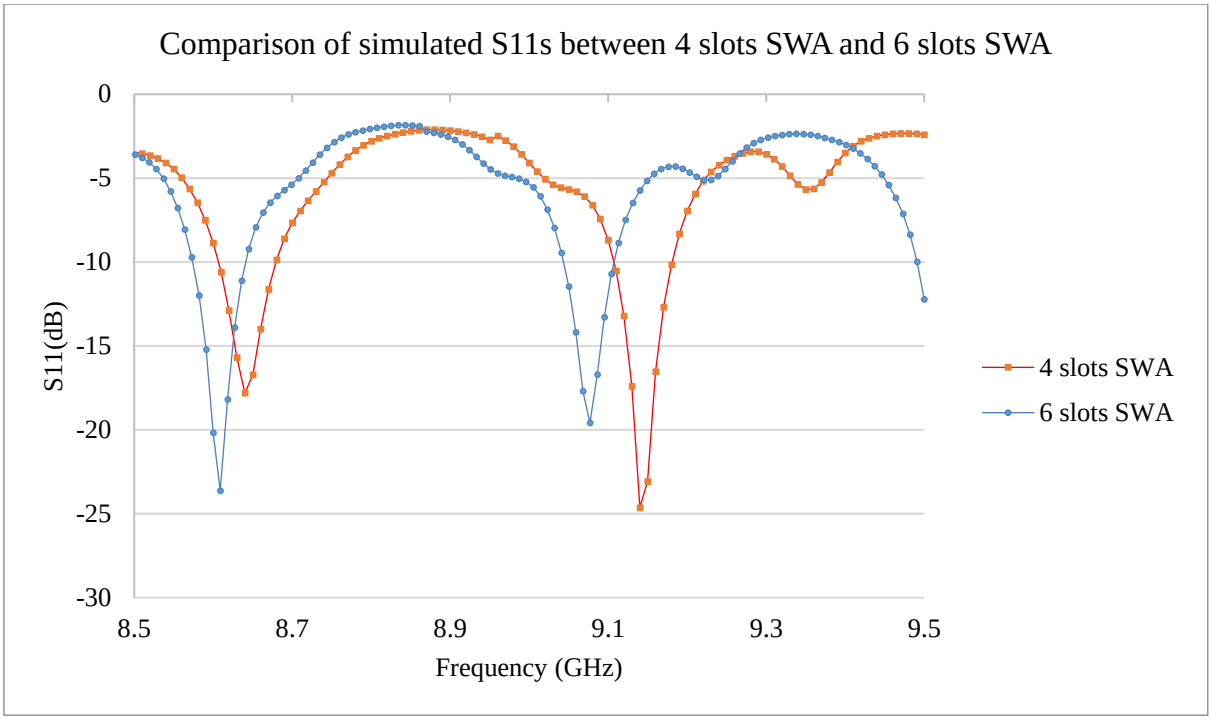

Fig.6.232 Comparison of simulated S11s between knitted SWA with 4 and 6 slots

The comparison of simulated radiation pattern between the knitted SWA with 4 slots and 6 slots at 9.15GHz is shown in Fig.6.233. From Fig.6.233, it can be seen clearly that in simulation, the knitted SWA with 6 slots had a maximum gain of 3.74dB, which was about 1.7dB higher than that of knitted SWA with 4 slots (2.03dB). Moreover, the 6 slots SWA had a 3dB beam width of 17 degree which was 7 degree less than that of 4 slots SWA (24 degree). For this 2 by 3 array, all the radiating elements were uniformly placed ($\lambda_g/2$ in this case). Therefore, increasing the number of radiating elements made the array more directional [124]. The radiation characteristics of SWA with 4 slots and 6 slots in simulation were compared and presented in Table.6.231. From Table.6.231 it can be seen that, in simulation, the knitted SWA with 6 slots had a higher maximum directivity and radiation efficiency than the knitted SWA with 4 slots, which consequently resulted in a higher maximum gain.

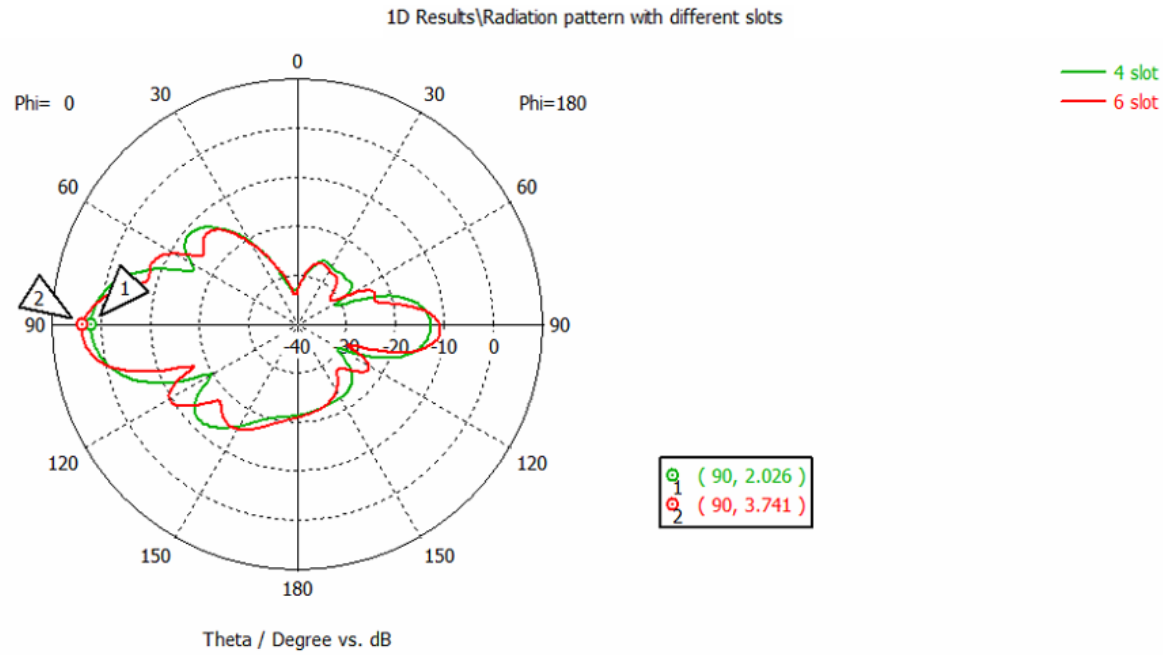

Fig.6.233 Comparison of simulated H-plane radiation pattern (RP) between knitted SWA with 4 and 6 slots

Table.6.231 Comparison of simulated radiation characteristics between knitted SWA with 4 and 6 slots

	Maximum Directivity (dBi)	Radiation Efficiency (dB)	Maximum Gain (dB)
4 slots SWA	11.68	-9.65	2.03
6 slot SWA	12.92	-9.18	3.74

6.3 Antenna Performance under Bending Conditions

Like the knitted waveguide, the knitted SWA is also a long, soft and flexible structure. Therefore, bending is still the major type of shape distortions occurs to it in practise. In this section, the performance of the knitted SWA with four stitched slots presented in section 6.2 was studied under shape distortion. Four different bending conditions were set, including both E-plane and H-plane bending. For both planes, the SWA was simulated and measured when it was bent to 90 degree and 180 degree. Bending effects on the SWA's performance was studied based on simulation and measurement respectively. Moreover, since the resonant frequencies of the SWA shifted after bending, the radiation patterns of a straight SWA and a bent SWA were compared at the resonant frequency of the straight SWA. For simulation, as CST MW studio cannot support elliptical cylinder bending, a SWA based on a rectangular waveguide (WR-90) with a length of 165mm was constructed and simulated instead of the knitted sample. For measurement, A piece of ROHACELL 51 foam which had a permittivity close to air (ε_r =1.071 at 10GHz) was employed as the base for the bending measurement as shown in Fig.6.314.

6.31 E-plane 90 degree bending

Fig.6.311 (a) presents a SWA based on WR-90 waveguide under E-plane 90 degree bending in simulation and Fig.6.311 (b) presents the knitted sample under E-plane 90 degree bending in measurement.

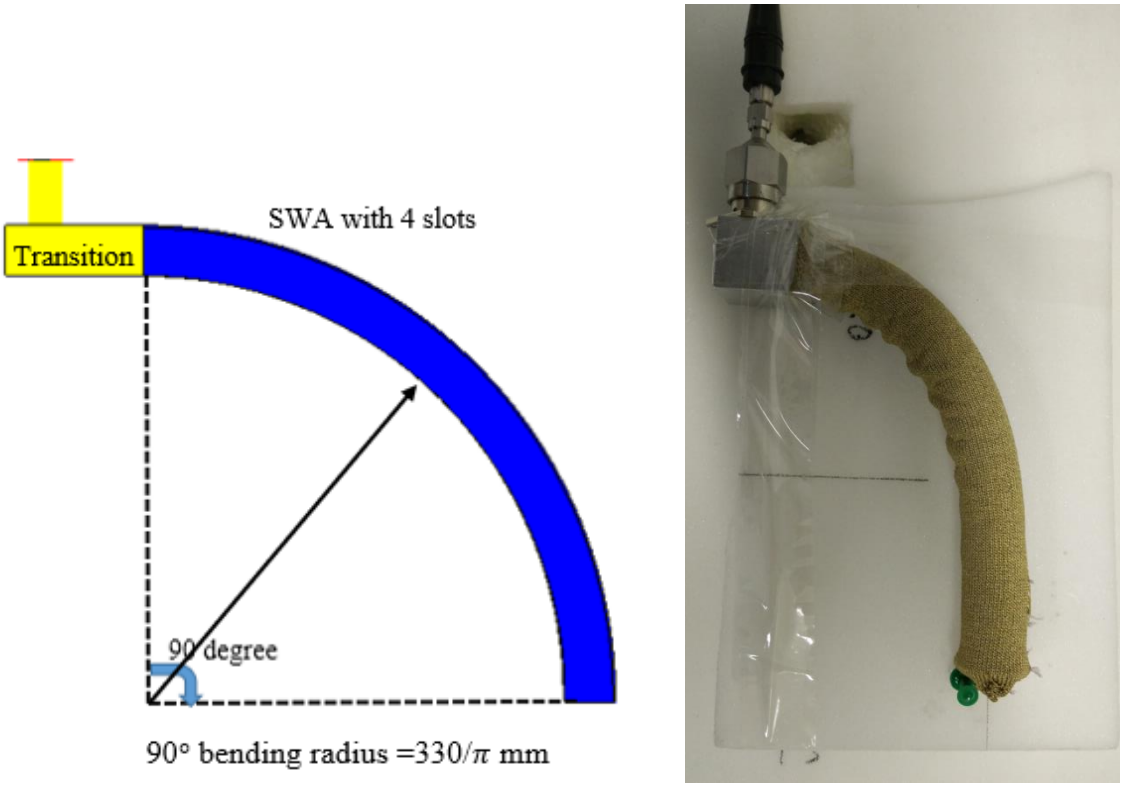

(a) (b)

Fig.6.311 A SWA with four slots under E-plane 90 degree bending

(a): A SWA based on WR-90 waveguide in simulation; (b): A knitted sample in measurement

Simulation (E-plane 90 degree bending):

The simulated reflection coefficients of a straight SWA and the SWA under E-plane 90 degree bending are shown in Fig.6.312. From Fig.6.312, it can be seen that the E-plane 90 degree bending had significant impacts on SWA's resonant frequencies. The straight SWA had resonant frequencies at 8.93GHz and 9.43GHz. After it was bent to 90 degree in E-plane, the resonant frequencies shifted downwards, from 8.93GHz to 8.33GHz and from 9.43GHz to 9.185GHz in simulation. The SWA demonstrated a robust input impedance matching ability, as its S11 remained below -20dB at the resonant frequencies after E-plane 90 degree bending. The shift of resonant frequency was caused by the shape distortion of SWA, as the slots were stretched and became longer due to the E-plane 90 degree bending in simulation.

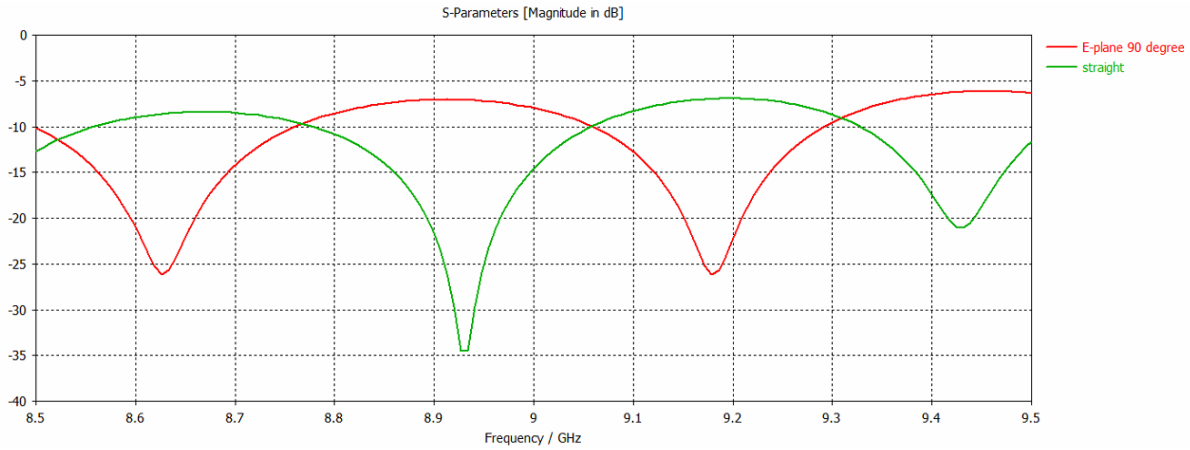

Fig.6.312 Comparison of simulated S11s of straight SWA and SWA under E-plane 90 degree bending.

Fig.6.313 presents the simulated 3D radiation pattern of this SWA under E-plane 90 degree bending at 9.43 GHz. Since the straight SWA had a resonant frequency at 9.43GHz in simulation, the H-plane radiation pattern of the E-plane 90 degree bent SWA at 9.43GHz was compared with that of the straight SWA at 9.43GHz and Fig.6.314 shows the result. From Fig.6.313 and Fig.6.314, it can be seen that the simulated radiation pattern of the SWA rotated along the bending direction when the E-plane bending occurred. This was because the radiating slots also moved along the bending direction when the SWA was E-plane bent. In simulation, the main beam was in boresight when the SWA was straight and moved 70 degree away from boresight when the SWA was bent 90 degree along E-plane. The

simulated maximum gain of the straight SWA was 2.03dB and it dropped to 1.4 dB after E-plane 90 degree bending.

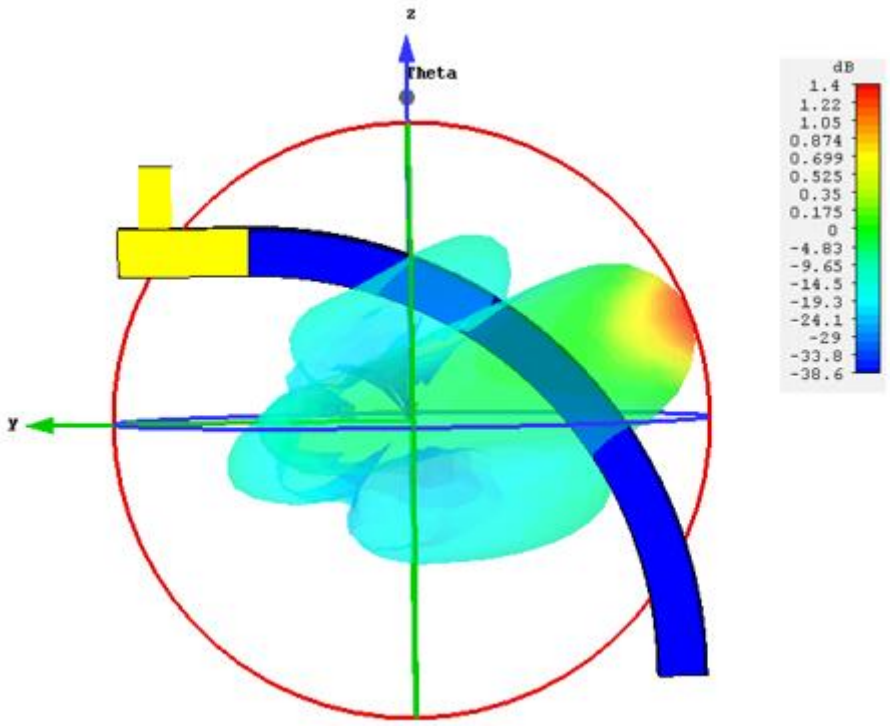

Fig.6.313 Simulated 3-D radiation pattern of a SWA under E-plane 90 degree bending at 9.43GHz

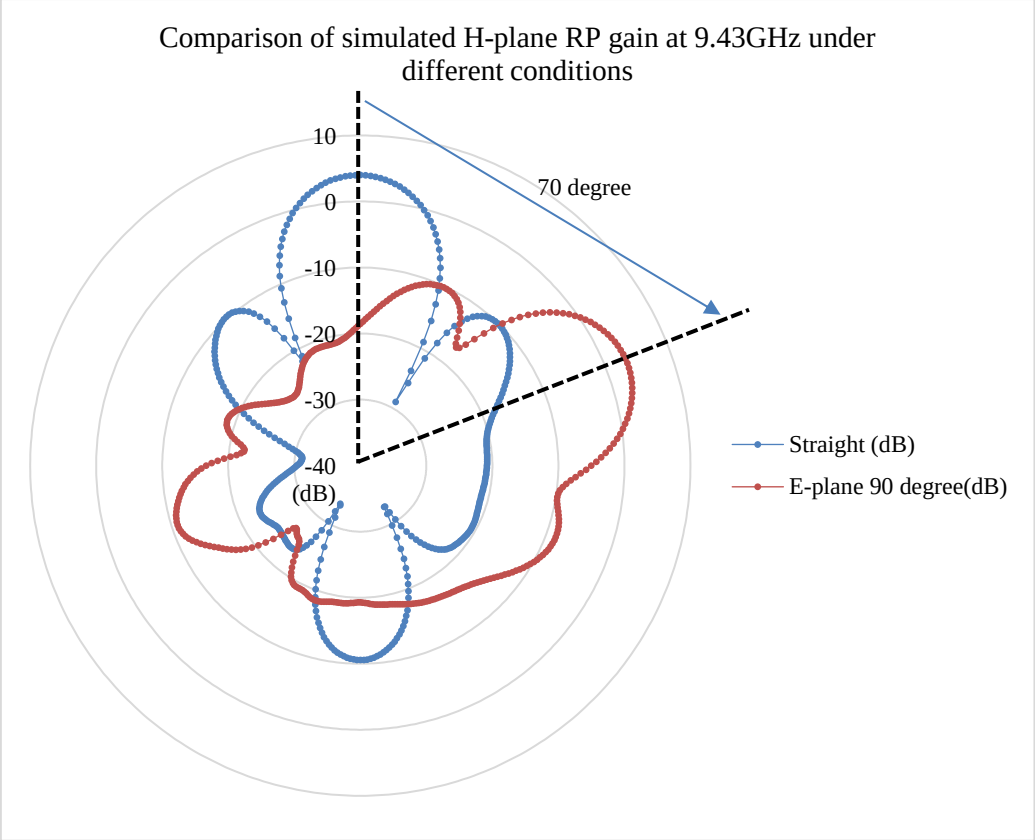

Fig.6.314 Comparison of simulated H-plane radiation patterns of a SWA when it is straight and under E-plane 90 degree bending

Measurement (E-plane 90 degree bending):

Fig.6.315 shows the radiation pattern measurement for the knitted SWA under E-plane 90 degree bending in an anechoic chamber. To get a good measurement result, the antenna was placed by tape as shown in Fig.6.315 (a) and (b) to ensure the slots were facing towards the receiving horn antenna. In this way, the main lobe of the SWA was captured.

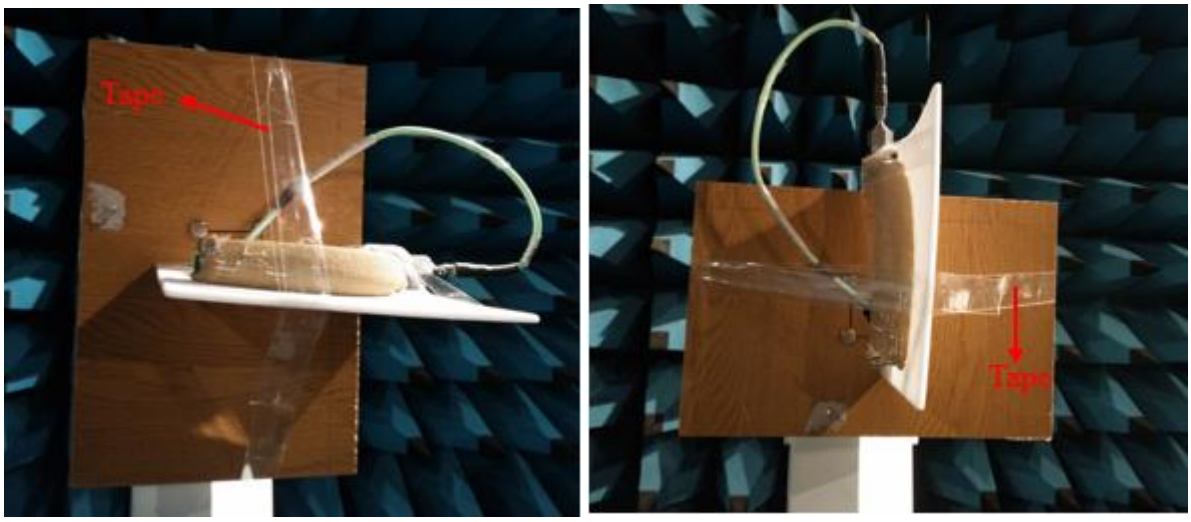

(a) (b)

Fig.6.315 Measurement setup for E-plane 90 degree bending in anechoic chamber: (a) E-plane radiation pattern; (b) H-plane radiation pattern

The measured reflection coefficients of a straight sample and the sample under E-plane 90 degree bending are compared in Fig.6.316. From Fig.6.316, it can be seen that instead of decreasing in simulation, the knitted SWA's resonant frequencies shifted upwards slightly, from 8.69 GHz to 8.73 GHz and from 9.185GHz to 9.23GHz after bending 90 degree along E-plane in practice. The measured reflection coefficient of the knitted SWA still remained acceptable (below -15dB) after E-plane 90 degree bending, which agreed with the simulation. The difference between the measured and simulated results regarding to the resonant frequency primarily was due to the fact that the simulated model was not the same as the knitted SWA and the slots were not actually stretched when the sample was bent.

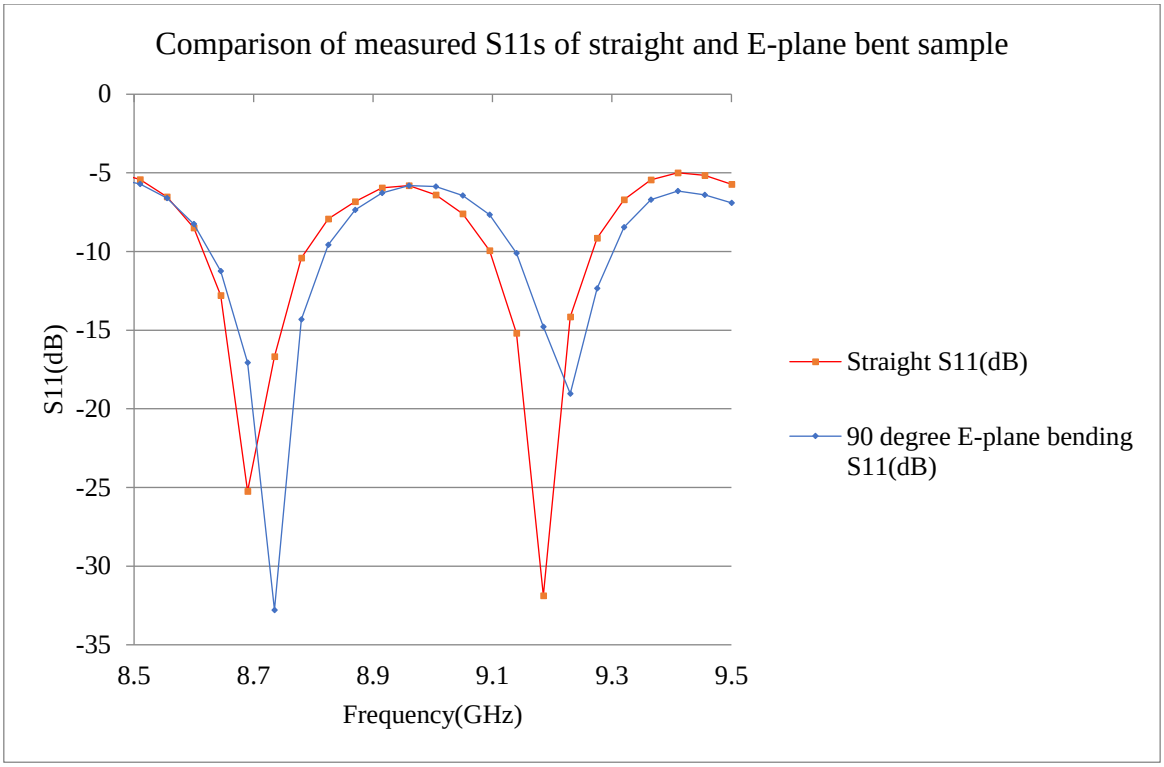

Fig.6.316 Comparison of measured S11s of straight sample and sample under E-plane 90 degree bending.

The radiation pattern of the knitted SWA under E-plane 90 degree bending was measured at 9.185GHz, which was the resonant frequency of the straight knitted SWA. Fig.6.317 presents the comparison of measured H-plane radiation pattern of the bent sample and straight sample at the same frequency. Since the receiving horn antenna in anechoic chamber can only capture the main lobe of the bent sample, the rotation of the SWA's radiation pattern due to the E-plane bending cannot be observed from Fig.6.317. From Fig.6.317, it can be seen that at 9.185GHz, the knitted SWA remained a similar radiation pattern in H planes after E-plane 90 degree bending. The measured maximum gain of the bent SWA dropped from 2.23dB to 0.347dB compared with the straight sample. Generally, the changes of measured radiation pattern due to the E-plane 90 degree bending agreed with the simulated results.

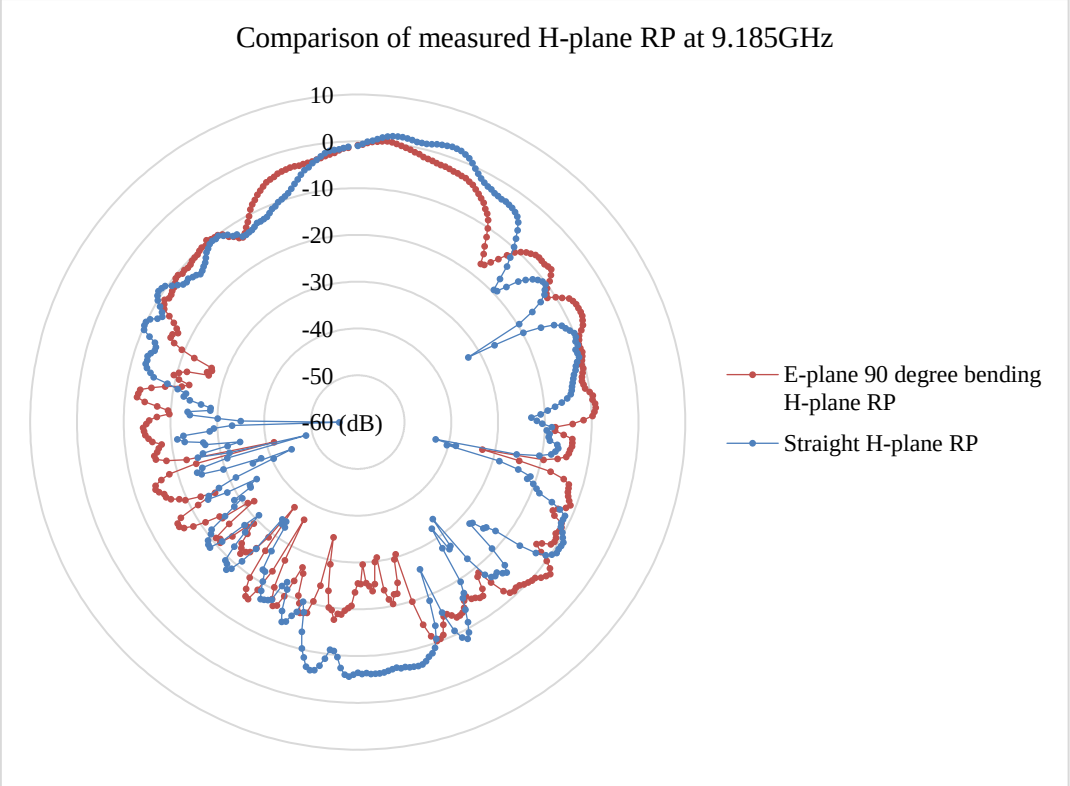

Fig.6.317 Comparison of measured H-plane radiation patterns of straight and E-plane 90 degree bent knitted SWA

6.32 E-plane 180 degree bending

Fig.6.321 (a) presents a SWA based on WR-90 waveguide under E-plane 180 degree bending in simulation and Fig.6.321 (b) presents the knitted sample under E-plane 180 degree bending in measurement.

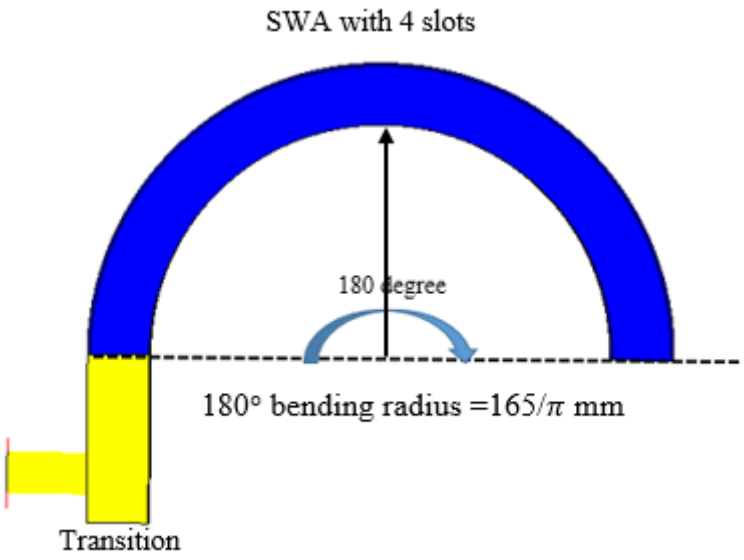

(a)

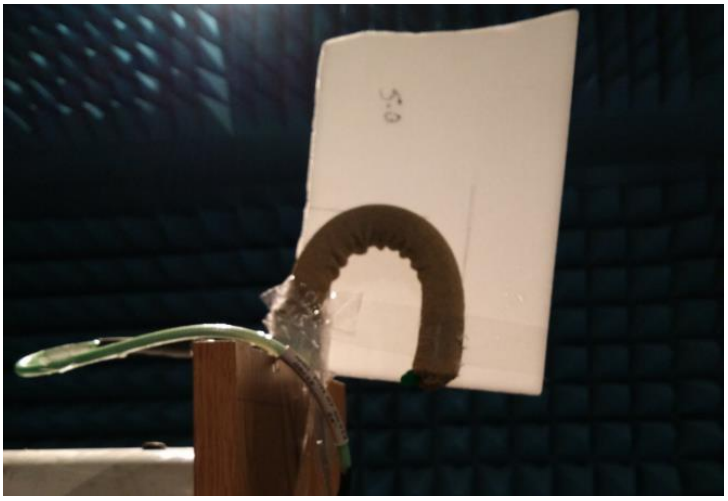

(b)

Fig.6.321 A SWA with four slots under E-plane 180 degree bending

(a): A SWA based on WR-90 waveguide in simulation (b): A knitted sample in measurement

Simulation (E-plane 180 degree bending):

Fig.6.322 presents the simulated reflection coefficients of the WSA under different E-plane bending conditions. From Fig.6.322, it can be seen that after E-plane 180 degree bending in simulation, the bent SWA still had a dual band behaviour and its resonant frequencies

(8.9GHz and 9.46GHz) were closed to that of the straight SWA (8.93GHz and 9.43GHz). Moreover, the S11 of E-plane 180 degree bent SWA remained acceptable, which was below -15dB at its resonant frequencies in simulation.

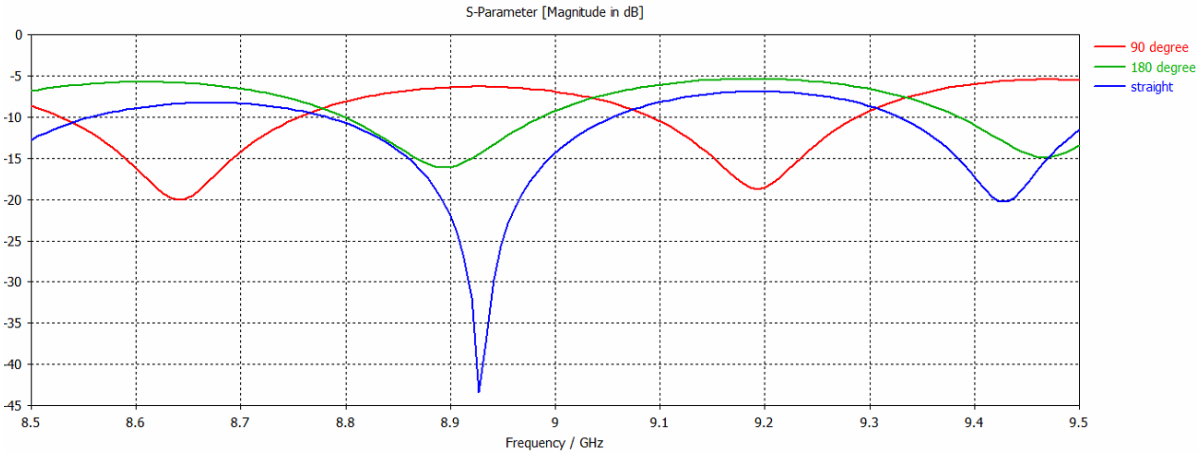

Fig.6.322 Comparison of simulated S11s of straight, E-plane 90 degree bent, E-plane 180 degree bent SWA.

Fig.6.323 shows the simulated 3D radiation pattern of this SWA under E-plane 180 degree bending at.9.43 GHz and Fig.6.324 shows the simulated H-plane radiation patterns of this SWA under different E-plane bending conditions at the same frequency. From Fig.6.323 and Fig.6.324, it can be seen that in simulation, the SWA's radiation pattern rotated further along the bending direction under E-plane 180 degree bending. Moreover, the SWA became less directional and its gain decreased after bending. Table.6.321 details the effects of E-plane bending on SWA's radiation characteristics in simulation.

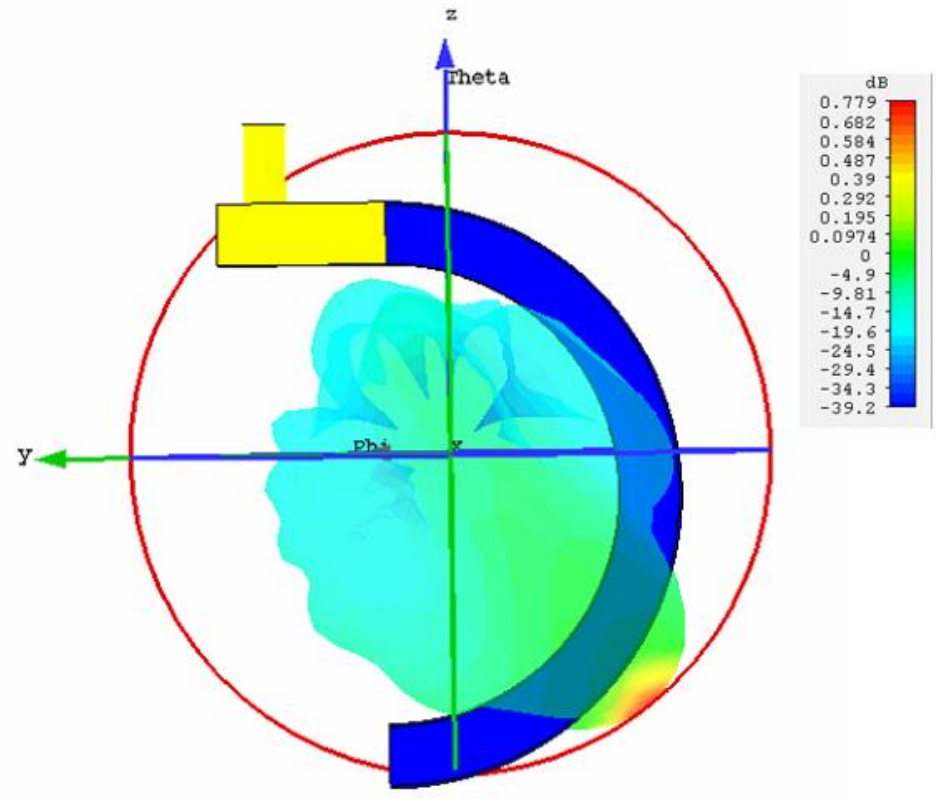

Fig.6.323 Simulated radiation pattern of SWA under E-plane 180 degree bending

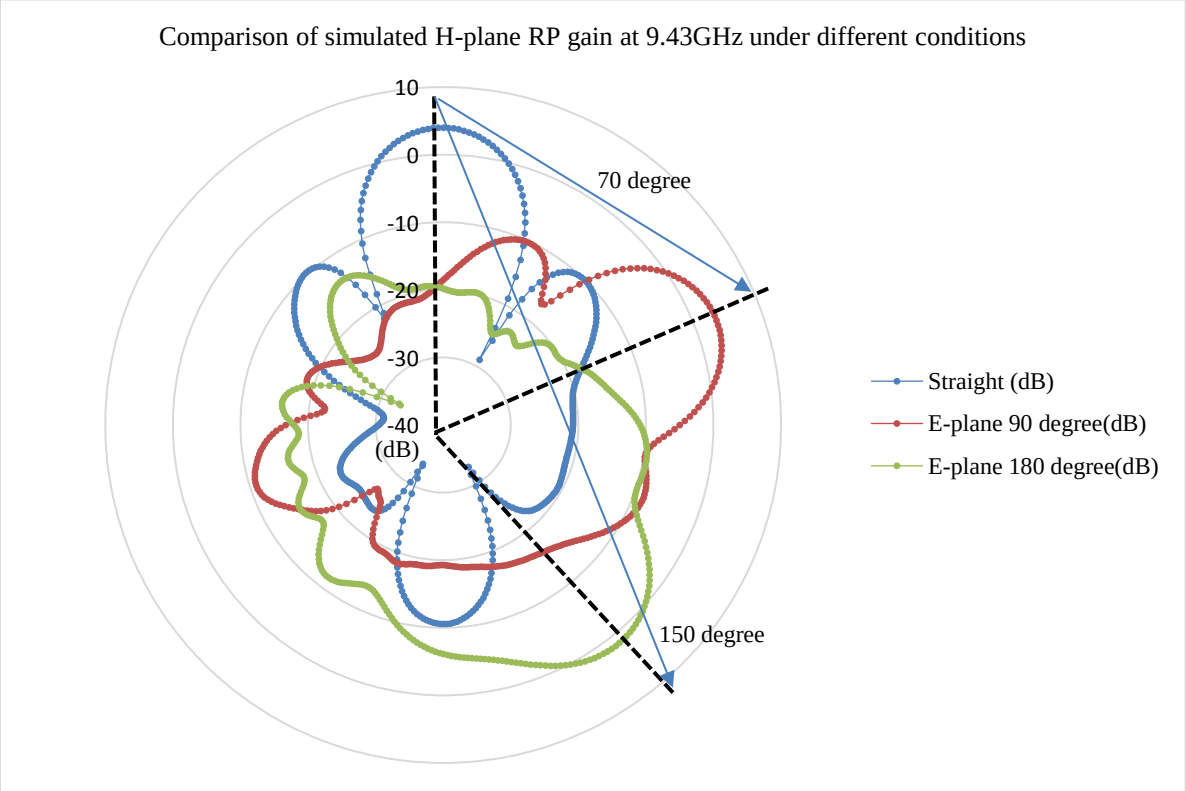

Fig.6.324 Comparison of simulated H-plane radiation pattern of straight, E-plane 90 degree bent, E-plane 180 degree bent SWA.

Table.6.321 Simulated radiation characteristics of SWA under different E-plane bending conditions

	Straight	E-plane 90 degree	E-plane 180 degree
Main beam direction	0 degree	70 degree	150 degree
Maximum gain at 9.43GHz	2.03dB	1.4dB	0.78dB
Beam width	24.5 degree	25 degree	28.4 degree

Measurement (E-plane 180 degree bending):

The performance of the knitted sample under E-plane 180 degree bending was measured. The measured reflection coefficients of the knitted SWA under different E-plane bending conditions are presented in Fig.6.325. From Fig.6.325, it can be seen that the resonant frequencies of the E-plane 180 degree bent SWA were 8.69GHz and 9.185GHz, which almost the same as that of the straight sample. Moreover, the measured result showed that the reflection coefficient of the knitted SWA was always below -15dB under different E-plane bending conditions.

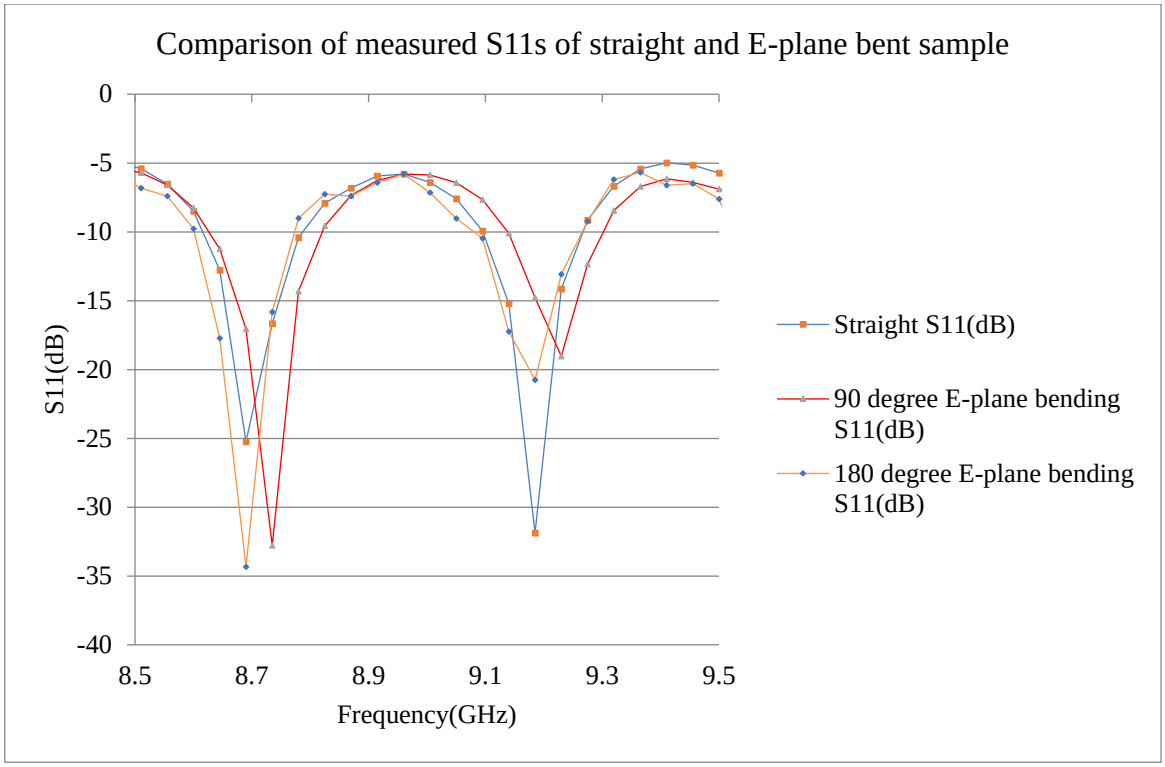

Fig.6.325 Comparison of measured S11s of straight, E-plane 90 degree bent, E-plane 180 degree bent sample.

The radiation pattern of the knitted SWA under E-plane 180 degree bending was measured at 9.185GHz. Fig.6.326 presents the comparisons of measured H-plane radiation pattern of the knitted SWA under different E-plane bending conditions at the same frequency. From Fig.6.326, it can be seen that at 9.185GHz, the E-plane 180 degree bent SWA still had a similar radiation pattern compared with the straight sample in H-plane. Table.6.322 shows that the measured maximum gain of the knitted SWA reduced further when the E-plane bending angle increased to 180 degree and the bent sample became less directional.

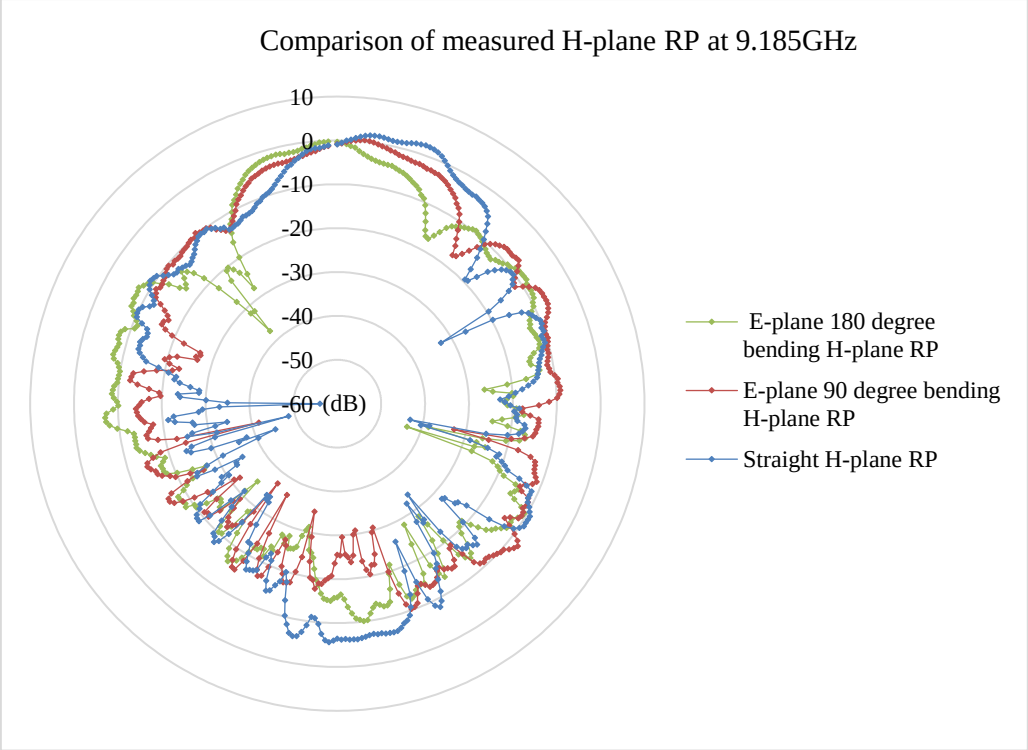

(b)

Fig.6.326 Comparison of measured radiation patterns of straight, E-plane 90 degree bent, E-plane 180 degree bent sample: (a) E-plane; (b) H-plane

Table.6.322 Measured radiation characteristics of knitted SWA under different E-plane bending conditions

	Straight	E-plane 90 degree	E-plane 180 degree
Measured max gain at 9.185GHz	2.23dB	0.347dB	-0.217dB
Beam width	26 degree	34 degree	27 degree

In conclusion, although I used a different simulated model (a SWA based on WR-90 rectangular waveguide) rather than the knitted sample in the measurement, the effects of E-plane bending had on SWA's performance in measurement generally agreed with that in

simulation. E-plane bending had little effects on knitted SWA's resonant frequencies as the slots on the waveguide were not actually stretched. E-plane bending also did not change the SWA's input impedance matching condition and bandwidth significantly. Moreover, when E-plane bending occurred, the SWA's radiation pattern rotated along the bending direction, and the main lobe pattern remained similar. Lastly, both simulation and measurement show that the SWA's gain decreased when the SWA was bent along E-plane and it dropped significantly as the bending angle increases.

6.33 H-plane 90 degree bending

Fig.6.331 (a) presents a SWA based on WR-90 waveguide under H-plane 90 degree bending in simulation and Fig.6.331 (b) presents the knitted sample under H-plane 90 degree bending in measurement.

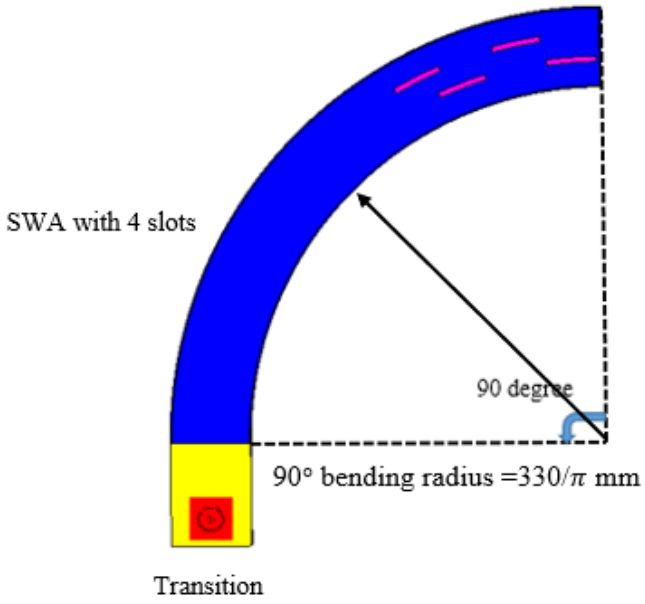

(a)

(b)

Fig.6.331 A SWA with four slots under H-plane 90 degree bending

(a): A SWA based on WR-90 waveguide in simulation (b): A knitted sample in measurement

Simulation (H-plane 90 degree bending):

The simulated reflection coefficients of a straight SWA and the SWA under H-plane 90 degree bending are shown in Fig.6.332. From Fig.6.332, it can be seen that in simulation, the resonant frequencies of the SWA shifted downwards slightly after H-plane 90 degree bending, from 9.43GHz to 9.36GHz and from 8.93GHz to 8.89GHz. This was because the slots were stretched slightly longer when the SWA was bent 90 degree along the H-plane in simulation. Moreover, in simulation, the SWA still had a reflection coefficient which was below -20dB at resonant frequencies after H-plane 90 degree bending.

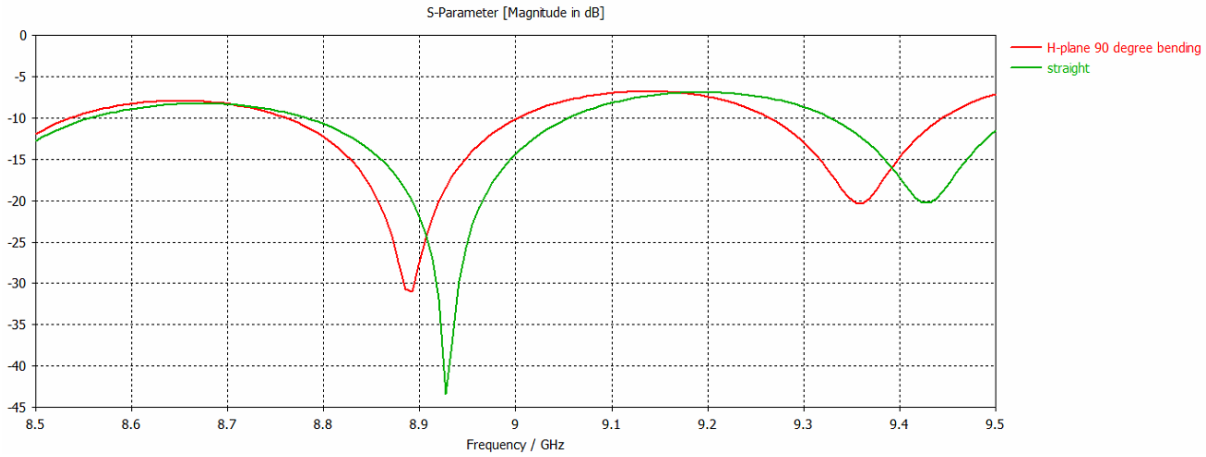

Fig.6.332 Comparison of simulated S11s of a straight SWA and SWA under H-plane 90 degree bending

The simulated 3D radiation patterns of a straight and an H-plane 90 degree bent SWA at 9.43GHz are presented in Fig.6.333 (a) and (b). Fig.6.333 shows that in simulation, the SWA kept a similar radiation pattern after H-plane 90 degree bending, but its radiation pattern was rotated approximately 90 degree along the bending direction. Fig.6.334 shows the comparison of this SWA's main lobe in polar form when it was straight and bent 90 degree along H-plane. From Fig.6.334, it can be seen clearly that the SWA's main lobe remained a similar pattern after H-plane 90 degree bending in simulation, while the simulated maximum gain of the SWA dropped from 2.03dB to 1.2dB.

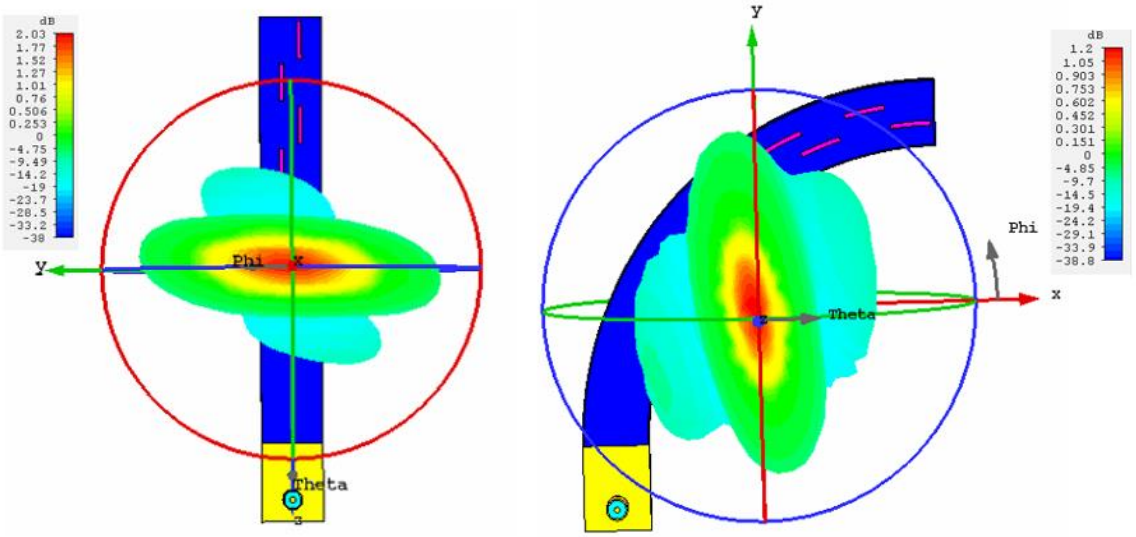

(a) (b)

Fig.6.333 Simulated 3D radiation pattern of the SWA: (a) straight; (b) under H-plane 90 degree bending

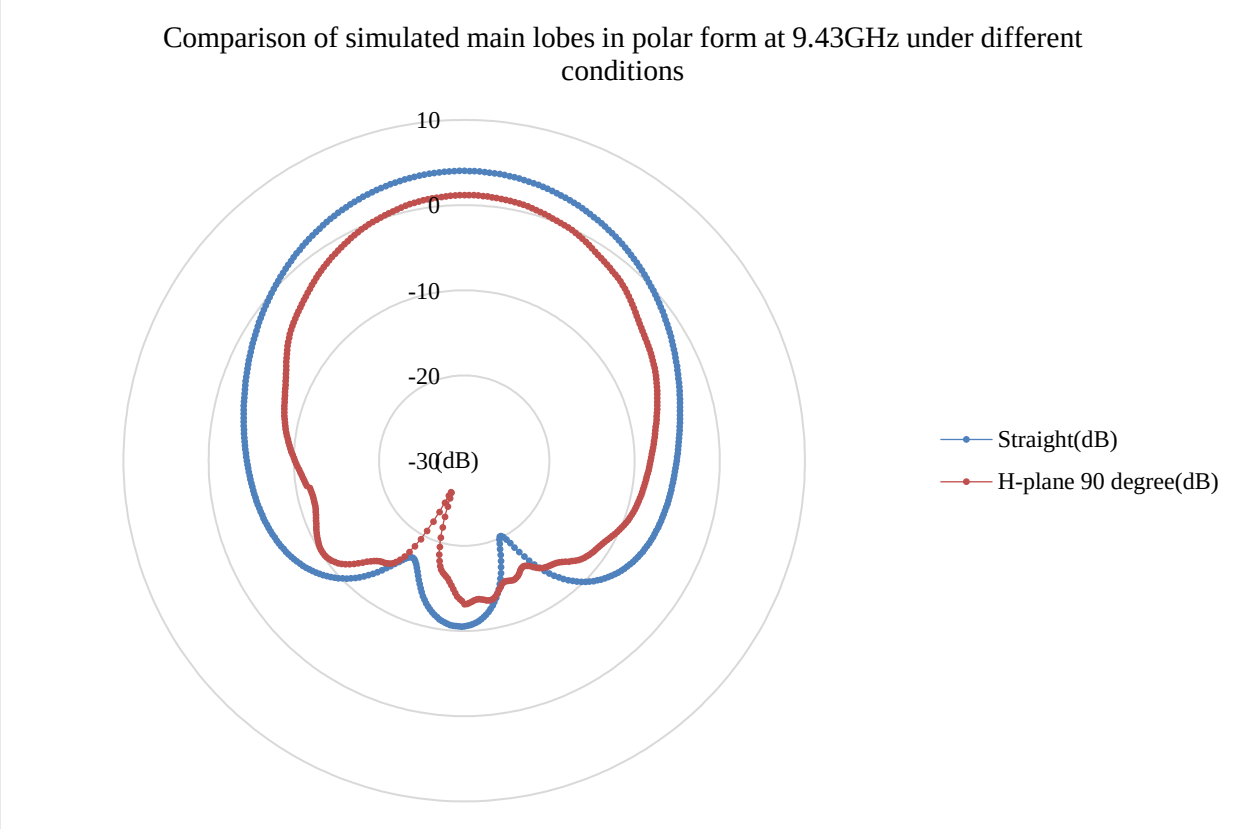

Fig.6.334 Comparison of simulated main lobes of a straight SWA and a H-plane 90 degree bent SWA at 9.43GHz

Measurement (H-plane 90 degree bending):

Fig.6.335 presents the measurement setup for the antenna under H-plane 90 degree bending in an anechoic chamber.

(a) (b)

Fig.6.335 Measurement setup for H-plane 90 degree bending in anechoic chamber: (a) H-plane radiation pattern; (b) E-plane radiation pattern

The reflection coefficient of the knitted SWA under H-plane 90 degree bending was measured and compared with that of the straight sample as shown in Fig.6.336. From Fig.6.336, it can be seen that in measurement, the knitted SWA's resonant frequencies shifted upwards, from 8.69 GHz to 8.73 GHz and from 9.19GHz to 9.23GHz after bending 90 degree along H-plane rather than shifting downwards in simulation. Additionally, the knitted SWA still had a reflection coefficient around -20dB at resonant frequencies after it was bent 90 degree along H-plane. The measurement showed a different result compared with the simulation for the SWA's resonant frequency, and this was due to the fact that instead of being stretched longer in simulation, the slots were actually compressed and became slightly shorter due to the H-plane 90 degree bending in measurement.

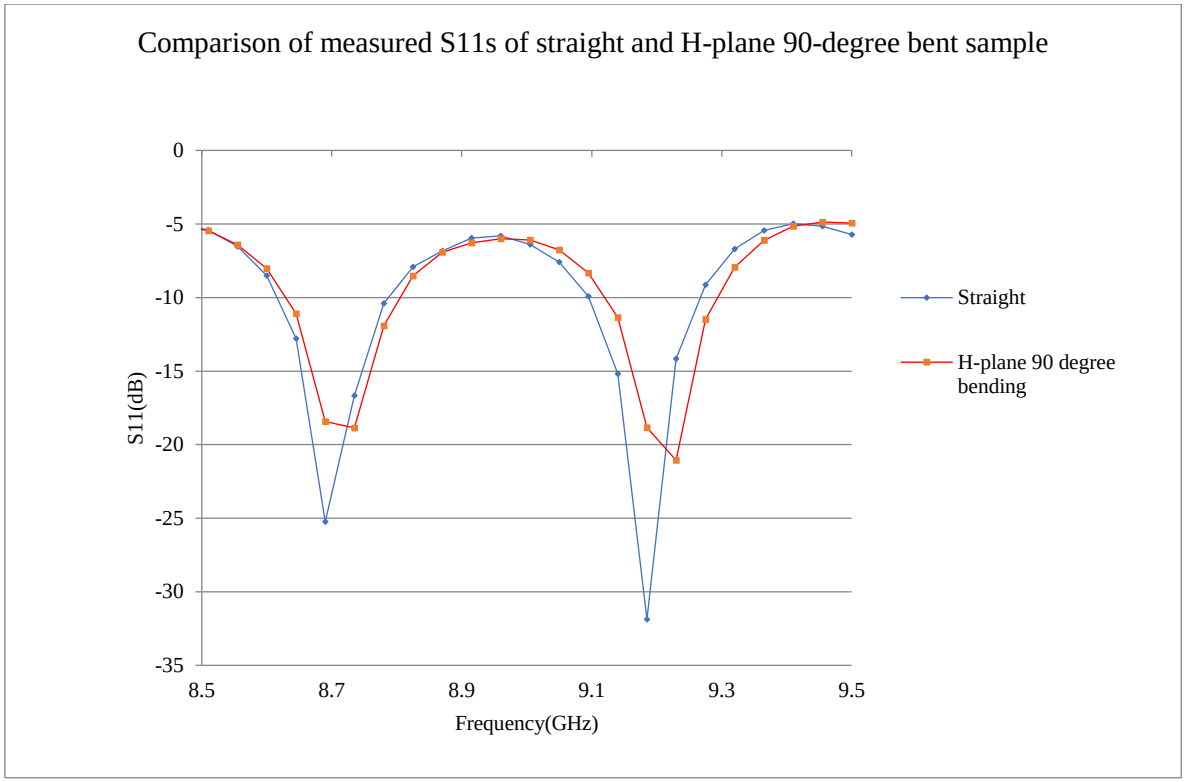

Fig.6.336 Comparison of measured S11s of a straight sample and sample under H-plane 90 degree bending.

Like the E-plane bending radiation pattern measurement, the receiving horn antenna in the anechoic chamber can only capture the main lobe of the knitted SWA for H-plane bending measurement. The simulation demonstrated that when the SWA was bent 90 degree along H-plane, its radiation pattern was also rotated approximately 90 degree to the bending direction. Therefore, I would expect a cross polarized (CP) transmission in measurement if the receiving antenna kept the same orientation as for the straight sample measurement. Fig.6.337 shows the measured results when the knitted SWA was bent 90 degree along H-plane while the receiving antenna kept the same orientation as for the straight sample measurement. From Fig.6.337, the measurement shows that the power received by the receiving horn antenna was very low due to the cross polarization, which justified our expectation. Therefore, the receiving horn antenna was rotated 90 degree to the bending direction to be aligned with E field of the knitted H-plane 90 degree bent SWA. Fig.6.338 shows the co-polarized measured H-plane radiation pattern of the knitted SWA under H-plane 90 degree bending at 9.185GHz. From Fig.6.338, it can be seen that at 9.185GHz, the knitted SWA still remained a similar radiation pattern in H-plane after H-plane 90 degree bending. Moreover, there was about 0.4dB gain drop for the H-plane 90 degree bent SWA

compared with the straight sample in measurement. Generally, the changes of measured radiation pattern due to the H-plane 90 degree bending agreed with simulation.

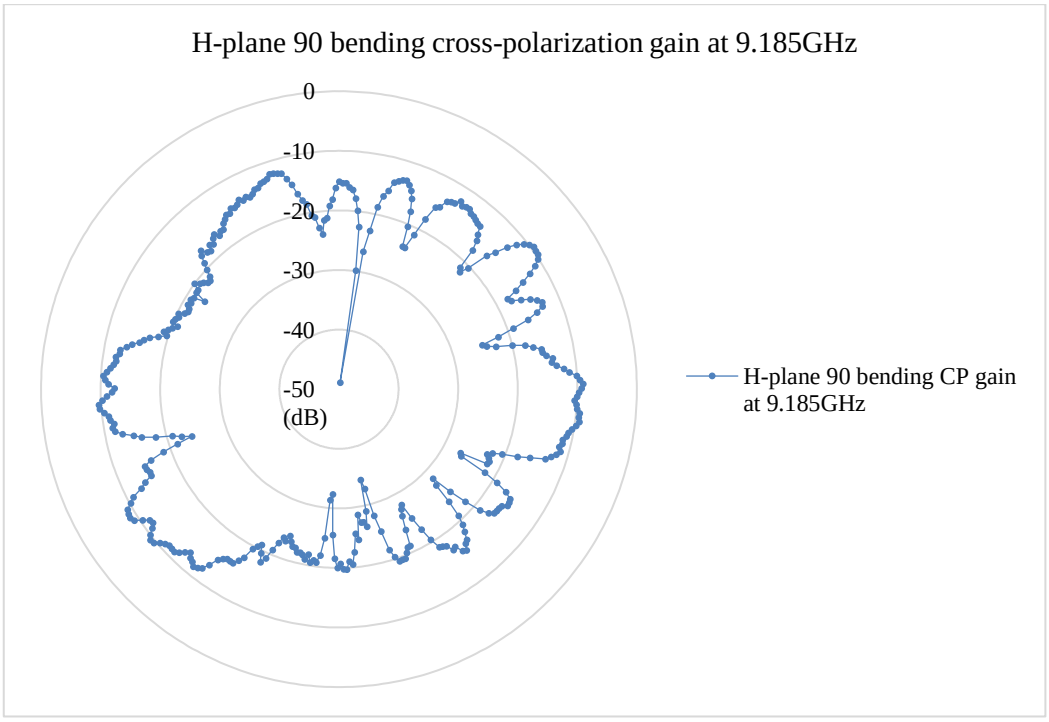

Fig.6.337 Cross polarized radiation pattern of H-plane 90 degree bent sample at 9.185GHz

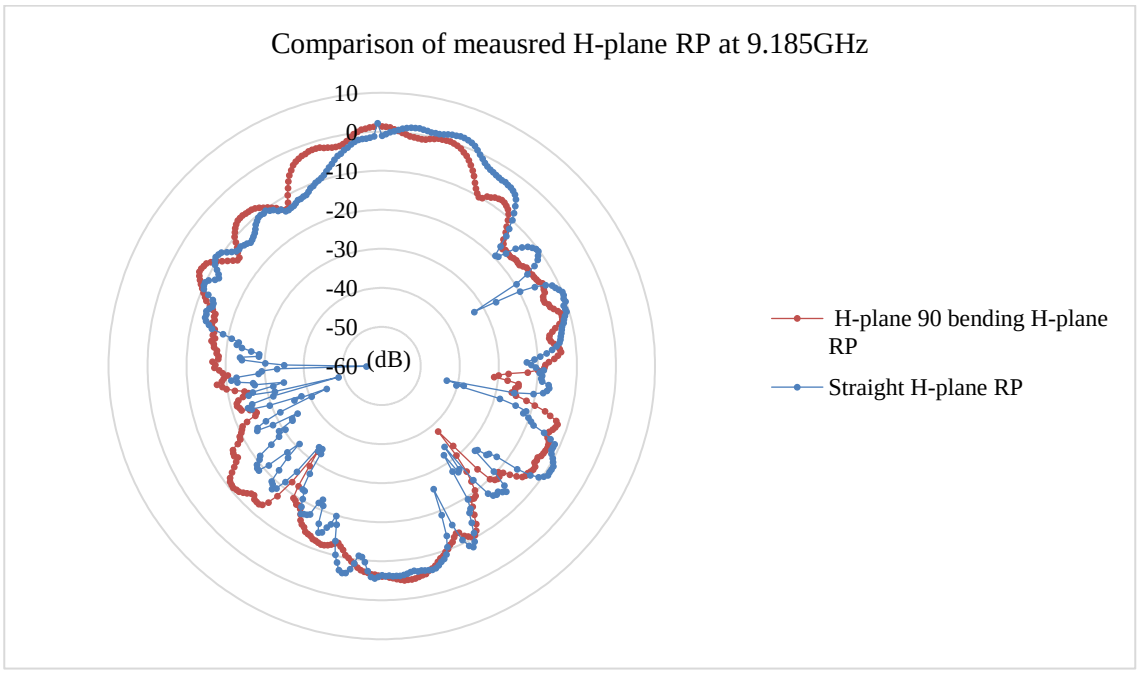

Fig.6.338 Comparison of measured H-plane co-polarized radiation patterns of straight and H-plane 90 degree bent sample

6.34 H-plane 180 degree bending

Fig.6.341 (a) presents a SWA based on WR-90 waveguide under H-plane 180 degree bending in simulation and Fig.6.341 (b) presents the knitted sample under H-plane 180 degree bending in measurement.

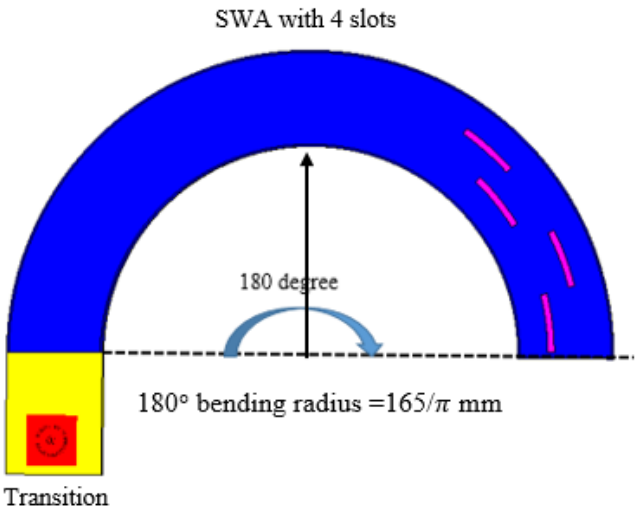

(a)

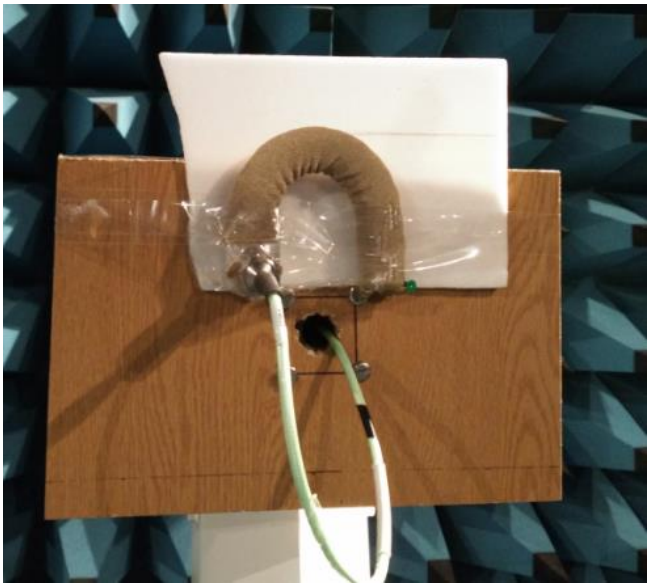

(b)

Fig.6.341 Knitted SWA with four stitched slots under E-plane 180 degree bending

(a): In simulation (b): In measurement

Simulation (H-plane 180 degree):

Fig.6.342 presents simulated reflection coefficients of the SWA under different H-plane bending conditions. From Fig.6.342, it can be seen that the resonant frequencies of the SWA shifted downwards further under H-plane 180 degree bending in simulation. This was because the slots were stretched longer as the H-plane bending angle increased in simulation.

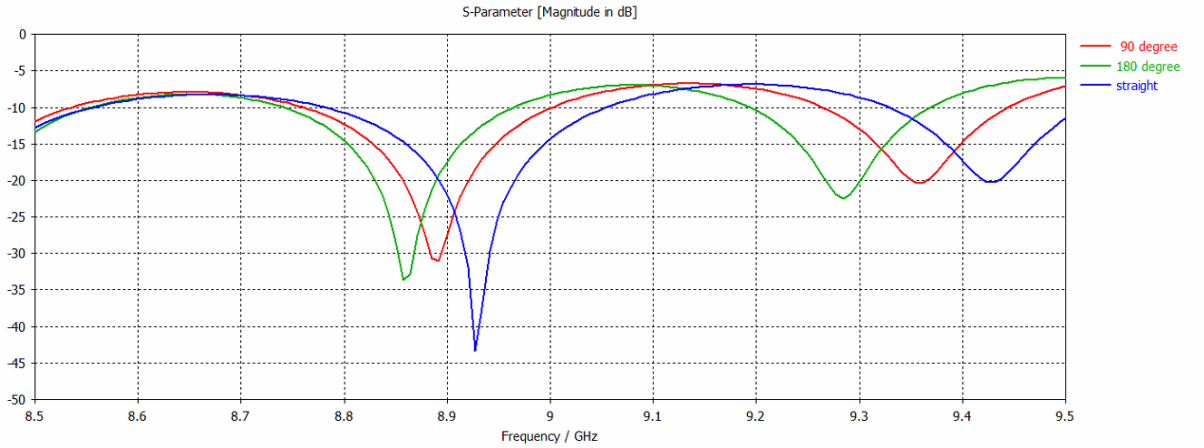

Fig.6.342 Comparison of simulated S11s of straight, H-plane 90 degree bent, H-plane 180 degree bent SWA.

The simulated 3D radiation patterns of straight and H-plane 180 degree bent SWA at 9.43GHz are presented in Fig.6.343 (a) and (b), respectively. Fig.6.343 shows that in simulation, the SWA's radiation pattern was rotated further (approximately 150 degree) along the bending direction when the SWA was bent 180 degree along H-plane. The main lobe pattern of the H-plane 180 degree bent SWA was plotted in polar form when phi (φ) was set 30 degree (180^o-150^o=30^o) in simulation as shown in Fig.6.344. From the comparison of simulated main lobe of the SWA under different H-plane conditions in Fig.6.344, it can be seen that the SWA's main lobe was able to remain a similar pattern when H-plane bending occurred, while the maximum gain of the SWA decreased when the H-plane bending angle increased. Table 6.341 details the H-plane bending's effects on the SWA's radiation characteristics in simulation.

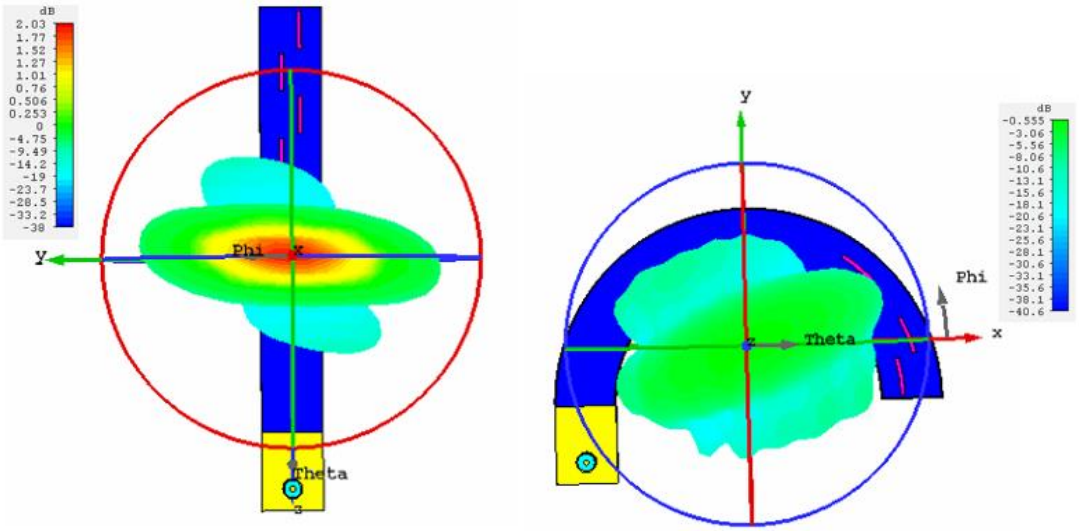

(a) (b)

Fig.6.343 Simulated 3D radiation pattern of SWA: (a) straight; (b) under H-plane 180 degree bending

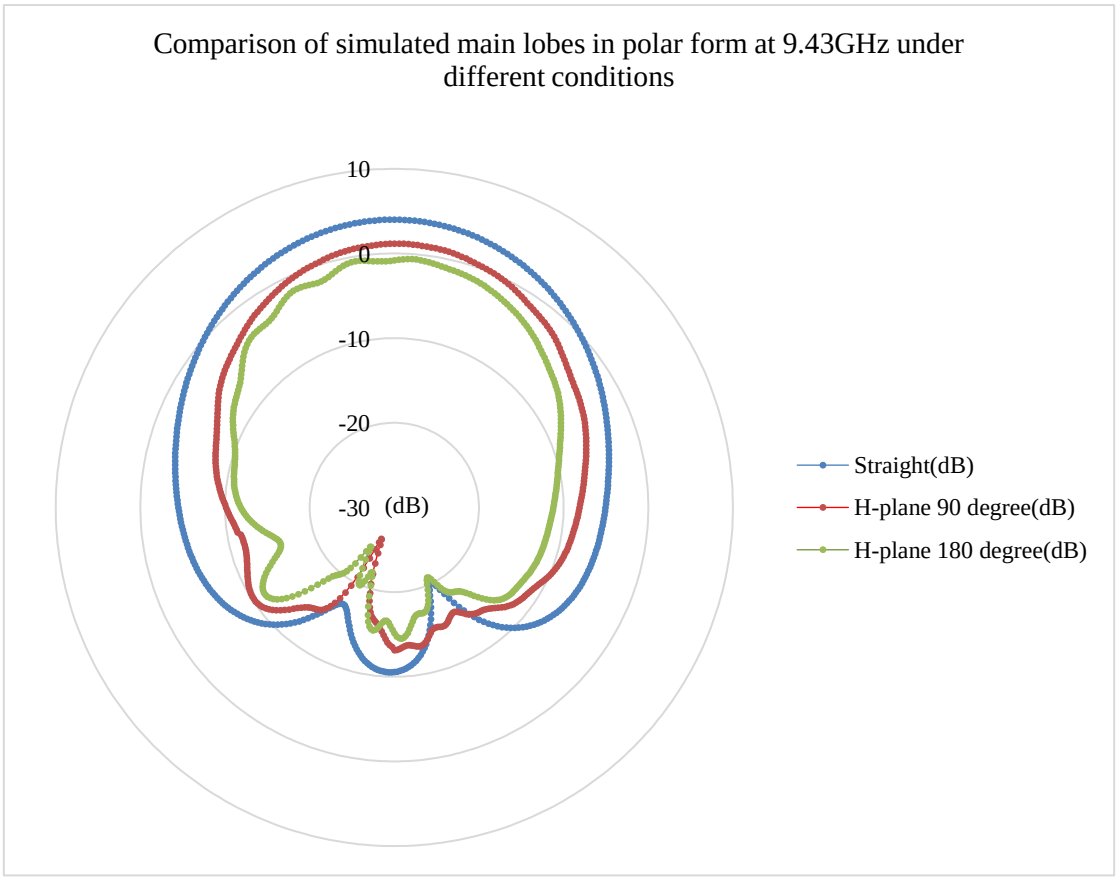

Fig.6.344 Comparison of simulated main lobes in polar form at 9.43GHz under different conditions

Table.6.341 Simulated radiation characteristics of SWA under different H-plane bending conditions

	Straight	H-plane 90 degree	H-plane 180 degree
Main beam rotation angle	0 degree	90 degree	Approximately 150 degree
Maximum gain at 9.43GHz	2.03dB	1.204dB	-0.56dB

Measurement (H-plane 180 degree):

Fig.6.345 (a) and (b) show the measurement setup for the knitted SWA under H-plane 180 degree bending in an anechoic chamber.

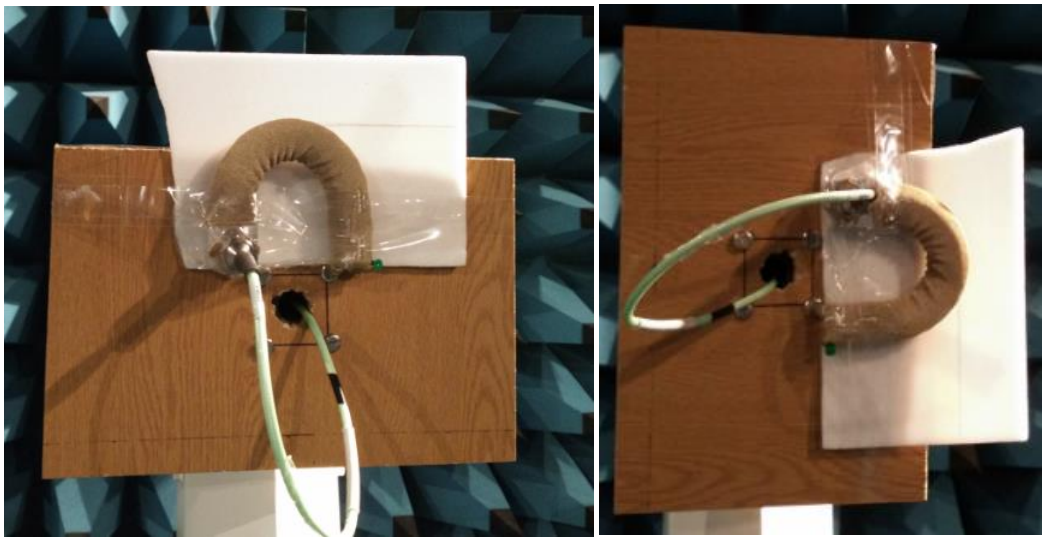

(a) (b)

Fig.6.345 Measurement setup for H-plane 180 degree bending in anechoic chamber: (a) H-plane radiation pattern; (b) E-plane radiation pattern

The measured reflection coefficients of the knitted SWA under different H-plane bending conditions are presented in Fig.6.346. From Fig.6.346, it can be seen that the resonant

frequencies of the knitted SWA only shifted upwards slightly due to the H-plane bending in measurement. The measured results showed that instead of being stretched in simulation, the slots were actually compressed slightly during the H-plane bending in practise.

Since it was difficult to capture the main lobe of the knitted SWA precisely after it was bent 180 degree along H-plane in the anechoic chamber, I did not have the measured radiation pattern for the knitted SWA under H-plane 180 degree bending. However, with the aid of simulation, I had a clear idea of H-plane bending's effects on SWA's performance. Similar to E-plane bending, the maximum gain of the knitted SWA dropped when H-plane bending occurred. Moreover, in practice, H-plane bending caused the knitted SWA to experience cross polarized transmission if the receiving antenna remained the same orientation.

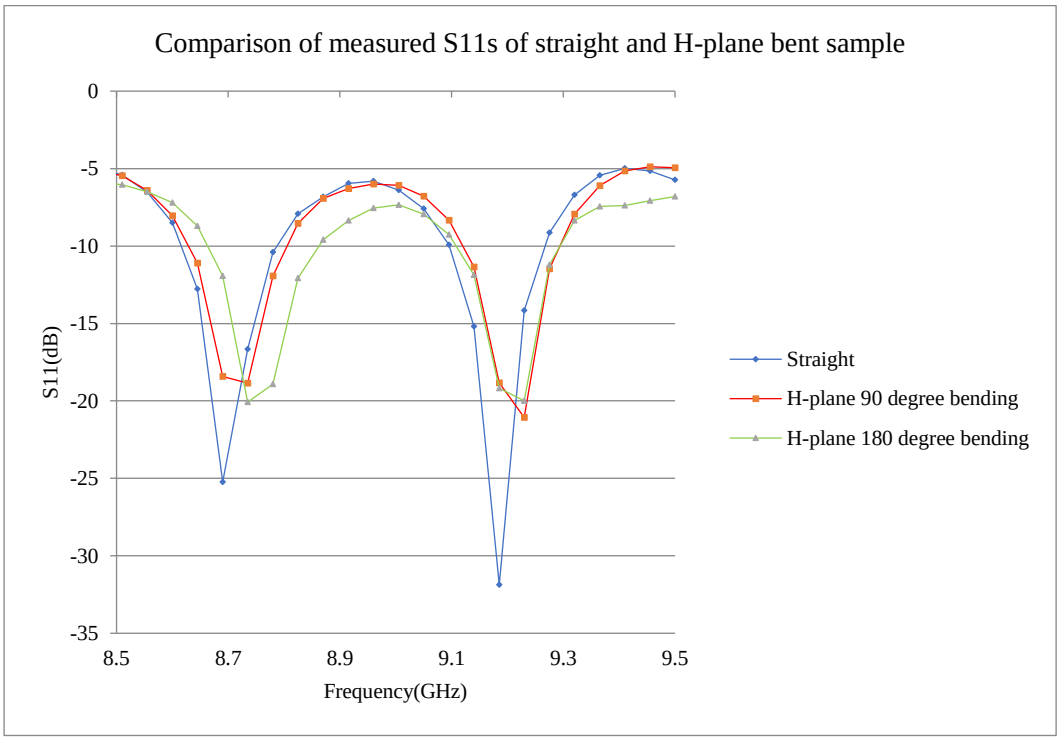

Fig.6.346 Comparison of measured S11s of straight, H-plane 90 degree bent, H-plane 180 degree bent sample.

6.4 Conclusion

In this chapter, the design and performance of several knitted slotted waveguide antennas (SWA) working at X band were presented. The stitched slots were tested to be able to improve the antenna's performance significantly and the extra slots on the SWA can increase the antenna's gain further. There were good agreements between the simulation and measurement. The final knitted SWA presented directional radiation characteristics with a maximum gain of 2.33dB at 9.185GHz. Moreover, the working bandwidth of stitched sample reaches 170MHz.

The performances of the knitted SWA with four stitched slots under bending conditions were also studied in simulation and measurement. Four different bending conditions including 90 degree and 180 degree bending along both principle E-plane and H-plane were set up, and the results were concluded as following.

E-plane bending:

In measurement, E-plane bending didn't shift the knitted SWA's resonant frequency significantly in measurement as the slots were not stretched or compressed when E-plane bending occurred. Furthermore, the SWA's reflection coefficient remained acceptable, which was at least below -15dB at the resonant frequencies. It meant that E-plane bending did not affect the SWA's input impedance significantly. When E-plane bending occurred, the knitted SWA's radiation pattern rotated along the bending direction. The main lobe remained a similar pattern, however, the SWA's gain reduced as the E-plane bending angle increased. To sum up, when the knitted SWA is bent along E-plane in practice, it must be placed in a position where the slots can face towards the receiving antenna to obtain a good transmission. If the knitted SWA and receiving antenna are both fixed in the position, the E-plane bending must be avoided.

H-plane bending:

H-plane bending shifted the knitted SWA's resonant frequency upwards slightly in measurement as the slots were compressed when the knitted SWA was bent along H-plane. Furthermore, the knitted SWA was able to remain a good input impedance matching condition at its resonant frequencies under H-plane bending. When H-plane bending occurred, the knitted SWA's radiation pattern was rotated along the bending direction.

Consequently, the H-plane bent SWA experienced a cross polarized transmission if the receiving antenna kept the same orientation. For the sake of a good transmission, the H-plane bending must be avoided if the orientation of the knitted SWA or the receiving antenna cannot be changed.
Overall, bending has little effect on the knitted SWA's resonant frequency, but it can affect the knitted SWA's radiation characteristics significantly, particularly when a severe shape distortion occurs to antenna.

Chapter 6 followed the research descried in chapter 5 and developed further. At this stage, the design and evaluation of knitted textile waveguides and knitted slotted waveguide antennas had accomplished. Moreover, shape distortion study was taken for all the knitted samples. Finally, conclusions were drawn regarding to the suitability's of applying knitted textile waveguides and knitted slotted waveguide antennas in practise, respectively.

Chapter 7: Knitted Textile Frequency Selective Surface

7.1 Introduction

Traditionally, electromagnetic devices are manufactured with hard materials such as metals and printed circuit boards. However, with the fast development of new materials and manufacturing techniques over the last few decades, electromagnetic structures can now be fabricated with commercial conducting textiles. It provides a lightweight and flexible alternative to conventional structures based on circuit board technology. For example, computerized textile manufacturing techniques can be applied to create various electromagnetic structures with periodic patterns such as frequency selective surface (FSS).

Chapter 7 started with the evaluation of several knitted slot FSSs working at WLAN band. The knitted slot FSSs exhibited a band-pass frequency-filtering property. A new concept for manufacturing electromagnetic textiles using a commercial computerized flat-bed knitting machine with laser ablation technique was discussed. The samples were knitted to have a double layer structure: a continuous conducting surface and a dielectric substrate backing. Laser ablation was then applied to slot the textiles to form the patterns of FSS. The serrated edges created during laser ablation process were modelled, and their impacts on FSS performances were also studied in simulation and measurement. Then, four knitted textile FSSs with hexagonal loop structures were presented. They were ultra-light weight as they only had a single layer structure formed by ultra-light yarns. These knitted hexagonal loop FSSs presented a high-pass response at various microwave frequencies. In the end, conclusions were drawn on this computerized knitting technique regarding its feasibility.

7.2 Knitted Cross Slot FSS

Traditionally, the starting point for manufacturing FSS was to take a single or double-sided sheet metal and patterned the surface by photo-lithographic/chemical etching or mechanical milling techniques [125]. In this new approach, I created the textile equivalent of a blank PCB metal with computerized flat-bed knitting techniques and applied laser ablation to slot the surface. Compared with the established manufacturing process, the new approach was more environmentally friendly as there was no chemical involved during the process. Moreover, it permitted a creation of large area structures with slotted patterns at high production rates and reduced cost.

All the knitted slotted FSS samples were manufactured using a Shima Seiki SWG091N computerized flat-bed knitting machine. The conducting textile was fabricated using a silver loaded nylon yarn (shieldex110f 24 dtex z turns) with the highest knitting density (the smallest stitch size of 25 stitch/inch) and the substrate was a knitted polyester which was similar to the one in textile waveguide in Chapter 5.

The first sample to be investigated was a knitted FSS with a grid of 10 by 10 cross slots. Fig.7.21 shows the geometry of a unit cell of the knitted cross slot FSS in simulation. Photograph of the knitted sample is presented in Fig.7.22. The manufacturing process of the knitted cross slot FSS started from a knitted double layer blanket as shown in Fig.7.23. The knitted blanket had a conducting surface and knitted polyester base. The conducting layer served as the textile equivalent of a conventional metallic sheet and the dielectric layer was to form a robust but flexible structure. Then, 10 by 10 cross slots were patterned on the knitted blanket with laser ablation technique to get the final sample. Before proceeding to measure the knitted cross slot FSS, a metallic FSS shown in Fig.7.24 was manufactured using a computerized milling machine and measured first. The metallic FSS shown in Fig.7.24 was made of aluminium and had the same unit cell as the simulated model shown in Fig.7.21, only without the dielectric base. It served as a reference to the knitted cross slot FSS. The normal incident, free-space reflectivity (S11) of the metallic reference FSS was measured by a fully calibrated NRL arch utilizing computer-controlled HP 8720D Vector Network Analyser as shown in Fig.7.25.

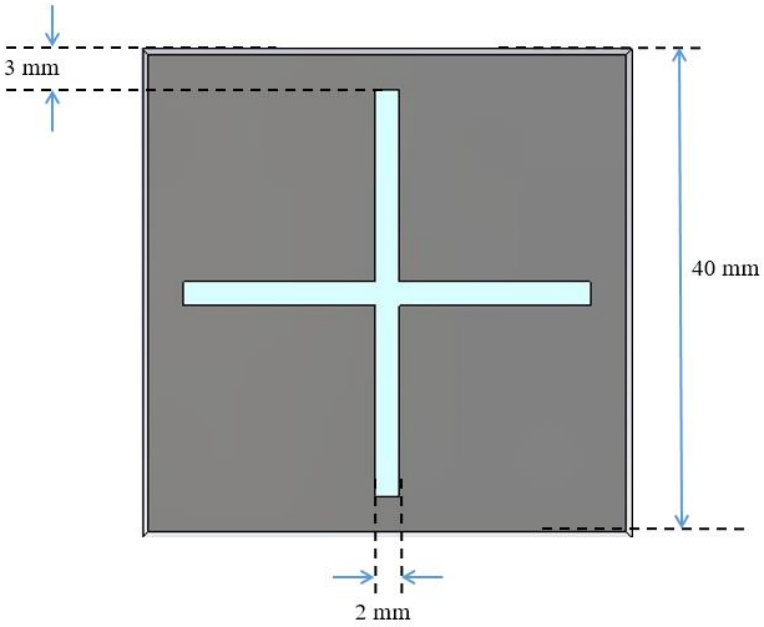

(a)

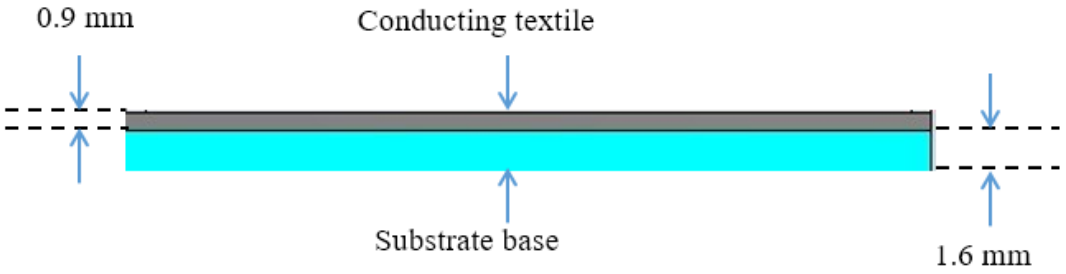

(b)

Fig.7.21 A unit cell of the knitted cross slot FSS in simulation: (a) Front view; (b) Side view

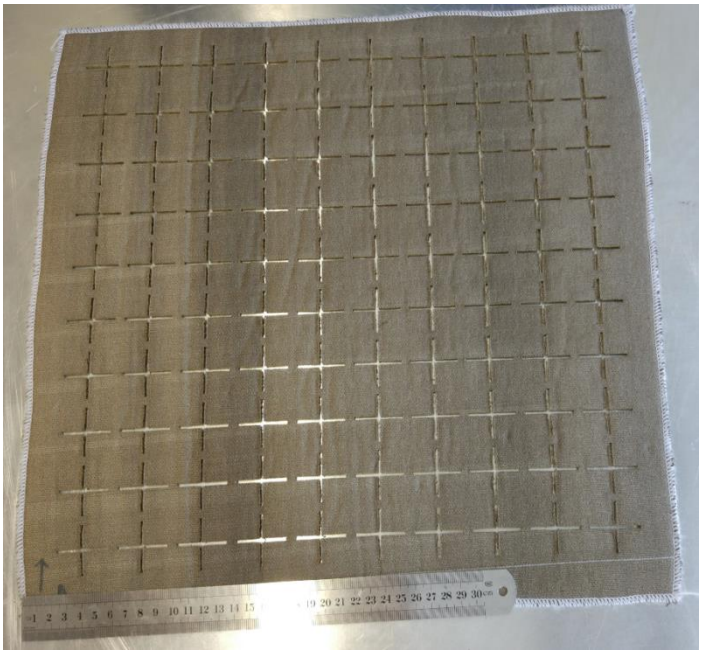

Fig.7.22. Photographs of the knitted cross slot FSS with a 10 by 10 grid:

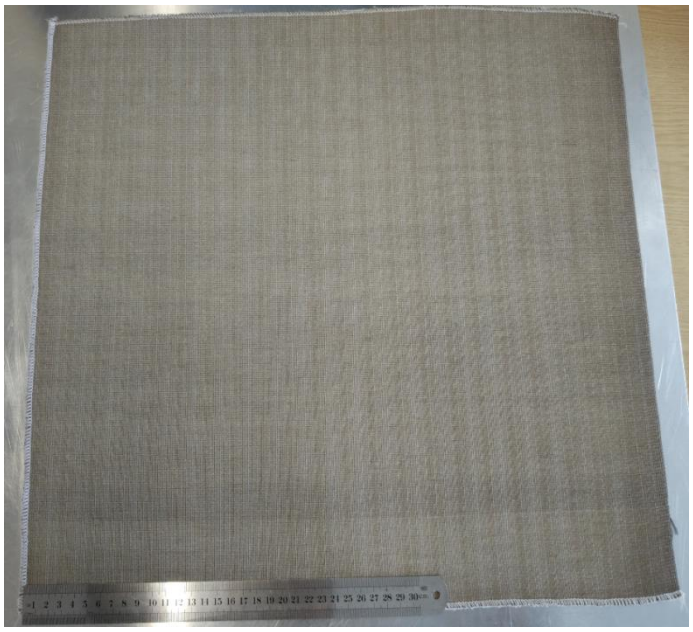

Fig.7.23 A knitted double layer blanket with a conducting surface and a substrate base

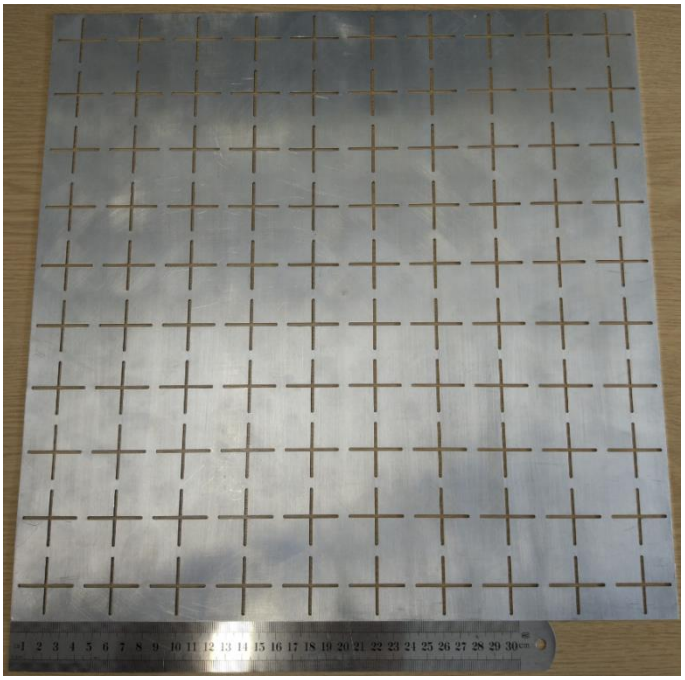

Fig.7.24 An aluminium cross slot reference FSS

Fig.7.25 Reflectivity measurement system

Fig.7.26 presents the simulated normal-incident free space reflectivity response (S11) and transmission response (S21) of the reference aluminum FSS. The metallic 10*10 cross slot FSS demonstrated a distinct band-pass frequency-filtering performance with an approximate 700MHz passing bandwidth (-3dB for S21) in simulation. Fig.7.27 shows the

comparison between the simulated and measured normal-incident free space reflectivity response (S11) of the reference aluminum FSS. From Fig.7.27, it can be seen that this cross slot FSS had a band-pass frequency-filtering property with a resonant frequency at 4.37GHz in both simulation and measurement. The band-pass characteristic shown in Fig.7.27 also agreed with the result I obtained from the equivalent circuit built for cross slot FSS in section 4.41. Moreover, the good agreement achieved between the measured and simulated S11 showed that the simulation can predict the FSS's performance and the arch measurement system was able to provide an accurate measurement.

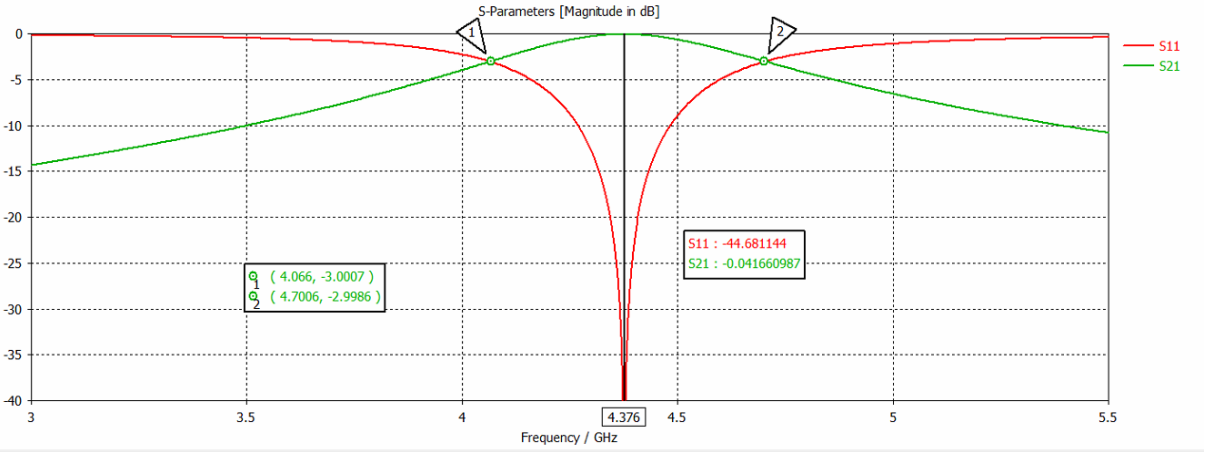

Fig. 7.26 Simulated S11 and S21of the metallic reference FSS

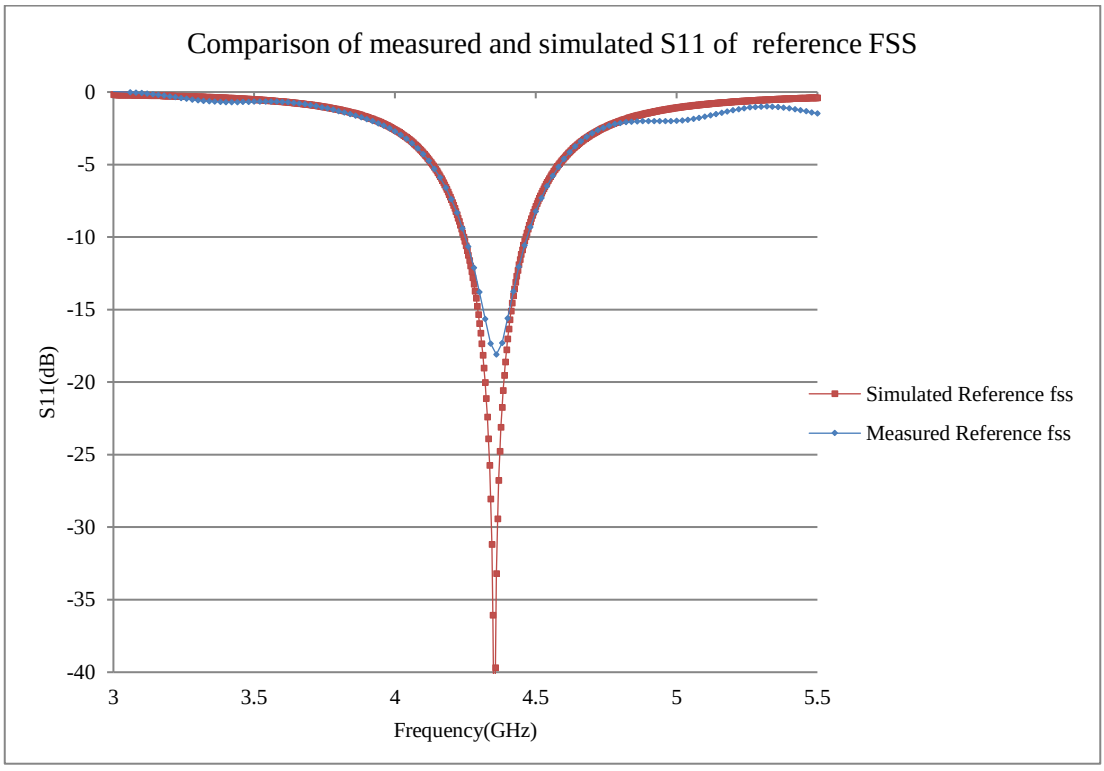

Fig.7.27 Simulated and measured S11 of the metallic reference FSS.

The knitted cross slot FSS was measured by the same procedure. The measured, reflectivity of the knitted cross dipole FSS was compared with the simulated results as shown in Fig.7.28. Two traces shown in Fig.7.28 corresponds to the knitted cross slot FSS responses illuminated by vertical (V) and horizontal (H) polarization, respectively. Fig.7.28 shows that the simulated and measured results did not agree with each other. The knitted cross slot FSS with vertical polarized illumination had a slightly higher resonant frequency (3.62GHz) than it was illuminated by the horizontal polarization (3.56GHz), and its simulated model had the highest resonant frequency (4.03GHz). The main reason for the disagreement between simulation and measurement was because for an "ideal" cross slot dipole FSS (such as the metallic reference and the simulated model), its response to both H and V polarization was identical. However, the knitted cross slot FSS had a different stitch structures in H and V directions due to the knitting technique. And the laser ablation resulted in serrated edges for the cross slots in both H and V directions as shown in Fig.7.29. From Fig.7.29, it can be seen clearly that the thread was burned by the high-temperature laser along the slots in both H and V directions. And the parallel laser cutting gave a better-defined edge to the slots than the perpendicular cutting. The parallel and perpendicular cut slots were referred to as "smooth" and "rough" slots, respectively in subsequent discussions. Consequently, the smooth and rough slots resulted in different resonant frequencies when the sample was illuminated vertically and horizontally as they had different effective slot circumference. Therefore, the unit cell shown in Fig.7.21 cannot predict the knitted cross slot FSS's performance correctly in simulation. In the following sections, I managed to build an equivalent simulated model for the knitted cross slot FSS with aid of CST.

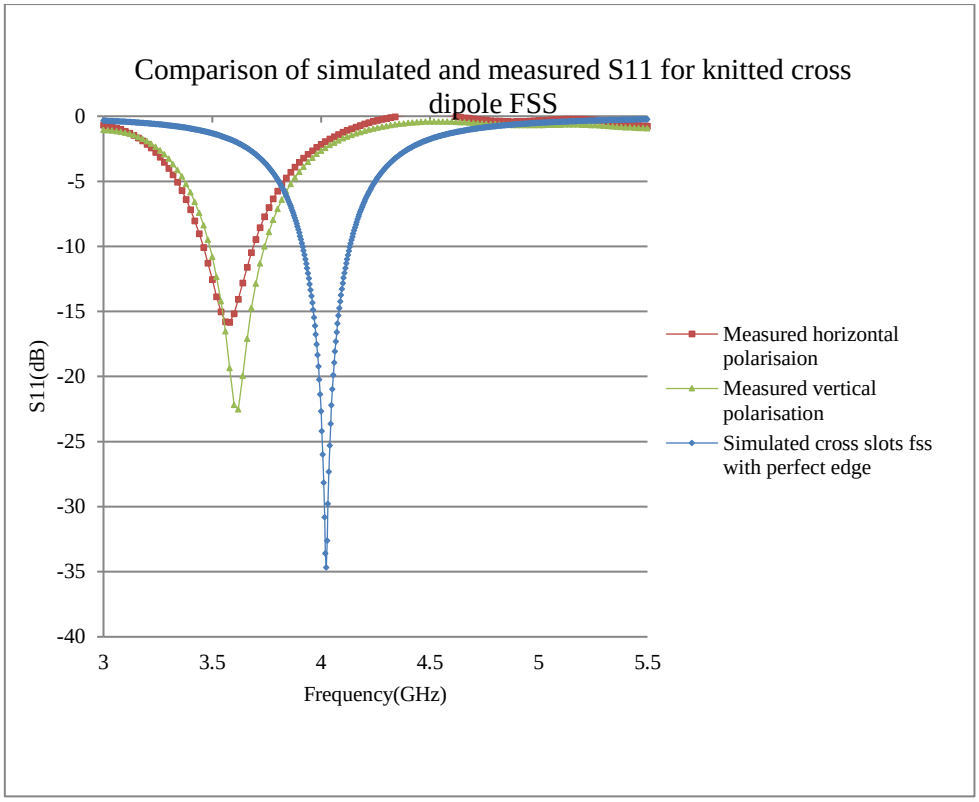

Fig.7.28 Comparison of simulated and measured S11s for the knitted cross slot FSS

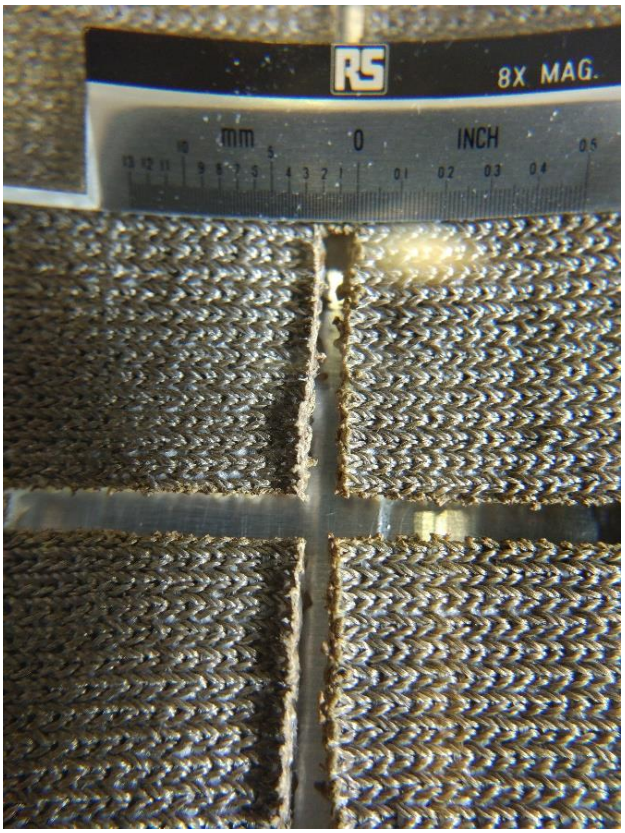

Fig.7.29 Photograph of a unit cell of the knitted cross slot FSS

7.3 Knitted Single Slot FSSs

To study the effects that the smooth and rough slots have on the knitted slotted FSS's performance, two more knitted samples with single slots were manufactured by the same knitting technique with the same textile materials: one with the slots cut parallel to the knitting direction and one with slots cut perpendicular to the knitting direction. Fig.7.31 presents the original model for a unit cell of the knitted single slot FSS in simulation. This original simulated model had perfect-defined slots. Fig.7.32 (a) and (b) show the knitted FSSs with smooth single slots and rough single slots. Fig.7.33 (a) and (b) present the photographs with high magnification. Two knitted single slot FSSs were measured by the same procedure. Fig.7.34 shows the measured reflectivity of the sample with smooth slots and the sample with smooth slots. The measured results were compared with the reflectivity of the original simulated model that had the perfect-defined slots in Fig.7.34. Fig.7.34 presents a similar result as Fig.7.27, the original simulated model with perfect-defined slots had the highest resonant frequency and knitted sample with smooth slots had a slightly higher resonant frequency than the knitted sample with rough slots. From Fig.7.34, it can be also seen that both smooth and rough slots had significant impacts on FSS's performance, and the rough slots reduced FSS's resonant frequency further than the smooth slots. Fig.7.33 shows that for the FSS with smooth slots, the laser cut the sample in parallel with the knitting direction. Therefore, only a small part on one side of the stitch was melted by the high-temperature laser. It resulted in small burnt spots along the smooth slots and increased the electrical length of the slots. While for the FSS with rough slots, laser cut the sample perpendicularly to the knitting direction. The threads were cut into half and melted at their ends. Consequently, numbers of large burnt spots were created along the rough slots and resulted in a longer electrical length than the smooth slots. This was the primary cause of resonant frequency differences between the ideal samples and two knitted samples.

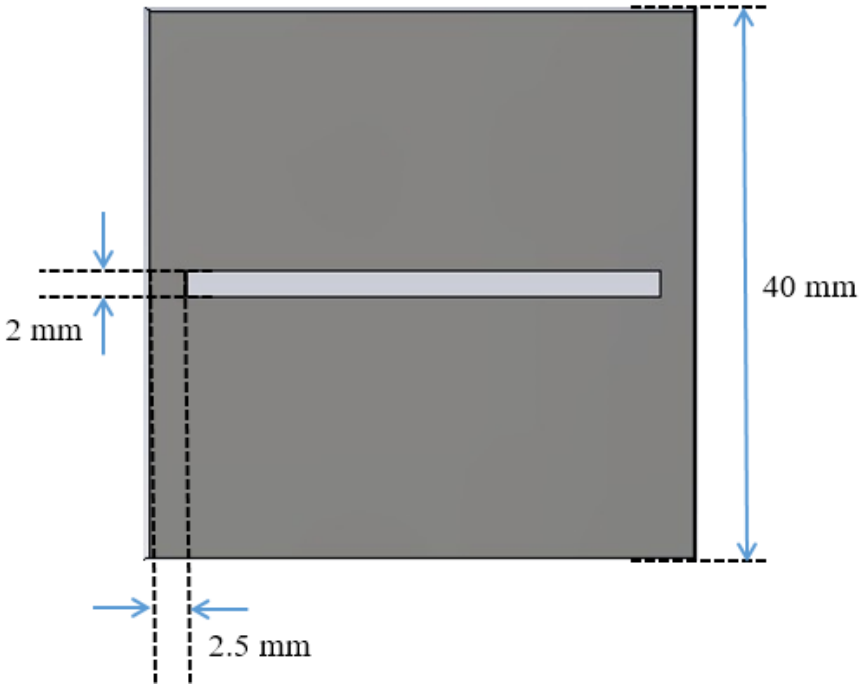

(a)

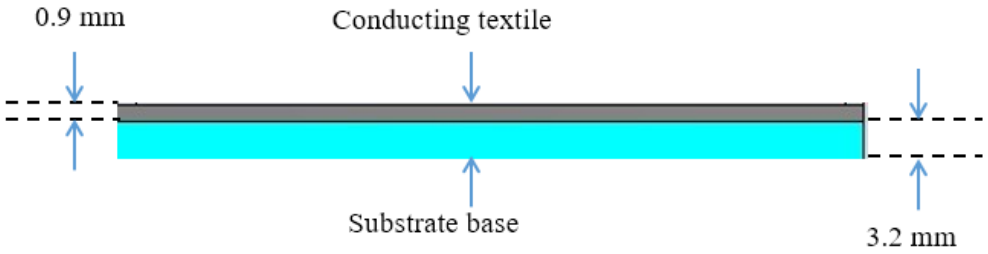

(b)

Fig.7.31 Original model for a unit cell of the knitted single slot FSS:
(a) Front view; (b) Side view

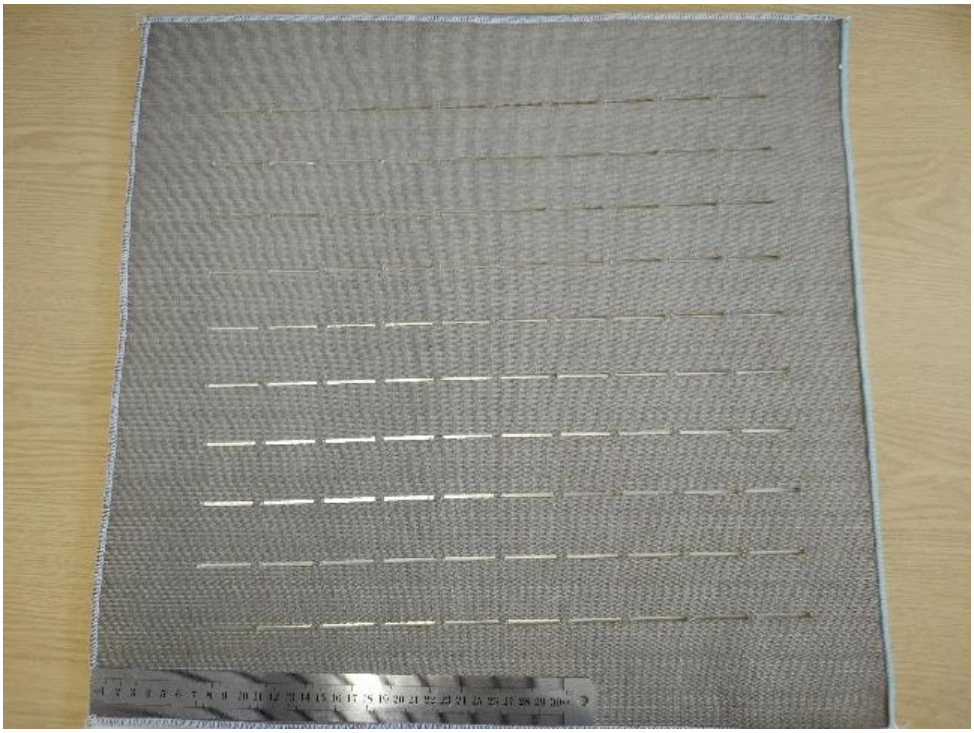

(a)

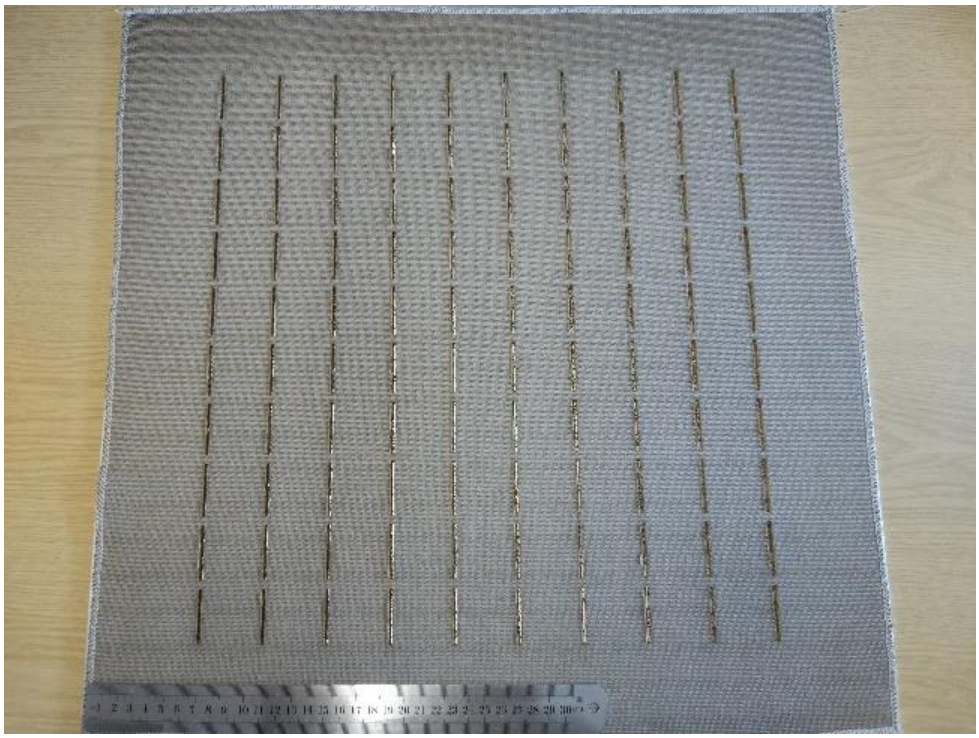

(b)

Fig.7.32 Photographs of knitted single dipole slots FSSs:
(a) Sample with smooth slots; (b) Sample with rough slots.

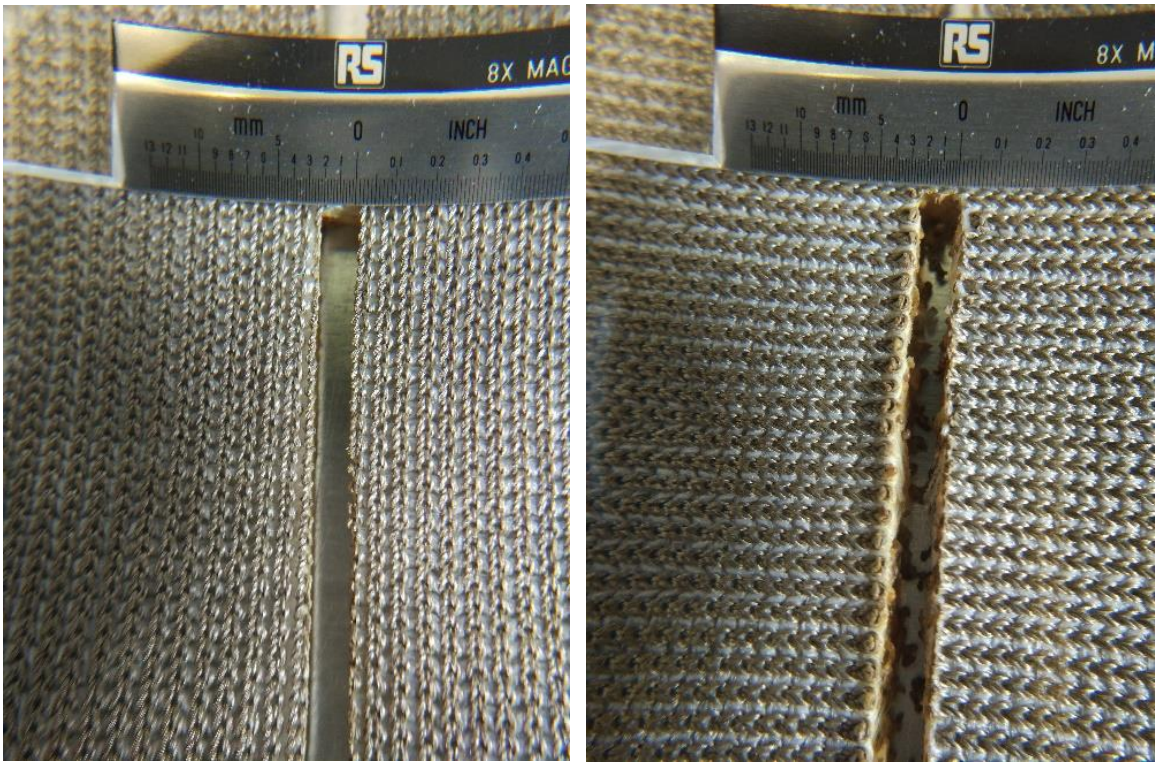

(a) (b)

Fig.7.33 High magnification photographs of knitted single slots FSSs.
(a) sample with smooth slots; (b) sample with rough slots.

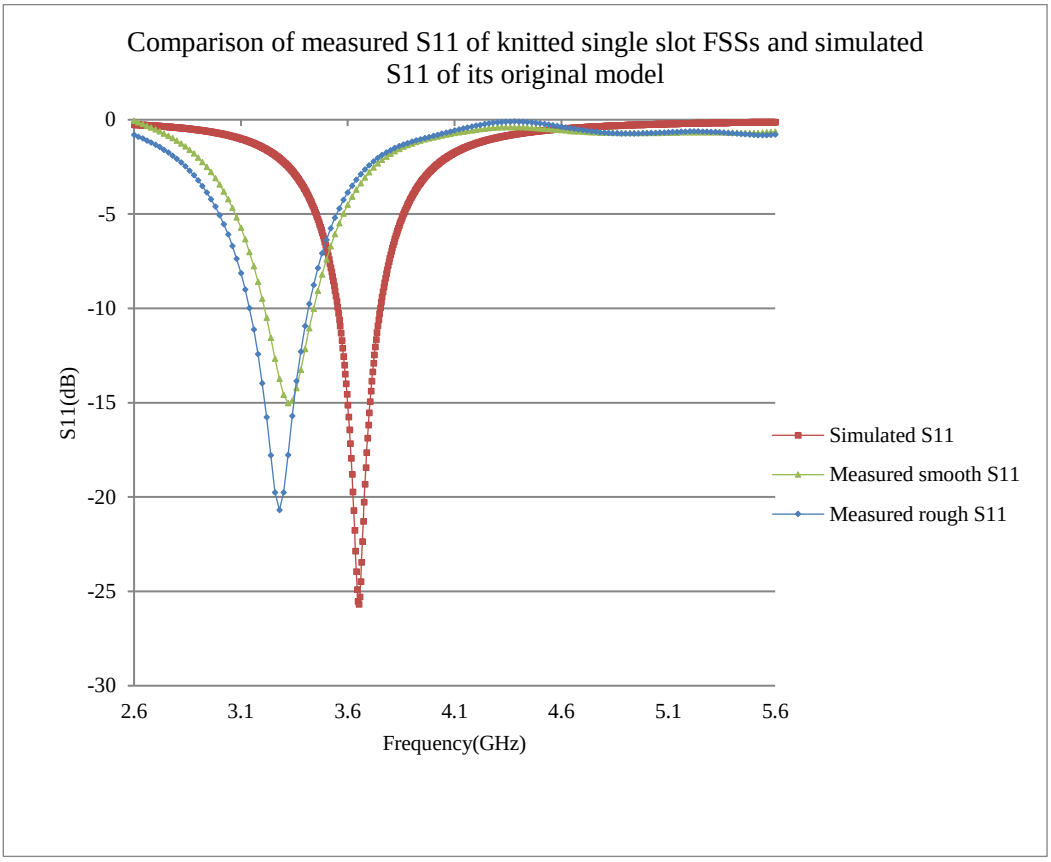

Fig.7.34 Measured S11s of two knitted single slot FSSs and simulated S11 of the original model

To build a simple geometrical model to simulate the knitted FSS with serrated slots effectively, it was assumed that the burnt spots created by the laser ablation followed a block profile and the smooth and rough slots can be modelled as a periodic structure with different block dimension as shown in Fig.7.35. According to careful measurement, the average block dimensions for each side of smooth and rough are approximated and listed in Table.7.31. However, the block width of the slots was difficult to measure. Therefore, with the aid of CST, the block width was optimized in simulation to provide a best match simulated results to the measurement. The optimization gave a block width of 0.3mm and 0.38mm for the smooth and rough slots respectively.

Table.7.31 block dimensions for smooth and rough slots in simulation

	block number	block gap (mm)	block length (mm)
smooth slot	18	0.5	1.5
rough slot	36	0.5	0.5

Fig.7.36 presents the comparison between the measured S11 of the knitted sample with smooth slots and its simulated model with a block width of 0.3mm. Fig.7.37 presents the comparison between the measured S11 of the knitted sample with rough slots and simulated S11 of its simulated model with a block width of 0.38mm. From Fig.7.36 and Fig.7.37, it can be seen that the measured results showed good agreements with the simulated results. Two knitted slot FSSs demonstrated a band-pass frequency response with co-polarized incident wave and reflected the cross-polarized incident wave. The predicted resonant frequencies for the knitted FSSs with single smooth slots and rough slots were 3.328GHz and 3.276GHz compared with the measured values of 3.32GHz and 3.28GHz, respectively. It showed that the periodic block model with optimized parameters built in simulation can predict the knitted single slot FSS's performance correctly. Fig.7.38 and Fig.7.39 shows the simulated normal-incident free space reflectivity response (S11) and transmission response (S21) of the knitted FSS with smooth slots and rough slots respectively. From Fig.7.38 and Fig.7.39, it can be seen that both knitted slot sample presented a band-pass frequency-filtering performance in simulation. They all had an approximate 400MHz passing bandwidth (-3dB for S21).

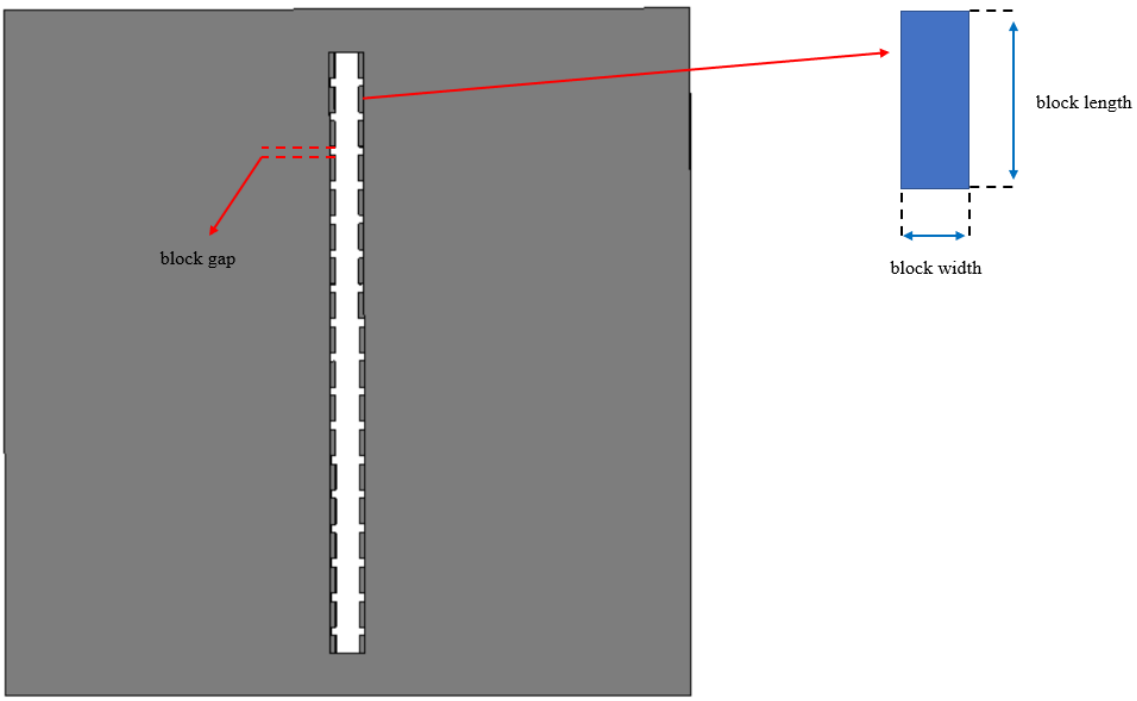

Fig.7.35 A periodic block model for a unit cell of the knitted FSSs with single serrated slots.

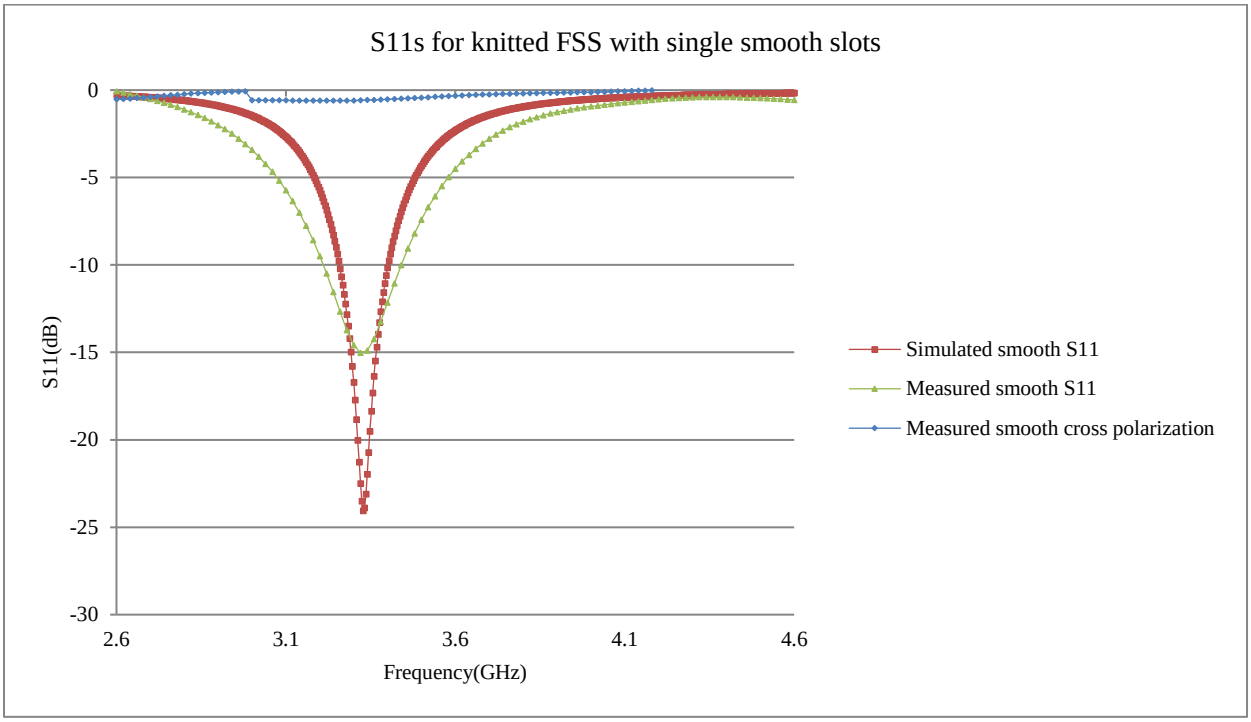

Fig.7.36 Comparison between the measured S11 of the knitted sample with smooth slots and its simulated model with a block width of 0.3mm.

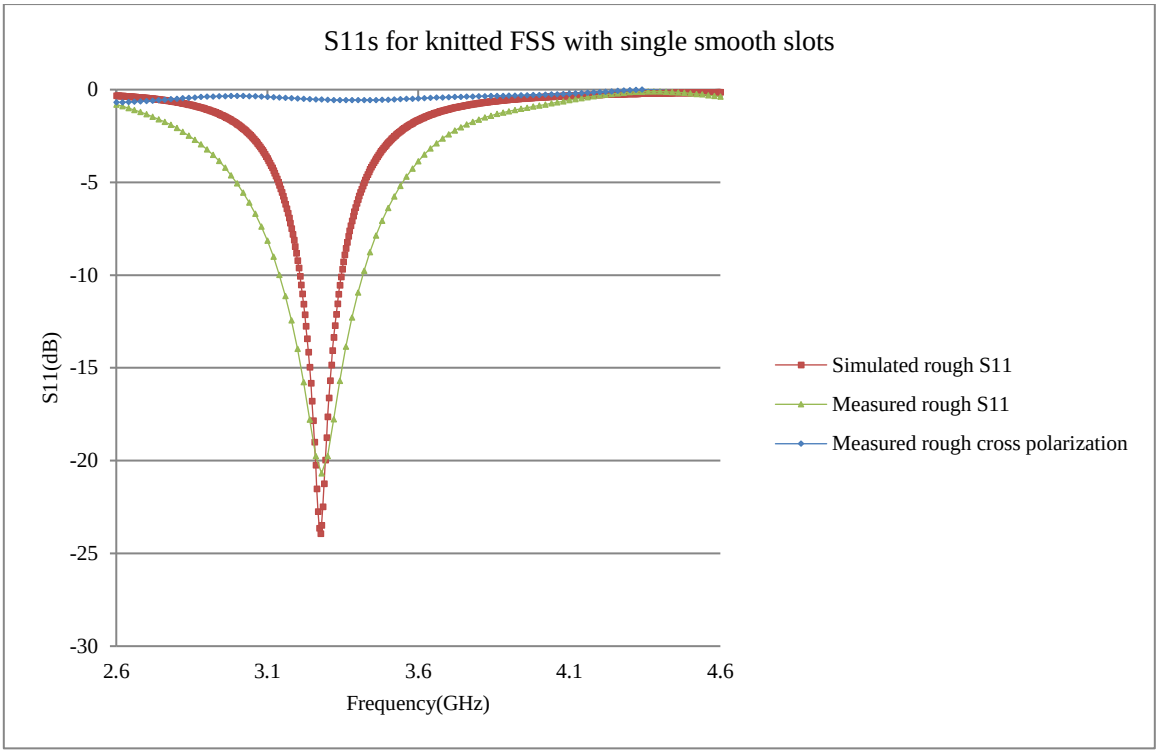

Fig.7.37 Comparison between the measured S11 of the knitted sample with rough slots and its simulated model with a block width of 0.38mm

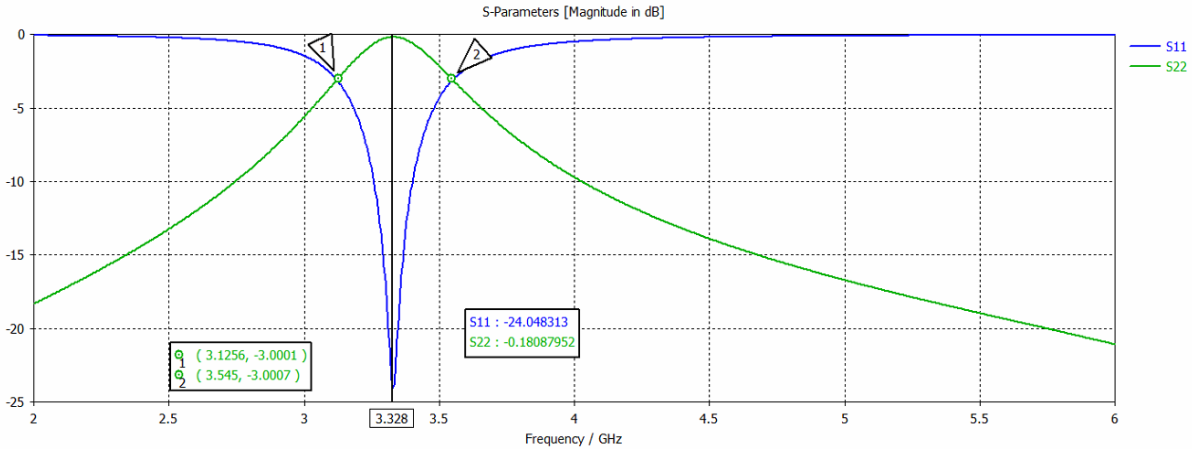

Fig.7.38 Simulated normal-incident free space reflectivity response (S11) and transmission response (S21) of knitted FSS with smooth slots

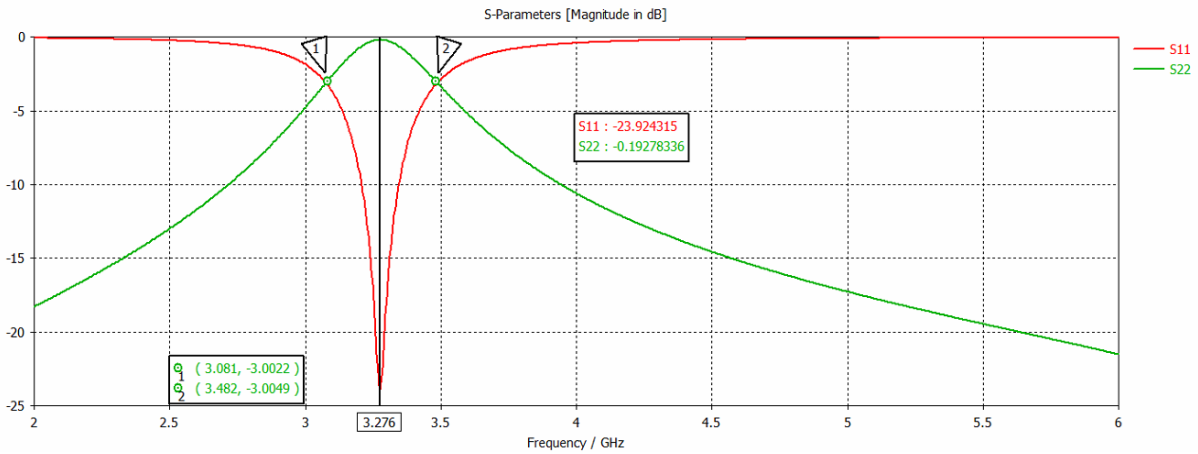

Fig.7.39 Simulated normal-incident free space reflectivity response (S11) and transmission response (S21) of knitted FSS with rough slots

7.4 Optimized Model for Knitted Cross Slot FSS

Based on the model established for the serrated slots, an attempt was made to simulate the knitted cross slot FSS with the block dimensions obtained in section 7.3. Fig.7.41 presents a unit cell of the original periodic block model for the knitted cross slot FSS. For the smooth slots, there were 16 blocks with a gap of 0.5mm, length of 1.5mm and width of 0.3mm at each side. For the rough slots, there were 32 blocks with a gap of 0.5mm, length of 0.5mm and width of 0.38mm at each side. Fig.7.42 shows the comparison between the measured S11 of the knitted cross slot FSS and the simulated S11 of its original simulation model. From Fig.7.42, it can be seen that the resonant frequencies of the original simulated model were slightly higher than that of the knitted sample in both vertical and horizontal directions. It showed that the parameters obtained from the single dipole slot FSSs were not directly transferable as the knitted cross slot FSS had a thinner substrate base than the knitted single slot FSS. Parameter optimization for block width was made to establish the correct simulated model for knitted cross slot FSS.

Table.7.41 presents the block dimensions for the optimized model of the knitted cross slot FSS in simulation. The block depths were optimized to 0.34mm and 0.43mm for the smooth slots and rough slots, respectively. Fig.7.43 shows the comparison of normal incident reflectivity between the knitted cross slot FSS and its optimized simulated model. From Fig.7.43, it can be seen that the simulated S11 of the optimized simulated model achieved a good agreement with the measured S11 of the knitted cross slot FSS for both vertical and horizontal polarizations. The predicted resonant frequencies for the knitted sample were 3.62GHz and 3.564GHz compared to the measured values of 3.62GHz and 3.58GHz. Fig.7.44 shows the simulated normal-incident free space reflectivity response (S11) and transmission response (S21) of the knitted cross slots FSS. It can be seen that the knitted cross slot FSS showed a band-pass frequency-selecting performance for both H and V illumination with an approximate 400 MHz passing bandwidth (-3dB for S21).

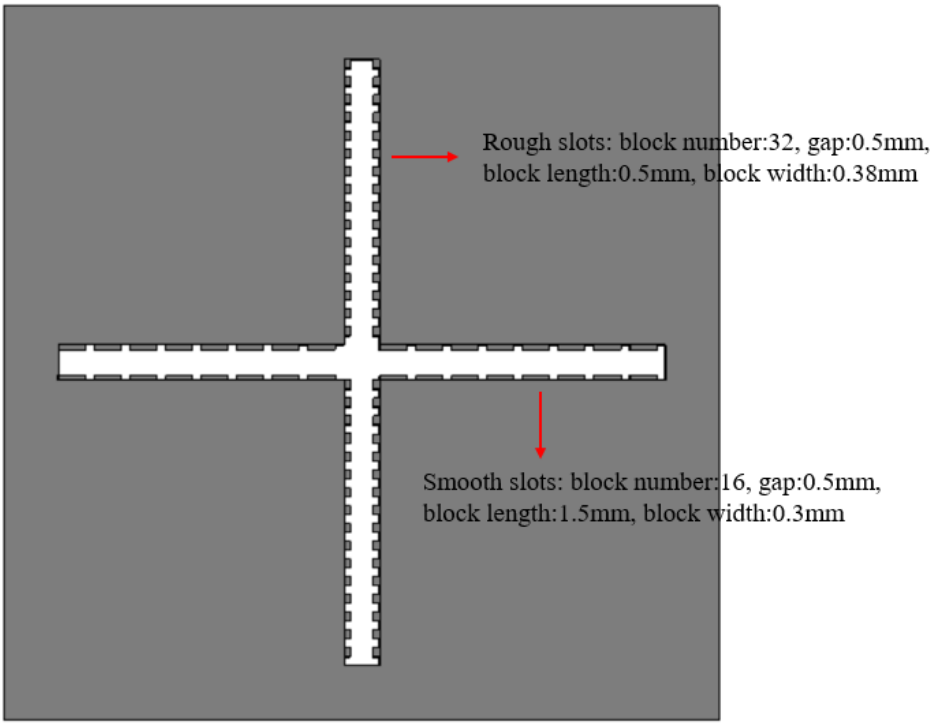

Fig.7.41 A unit cell of the original periodic block model for the knitted cross slot FSS

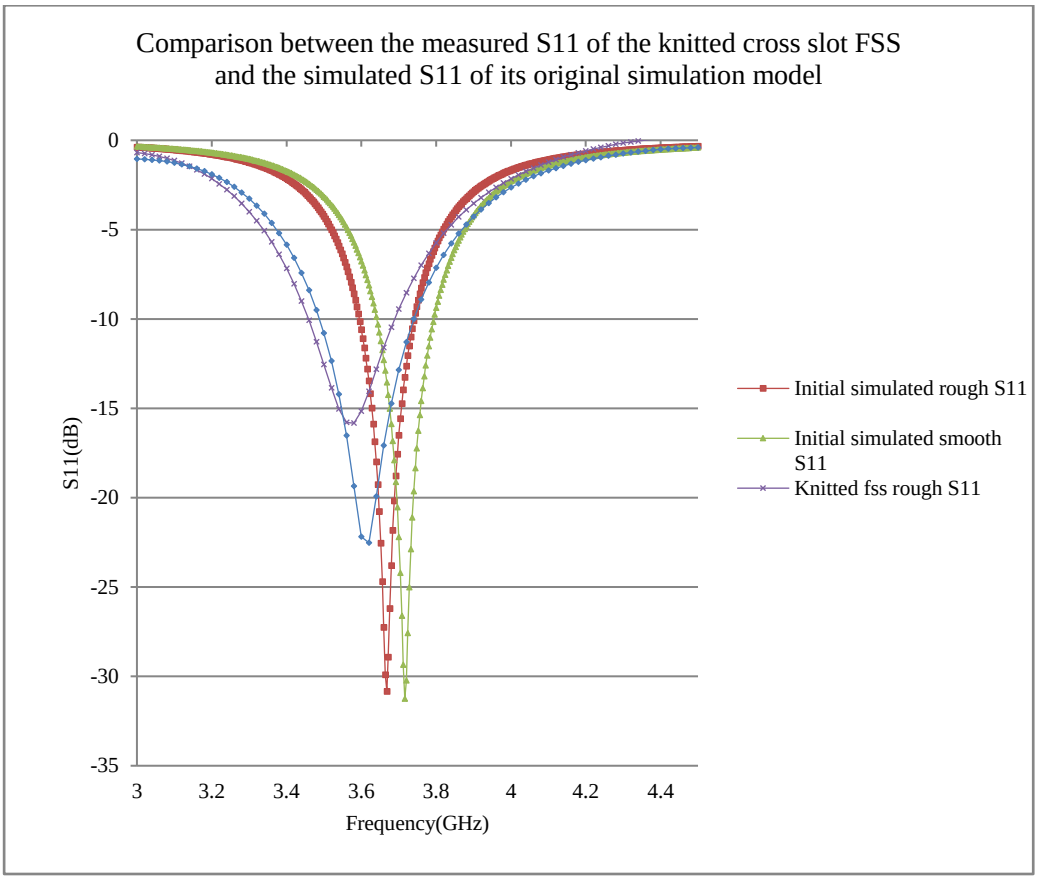

Fig.7.42 Comparison between the measured S11 of the knitted cross slot FSS and the simulated S11 of its original simulation model

Table.7.41 Optimized block dimensions for slots of cross slot FSS in simulation

	block number	block gap (mm)	block length (mm)	block width (mm)
smooth slot	16	0.5	1.5	0.34
rough slot	32	0.5	0.5	0.43

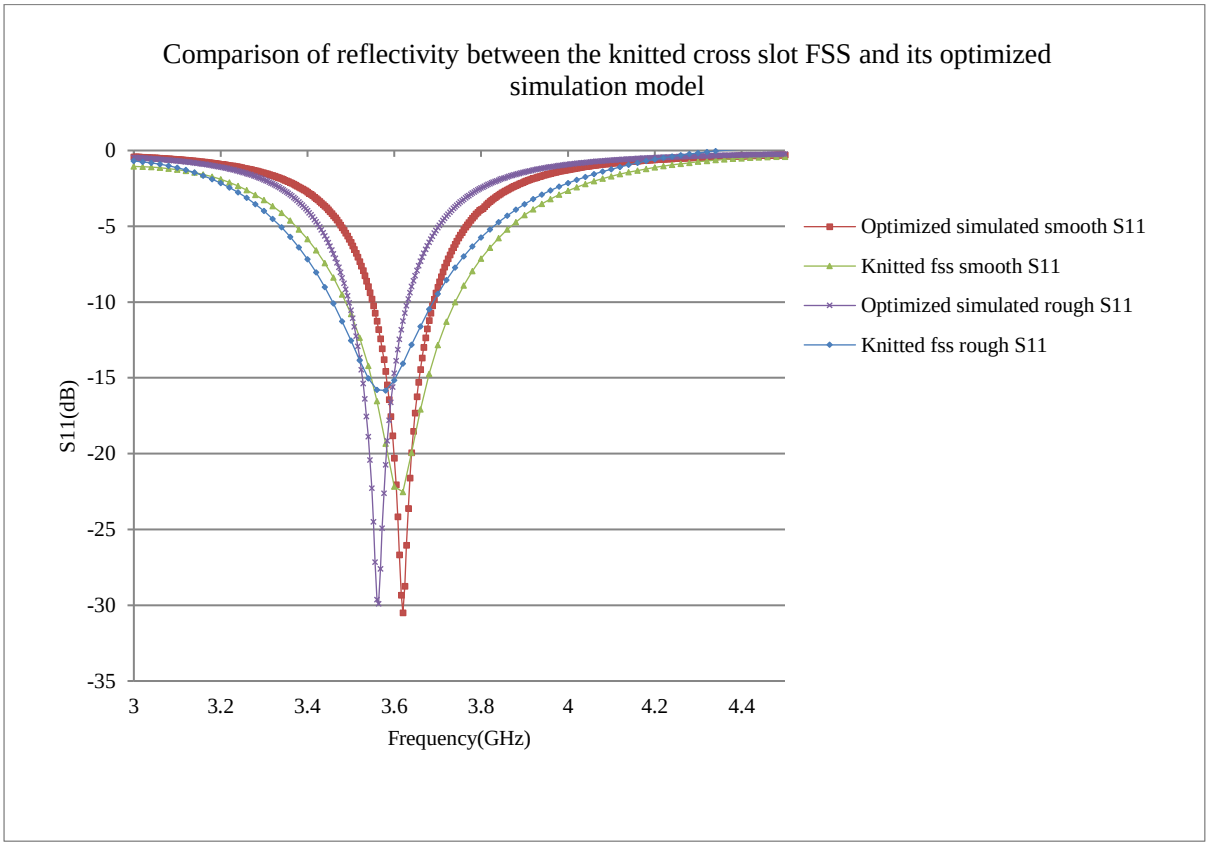

Fig.7.43 Comparison of reflectivity between the knitted cross slot FSS and its optimized simulation model

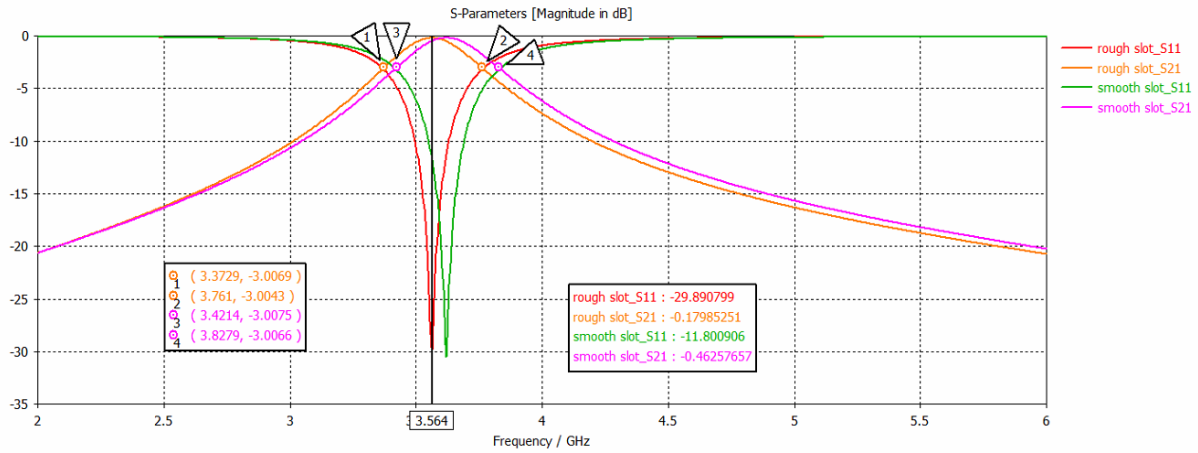

Fig.7.44 Simulated normal-incident free space reflectivity response (S11) and transmission response (S21) of knitted cross slots FSS

To conclude, the effects that the serrated slots had on knitted cross slot FSS's performance were studied and a simple simulation model was established successfully to predict the knitted slot FSSs' performance.

7.5 Ultra-light Weight, Knitted Loop FSSs

In the previous sections, computerised knitting with laser ablation technique has realized the fast manufacture of large area textile slot FSSs. The computerized knitting technique itself can also permit the fast creation of textile FSSs with complex periodic surface patterns. Four experimental textiles hexagonal loop FSSs were knitted and presented in this section. During the knitting process, only a single layer structure was created, which made these textile FSSs ultra-light weight. The conducting unit cells were created with a silver loaded nylon yarn (shieldex110f 24 dtex z turns) and the substrate base which separated the ECA (electrically conducting area) was knitted by an ultra-light weight non-conducting yarn (monofilament 1/75nm 75%polyester 25% nylon). Fig.7.51 shows the photographs of four knitted samples. It can be seen that they shared a similar periodic structure, just with different unit cell dimensions. Fig.7.52 shows the hexagonal loops of each sample. I numbered four samples based on their hexagonal loop sizes, from small to large as shown in Fig.7.51 and Table.7.51. The weights of each sample were also measured and shown in Table.7.52. Fig.7.53 presents the weight measurement for sample 1 as an example. All the knitted loop FSSs were ultra-light, each sample had an approximate size of 300mm by 200mm only with a total weight (including border) around 9g as shown in Table.7.52.

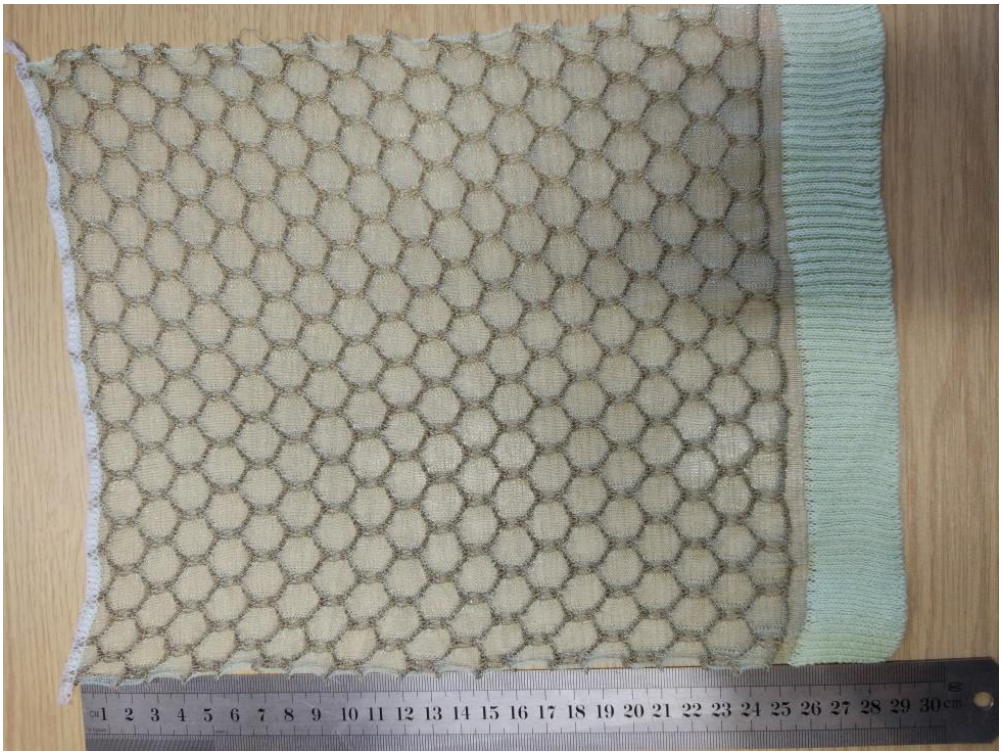

(a) Sample 1

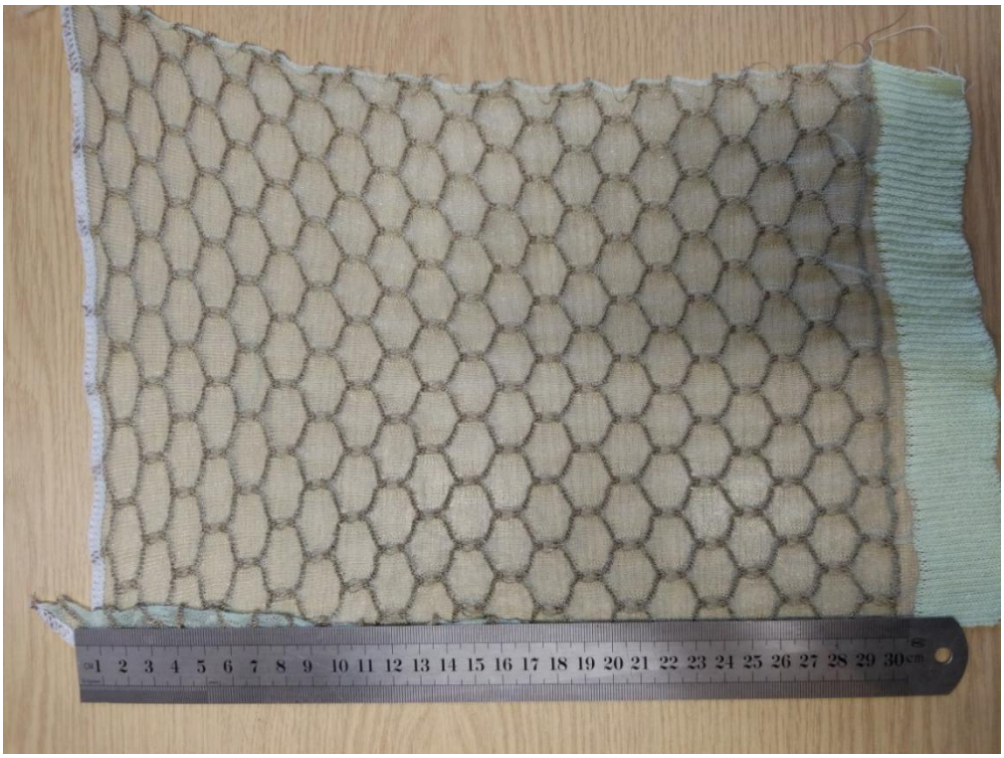

(b) Sample 2

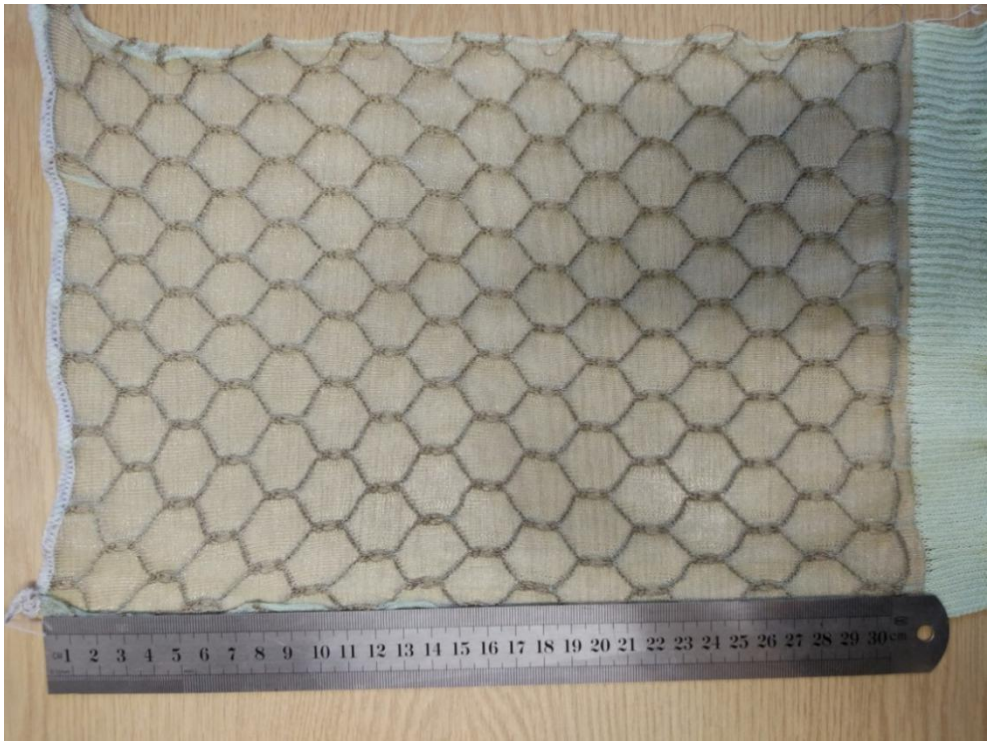

(c) Sample 3

(d) Sample 4

Fig.7.51 Four ultra-light weight knitted loop FSSs:

(a) Sample 1; (b) Sample 2; (c) Sample 3; (d) Sample 4

Table.7.51 Dimensions of hexagonal loops of four knitted samples

Sample 1	Sample 2	Sample 3	Sample 4
7mm*10mm	8mm*12mm	10mm*15mm	10mm*20mm

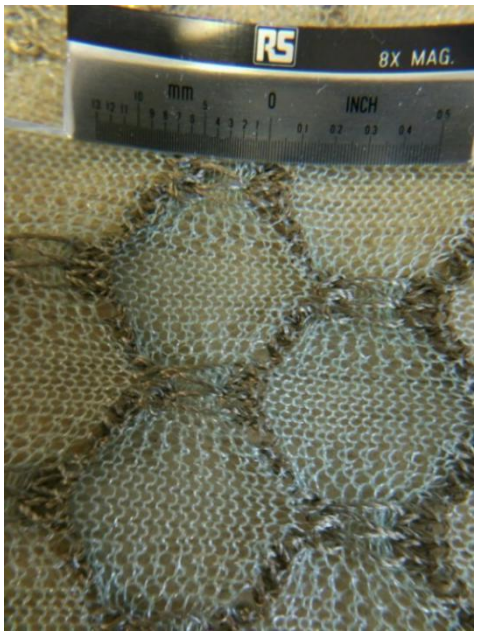

(a) Sample 1

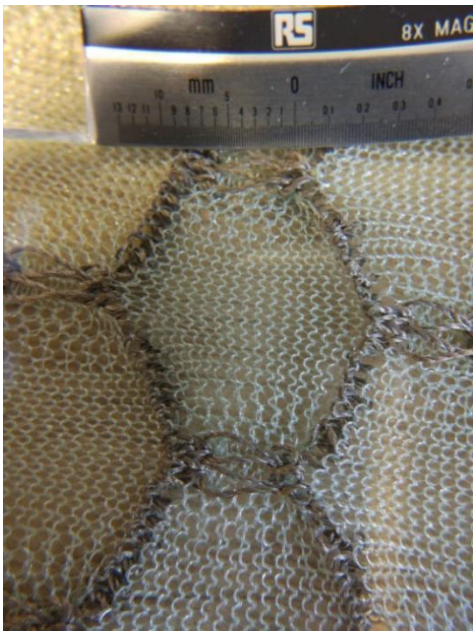

(b) Sample 2

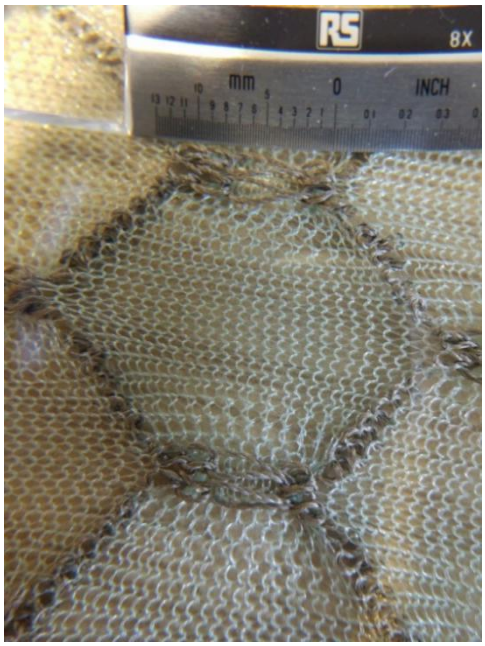

(c) Sample 3

(d) Sample 4

Fig.7.52 Magnified photographs for the hexagonal loop of four samples:

(a) Sample 1; (b) Sample 2; (c) Sample 3; (d) Sample 4

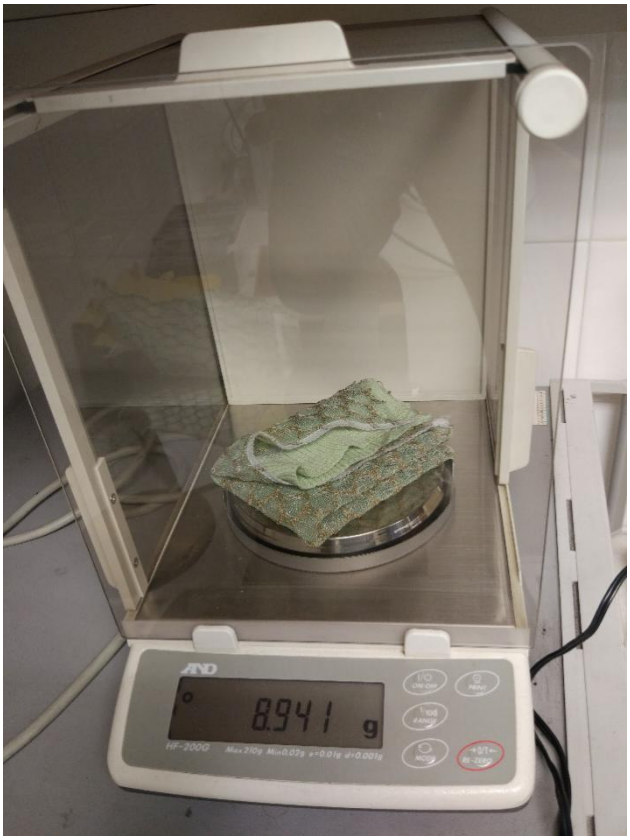

Fig.7.53 Weight measurement for sample 1

Table.7.52 Weights of four textile samples

Sample 1	Sample 2	Sample 3	Sample 4
8.941g	9.574g	9.101g	8.4g

According to the careful measurement, four textiles hexagonal loop FSSs were simulated in CST. Fig.7.54 presents a simulated unit cell for sample 1 as an example. In simulation, the permittivity of the substrate base was assumed as 1, which was the same as air and the conductivity of ECA was initially set as 4000 S/m. The simulated normal incident, free space reflectivity (S11) and transmission responses (S21) of four samples illuminated by vertical polarization are shown in Fig.7.55. Fig.7.55 shows that the four textile hexagonal loop FSSs all exhibited a good transmission with a rejection band in simulation. At certain frequencies, the S11 of four samples approached to 0 and S21 dropped below -10dB, which proved that the textile loop FSSs acted as band-stop filters when illuminated by vertical polarization. Fig.7.56 shows the comparison of simulated S11s of four samples. From Fig.7.56, it can be seen that the four simulated FSSs had multiple resonances. To analysis them, only the first resonant frequency of four samples was considered. In simulation, sample 1 with the smallest hexagonal loop size had the highest response frequency and vice versa. The simulated result of the hexagonal loop FSSs agreed with the theoretical result obtained from the equivalent circuit built in section 4.42.

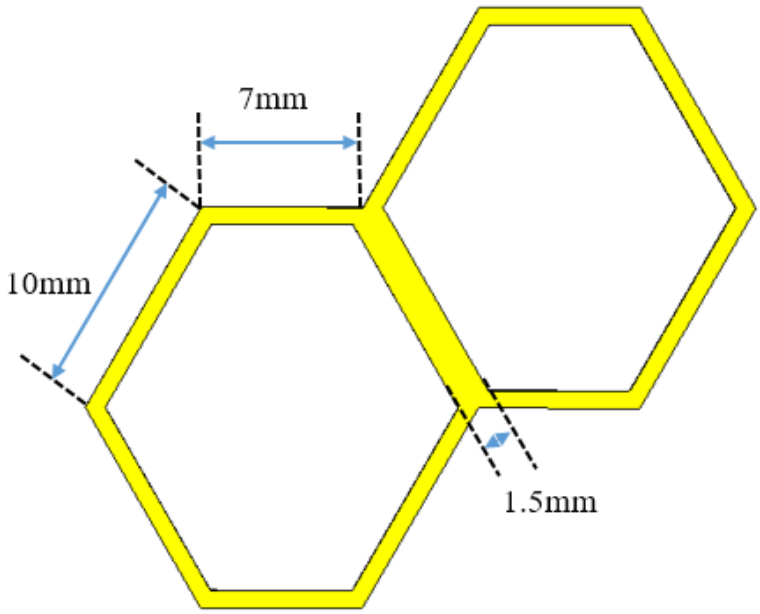

Fig.7.54 a unit cell of sample 1 in simulation

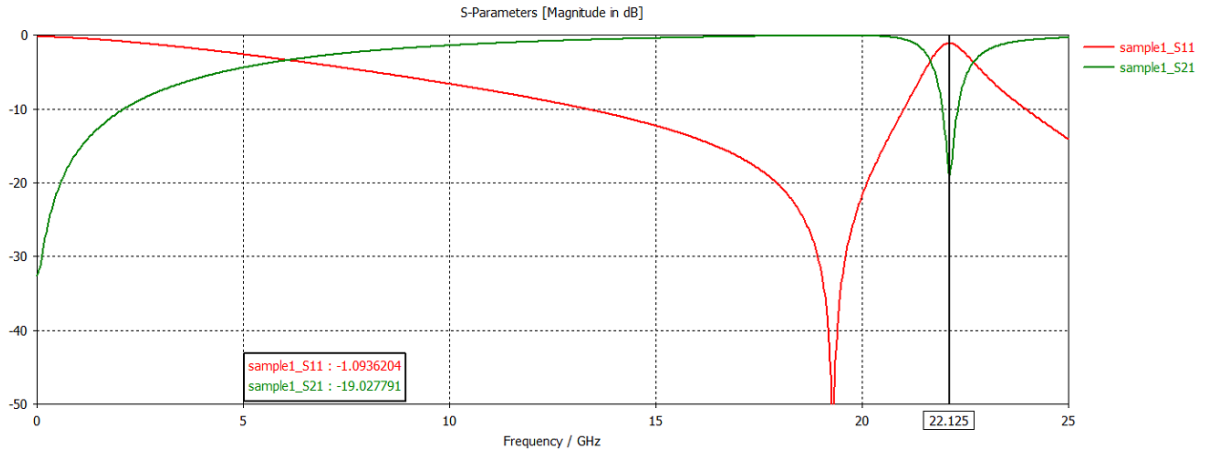
S-Parameters [Magnitude in dB]
sample1_S11
sample1_S21
sample1_S11 : -1.0936204
sample1_S21 : -19.027791
22.125
Frequency / GHz

(a)

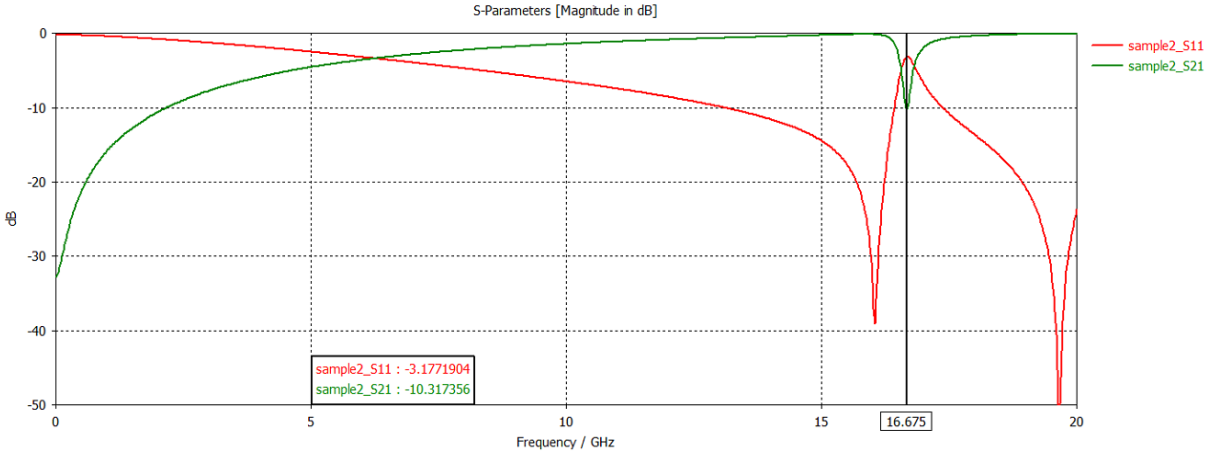
S-Parameters [Magnitude in dB]
sample2_S11
sample2_S21
sample2_S11 : -3.1771904
sample2_S21 : -10.317356
16.675
dB
Frequency / GHz

(b)

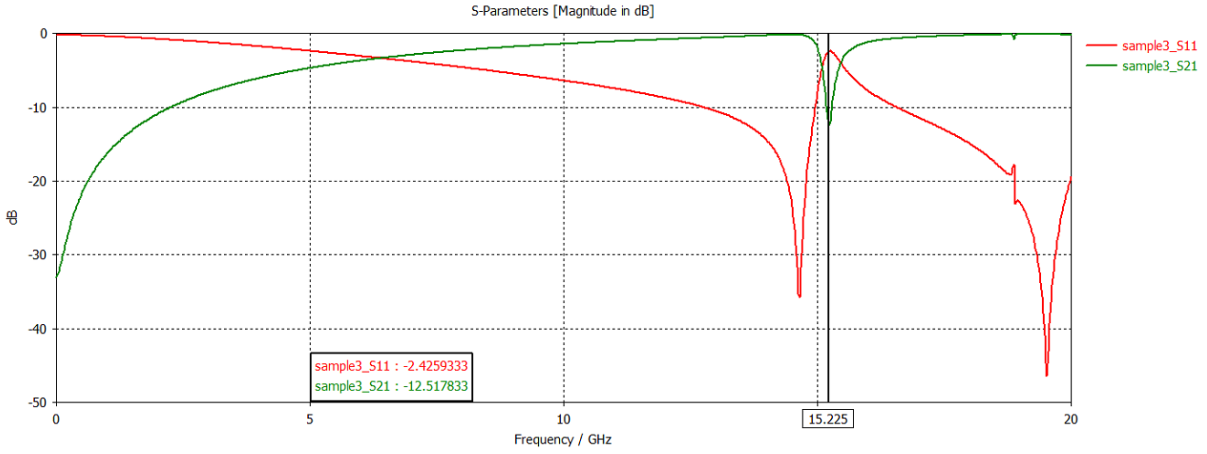
S-Parameters [Magnitude in dB]
sample3_S11
sample3_S21
sample3_S11 : -2.4259333
sample3_S21 : -12.517833
15.225
dB
Frequency / GHz

(c)

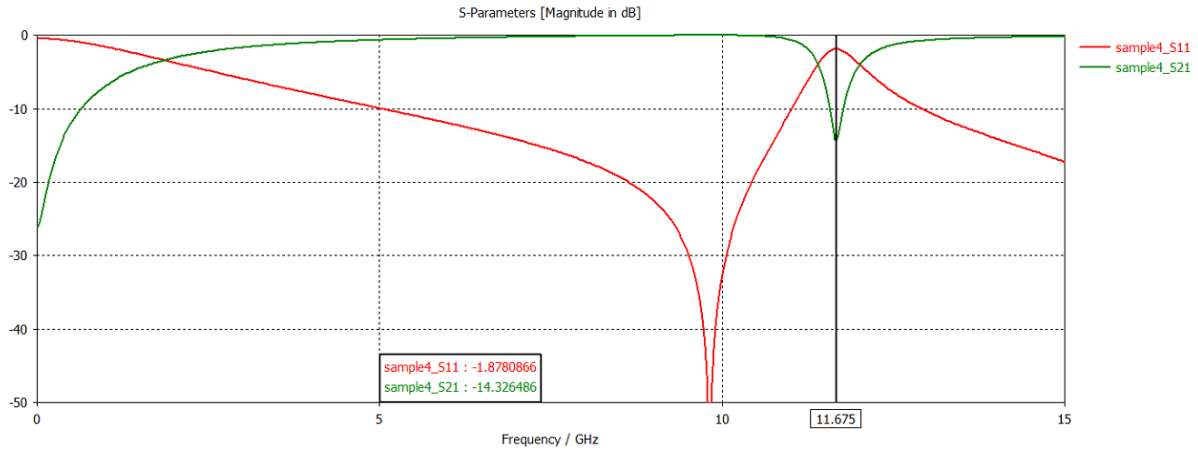

(d)

Fig.7.55 Simulated S11 and S21 of four samples illuminated by vertical polarization with conductivity of 4000 S/m : (a) sample 1; (b) sample 2; (c) sample 3; (d) sample 4

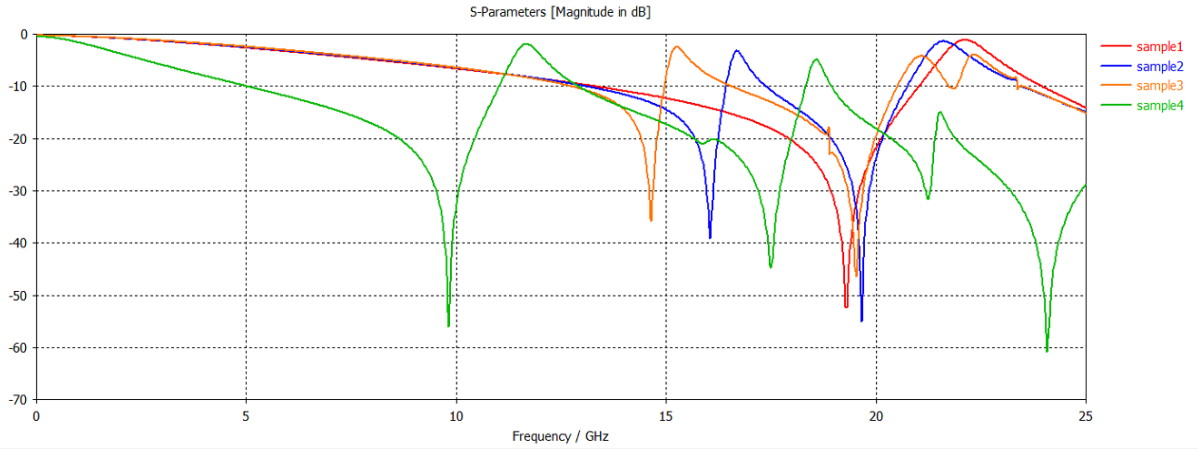

Fig.7.56 Simulated S11s of four samples illuminated by vertical polarization with conductivity of 4000 S/m

The knitted loop FSSs were inherently flexible structures, but to characterize them they were arranged and measured as flat planar surfaces. To facilitate the measurement, all the samples were gently stretched in both linear dimensions to equalize any shape distortion and to produce a flat surface with a symmetrical surface pattern. Their normal incident, free space vertical polarized reflectivity (S11) and transmission response (S21) were measured and the measured results are shown in Fig.7.57 and Fig.7.58. From Fig.7.57 and Fig.7.58, it can be seen that all four knitted loop FSSs exhibited a high-pass frequency response in measurement instead of a band-stop characteristic in simulation. Fig.7.57 also shows that

four textile samples demonstrated a frequency selective characteristic which presented the same trend as the simulated results. Textile sample 1 with the smallest hexagonal loop size had the highest response frequency. And textile sample 4 with the largest hexagonal loop size had the lowest response frequency. However, the measured responses of the textile samples did not present multiple resonances. From Fig.7.56, it can be seen that in simulation, multiple resonances and the first frequency-rejecting band of hexagonal loop FSSs appeared at high frequency (above 10GHz). While in measurement, textile samples only presented a good transmission performance with single resonance at high frequency as shown in Fig.7.57 and Fig.7.58.

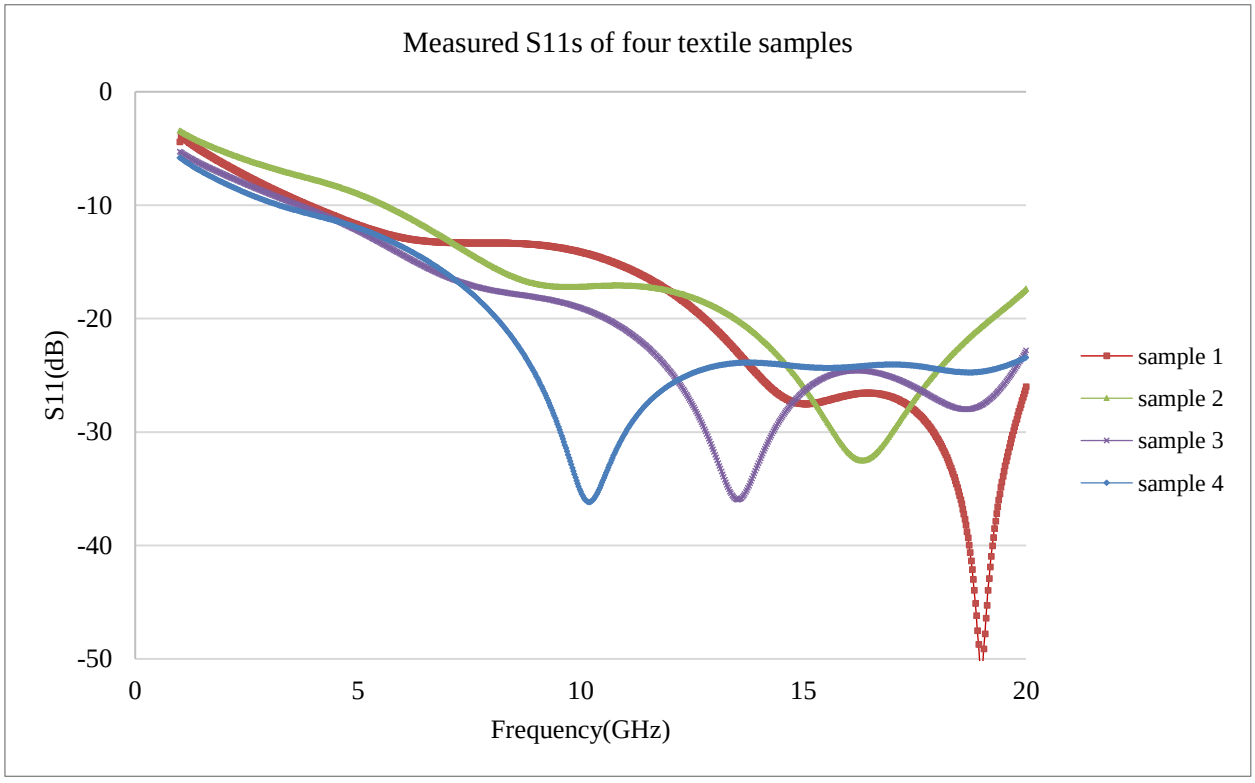

Fig.7.57 Measured S11s of the four knitted ultra-light weight hexagonal loop FSSs illuminated by vertical polarization

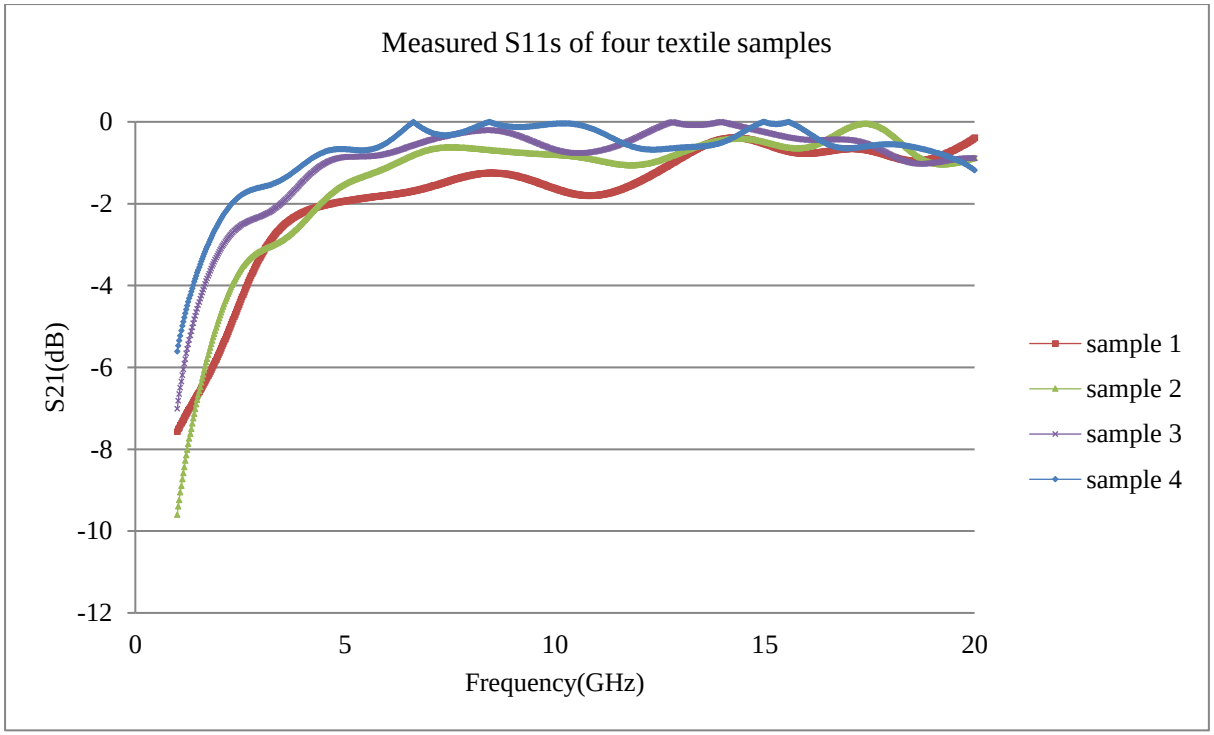

Fig.7.58 Measured S21s of the four knitted ultra-light weight hexagonal loop FSSs illuminated by vertical polarization

The difference between simulated and measured results was due to the fact that, in simulation the hexagonal loop FSSs were constructed by continuous conducting solids with a constant conductivity. However, in practice, all the ECA on textile loop FSSs was knitted by a conducting yarn. From Fig.7.52, it can be seen that there were air gaps between adjacent conducting stitches. When frequency increased, air gaps became more significant and the textile loop FSSs turned into an inhomogeneous structure which consisted of conducting stitches and air gaps. Precise calculation of the ECA's conductivity on textile samples was very difficult. But according to effective medium theory [127], its effective value can be approximated by Bruggeman's unsymmetrical effective medium model [128]. Based on Bruggeman's model, the effective conductivity of ECA of textile loop FSSs can be calculated from equation (64):

$$\sigma_e = (1-\alpha)^{\frac{3}{2}}\sigma_o \quad \ldots\ldots\ldots\ldots\ldots\ldots (64)$$

Where σ_e is the effective conductivity of ECA, α is the fraction of air gaps in ECA and σ_o is the original conductivity of ECA.

In this case, the original conductivity σ_o of ECA was assumed to be 4000 S/m and the fraction of air gap α increased when frequency became higher. The relation between the effective conductivity σ_e and the air gap fraction α is described in Fig.7.59. It can be seen that the effective ECA's conductivity on the textile loop FSSs dropped quickly when the air gap fraction increased.

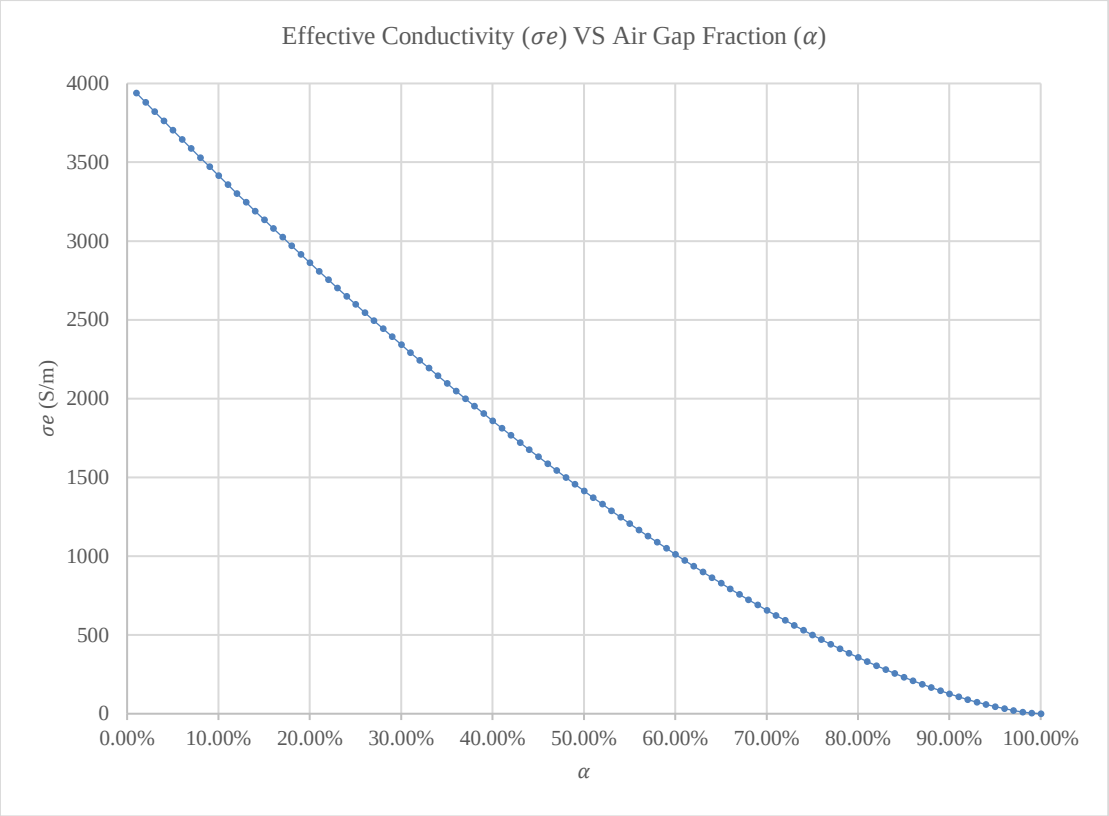

Fig.7.59 Effective conductivity of ECA against air gap fraction

To study the effects of low ECA conductivity on knitted FSS's performance, Sample 4 was selected as an example. Sample 4 was simulated with different ECA conductivities from 4000s/m to 15s/m and the results were compared in Fig.7.57. Fig.7.57 indicates that FSS's selectivity increased with a higher conductivity. When the ECA's conductivity dropped to a very low value, for example 15s/m in this case, sample 4 almost stopped function. Similar statement was also reported in [126].

To conclude, when frequency increased, air gap between conducting stitches became more significant and ECA's effective conductivity dropped. At high frequency, the ECA's conductivity was too low to cause the rejection or multiple resonances of a knitted FSS in practise. This was the primary reason why the textile samples demonstrated a different

performance at high frequency in measurement compared to simulation with a constant ECA conductivity of 4000s/m.

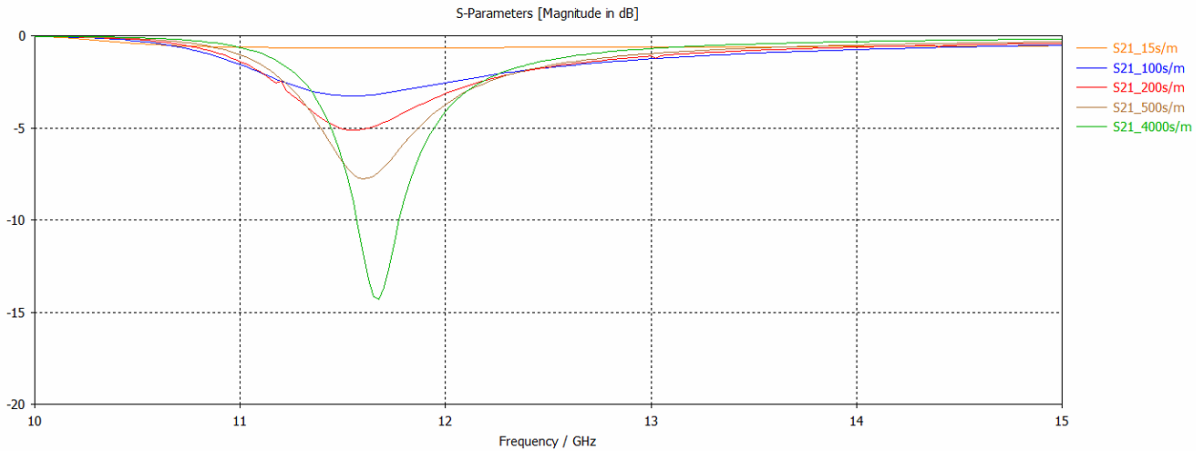

Fig. 7.60 Comparison of simulated S21 of sample 4 with different ECA conductivity

7.6 Conclusion

Chapter 7 began with the presentation of a knitted textile FSS with a 10 by 10 cross slot grid. The textile FSS was knitted by the same knitting technique described in the previous chapters and demonstrated a typical slot FSS performance. It had a band-pass frequency response, and the resonant frequency was 3.62GHz and 3.58GHz for vertical and horizontal polarization, respectively. Laser ablation, which is a fast efficient and economical technique, was successfully applied to create slot FSSs from knitted textile blankets. During the laser ablation, serrated cutting edges were produced on the textiles in both vertical and horizontal directions. And the "roughness" of the serrated edge depended on the orientation of the stitch structure relative to the cutting direction of the laser. The parallel cut resulted in smooth slots and perpendicular cut resulted in rough slots, respectively. The serrated slots on the knitted samples acted to reduce the FSSs' resonance frequency significantly and rough slots had a bigger effect than smooth slots. A periodic block model was established to describe the performance of knitted slot FSSs correctly in simulation. The optimized dimensions for the smooth and rough slots were presented respectively.

In this chapter, I also introduced four experimental ultra-light weight FSSs with hexagonal loops. These knitted loop FSSs showed a high-pass response with a frequency selective characteristic. The resonant frequency of the knitted loop FSS was determined by the size of hexagonal loop. The sample with the smallest unit cell size had the highest response frequency and vice versa. According to the equivalent circuit I built, a loop FSS was expected to have a band-stop frequency response, however the knitted loop FSSs presented a high-pass response in measurement. The difference between simulation and measurement was caused by the fact that the knitting density of the ECA on textile loop FSS was not high enough. When frequency increased, the air gaps between stitches became more significant, which resulted in a lower effective conductivity of ECA. Consequently, the textile loop FSS was not able to demonstrate rejection at high frequency. This is an on-going project and I are still developing an equivalent model based on Bruggeman's approximation to predict the knitted textile hexagonal loop FSS's performance accurately in simulation.

Chapter 8. Conclusion and Future Work

8.1 Conclusion

This research focused on the investigation of textile electromagnetic structures manufactured by a computerized knitting technique. A commercial flat-bed knitting machine was employed to fabricate various types of textile RF device including waveguides, slotted waveguide antennas and frequency selective surfaces. These textile electronics were studied based on simulation and measurement.

1. In this contribution, I firstly proposed an original 3D knitted textile waveguide [109]. I also studied performance of knitted waveguides under different shape distortion conditions, both in simulation and measurement [110]. The knitted textile waveguide demonstrated a stable transmission performance at X-band under E and H plane bending.
2. In this thesis, I also presented a 3D knitted textile slotted waveguide antenna (SWA) [123] developed from the knitted waveguide in [109]. It provided a directional radiation pattern with a maximum gain of 2.33dB at 9.2GHz in measurement. Special attention was required when using this knitted SWA in practice as transmitter or receiver because it was a soft structure and bending could cause poor or cross polarized transmission.
3. I extended our research interests to textile frequency selective surfaces (FSS). Various types of textile FSS were investigated including cross slot and hexagonal loop. Laser ablation which is a fast and efficient technique was applied to create the periodic cross slot patterns. During the laser ablation, serrated cutting edges were created on the textiles in both vertical and horizontal directions. A simple and effective model was developed in simulation to describe the performance of textile cross slot FSSs. The textile cross slot FSS was sensitive to illuminating polarization as the laser cutting process resulted in different effective slot lengths in different directions. Measurement showed that the knitted textile FSS with a 10 by 10 cross slot grid demonstrated a band-pass frequency response, and the resonant frequency was 3.62GHz and 3.58GHz for vertical and horizontal illumination respectively.
4. Lastly, I also reported four experimental hexagonal loop FSSs. They were knitted in a single layer structure to have an ultra-light weight (about 150g/m^2). Measurement

showed that these ultra-light weight knitted FSSs all exhibited a high-pass response with a frequency selective property. This is an ongoing project and I are attempting to develop an effective simulation model to predict the knitted textile hexagonal loop FSS's performance accurately.

8.2 Future Work

In this research, computerized knitting has been tested to be an effective alternative to the traditional textile RF device manufacturing techniques. It can realize an environmental-friendly fast production of large area textile electronics with complex structures. Various types of textile electromagnetic component were knitted and studied. While there are still some aspects which are not covered in this thesis and further research listed below needs to be performed in the future.

- The knitted slotted waveguide antenna described in chapter 6 was linear polarized. When H-plane bending occurred, its radiation pattern rotated along the bending direction. The measurement showed that the H-plane bent SWA would experience a cross polarized transmission if the receiving antenna was kept the same orientation. Consequently, H-plane bending must be avoided in practice if the orientation of the knitted SWA or the receiving antenna cannot be changed. However, if I can manage to develop a knitted SWA with a circular polarized radiation, H-plane bending will no longer to a problem.
- In this thesis, to characterize the textile FSSs, knitted samples were all arranged and measured as flat planar surfaces. However, knitted textile FSSs are inherently soft and flexible. They are likely to be stretched, compressed and curved when applied in practise. When a textile FSS is under these conditions, it will no longer have uniform cell size. Therefore, the deformed textile FSS can no longer be analysed and modelled as a single unit cell and its performance will be different. Further research needs to focus on the study of the textile FSS's performance under different deformations.
- The study on the textile hexagonal loop FSSs showed that when the ECA (electrically conducting area) was fabricated with a low knitting density, its conductivity demonstrated inconsistency at different frequencies. The air gaps between conducting stitches became more significant at high frequency, which resulted in a lower effective conductivity of the knitting conducting patterns and affected the FSS's performance. I aim to develop a simple equivalent model to predict the knitted textile electronics' performance accurately at high frequency in the future.

Reference

[1] Asis Patnaik and Sweta Patnaik, "Origin of Smart Textiles", *Fibres to Smart Textile, Advance in Manufacturing, Technologies and Applications*, Chapter: 17.2, PP:331-333. CRC Press, 1st Edition, Aug 2019.

[2] Steve Mann. "An historical account of the 'WearComp' and 'WearCam' inventions developed for applications in 'personal imaging". *Digest of Papers. First International Symposium on Wearable Computers*. USA, 13-14 Oct 1997.

[3] O. Shivers, et al., "Body Talk and the Body Net: A personal Information Infrastructure, Personal Information Architecture," *Note 1, MIT Laboratory for Computer Science*, Cambridge, MA, December 1993.

[4] T. Zimmerman, "Personal area Networks: Near Field Intra-Body Communications," *MIT Media Lab*, IBM Systems J., Vol. 35, No. 3&4, 1996.

[5] Levi's and Philips, "2000 Philips/Levi's ICD+ Jacket", *Vhm design Futures*, project 192, Summer 2000.

[6] A. Schmidt, H.-W. Gellersen, C. Merz, "Enabling implicit human computer interaction: a wearable RFID-tag reader", *Digest of Papers. Fourth International Symposium on Wearable Computers*, IEEE, Oct. 2000.

[7] P. J. Massey, "GSM Fabric Antenna for Mobile Phones Integrated within Clothing", *IEEE Antennas and Propagation Society International Symposium*, Volume: 3, P: 452-455, Boston, USA, July 2001.

[8] The Hug Shirt, Cute Circuit. [Online] http://cutecircuit.com/the-hug-shirt/

[9] Markets and Markets, "Smart Clothing Market by Textile Type, Product Type, End-User, and Geography - Global Forecast to 2024", Market Research Report, PP:139, Nov 2019, [Online] https://www.marketsandmarkets.com/Market-Reports/smart-clothing-market56415040.html?gclid=Cj0KCQiA2vjuBRCqARIsAJL5aJvRL8QVH2g02xAg3jgjI31hsP XT8pYwTyKpxboJJgh1fgd8NgrCgaAtmhEALw_wcB.

[10] P. S. Hall and Y. Hao, Antennas and Propagation for Body-Centric Wireless Communications. London, UK: Artech House, 2012.

[11] J. Lebaric, A. T. Tan, “Ultra-Wideband RF Helmet Antenna”, IEEE MILCOM 2000, Volume: 2, P: 591-594, Oct 2000.

[12] P. J. Massey, “GSM Fabric Antenna for Mobile Phones Integrated within Clothing”, *IEEE Antennas and Propagation Society International Symposium*, Volume: 3, P: 452-455, Boston, USA, July 2001.

[13] S. Zhu and R.J. Langley, “Dual band Body Worn Antenna”, *Second European Conference on Antennas and Propagation (EuCAP),* p: 1-4, 11-16 Nov 2007.

[14] Milan Svanda, Milan Polivka, “Dual Band Wearable UHF RFID Tag”, *The Second European Conference on Antennas and Propagation (EuCAP),* IET, Edinburgh, UK, 11-16 Nov. 2007.

[15] L. Vallozzi, W. Vandendriessche, H. Rogier, C. Hertleer and M. Scarpello, “Wearable Textile GPS Antenna for Integration in Protective Garments”, *Proceedings of the Fourth European Conference on Antennas and Propagation*, IEEE, Barcelona, Spain, 12-16 April 2010.

[16] T. Kennedy, P. Fink, A. Chu, N. Champagne and G. Lin, “Body-Worn E-Textile Antennas: The Good, the Low-Mass, and the Conformal”, *IEEE Transactions on Antennas and Propagation*, IEEE, Volume: 57 , Issue: 4 , April 2009.

[17] T. Blecha, R. Linhart and J. Reboun, “Screen Printed Antennas on Textile Substrate”, *Electronics System-Integration Technology Conference (ESTC),* P: 1-4, Sep 2014.

[18] R. Valmiro, H. Kitaguti and S. Barbin, “A silk-screen printed RFID tag antenna”, Asia-Pacific Microwave Conference (APMC), P: 1-2, Dec 2015.

[19] S. Zhang, R. Seager, A. Chauraya, W. Whittow and Y. Vardaxoglou, “Textile manufacturing techniques in RF devices”, *Loughborough Antennas and Propagation Conference (LAPC)*, P: 182-186, Nov 2014.

[20] W. Whittow, A. Chauraya, J. Vardaxoglou, Y. Li, R. Torah, K. Yang, S. Beeby, and J. Tudor, “Inkjet-Printed Microstrip Patch Antennas Realized on Textile for Wearable Applications,” *IEEE Antennas and Wireless Propagation Letters*, Volume: 13, P: 71-74, 2014.

[21] J. Choi, Y. Kim, K. Lee and Y. Chung, “Various wearable embroidery RFID tag antenna using electro-thread”, *Antennas and Propagation Society International Symposium*, P: 1-4, July 2008.

[22] N. Ishak, M. Jamlos, M. Jamlos, S. Ahmad and M. Karim, “Embroidery Wearable Snail Antenna (EWSA) design”, *IEEE International RF and Microwave Conference (RFM)*, P: 82-85, Dec 2013.

[23] L. Bao, P. Ooi and J. Chin, “The Effect of Different Structures of Embroidery Patch Antenna on Polymer Substrate with Identical Embroidery Properties”, *IEEE Antennas and Propagation Society International Symposium (APSURSI)*, P: 840-841, July 2014.

[24] W. Whittow, “3D Printing, Inkjet Printing and Embroidery Techniques for Wearable Antennas”, *10th European Conference on Antennas and Propagation (EuCAP)*, P: 1-4, April 2016.

[25] A. Chauraya, R. Seager, W. Whittow, S. Zhang and Y. Vardaxoglou, “Embroidered Frequency Selective Surfaces on Textiles for Wearable Applications”, *IEEE Loughborough Antennas and Propagation Conference (LAPC)*, P: 388-391, 2013.

[26] R. Seager, A. Chauraya, J. Bowman, M. Broughton and N. Nimkulrat, “Fabrication of Fabric Based Frequency Selective Surfaces (FSS)”, *IEEE European Conference on Antennas and Propagation (EuCAP)*, P: 1978-1980, April 2014.

[27] R. Seager, S. Zhang, A. Chauraya, W. Whittow, Y. Vardaxoglou, T. Acti, and T. Dias, “Effect of the Fabrication Parameters on the Performance of Embroidered Antennas,” *IET Microwaves, Antennas & Propagation*, volume: 7, No: 14, P. 1174–1181, Nov 2013.

[28] T. Nguyen, J. Chung and B. Lee, “Radiation Characteristics of Woven Patch Antennas Composed of Conductive Threads”, *IEEE Transactions on Antennas and Propagation*, Volume: 63, Issue: 6, P: 2796-2801, March 2015.

[29] Y. Ouyang and W. J. Chappell, “High Frequency Properties of Electro Textiles for Wearable Antenna Applications,” *IEEE Transactions on Antennas and Propagation*, Volume: 56, No: 2, P: 381-389, Feb 2008.

[30] R. Seager, A. Chauraya, M. Broughton and J. Bowman, “Towards Conformal Woven Frequency Selective Surfaces (FSS)”, *Loughborough Antennas & Propagation Conference (LAPC)*, P: 1-3, Nov 2015.

[31] D. Patron, W. Mongan, T. Kurzweg and A. Fontecchio, “On the Use of Knitted Antennas and Inductively Coupled RFID Tags for Wearable Applications”, *IEEE Transactions on Biomedical Circuits and Systems*, Volume: 10, Issue: 6, P: 1047-1057, April 2016.

[32] S. Zhang, A. Chauraya, R. Seager, Y. Vardaxoglou, W. Whittow, T. Acti, T. Dias, “Fully Fabric Knitted Antennas for Wearable Electronics”, USNC-URSI Radio Science Meeting (Joint with AP-S Symposium), P: 215, July 2013.

[33] A. Tennant, W. Hurley and T. Dias, “Experimental Knitted, Textile Frequency Selective Surfaces”, *IET Electronics Letters*, Volume: 48, Issue: 22, P: 1386-1388, Oct 2012.

[34] T. Hussain, Q. Cao, J. Kayani and I. Majid, “Miniaturization of Frequency Selective Surfaces Using 2.5-D Knitted Structures: Design and Synthesis”, IEEE Transactions on Antennas and Propagation, Volume: 65, Issue: 5, P: 2405-2412, May 2017.

[35] P. Gupta, “What Are the Main Differences Between Weaving and Knitting and Woven and Knitted Fabrics?”, Felt Magnet, [online] https://feltmagnet.com/textiles-sewing/What-are-the-main-differences-between-Weaving-and-Knitting, May 2017.

[36] Fabric Manufacturing Technology, “What is Sizing, Purpose of Textile Sizing, Properties of Sized Yarn”, *Textile Fashion Study*, [online] http://textilefashionstudy.com/what-is-sizing-purpose-of-textile-sizing-properties-of-sized-yarn/,11 May 2012.

[37] Knitting, “What Is Knitting and Weaving|Difference between Knitting and Weaving”, *Textile Fashion Study*, [online] http://textilefashionstudy.com/what-is-knitting-and-weaving-difference-between-knitting-and-weaving/, May 2012.

[38] Shima Seiki SWG091N Knitting Machine, “Datasheet”, *Shima Seiki MFG., LTD*, Japan.

[39] Laura Corchia, Giuseppina Monti, Luciano Tarricone, “Wearable Antennas: Nontextile Versus Fully Textile Solutions”, *IEEE Antennas and Propagation Magazine*, Volume: 61 , Issue: 2, PP:71-83, April 2019.

[40] N. Chahat, M. Zhadobov, and R. Sauleau, "Yagi-Uda Textile Antenna for on-body Communications at 60 GHz", *7th European Conf. Antennas and Propagation*, 2013, pp. 411–413.

[41] G. Monti, L. Corchia, and L. Tarricone, "Fabrication Techniques for Wearable Antennas," *European Microwave Conf*, Nuremberg, Germany, 2013, pp. 1747–1750.

[42] L. Catarinucci, R. Colella, and L. Tarricone, "Smart Prototyping Techniques for UHF RFID tags: Electromagnetic Characterization and Comparison with Traditional Approaches," *Electromagn. Res*, vol. 132, pp. 91–91, 2012.

[43] B. Sanz-Izquierdo and J. C. Batchelor, "WLAN Jacket Mounted Antenna," *Int. Workshop Antenna Technology: Small and Smart Antennas Metamaterials and Applications*, 2007, pp. 57–60.

[44] S. Hong, S. H. Kang, Y. Kim, and C. W. Jung, "Transparent and Flexible Antenna for Wearable Glasses Applications," *IEEE Trans. Antennas Propag*, vol. 64, no. 7, pp. 2797–2804, 2016.

[45] A. Vorobyov, C. Henemann, and P. Dallemagne, "Liquid Metal Based Antenna for Wearable Electronic," *10th European Conf. Antennas and Propagation*, 2016, pp. 1-3.

[46] Q. Liu, K. L. Ford, R. Langley, A. Robinson, and S. Lacour, "Stretchable Antennas," *European Conf. Antennas and Propagation*, 2012, pp. 10–13.

[47] O. O. Rakibet, C. V. Rumens, J. C. Batchelor, and S. J. Holder, "Epidermal Passive RFID Strain Sensor for Assisted Technologies," *IEEE Antennas Wireless Propag. Lett*, vol. 13, pp. 814–817, Apr. 2014.

[48] N. H. M. Rais, P. J. Soh, F. Malek, S. Ahmad, N. B. M. Hashim and P. Hall, "A Review of Wearable Antenna", *Loughborough Antennas & Propagation Conference (LAPC)*, P: 225-228, Nov 2009.

[49] K.Eom and H.Arai, "Smart suit: Wearable sheet-like waveguide for body-centric wireless communications", Wireless Technology Conference (EuWIT), 2010 European, IEEE, 2010.

[50] Kamardin, K and Rahim, M.K.A, "Textile Waveguide Sheet with Artificial Magnetic Conductor Structures for Body Centric Wireless Communication", Applied Electromagnetics (APACE), 2012 IEEE Asia-Pacific Conference, pp. 257 – 261, Dec. 2012.

[51] Kunsun Eom and Arai, H, "Flexible sheet-shaped waveguide for body-centric wireless communications", Radio and Wireless Symposium (RWS), 2010 IEEE, pp. 76 – 79, Jan. 2010.

[52] Sanz-Izquierdo, B and Wu, L, "Textile integrated waveguide slot antenna", Antennas and Propagation Society International Symposium (APSURSI), 2010 IEEE, July 2010.

[53] Moro, R and Agneessens, S, "Wearable textile antenna in substrate integrated waveguide technology", Electronics Letters, Volume:48, Issue: 16, pp:985 – 987, Aug.2012.

[54] Sen Yan and Soh, P.J, "Wearable dual-band composite right/ left-handed waveguide textile antenna for WLAN applications", Electronics Letters, Volume: 50, Issue: 6, pp:424 – 426, March. 2014.

[55] P. Saloncn, L. SydHnheimo, M. Keskilammi and M. Kivikoshi, "A Small Planar Inverted-F Antenna for Wearable Applications" *3rd International Symposium on Wearable Computers*, P.95-98, San Francisco, October 1999,

[56] P. J. Massey, "Mobile phone fabric antennas integrated within clothing", *IEEE Eleventh International Conference on Antennas and Propagation*, Publication No.480, Manchester, UK, April 2001.

[57] P. Salomen, L. Hurme, "A Novel Fabric WLAN Antenna for Wearable Applications", *IEEE Antennas and Propagation Society International Symposium*, USA, 2003

[58] C. Hertleer, A. Tronquo, H. Rogier, L. Vallozzi, L. Langenhove, "Aperture-Coupled Patch Antenna for Integration into Wearable Textile Systems", *IEEE Antennas and Wireless Propagation Letters*, Volume: 6, PP: 392 – 395, August 2007.

[59] Luigi Vallozzi, Hendrik Rogier, Carla Hertleer, "Dual Polarized Textile Patch Antenna for Integration into Protective Garments", *IEEE Antennas and Wireless Propagation Letters*, Volume: 7, PP: 440 – 443, May 2008.

[60] E. Kaivanto, J. Lilja, M. Berg, E. Salonen, P. Salonen, "Circularly Polarized Textile Antenna for Personal Satellite Communication", *IEEE Proceedings of the Fourth European Conference on Antennas and Propagation*, Barcelona, Spain, July 2010.

[61] Antenna Theory, “Specific Absorption Rate (SAR)”, [online] http://www.antenna-theory.com/definitions/sar.php.

[62] P. Salonen, Fan Yang, Y. Rahmat-Samii, M. Kivikoski, “WEBGA - wearable electromagnetic band-gap antenna”, *IEEE Antennas and Propagation Society Symposium*, USA, June 2004.

[63] Shaozhen Zhu, Richard Langley, “Dual-Band Wearable Textile Antenna on an EBG Substrate”, *IEEE Transactions on Antennas and Propagation*, Volume: 57, Issue: 4, PP: 926-935, April 2009.

[64] Adel Y. I. Ashyap, Zuhairiah Zainal Abidin, “Compact and Low-Profile Textile EBG-Based Antenna for Wearable Medical Applications”, *IEEE Antennas and Wireless Propagation Letters*, Volume: 16, PP: 2550-2553, July 2017.

[65] Ala Alemaryeen, Sima Noghanian, “On-Body Low-Profile Textile Antenna with Artificial Magnetic Conductor”, *IEEE Transactions on Antennas and Propagation*, Volume: 67, Issue: 6, PP: 3649-3656, June 2019.

[66] M. Tanaka and J. Jang, “Wearable Microstrip Antenna”, *IEEE Antennas and Propagation Society International Symposium*, Volume: 2, P: 704-707, June 2003.

[67] Q. Bai and R. Langley, “Fabric patch antenna array bending study”, *Loughborough Antennas and Propagation Conference (LAPC)*, P: 1-4, 12-13 Nov 2012.

[68] Q. Bai, J. Rigelsford and R. Langley, “Crumpling of Microstrip Antenna Array”, *IEEE Transactions on Antennas and Propagation*, Volume: 61, Issue: 9, P: 4567-4576, 18 June 2013.

[69] A. Tennant, W. Hurley and T. Dias, “Experimental Knitted, Textile Frequency Selective Surfaces”, *IET Electronics Letters*, Volume: 48, Issue: 22, October 25 2012.

[70] A. Chauraya, R. Seager, W. Whittow, S. Zhang and Y. Vardaxoglou, “Embroidered Frequency Selective Surfaces on Textiles for Wearable Applications”, *IEEE Loughborough Antennas and Propagation Conference (LAPC)*, P: 388-391, 2013.

[71] R. Seager, A. Chauraya, J. Bowman, M. Broughton and N. Nimkulrat, “Fabrication of Fabric Based Frequency Selective Surfaces (FSS)”, *IEEE European Conference on Antennas and Propagation (EuCAP)*, P: 1978-1980, April 2014.

[72] M. Ghebrebrhan, F. Aranda, G. Walsh, “Textile Frequency Selective Surface”, *IEEE Microwave and Wireless Components Letters*, Volume: 27, Issue: 11, P: 989-991, Oct 2017.

[73] W. Whittow, Y. Li, R. Torah, K. Yang, S. Beeby and J. Tudor, “Printed Frequency Selective Surfaces on Textiles”, *IET Electronics Letters*, Volume: 50, Issue: 13, P:916-917, June 2014.

[74] Leticia Alonso-González, Samuel Ver-Hoeye and Miguel Fernández-Garcia, “Broadband Flexible Fully Textile-Integrated Band-stop Frequency Selective Surface”, IEEE Transactions on Antennas and Propagation, Volume: 66, Issue: 10, pp: 5291-5299, Oct. 2018

[75] IEEE, “IEEE standard definitions of fundamental waveguide terms”, *IEEE*, New York: Institute of Electrical and Electronics Engineers, P: 1-10, 1980.

[76] Marcuvitz, Nathan, “Waveguide as Transmission Line”, *Waveguide Handbook*, [UK]: Constable and Company Ltd., Chapter 1, P: 1-3. 1965.

[77] F. R. Connor, “Waveguide Theory”, *Introductory Topics in Electronics and Telecommunication Wave Transmission*, P: 52-64, London: Edward Arnold, ISBN 0-7131-3278-7, 1971.

[78] Keith W. Whites, “lecture 10: TEM, TE and TM modes for Waveguides”, *EE48: Microwave Engineering*, Lecture Notes, Dakota School of Mines and Technology, 2013.

[79] Dr. S. Cruz-Pol, In “Rectangular Waveguides”, *INEL: 6216*, Lecture Notes, University of Puerto Rico Mayagüez.

[80] IET, “Cut-off Wavelengths and Frequencies of Standard Rectangular Waveguides”, *Electronic Letters*, Institution of Engineering and Technology, Volume: 5, Issue: 17, P: 410-412, 21 August 1969.

[81] B.K. Wang, K.Y. Lam, M.S. Leong and P.S. Kooi, “Elliptical Waveguide Analysis Using Improved Polynomial Approximation”, *Microwaves, Antennas and Propagation IEE Proceedings*, Volume 141, Issue 6, P: 483-488, Dec 1994.

[82] G.D. Tsogkas, J.A. Roumeliotis and S.P. Savaidis, “Cut-off Wavelengths of Elliptical Metallic Waveguides”, *IEEE Transactions on Microwave Theory and Techniques*, Volume: 57, Issue: 10, P: 2406-2415, Oct 2009.

[83] Marcuvitz, Nathan, “Elliptical Waveguides”, *Waveguide Handbook*, [UK]: Constable and Company L,td, Chapter 2, P: 80-88. 1965.

[84] https://www.ebay.com/itm/Waveguide-Elbow-Bend-H-Plane-CPR90-WR90 /362377447241.

[85] Rayleigh, Lord, “On the passage of electric waves through tubes, or the vibrations of dielectric cylinders”, Phil. Mag. (Ser. 5) 53, No. 261, 125-132. 1897.

[86] Buchholz, H, “The influence of the curvature of rectangular waveguides on the phase dimension of ultra-short waves”, Elek. Nachrichtentech, 16, No.3, 73-85, 1939.

[87] Morimoto, S, “Electromagnetic waves passing through curved waveguides”, *Research on wave guides and electromagnetic horns (Rept. III)*. Electrotech. J. (Tokyo) 4, 64-67, 1940.

[88] Kislyuk, M. Zh., “Waveguide bend of rectangular cross-section”, *Radio Eng*. I6, No. 4, 1-8; transl. of Radiotekhnika, 16, No.4, 3-10. 1946.

[89] Rice, S. 0, “Reflections from circular bends in rectangular wave guides-matrix theory”, *Bell Syst. Tech. J*. 27, No.2, 305-349. 1948.

[90] Andreasen.M.G, “Propagation of fundamental waves in circular and square curved waveguides of constant curvature”, *Arch. Elek*. Ubertragung 12, No. 9, 414-418.1958.

[91] J. Alan Cochran, Robert G. Pecina, “Mode propagation in continuously curved waveguides”, *Radio Science*, Volume: 1, Issue: 6, PP: 679 – 696, June 1966.

[92] J. Kemp, “Waveguides in electrical communication”, *Journal of the Institution of Electrical Engineers - Part III: Communication Engineering, including the Proceedings of the Wireless Section of the Institution*, Volume: 90, Issue: 11, Sep 1943.

[93] H. Meng, T. Li, W. Dou, “Design of Slotted Waveguide Antenna Array at W Band”, *10th UK-Europe-China Workshop on Millimetre Waves and Terahertz Technologies (UCMMT)*, P:1-2, Sep 2017.

[94] D. M. Pozar, “Transmission Line Theory”, *Microwave Engineering*, 2nd Edition, Chapter 2, P: 56-65, John Wiley & Sons, Inc, 1998.

[95] T. K. Wu, “Fundamentals of Periodic Structures”, *Frequency Selective Surface and Grid Array*, Chapter 1, P. 1-18, John Wiley & Sons, Inc, 1995.

[96] P. P. Sarkar, S. K. Chowdhury, "Experimental Investigation on the Frequency Selective Property of An Array of Printed Dipoles", *National Conference on Microwave, Antenna and propagation*, P: 115-116, 2001.

[97] M. K. Pain, P. P. Sarkar, "Theoretical Investigation on Reduction of Patch Area of a Frequency Selective Surface", *National Conference in Engineering Education*, Feb 2008.

[98] P. Samaddar, P. P. Sarkar, "Polarization Independent Triple Band Single Layer Frequency Selective Structure", *International Journal of Computer Applications in Engineering Sciences*, Volume 3, P: 87-89, 2013

[99] M. K. Pain, P. P. Sarkar. "A Novel Investigation on Size Reduction of a Frequency Selective Surface", *Microwave, Optical, Technol Letters*, Volume 49, No 11, P: 2820-2821, 2007.

[100] P. Samaddar, P. P. Sarkar, "Band Pass Planer and Hemispherical FSS Comprising of Tripole Element", *National Conference on Communication, Device, Information and Intelligence Systems (CDIIS)*, March 2014.

[101] R. Ulrich, "Far-infrared Properties of Metallic Mesh and Its Complementary Structure", *Infrared Physics*, Vol.7, P. 37-55, Pergamon Press Ltd, 1967.

[102] T. Leonard and L. Young, "Frequency Selective Surfaces", *Antennas and Propagation Society International Symposium*, Volume: 15, P. 560-563. June 1977.

[103] S. W. Lee, G. Zarrillo and C. L. Law, "Simple Formulas for Transmission through periodic metal grids or plates", *IEEE Trans on Antennas and Propagation*, Volume: 30, Issue: 5, P. 904-909, Sep 1982.

[104] R. Mittra, C. Chan and T. Cwik, "Techniques for Analyzing Frequency Selective Surface- A Review", *Proceeding of the IEEE*, Volume: 76, Issue: 12, Dec 1988.

[105] Munk. B.A, "Frequency Selective Surfaces: Theory and Design", Wiley Online Library, Hoboken, NJ, USA, Volume 29, 2000.

[106] A.O. Tuzov, "Scattering of Electromagnetic Waves Incident Normally on Square Patch-Type FSS Placed at the Interface between Two Dielectric Media", *Classical Physics*, Cornell University, 18 May 2017.

[107] Filippo Costa, Agostino Monorchio and Giuliano Manara, “Efficient Analysis of Frequency-Selective Surfaces by a Simple Equivalent-Circuit Model”, *IEEE Antennas and Propagation Magazine*, Volume: 54, Issue: 4, pp.35-48, Aug. 2012.

[108] M. Ohira, H. Deguchi, M. Tsuji and H. Shigesawa, “Analysis of Frequency-Selective Surfaces with Arbitrarily Shaped Element by Equivalent Circuit Model”, *Electronics and Communications in Japan* (Part II: Electronics), 88, 6, pp. 9-17, June 2005.

[109] X. Jia and A. Tennant, “A Knitted Textile Waveguide”, *Antennas and Propagation Conference (LAPC), Loughborough*, IEEE, pp: 679-682 Nov 2014.

[110] X. Jia and A. Tennant, “Knitted Textile Waveguide Bending”, *Antennas and Propagation (EUCAP), Portugal, 9 th European Conference*, IEEE, pp: 1-4, April 2015.

[111] X. Jia and A. Tennant, “Moisture Effects on a Knitted Waveguide*”, Antennas and Propagation Conference (LAPC)*, Loughborough, IEEE, Nov 2016.

[112] Sareh.T, Mohammadreza. K and Simarjeet.S.S, “Modified Fabry–Perot interferometric method for waveguide loss measurement”, *Applied Optics*, Volume 37, Issue 35, PP:6625. 2008.

[113] Eric Bogatin, “How Return Loss Gets its Ripples”, *BeTheSignal*, Published by Prentice Hall, 2009.

[114] P130 Technical data sheet, Statex Produktions & Vertriebs GmbH, Bremen, Germany.

[115] A.Andryieuski, S.M.Kuznetsova, S.V.Zhukovsky, Y.S.Kivshar and A.V. Lavrinenko, “Water: Promising Opportunities For Tunable All-dielectric Electromagnetic Metamaterials”, *Nature*, Scientific Reports Volume 5, Article number: 13535, 2015.

[116] IET, “Sir Joseph John Thomson, O.M., F.R.S.”, in *Journal of the Institution of Electrical Engineers*, Volume: 87, Issue: 528, Pages: 718 – 719, 1940.

[117] McLachlan, Norman W, “Theory and application of Mathieu functions”, Page: 8, 1947.

[118] W. H. Watson, "The Physical Principles of Waveguide Transmission and Antenna Systems," Oxford Univessity Press, New York, 1947.

[119] A. Hu and C. Lunden, “Rectangular-ridge waveguide slot array”, *IRE Transactions on Antennas and Propagation*, Volume: 9, Issue: 1, Pages 102-105, 1961.

[120] J. Ramsay and B. Popovich, “Series slotted waveguide array antennas”, *IRE International Convention Record*, Volume:11, Pages: 30-55, 1963.

[121] I. da Costa, R. Santos, “A dual-band slotted waveguide antenna array for radars applications”, *Microwave and Optoelectronics Conference (IMOC)*, 2015 SBMO/IEEE MTT-S International, IEEE, Jan. 2016.

[122] R. Hermansyah, F. Zulkifli, E. Rahardjo, “Radiation characteristics of slotted waveguide array antenna for X-Band dual-polarized weather radar”, *Progress in Electromagnetic Research Symposium*, IEEE, Nov. 2016.

[123] X. Jia and A. Tennant, “A Knitted Slotted Waveguide Antenna”, *Antennas and Propagation Conference (LAPC)*, Loughborough, IEEE, Nov 2015.

[124] A. Balanis, “Chapter 6.4 N-Element Linear Array: Directivity”, *Antenna Theory: Analysis and Design*, 3rd Edition, Wiley-Interscience, 2005.

[125] J. C. Batchelor, E. A. Parker, J. A. Miller, V. Sanchez-Romaguera and S.G. Yeates, “Inkjet Printing of Frequency Selective Surfaces”, *IET Electronics Letters*, Volume: 45, No: 1, PP: 7-8, January 2009

[126] W.G. Whittow, Y. Li, R. Torah, K. Yang, S. Beeby, J. Tudor, “Printed Frequency Selective Surfaces on Textiles”, *Electronics Letters*, Volume: 50, Issue: 13, PP: 916-917. June 2014.

[127] Serge Berthier, Jacques Lafai, “Effective medium theory: Mathematical determination of the physical solution for the dielectric constant”, *Optics Communications*, Volume 33, Issue 3, Pages 303-306, June 1980.

[128] Rolf Landauer, “Electrical conductivity in inhomogeneous media”, *AIP Conference Proceedings*, Volume 40, Issue 2, 1978.